SUPERCONDUCTIVITY, INCLUDING HIGH-TEMPERATURE SUPERCONDUCTIVITY

On the influence of a magnetic field on structural transitions in HTSCs

A. A. Mamaluĭ* and I. N. Sablin

National Technical University "Khar'kov Polytechnical Institute," ul. Frunze 21, Khar'kov, 61002, Ukraine
(Submitted March 13, 2001; resubmitted April 28, 2001)
Fiz. Nizk. Temp. **27**, 1227–1231 (November 2001)

The question of the influence of mechanical stresses, induced by pinning of magnetic flux, on low-temperature structural phase transitions in HTSC systems is examined. A model is applied to a specific structural transition in $YBa_2Cu_3O_{6+x}$ and makes it possible to describe the experimentally observed anomalies of various physical properties exhibiting hysteretic behavior in the temperature range 50–200 K. The magnetostriction induced change, studied in this work, in the position of the boundaries of the hysteretic region is estimated. © *2001 American Institute of Physics.* [DOI: 10.1063/1.1421454]

1. INTRODUCTION

A characteristic feature of high-temperature superconductors (HTSCs) is the existence of strong anharmonic effects. This feature is manifested, for example, in the librational modes of the apical chain oxygen in $YBa_2Cu_3O_{6+x}$. In discussions of mechanisms of HTSC a great deal of attention is devoted to the analysis of the role of lattice anharmonicity and the associated structural instability.[1] The structural instability of $YBa_2Cu_3O_{6+x}$ is apparently responsible for the anomalies observed in the temperature dependences of the lattice constants, the thermal expansion coefficient in the direction of anharmonic oscillations of oxygen ions, the thermal conductivity, and other parameters.[2–5] In connection with the possibility of structural changes, the effect of pressure on the critical temperature has been studied in a number of works.[6]

A magnetic field is also an external factor that influences a structural phase transition.[7,8] For example, in the compound $BaTiO_3$, possessing perovskite structure and consequently similar to superconducting copper oxides, a 20 T magnetic field shifts the structural phase transition from the high-temperature unpolarized phase into the ferroelectric phase by 0.2–0.3 K depending on the geometry of the experiment.[8] The dynamics of the ferroelectric interphase boundaries in strong magnetic fields was studied in Ref. 9, and it was noted that a similar situation is possible for HTSC systems. In Refs. 8 and 9 it was assumed that the influence of the magnetic field is due primarily to the magnetoelectric effect, which dominates magnetostriction, so that the latter can be neglected. However, the low-temperature structural transition observed in HTSC systems, which occurs at a temperature below the critical temperature T_c, is probably due to the strong magnetostriction due to pinning of the magnetic flux.[10,11] In the present work the influence of the pinning-induced mechanical stresses on the structural phase transition in HTSCs is investigated.

2. DESCRIPTION OF THE MODEL

We shall study a type–II superconductor in the form of an infinite plate of thickness $2d$ placed in a magnetic field B_a oriented parallel to the plane of the sample. The plate is arranged perpendicular to the z axis, and the center of the plate lies at the center of the coordinate system. A model of a critical state is proposed for describing the electrodynamics of the superconductor. Let the magnetic field initially be zero inside and outside the sample. In addition, let the critical current j_c be independent of the magnetic induction. Then Maxwell's equation for the induction $B_z = B$ is

$$\frac{dB}{dz} = \begin{cases} \mu_0 j_c, & (d-l) < z < d \\ 0, & |z| < (d-l) \\ -\mu_0 j_c, & -d < z < (l-d) \end{cases} \tag{1}$$

with the boundary condition $B(\pm d) = B_a$, where μ_0 is the magnetic permeability of the vacuum and $l = B_a/(\mu_0 j_c)$. Using Eq. (1) we find

$$B = \begin{cases} B_a - \mu_0 j_c (d-z), & (d-l) \leqslant z \leqslant d \\ 0, & |z| < (d-l). \\ B_a - \mu_0 j_c (d+z), & -d \leqslant z \leqslant (l-d) \end{cases} \tag{2}$$

The expressions for the pinning-induced stresses $\sigma(z)$ with a prescribed magnetic flux density distribution $B(z)$ and their averages along the z axis are[10]

$$\sigma = \frac{1}{2\mu_0}(B^2(z) - B_a^2)$$

$$= \begin{cases} -B_a j_c (d-z) + \frac{1}{2}\mu_0 j_c^2 (d-z)^2, & (d-l) \leqslant z \leqslant d \\ -B_a^2/2\mu_0, & |z| < (d-l), \\ -B_a j_c (d+z) + \frac{1}{2}\mu_0 j_c^2 (d+z)^2, & -d \leqslant z \leqslant (l-d) \end{cases} \tag{3}$$

$$\bar{\sigma}=\frac{1}{2\mu_0 d}\int_0^d (B^2(z)-B_a^2)dz=-\frac{B_a^2}{2\mu_0}+\frac{B_a^3}{6\mu_0^2 j_c d}. \quad (4)$$

The relations presented above are valid for $l\leqslant d$. If this inequality is violated, then l in Eqs. (2) and (3) must be replaced by d. Then, instead of Eq. (4) we have

$$\bar{\sigma}=\frac{1}{6}\mu_0 j_c^2 d^2-\frac{1}{2}B_a j_c d. \quad (5)$$

A model Hamiltonian, derived using the idea of a local normal coordinate (LNC), designated as $q_{\mathbf{n}}$, is used to investigate the structural phase transitions,[12] including in HTSCs:[13]

$$H=\sum_{\mathbf{n}}\left(\frac{1}{2}m\dot{q}_{\mathbf{n}}^2+V(q_{\mathbf{n}})\right)+\frac{1}{4}\sum_{\mathbf{n},\mathbf{n}'}\varphi_{\mathbf{n}\mathbf{n}'}(q_{\mathbf{n}}-q_{\mathbf{n}'})^2+H_d, \quad (6)$$

where m is the effective mass corresponding to the critical mode; $\varphi_{\mathbf{n}\mathbf{n}'}$ describes the coupling of the displacements of the LNC; $V(q_{\mathbf{n}})$ is an anharmonic local potential, which here is assumed to be of the form $V(q_{\mathbf{n}})=(-A/2)q_{\mathbf{n}}^2+(B/4)q_{\mathbf{n}}^4$; H_d is the part of the Hamiltonian that describes the coupling of the critical mode and the lattice deformation:

$$H_d=\sum_{\mathbf{n},\alpha}\frac{1}{2}M\dot{u}_\alpha^2(\mathbf{n})+\frac{1}{2}\sum_{\mathbf{n},\alpha,\beta,\gamma,\delta}u_{\alpha\beta}(\mathbf{n})u_{\gamma\delta}(\mathbf{n})C_{\alpha\beta\gamma\delta}$$

$$+\sum_{\mathbf{n},\alpha,\beta}u_{\alpha\beta}(\mathbf{n})q_{\mathbf{n}}^2G_{\alpha\beta}-\sum_{\mathbf{n},\alpha,\beta}u_{\alpha\beta}(\mathbf{n})\sigma_{\alpha\beta}(\mathbf{n}), \quad (7)$$

where $u_{\alpha\beta}(\mathbf{n})$ and $\dot{u}_\alpha(\mathbf{n})$ are, respectively, the displacement and velocity of the center of mass of the nth cell with mass M; $C_{\alpha\beta\gamma\delta}$ are the stiffness coefficients; and, $G_{\alpha\beta}$ determine the coupling of the soft mode and the deformation.

Calculating the free energy in the pseudoharmonic approximation and neglecting resonance terms of the form $\langle\delta q_{\mathbf{n}}\delta u_{\alpha\beta}(\mathbf{n})\rangle$, which contain the fluctuation parts separated from $q_{\mathbf{n}}$ and $u_{\alpha\beta}(\mathbf{n})$, we obtain from the condition that this term be minimum the following equations for the equilibrium values $\langle q_{\mathbf{n}}\rangle$ and $\langle u_{\alpha\beta}(\mathbf{n})\rangle$:

$$-A\langle q_{\mathbf{n}}\rangle+B\langle q_{\mathbf{n}}\rangle^3+3B\langle q_{\mathbf{n}}\rangle\langle\delta q_{\mathbf{n}}^2\rangle$$

$$+2\langle q_{\mathbf{n}}\rangle\sum_{\alpha,\beta}\langle u_{\alpha\beta}(\mathbf{n})\rangle G_{\alpha\beta}+\sum_{\mathbf{n}'}\varphi_{\mathbf{n}\mathbf{n}'}(\langle q_{\mathbf{n}}\rangle-\langle q_{\mathbf{n}'}\rangle)=0; \quad (8)$$

$$\sum_{\gamma,\delta}\langle u_{\alpha\beta}(\mathbf{n})\rangle C_{\alpha\beta\gamma\delta}+(\langle q_{\mathbf{n}}\rangle^2+\langle\delta q_{\mathbf{n}}^2\rangle)G_{\alpha\beta}-\sigma_{\alpha\beta}(\mathbf{n})=0.$$

We also used another approximation: all quantities characterizing phonons are calculated for the ''effective'' crystal. Then, in Eq. (8) the quantities $\langle q_{\mathbf{n}}\rangle$, $\langle u_{\alpha\beta}(\mathbf{n})\rangle$, and $\sigma_{\alpha\beta}(\mathbf{n})$ are replaced by the volume-averages $\langle\bar{q}\rangle$, after which Eq. (8) is solved again but now with the local values. Then, for example, in the mean-field approximation, whose applicability is limited to the long-range case, the correlation function is

$$\langle\delta q_{\mathbf{n}}^2\rangle=\langle\delta q^2\rangle=\frac{1}{2\omega}\coth\frac{\omega}{2T}, \quad (9)$$

where the Boltzmann constant is set equal to 1. The equation for the average vibrational frequency is

$$m\omega^2=\Delta^2+\varphi_0, \quad (10)$$

where $\varphi_0=\Sigma_{\mathbf{n}'}\varphi_{\mathbf{n}\mathbf{n}'}$, and the single–particle potential is

$$\Delta^2=-A+3B(\langle\bar{q}\rangle^2+\langle\delta q^2\rangle)+2\sum_{\alpha,\beta}\langle\bar{u}_{\alpha\beta}\rangle G_{\alpha\beta}. \quad (11)$$

3. DISCUSSION

The anomalies of various thermodynamic and kinetic properties of $YBa_2Cu_3O_{6+x}$ and their hysteretic behavior in the temperature range 50–200 K[2–5] are presumably due to a first-order structural phase transition occurring in the system.[13] A first-order phase transition can also be described in the model adopted by taking account of stresses.[14] Since hysteresis is observed in a quite wide region, the stresses should have a large effect and should result in large values of the pressure derivative $\partial T_s/\partial P$, where T_s is the temperature of the structural phase transition. Specifying the model for the given situation, we assume that this transition is possible as a result of the ''condensation'' of the optical mode B_{1u}, associated with the motion of the chain oxygen O1 in the direction of the c axis, at the center of the Brillouin zone. The transition occurs with the formation of a polar phase, and we shall employ information about the double-well nature of the potential in which the oxygen O1 occupies a position shifted perpendicular to the basal plane by the amount $\delta_z=\pm 0.4$ Å.[15] The displacement of the atoms O1 will be in this case the LNC [from Eqs. (8)]. It has been concluded on the basis of measurements of the permittivity by the ultrasonic method and observations of anomalies made in Ref. 16 at temperatures 90 and 170 K that resonance displacement-type ferroelectric phase transitions occur in $YBa_2Cu_3O_{7-\sigma}$. In addition, the authors of Ref. 17, who also observed spontaneous polarization, reported the existence of a piezoelectric effect along the c axis.

We shall now apply the model described above to a $YBa_2Cu_3O_{6+x}$ single crystal in the form of a plate whose c axis is aligned along the z axis. We replace the local stresses (7) by the averages (5) and take account of the one-dimensional deformations only. Here, we take for the effective mass of an oxygen atom participating in a critical vibration $m=400$ Å^{-2} eV^{-1}. The corresponding component of the tensor of elastic moduli $c_{33}=150$ GPa;[18] it is related with C_{3333} from Eq. (7): $c_{33}=C_{3333}/V_c$, where V_c is the unit cell volume in $YBa_2Cu_3O_{6+x}$; and, we take the initial frequency to be $\sqrt{A/m}=336$ cm^{-1}.[19] Then a 20 T magnetic field with critical current $j_c=5\times10^4$ A/cm^2 (Ref. 20) and plate thickness 0.001 m shifts the lower boundary of stability of the high-temperature phase occurring at 50 K by approximately 0.3 K in the direction of higher temperatures. The effect being described is relatively weak and depends on many factors—the geometry of the sample, the critical current, and so on. In the situation at hand the pinning-induced magnetostriction is not the highest possible. For film samples, where the critical field values at nitrogen temperatures are two orders of magnitude larger than that used in the estimate, the effect can be expected to increase.

The effect of a magnetic field, due to the pinning-induced magnetostriction, on a structural phase transition is characterized by a number of features. The result will depend on the magnetic past history of the sample. Another feature is that the magnetic flux and therefore the stresses are distributed nonuniformly. The investigation of phase transitions in the presence of such a nonuniformity is a separate problem and can be solved, for example, on the basis of the Landau theory.[21,22] In Ref. 22 such a problem was modeled by the situation with helium, where the vertical column of liquid ^{4}He was studied in the Earth's gravitational field and the problem was to find T_λ as a function of height. Our model can be used to derive an equation similar to the equation expressing the minimization of the free energy in the Landau theory. If the coupling of the LNC only with a one-dimensional deformation, corresponding to a sample geometry where for definiteness the z axis is oriented in the [001] direction of a lattice with period c in the same direction, is taken into account approximately in the general model adopted here, retaining for this in Eq. (8) only the corresponding parameters $G_{33}\equiv G$ and $C_{3333}\equiv C$ and introducing dimensionless quantities, the local ones depending only on the coordinate z, and the index indicating the position in space is dropped,

$$\langle U\rangle=\frac{G}{A}\langle u\rangle,\quad P=\frac{G^2}{CB},\quad \Sigma=\frac{G_\sigma}{CA},$$

$$\langle Q\rangle=\sqrt{B/A}\langle q\rangle,\quad Z=\sqrt{2A/c^2\varphi_0}z, \tag{12}$$

then, combining the expression (8) and passing to the continuum limit (see Ref. 12), we obtain the desired equation in the form

$$\langle Q\rangle(\langle\delta Q^2\rangle(3-2P)-1+2\Sigma)$$
$$+\langle Q\rangle^3(1-2P)-\frac{d^2}{dZ^2}\langle Q\rangle=0. \tag{13}$$

This equation, in contrast to the equations of Landau's theory, has no artificially introduced parameters, including temperature-dependent ones, while all drawbacks characteristic of the mean-field approximation remain in the model employed. The equation (13) cannot be solved analytically, and we confine ourselves only to qualitative arguments. Thus, for certain conditions an equilibrium boundary can arise between both phases in the sample.[21] Since boundaries are present (the surfaces of the plate), a classification of conditions on them for the differential equation (13) is admissible.[23] Simplified numerical solutions of Eq. (13) and constructions of the profiles of the dimensionless order parameter $\langle Q\rangle$ of the structural transition, which illustrate to some extent the general discussions concerning the properties of Eq. (13), though they do not specify what kind of structural transition occurs, were obtained in the classical limit[12] with the following parameters and boundary conditions:

$$P=0.4,\quad \Omega_d=2\sqrt{\varphi_0/A}=500,\quad t=\frac{9BT}{\Omega_d^2A^2}=1,$$

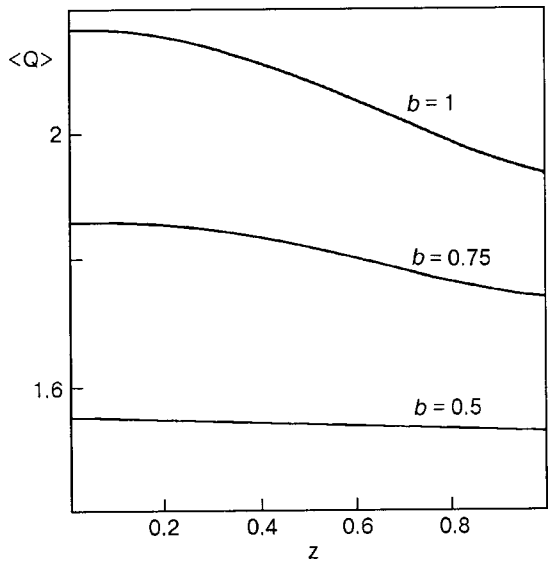

FIG. 1. Order-parameter profiles for various values of the field b and fixed plate thickness $2D=2$.

$$\langle Q\rangle\Big|_{Z=0}=\langle\overline{Q}\rangle,\quad \frac{d}{dZ}\langle Q\rangle\Big|_{Z=0}=0, \tag{14}$$

where $\langle\overline{Q}\rangle$ is the value of the order parameter obtained by solving Eq. (13) with volume-averaged stresses.

Figures 1 and 2 show the computational results for the profiles of the order parameter $\langle Q\rangle$ of the structural transition in a single-domain sample in a low–temperature ordered phase for various values of the dimensionless quantities, specifically, the field $b=B\sqrt{G/CA\mu_0}$ and the half-width D of the plate, scaled as $D=j_cd\sqrt{G\mu_0/CA}$. Such dependences for the above-described phase transition in $YBa_2Cu_3O_{6+x}$ could indicate an ''optical'' deformation consisting of a displacement of the atoms of chain oxygen along the c axis relative to the rest of the ionic core. In any case they make a corresponding contribution to the scattering function. In ad-

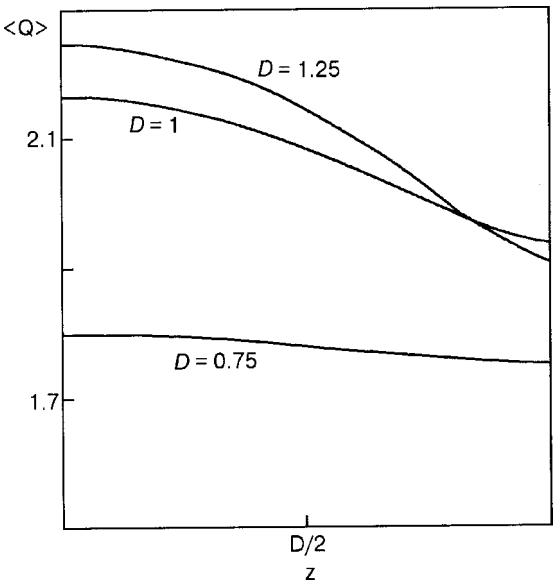

FIG. 2. Order-parameter profiles for various values of the plate thickness D and fixed field $b=1$.

dition, because of the presence of an internal parameter (order parameter) in the system, the pinning-induced deformations calculated on the basis of the elasticity theory, for example in Ref. 24, are no longer linearly dependent on the stresses and must now be determined from equations of the type (8) and (13).

In summary, it can be concluded that pinning-induced stresses can have an appreciable effect on a structural low-temperature transition in HTSC systems, at least compared with the values characteristic for the magnetoelectric effect,[8] and are unique.

*E-mail: mamalui@kpi.kharkov.ua

[1] N. M. Plakida, Phys. Scr. **29**, 8 (1989).
[2] A. Jezowski, Solid State Commun. **71**, 419 (1989).
[3] S. A. Gridnev, O. I. Ivanov, and O. V. Dybova, Sverkprovodniki: Fiz. Khim. Tekh. **3**, 65 (1990).
[4] G. Cannelli, M. Canali, R. Cantelli, F. Cordero, S. Ferraro, M. Ferreti, and F. Trequattrini, Phys. Rev. B **45**, 931 (1992).
[5] A. A. Mamaluĭ, D. S. Palatnik, K. V. Bednov, M. A. Obolenskiĭ, and A. V. Bondarenko, Fiz. Nikz. Temp. **19**, 1180 (1993) [Low Temp. Phys. **19**, 839 (1993)].
[6] V. P. D'yakonov, I. M. Fita, N. A. Doroshenko, M. Baran, and G. Shichmak, JETP Lett. **63**, 825 (1996).
[7] M. A. Krivoglaz and V. D. Sadovskiĭ, Fiz. Met. Metalloved. **18**, 502 (1964).
[8] D. Wagner and D. Bauerle, Phys. Lett. A **83**, 347 (1981).
[9] A. Gordon, I. D. Vagner, and P. Wyder, Physica C **235–240**, 1575 (1994).
[10] H. Ikuta, N. Hirota, Y. Nakayama, K. Kishio, and K. Kitazawa, Phys. Rev. Lett. **70**, 2166 (1993).
[11] L. Z. Lubyany, A. A. Mamalui, and I. N. Sablin, Functional Materials **7**, 447 (2000).
[12] V. L. Aksenov, N. M. Plakida, and S. Stamenkovich, *Neutron Scattering by Ferroelectrics* (Énergoatomizdat, Moscow, 1984).
[13] A. P. Saĭko, V. E. Gusakov, and V. S. Kuz'min, JETP Lett. **56**, 411 (1992).
[14] E. Pytte, Phys. Rev. B **5**, 3758 (1972).
[15] C. Greaves and P. R. Slater, Solid State Commun. **74**, 591 (1990).
[16] V. Müller, C. Hucho, K. de Groot, D. Winau, D. Mauer, and K. H. Rieder, Solid State Commun. **72**, 997 (1989).
[17] D. Mihailovic and A. J. Heeger, Solid State Commun. **75**, 319 (1990).
[18] E. Zouboulis, S. Kumar, U. Welp, G. H. Chen, S. K. Chan, M. Grimsditch, J. Downer, and L. McNeil, Physica C **190**, 329 (1992).
[19] Yu. É. Kitaev, M. F. Limonov, A. P. Mirgorodskiĭ, A. G. Panfilov, and R. A. Évaristov, Fiz. Tver. Tela (St. Petersburg) **36**, 865 (1994) [Phys. Solid State **36**, 475 (1994)].
[20] A. I. Buzdin and V. V. Moshchalkov [Eds.], *Physical Properties of HTSCs* (2) (Giperoks, Moscow, 1991).
[21] N. Giordano, P. Muzikar, and S. S. C. Burnett, Phys. Rev. B **36**, 667 (1987).
[22] V. A. Slyusarev and M. A. Strzhemechnyĭ, Zh. Éksp. Teor. Fiz. **58**, 1757 (1970) [Sov. Phys. JETP **31**, 941 (1970)].
[23] R. Lipowsky and W. Speth, Phys. Rev. B **28**, 3983 (1983).
[24] T. M. Johansen, Phys. Rev. B **60**, 9690 (1999).

Translated by M. E. Alferieff

Effect of strong surface pinning on the surface impedance of a superconductor in a mixed state

D. A. Luzhbin*

G. V. Kurdyumov Insitute of Metal Physics, Ukrainian National Academy of Sciences, Akademician Vernadskiĭ Blvd., 36, Kiev, 03680, Ukraine

(Submitted April 19, 2001)
Fiz. Nizk. Temp. **27**, 1232–1236 (November 2001)

The field and frequency dependences of the surface impedance of a type-II superconductor in a mixed state in a constant magnetic field perpendicular to the surface are calculated taking account of the nonlocality of the elastic moduli of the vortex lattice. It is shown that if there is no surface pinning, a correct analysis of the elastic properties of the vortex ensemble results in the Coffey–Clem model with small corrections. For strong surface pinning, the surface resistance is predicted to decrease substantially at low frequencies. It is shown that the results obtained when dispersion is taken into account by renormalizing the elastic moduli [E. B. Sonin, A. K. Tagantsev, and K. B. Traito, Phys. Rev. B **46**, 5830 (1992)] are incorrect.
 [DOI: 10.1063/1.1421455]

1. INTRODUCTION

A general method for measuring electromagnetic properties of superconductors (SCs) in a mixed state, for investigating mechanisms of pinning and the motion of vortices, and for determining the microscopic parameters characterizing the motion of vortices (viscosity, pinning constant, Hall constant) is measurement of the complex surface impedance of a SC as a function of the frequency ω and amplitude of the ac electromagnetic field, temperature, and constant magnetic field.[1–4] High-frequency methods are much more sensitive than measurements in a constant current (because of phase-sensitive detection) and give richer information about the dynamics of a vortex ensemble. Consequently, in order to construct a correct interpretation of the many experimental data the theory of the response of a vortex lattice (VL) to an ac field must be understood in detail.

One of the first phenomenological theories making it possible to take into account consistently the contribution of vortices to the surface impedance on a SC is the Coffey–Clem (CC) theory.[5–7] Following Refs. 5–7, the surface impedance of a SC in the mixed state is given by the expression

$$Z_{CC} = -i\omega\mu_0\lambda_{ac}(\omega,B,T) \tag{1}$$

$$\lambda_{ac}(\omega,B,T) = \left(\frac{\lambda^2(B,T)+\lambda_C^2(\omega,B,T)}{1+2i\lambda^2(B,T)/\delta_{nf}^2(\omega,B,T)}\right)^{1/2}, \tag{2}$$

where $\lambda(B,T)$ is the London penetration depth; $\lambda_C(\omega,B,T)$ is the Campbell penetration depth at which disturbances in a VL decay; the quantity δ_{nf} determines the dissipative contribution of normal quasiparticles. In the low-temperature limit ($T \ll T_C$) and at microwave frequencies the term with δ_{nf} in Eq. (2) can be dropped. This is the case that we shall study below.

In the present paper it will be shown that a correct analysis of the elastic properties of a vortex ensemble, specifically, the variance of the elastic moduli of a VL, gives exponential decay of the electromagnetic wave in the SC and, correspondingly, a modification of the expression (1). In addition, the approach described is used to construct a model of the surface impedance for SC with strong surface pinning.

2. THEORY

Let us consider a SC in an external perpendicular constant magnetic field B_a ($B_{c1} \ll B_a \ll B_{c2}$), which is in equilibrium with induction B_0 inside the sample. According to Ref. 8, the elastic energy of a deformed VL is given by the expression

$$F_{\rm el} = \frac{1}{2}\int_{BZ} u_\alpha(k)\Phi_{\alpha\beta}(k)u_\beta^*(k)\frac{d^3k}{8\pi^3}, \tag{3}$$

where the integration extends over the first Brillouin zone of the VL; $u_\alpha(k)$ is the Fourier transform of the deformation field; $\Phi_{\alpha\beta}(k) = (C_{11}-C_{66})k_\alpha k_\beta + \delta_{\alpha\beta}[(k_x^2+k_y^2)C_{66}+k_z^2C_{44} + \alpha_L]$ is the elastic matrix of the VL; C_{ii} are the corresponding nonlocal (k-dependent) elastic moduli of the VL; and, α_L is the Labush parameter. For a uniform deformation field $\mathbf{u}(k) = (u_x(k_z),0,0)$ the elastic energy can be represented as[7,8]

$$F_{\rm el} = \frac{1}{2}\int_{-\infty}^{+\infty} |u_x(k)|^2[C_{44}(k)k^2+\alpha_L]\frac{dk}{2\pi}. \tag{4}$$

According to Ref. 9, for $a \ll \pi\lambda$ (which is equivalent to the condition $B_a \gg B_{c1}$) the quantity $C_{44}(k)$ is given by

$$C_{44}(k) = \frac{B_0^2}{\mu_0}\left[\frac{1}{1+k^2\lambda^2}+\frac{L^2}{\lambda^2}\right]. \tag{5}$$

where $L \simeq a/\pi$ (for an isotropic SC) and $a = a(B_0)$ is the characteristic intervortex distance.

We shall consider the case where a current $J = J_0 \exp(-z/\lambda)$ flows in a layer λ near the surface; this current gives rise to the above-examined deformation of the VL. The equilibrium deformation field is determined by the minimum of the functional[9]

$$F=\int_{-\infty}^{+\infty}[(C_{44}(k)k^2+\alpha_L)|u(k)|^2-2J(k)u(k)B_0]\frac{dk}{4\pi}, \tag{6}$$

where $J(k)$ is the Fourier transform of the current.

It follows from Eqs. (4)–(6) that

$$u(z)=\frac{\mu_0 J_0\lambda}{B_0L^2(k_2^2-k_1^2)}\left(\frac{\exp(-k_1z)}{k_1}-\frac{\exp(-k_2z)}{k_2}\right), \tag{7}$$

where

$$2k_1^2=P+(P^2-4Q)^{1/2},\quad 2k_2^2=P-(P^2-4Q)^{1/2},$$

$$P=L^{-2}+\lambda^{-2}+(\lambda/L\lambda_C)^2,$$

$$Q=(L\lambda_C)^{-2},\quad \lambda_C^2=B_0^2/\mu_0\alpha_L.$$

Let the current J be induced by an electromagnetic wave $h=h_{rf}\exp(-i\omega t-z/\lambda)$ incident on the SC. Taking account of the VL motion arising in this case (in the quasistationary approximation, valid in the microwave range) reduces to replacing λ_C by $\lambda_C(\omega)=\lambda_C(1-i\omega/\omega_p)^{-1/2}$, where $\omega_p=\alpha_L/\eta$, in Eq. (7) or equivalently α_L by $\alpha_L(\omega)=\alpha-i\omega\eta$ in Eq. (6). The motion of the VL results in a local change of the induction in the SC and correspondingly to the generation of an electric field, which makes an additional contribution to energy dissipation. According to Ref. 10, the ac component of the induction $\delta B(z,t)$ ($\mathbf{B}=(\delta B(z)\times\exp(-i\omega t),0,B_0)$, where B_0 is the stationary value of the induction) is determined by solving the equation

$$\delta\mathbf{B}+\lambda^2\mathrm{curl}\,\mathrm{curl}\,\delta\mathbf{B}=\mathrm{curl}[\mathbf{u}(z)\times\mathbf{B}_0] \tag{8}$$

with boundary condition $\delta\mathbf{B}(0)=h_{rf}$. The electric field is found from the equation $\mathrm{curl}\,\mathbf{E}=-\partial\mathbf{B}/\partial t$.

Determining the surface impedance as the ratio of the tangential components of the electric $\mathbf{E}$ and magnetic $\delta\mathbf{B}$ fields at the surface of the SC, we obtain

$$Z=i\omega\mu_0\left\{-\lambda+\frac{1}{L^2(k_2^2-k_1^2)}\times\left(\frac{1}{k_2(1+\lambda k_2)}-\frac{1}{k_1(1+\lambda k_1)}\right)\right\}. \tag{9}$$

Let us consider a SC with a strong surface pinning, which could arise because of an arbitrary degradation of the surface. From the standpoint of the response of the VL this is equivalent to the condition $u(0)=0$ or

$$\int_{-\infty}^{+\infty}u(k)dk=0. \tag{10}$$

Minimizing the expression (6) under the condition (10) gives

$$u(z)=\frac{\mu_0J_0\lambda^3}{B_0L^2(k_2-k_1)(1+\lambda^2k_1k_2)}\times(\exp(-k_1z)-\exp(-k_2z)) \tag{11}$$

and, correspondingly,

$$Z=i\omega\mu_0\left\{-\lambda+\frac{\lambda^2}{L^2(k_2-k_1)(1+\lambda^2k_1k_2)}\times\left(\frac{1}{1+\lambda k_2}-\frac{1}{1+\lambda k_1}\right)\right\}. \tag{12}$$

3. ANALYSIS

In both cases Eqs. (7) and (11) correspond to nonexponential penetration of the mixed field into the SC, in contrast to the CC model where the field penetrates to depth λ_{ac}:[7] $\delta B\sim\exp(-z/\lambda_{ac})$. The nonexponential nature of the field distribution appears as a result of the second term in Eq. (5): as $L\to0$ we obtain the CC result for the field distribution and the surface impedance distribution. Formally, as $L\to0$ the modulus C_{44} transforms into C_{11}, i.e. it corresponds to the case of a constant magnetic field parallel to the surface of the SC. Thus, the CC theory is an exact result for parallel orientation of the magnetic field. Physically, the presence of the term with L in Eq. (5) makes it possible to satisfy the boundary condition $\partial u(0)/\partial z=0$ in Eq. (7).

We shall now estimate the contribution of the term under study. Expanding the expression (9) in powers of $L/\lambda\ll1$ up to the first nonvanishing terms, we obtain

$$Z=-i\omega\mu_0\left\{\lambda_{ac}(\omega)-\frac{L^2\lambda_C^2(\omega)}{\lambda\lambda_{ac}^4(\omega)}[\lambda_{ac}(\omega)-\lambda]^2\right\}. \tag{13}$$

The analogous expansion for strong surface pinning gives

$$Z=-i\omega\mu_0\left\{\lambda_{ac}(\omega)-\frac{L\lambda_C^3(\omega)}{\lambda^2\lambda_{ac}(\omega)}\right\}. \tag{14}$$

According to Eqs. (13) and (14), the impedance can be written as $Z=Z_{CC}(\omega,B)-Z_{\mathrm{non}}(\omega,B)$, where $Z_{CC}(\omega,B)$ is determined by the expression (1), $Z_{\mathrm{non}}(\omega,B)$ is a correction due to the variance of the modulus C_{44}. The field dependences of the surface resistance ($\mathrm{Re}\,Z$) for Eqs. (9) and (12) are shown in Fig. 1 for low and high frequencies (compared with ω_p) with the following values of the parameters: $\lambda=0.1\,\mu$m, $\Phi_0\eta/B=10^{-6}$ N·s/m^2, and $\Phi_0\alpha_L/B=10^5$ N/m^2,[2] corresponding to typical values for HTSC materials. It is evident that if there is no surface pinning, the difference between the result obtained in the CC model and the exact relation (9) is negligible and can be neglected in all practical calculations. For strong surface pinning the difference becomes larger and can reach 50% at low and of the order of 10% at high frequencies (see Figs. 2 and 3). The frequency dependence of $\mathrm{Re}\,Z_{\mathrm{non}}$ with fixed B_0 has the following form (with constant pinning): $\mathrm{Re}\,Z_{\mathrm{non}}\sim\omega^2$ ($\omega\ll\omega_p$) and $\mathrm{Re}\,Z_{\mathrm{non}}\sim\omega^{-3/2}$ ($\omega\gg\omega_p$). The frequency dependence of the relative contribution Z_{non} to the surface resistance is displayed in Fig. 3 for various values of the external field B_a.

In conclusion, we shall compare the results obtained with the results of the model developed in Refs. 11 and 12.

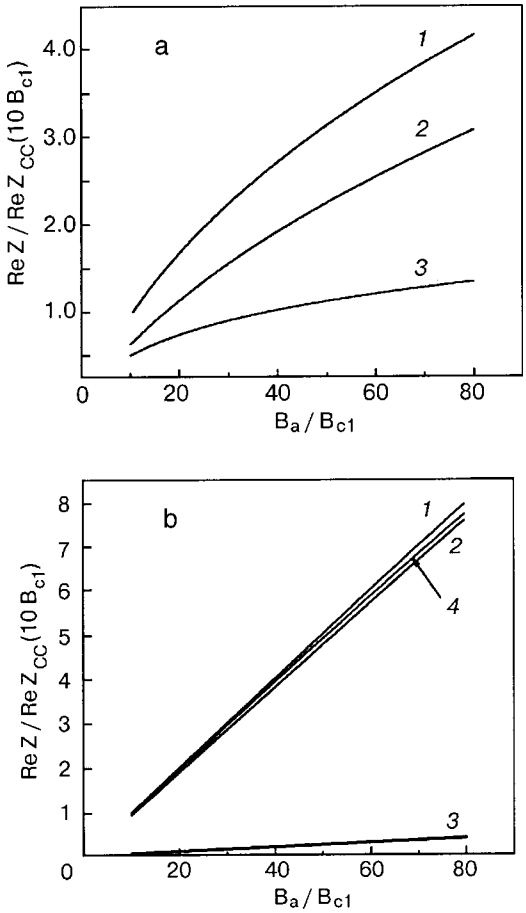

FIG. 1. Field dependences (at fixed frequencies $\omega=0.04\omega_p$ (a) and $25\omega_p$ (b)): 1—surface resistance in the CC model (1); 2—surface resistance in the case of surface pinning (12); 3—the term $\mathrm{Re}Z_{\mathrm{non}}$ (14); 4—surface resistance in the model of Refs. 11 and 12 in the presence of surface pinning. In the scales of the figure there is no difference between the curve 1 and the exact function (9).

In contrast to the approach proposed in the present work, in Refs. 11 and 12 the nonlocal expression (5) was replaced by a local renormalized value

$$C_{44}^{*}=B_0H_0-C_{44}(k=0,\,L=0)=B_0|M_0|, \tag{15}$$

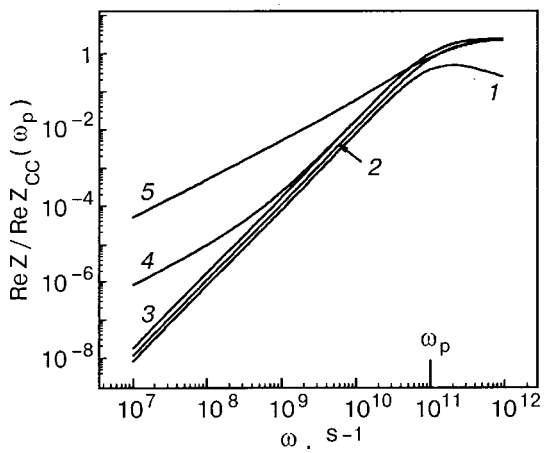

FIG. 2. Frequency dependences (with fixed external field $B_a=15B_{C1}$) of the term $\mathrm{Re}\,Z_{\mathrm{non}}$ (14) (1); surface resistance: with surface pinning (12) (2); in the CC model (1) (3); in the model of Refs. 11 and 12 without surface pinning (4); in the model of Refs. 11 and 12 with surface pinning (5).

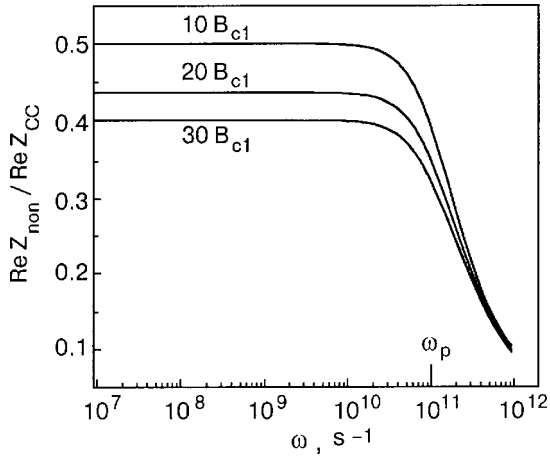

FIG. 3. Frequency dependence of the relative contribution of the quantity Z_{non} (14) to the surface resistance for various values of the external field.

where M_0 is the equilibrium value of the magnetization. In solving the equation for a viscous motion of vortices $\alpha\mathbf{u}+\eta\partial\mathbf{u}/\partial t=[\mathbf{J}\times\mathbf{B}_0]+C_{44}^{*}\partial^2\mathbf{u}/\partial z^2$ together with Eq. (8) under the corresponding boundary conditions for $u(z)$, the field distribution and the surface impedance were calculated. It was shown that in the absence of volume pinning ($\alpha_L=0$) the surface resistance at low frequencies decreases substantially. However, in real HTSC samples at low frequencies it is the quantity α_L that determines the dynamics of the VL; for α_L given above the theory of Refs. 11 and 12 gives an unexpected result: the surface resistance with surface pinning is greater than in the absence of surface pinning, and both values are much greater than the surface resistance in the CC model. The field and surface dependences of $\mathrm{Re}\,Z$ in the model of Refs. 11 and 12 in the presence and absence of surface pinning are presented in Figs. 1 and 2.

4. CONCLUSIONS

In this work the linear response of a SC in a mixed state to an ac field (surface impedance) was calculated for the case of a constant magnetic field perpendicular to the surface on the basis of the linear theory of elasticity taking account of the variance of the elastic matrix of the VL. It was shown that, just as for a parallel magnetic field, in the absence of surface pinning the surface impedance of the SC is described by the CC theory (1). The presence of strong surface pinning (10) can result (at low frequencies) in a substantial decrease of energy absorption in the SC. The frequency dependence of $\mathrm{Re}\,Z$ is also determined by the expression (1): at low frequencies the corrections have the same dependence as the main term ($\sim\omega^2$), and at high frequencies their contribution becomes small (Figs. 2 and 3) and is not observable experimentally.

It was also shown that taking account of the nonlocal nature of the elastic moduli of the VL by renormalization (15)[11,12] leads to incorrect results: the value of $\mathrm{Re}\,Z$ at low frequencies is several orders of magnitude greater than the corresponding value in the CC theory.

*E-mail: luzhbin@d24.imp.kiev.ua

[1] J. Owliaei, S. Sridhar, and J. Talvacchio, Phys. Rev. Lett. **69**, 3366 (1992).
[2] M. Golosovsky, M. Tsindlekht, and D. Davidov, Semicond. Sci. Technol. **9**, 1 (1996).
[3] I. S. Ghosh, L. F. Cohen, and J. C. Gallop, Semicond. Sci. Technol. **10**, 936 (1997).
[4] N. Belk, D. E. Oates, D. A. Feld, G. Dresselhaus, and M. S. Dresselhaus, Phys. Rev. B **53**, 3459 (1996).
[5] M. W. Coffey and J. R. Clem, IEEE Trans. Magn. **27**, 2136 (1991).
[6] M. W. Coffey and J. R. Clem, Phys. Rev. Lett. **67**, 386 (1991).
[7] E. H. Brandt, Phys. Rev. Lett. **67**, 2219 (1991).
[8] E. H. Brandt, Rep. Prog. Phys. **58**, 1465 (1995).
[9] E. H. Brandt, Phys. Rev. B **48**, 6699 (1993).
[10] C. J. van der Beek, V. B. Geshkenbein, and V. N. Vinokur, Phys. Rev. B **48**, 3393 (1993).
[11] E. B. Sonin, A. K. Tagantsev, and K. B. Traito, Phys. Rev. B **46**, 5830 (1992).
[12] E. B. Sonin and K. B. Traito, Phys. Rev. B **50**, 13547 (1994).

Translated by M. E. Alferieff

Coherent quantum phenomena in a normal cylindrical conductor with a superconducting coating

G. A. Gogadze*

Department of Applied Physics, Chalmers University of Technology and Göteborg University, SE-41296 Göteborg, Sweden; B. I. Verkin Institute for Low Temperature Physics and Engineering of the National Academy of Science of Ukraine, 47 Lenin Ave., 61103 Kharkov, Ukraine

R. I. Shekhter and M. Jonson

Department of Applied Physics, Chalmers University of the Technology and Göteborg University, SE-41296 Göteborg, Sweden

(Submitted April 28, 2001)
Fiz. Nizk. Temp. **27**, 1237–1249 (November 2001)

The thermodynamic properties of a mesoscopic-size, simply connected cylindrical normal metal in good metallic contact with superconducting banks are studied theoretically. It is commonly accepted that if the superconductor thickness is quite small (of the order of the coherence length), as is assumed to be the case here, a vector potential field, whose value can be varied, exists inside the normal layer. It is further assumed that the quasiparticles with energy $E<\Delta$ (2Δ is the superconducting gap) move ballistically through the normal metal and undergo Andreev scattering caused by the off-diagonal potential of the superconductor. An equation is obtained within the multidimensional quasiclassical method which permits us to determine the spectrum of the Andreev levels and to calculate the density of states of the system in question. It is shown that the Andreev levels shift as the trapped flux Φ changes inside the normal conductor. At a certain flux value they coincide with the Fermi level. A resonance spike in the density of states $\nu(E)$ appears in this case, since near $E=0$ there is strong degeneracy of the quasiparticle states in respect to the quantum number q characterizing their motion along the cylinder axis. As a result, a macroscopic number of q states contribute to the amplitude of the effect. As the flux is increased, the density of states $\nu(E)$ behaves as a stepwise function of Φ. The distance between the steps is equal to the superconducting flux quantum $hc/2e$. © *2001 American Institute of Physics.* [DOI: 10.1063/1.1421456]

INTRODUCTION

Quantum interference phenomena in condensed matter were first observed in superconductors. Soon after the microscopic Bardeen-Cooper-Schrieffer theory of superconductivity[1] appeared, the effect of flux quantization was detected experimentally in a superconducting ring.[2,3] This effect had been predicted previously by F. London,[4] who showed that in a doubly connected superconductor a certain quantity (fluxoid) could take only quantized values. The fluxoid is determined by the sum of magnetic fluxes through the superconductor cross section plus an integral term dependent on the superfluid current. In a bulk superconductor with an orifice, flux quantization exists in its direct meaning, since the magnetic field does not penetrate inside the superconductor. The integration path used to calculate the integral fluxoid term can be chosen to lie rather deep inside the metal, where the superfluid current is zero.

For a thin-wall cylinder the flux can take any value, and flux quantization shows up as oscillations of the current circulating over the cylinder surface. The oscillation period of the magnetic field flux is equal to one superconducting flux quantum $\Phi_0=hc/2e$.

It was thought for a long time that flux quantization could exist only in superconductors and was associated with (i) the sensitivity of quantum electron states to the vector potential field (the Aharonov-Bohm effect[5]), and (ii) the presence of an off-diagonal long-range order in superconductors.[6] In 1970 Kulik published an important theoretical paper[7] describing the behavior of a thin-wall cylindrical normal conductor in the vector potential field excited by an inserted solenoid. That was the first evidence suggesting that coherent quantum properties are possible in normal (nonsuperconducting) systems of quite small (though ''macroscopic'' on the atomic scale) dimensions at low temperatures. It turns out that the magnetic moment of such a system is an oscillatory function of the magnetic flux through the cylinder orifice, and the oscillation period is equal to one flux quantum of the normal metal, hc/e. The quantization effect takes place in the absence of off-diagonal long-range order.

Reference 7 has stimulated much interest in quantum interference effects in normal condensed media. It has become clear that the Aharonov-Bohm effect is possible in solids because the electron retains its ''phase memory'' over a finite length $\xi_N=\hbar v_F/\pi T$, which has the meaning of a coherence length in a system with a disturbed long-range order (v_F is the Fermi velocity, and T is the temperature). With an infinitely long electron mean free path and at temperatures $T\sim 1$ K, ξ_N is about 10^{-3} cm, and coherent quantum phenomena become possible in normal conductors whose transverse dimensions are of the order of ξ_N. However, because a

doubly connected conductor should have a very small cross section, the idea of an experiment with an inserted solenoid seemed problematic. The need arose to study coherent quantum effects in simply connected cylindrical conductors in a magnetic field and to analyze the influence of surface and bulk collisions on the oscillation amplitudes. It was shown[8] for the first time in 1972 that flux quantization is possible in pure cylindrical solid conductors placed in a weak longitudinal magnetic field (such that the cyclotron radius much exceeds that of the cylinder). The oscillations of thermodynamic quantities in simply connected normal conductors present a more complicated case, which involves two oscillatory components in their magnetic-field dependence. One of them is intricately dependent on the number of the harmonics and the magnetic field and is correlated with the electrons of the central Fermi surface section. The other is characterized by a universal (independent of the dispersion relations for the carriers) period of the magnetic field flux hc/e. The latter oscillations are caused by the skipping-orbit electrons localized in a thin layer (with a thickness of about the de Broglie electron wavelength) near the cylinder surface. The effect is due to size quantization and to the sensitivity of the phase of the electron wave function to the vector potential field.

The spectrum of magnetic surface levels responsible for the coherent phenomena in a normal cylindrical conductor in a weak magnetic field was obtained in Ref. 8. The nature of these levels is different from what was described by Nee and Prange.[9] The magnetic surface levels at a flat boundary are genetically related to the magnetic field and vanish when the field is zero. In a cylinder the magnetic surface levels are formed by the sample boundary, but the magnetic flux is included directly in the expression for the electronic energy spectrum. This expression has been used to calculate a number of specific effects.[8,10–14] In particular, the effect of doubling the oscillation period of the critical temperature has been calculated for a superconducting hollow cylinder with allowance for the quantization of single-particle excitations.[15] When the electron spectrum is smeared, a characteristic period of the Little-Parks effect[16–18] equal to the superconducting flux quantum $hc/2e$ appears. We should also mention the Aharonov-Bohm effect for electrons localized above liquid helium covering the surface of a dielectric cylinder, with the magnetic field applied along its axis.[19] In such a system the electrons which obey Boltzmann statistics move along quasiclassical trajectories and acquire equal increments of wave function phase. As a result the system experiences magnetic-moment oscillations with a universal period hc/e of magnetic flux.

The effect of flux quantization in a normal, simply connected cylindrical conductor was experimentally detected by Brandt, Gitsu, Nikolaeva and Ponomarev[20] (see also Refs. 21 and 22) while investigating the longitudinal magnetoresistance of pure Bi single crystals. This was the first observation of an interference effect related to flux quantization in nonsuperconducting condensed media.

An important distinctive feature of flux quantization in normal metals is the presence of the factor $\cos(2\pi k_F R+\alpha)$ in the oscillation amplitude ($\hbar k_F$ is the Fermi momentum, and α is a auxiliary phase). The implication is that in normal metals a variation of R (fluctuation) by a value of the order of the atomic spacing causes a 100% change in the effect.[23] In this case the flux quantization effect should vanish after oscillation amplitude averaging along the cylinder axis. For this reason the effect was observed experimentally in semimetals, where fluctuations on the scale of the atomic radius are unimportant for the amplitude of flux quantization because of the smallness of the effective mass of the carriers. In currently accepted terms, this feature of flux quantization amplitudes in normal metals reflects the mesoscopic character of the effects.[24]

The concepts of interference phenomena in condensed media have been further extended to dirty systems. Now we understand that because of its mesoscopic character, the flux quantization effect with period hc/e is only possible in small metallic rings where no averaging over different impurity configurations is required.[25,26] In this case we are dealing with interference effects in the conductivity of low-dimensional conductors, since with increasing impurity concentration the oscillation amplitude of the thermodynamic (and kinetic) magnitudes decreases exponentially. In rather long dirty cylindrical conductors (or a large number of rings) the hc/e quantization disappears.

Along with mesoscopic flux quantization in normal metals, there is another important class of interference phenomena induced by weak localization. These phenomena were predicted theoretically by Altshuler, Aronov, and Spivak[27] in 1981, when they were calculating the quantum correction to the conductivity of a metallic thin-wall cylinder in a longitudinal magnetic field. The quantum correction evolves from interference of the wave functions of the particles moving along different trajectories. For arbitrary trajectories the difference between the wave function phases is a random quantity, and the wave interference (after trajectory averaging) makes zero contribution to the conductivity. The sole exceptions are self-crossing trajectories, when each trajectory can be related to its time-reversed counterpart. The electron on the reversed trajectory experiences scatterings identical to those on the initial trajectory but in a reversed sequence.

When the flux is trapped in the cylinder hole, the phase difference of the interfering waves can be varied, which makes the magnetoresistance oscillate with the magnetic flux period $hc/2e$.[27]

To observe this effect, the cylinder radius should not exceed the distance along which the electron retains its ''phase memory.'' This scale is $L_\Phi=(D\tau_\Phi)^{1/2}$, where D is the diffusion coefficient, and τ_Φ is the phase break time, which is dependent on temperature. Magnetoresistance oscillations in dirty metallic cylinders with flux period $hc/2e$ were first observed experimentally by Yu. Sharvin and D. Sharvin.[28,29] These experiments prove that elastic scattering does not disturb the phase coherence of the electrons. Only inelastic processes (changing the energy condition of the electron) can influence the ''phase memory'' by smearing the interference situation. The effect does not disappear on averaging over the impurity distributions. In contrast to the mesoscopic effects, the $hc/2e$ oscillations vanish in rather weak magnetic fields.

The experimental detection of the Aharonov-Bohm effect in condensed media has become possible due to the re-

cent advance in the technology for producing metallic, semimetallic, and semiconducting cylinders and rings. In their experiments Brandt *et al.*[20–22] used casting technology to produce Bi single crystals from the liquid phase. Cylindrical samples of high purity were obtained under a glass coating which was not removed during the measurement. The coating reinforced the samples mechanically and protected their surfaces from environmental influences. Experimental measurements on such samples ensured reproducible results even several years later (private communication by Ya. G. Ponomarev).

Observation of interference effects in disordered media has become possible due to miniaturization of structures and to the progress in microelectronic lithography. The experiments performed by Yu. Sharvin and D. Sharvin,[28,29] Webb *et al.*,[25] and Chandrasekhar *et al.*[26] have clarified the possibility of making quite small instruments taking advantage of new mesoscopic features of the physics of condensed matter.

Quantum interference phenomena have been discussed in detail in a number of surveys[24,30–33] and articles.[34–36]

This study is concentrated on coherent quantum phenomena in a mesoscopic-size cylindrical normal conductor contiguous with a superconductor.

In recent years there has been extensive work in the field of mesoscopic systems, including superconducting structures in proximity with normal metals. The experimental work[37] discussed the magnetic response of clean Ag-coated Nb proximity cylinders in the μK region. In the mesoscopic temperature regime the normal-metal–superconductor system shows the as yet unexplained paramagnetic reentrant effect, discovered some years ago.[38] The theoretical paper[39] reported numerical results for the local density of states in the semiclassical Andreev billiards. It was shown that an energy gap develops in a chaotic billiards near the Fermi energy, but there is no gap found in a circular billiards.

For our system we believe that the contact between the pure normal and superconducting metals is good. As a result, Andreev scattering[40] of quasiparticles appears to be the main mechanism responsible for the formation of quantum states in the normal metal. It is assumed that the width of the superconducting layer on the cylinder boundary is of the order of the coherence length ξ_0. In this case the fluxoid is quantized, and the value of the trapped flux may change continuously. It is assumed that the cylinder radii $R \gg \xi_0$.

A dispersion relation has been derived for the excitation spectrum, and the quasiclassical picture of the quasiparticle motion has been analyzed.

In previous studies on normal cylinders[7,8] the formation of quantum states was associated with specular electron reflection at the metal boundary. After each reflection from the boundary, the electron traveled along a trajectory tangent to a caustic whose radius was dependent on the magnetic quantum number. After Andreev scattering at the NS boundary of the cylinder, the trajectory of the quasiparticles is more complicated. The energy of a ''particle'' type of excitation is higher than the Fermi energy, and its momentum exceeds the Fermi momentum $\hbar k_F$, too. As a result of Andreev scattering the ''particle'' transforms into a ''hole'' whose momentum is smaller than $\hbar k_F$. It follows from the law of conservation of angular momentum that the ''particle'' and the ''hole'' have different caustic radii, the caustic radius of the latter being larger. This feature of the quasiparticle motion was taken into account in deriving the condition for quasiclassical quantization of excitations. That condition for quantization has been obtained within the multidimensional quasiclassical method, which permit us to determine the spectrum of the Andreev levels and to calculate the density of states of the system in question.

The density of states as a function of Φ has a steplike behavior and experiences jumps at $\Phi = hc(s+1)/2e$ (where s is a natural number), i.e., it has a resonance character. The distance between steps is equal to the flux quantum $hc/2e$. Giant-amplitude oscillations of the conductance of an SNS contact were predicted in Refs. 41 and 42 for the case when the phase difference of the order parameter of the superconductors is equal to an odd number times π. For our system the resonance spikes of the density of states can be explained as follows.

Let us consider two points A and B on a given section of cylinder. Let us assume that a quasiparticle moves along the line AB. In the case where the distance AB is of a mesoscopic scale there exists a Josephson current between these points. The energy spectrum of such a local SNS contact is determined by the order parameter phase difference at points A and B, which depends on the flux Φ and the radial angle α between those points. The energy of the Andreev level reaches the Fermi surface whenever $\Phi = \Phi_0(s+1)$. In this case the spectrum exhibits strong degeneracy insofar as it becomes independent of the longitudinal (along the cylinder axis) component of the quasimomenta. The range of degeneracy depends on the total flux Φ. Therefore, in this case the density of states experiences a resonance increase with amplitude, showing a steplike behavior with increasing Φ.

FORMULATION OF THE PROBLEM

Let us consider a pure, simply connected normal cylinder of radius R. The particles with energy $E < \Delta$ experience Andreev scattering at their superconducting boundaries. It is assumed that the width of the superconducting layer is of the order of the coherence length ξ_0 (or λ_L). In this case the fluxoid Φ_L is quantized,

$$\Phi_L = \Phi + \frac{\pi\lambda_L^2}{c} \oint \mathbf{j}\cdot d\mathbf{s} = n\Phi_0, \quad n = 0,1,2,...$$

and the value of the trapped magnetic flux $\Phi = \eta\Phi_0$ through the superconductor cross section may change continuously (λ_L is the London penetration depth, j is the superfluid current, and $\Phi_0 = hc/2e$).

In this Section we deduce a quasiclassical equation describing the spectrum of quasiparticles in the normal part of the cylinder. To clear up the systematics of the states it is useful to proceed from the Bogoliubov-de Gennes equations:[43]

$$\begin{aligned} &\hat{H}_e u(\mathbf{r}) + \Delta(\mathbf{r})v(\mathbf{r}) = Eu(\mathbf{r}), \\ &-\hat{H}_e^*(\mathbf{r}) + \Delta^*(\mathbf{r})u(\mathbf{r}) = Ev(\mathbf{r}). \end{aligned} \tag{1}$$

Here $\binom{u}{v}$ is the two-component wave function of a quasiparticle, E stands for the energy eigenvalues,

$$\hat{H}_e=\frac{1}{2m^*}\left[-i\hbar\nabla-\frac{e}{c}\mathbf{A}\right]^2-\zeta$$

is the single-particle Hamiltonian, dependent on the vector potential $\mathbf{A}$, ζ is the chemical potential of the metal, and m^* is the effective electron mass. It is hard to solve Eq. (1) exactly, but the problem can be much simpler if we use the stepwise potential approximation for Δ. Within the gauge chosen for $\mathbf{A}$, the order parameter is preassigned by the expression:

$$\Delta(\mathbf{r})=\Delta(r)\exp(-i[\eta]\theta),$$
$$\Delta(\mathbf{r})=\begin{cases}\Delta, & r>R,\\ 0, & r<R,\end{cases} \tag{2}$$

where θ is the angle, which varies in the interval $0\leqslant\theta\leqslant 2\pi$, and $[\eta]$ is the integer part of η. With this choice of the pairing potential it is a single-valued function of the coordinates. We disregard the distortions of the excitation trajectories caused by the magnetic field. In this study we confine our consideration to the vector potential field, taking into account its influence on the phase increment in the wave function of the excitation. The case of weak magnetic field will be the subject of another paper.

As was shown in Refs. 7 and 8, the interference patterns of the oscillations of thermodynamic values have a common cause, namely the Aharonov-Bohm effect. To describe the field of the vector potential, we shall consider a normal hollow cylinder whose inner radius tends to zero. Let us assume that a solenoid is inserted into the orifice of the cylinder. It excites the field of the vector potential. It is hard to realize the situation in practice. Nevertheless, it is interesting to consider it because it demonstrates unambiguously the fact of flux quantization. According to a calculation,[8] in a simply connected cylinder the oscillations that arise have the largest amplitudes in the vector potential field because they take contributions from all electron states with arbitrary magnetic quantum numbers. When such a cylinder, with specular reflection of quasiparticles at the dielectric boundary, is placed in a weak magnetic field, the surface states with the highest magnetic quantum numbers m (the ''whispering gallery'' type states) are responsible for the oscillations with the quantum flux period hc/e.[8]

Having performed the gauge transformation in Eqs. (1), we can change over to the real pairing potential. In this case the wave function can be written as

$$u(\mathbf{r})=u'(\mathbf{r})\exp\left(-i\frac{[\eta]}{2}\theta\right),$$
$$v(\mathbf{r})=v'(\mathbf{r})\exp\left(i\frac{[\eta]}{2}\theta\right). \tag{3}$$

The components u' and v' of the new wave function are dependent only on the radial variable. Therefore, Eqs. (1) can be solved as

$$u'(\mathbf{r})=u'(r)\exp[i(m\theta+qz)],$$
$$v'(\mathbf{r})=v'(r)\exp[i(m\theta+qz)], \tag{4}$$

where m is the magnetic quantum number, and q is the wave vector component along the axis of the cylinder. Proceeding from the single-valuedness requirement for the initial wave functions, we arrive at the following condition: the parity of $2m$ is determined by the parity of the trapped flux quanta $[\eta]$. Substituting the solution of the type given in Eqs. (4) into Eqs. (1), we obtain the equation for the radial function of the problem. Its matrix form is

$$\sigma_z\frac{\hbar^2}{2m^*}\left[-\frac{d^2}{dr^2}-\frac{1}{r}\frac{d}{dr}+\left(m-\sigma_z\frac{\tilde{\eta}}{2}\right)^2\frac{1}{r^2}-(k_F^2-q^2)\right]R_\pm(r)+\sigma_x\Delta(r)R_\pm=ER_\pm(r), \tag{5}$$

where σ_x,σ_z are the Pauli matrices, $\tilde{\eta}=\eta+[\eta]$, and the $\pm$ on R refers to a ''particle'' or a ''hole'' radial function, respectively. In a normal metal ($r<R$) we have $\Delta(r)=0$, and Eq. (5) reduces to the equation for the Bessel function:

$$R(r)\sim J_{\mp\tilde{\eta}/2}\left[\left(k_r\pm\frac{E}{\hbar v_r}\right)r\right]. \tag{6}$$

Here the notations $k_r=\sqrt{k_F^2-q^2}$ (the radial wave number) and v_r (the radial velocity) are introduced. The solution of Eq. (6) for $\eta=1$ coincides in form with the wave function found for the vortex lines of a pure type-II superconductor,[44,45] if magnetic effects are neglected. We can thus see that the angular momentum is $\hbar(m-\tilde{\eta}/2)$ for the ''particle'' and $\hbar(m+\tilde{\eta}/2)$ for the ''hole.''

In the superconducting region ($r>R$) the solution of Eq. (5) is expressed in terms of the Hankel functions $H_m^{(1)}(k_r r)$ and $H_m^{(2)}(k_r r)$. Matching these solutions at the NS boundary, we can obtain the equation for the quasiparticle spectrum. It is, however, hard to derive the general expression for the quasiparticle spectrum of the system by this method even in the case of our chosen stepwise potential $\Delta(r)$. The thermodynamic values can be calculated more conveniently using the approach based on derivation of the equation for the spectrum which gives asymptotically correct estimates of the energy levels. To do this we employ the multidimensional quasiclassical method.

Keller and Rubinow[46] have generalized the conditions of the Bohr-Sommerfeld quasiclassical quantization. Commonly, such conditions have been derived assuming that the quasiclassical wave function was

$$\Psi_0(q_i,t)=A(q_i,t)\exp(iS(q_i,t)/\hbar), \tag{7}$$

where $S(q_i,t)$ is the total action and the amplitude $A(q_i,t)$ is a single-valued function of the coordinates q_i. Because of continuity of the function Ψ_0, the difference ΔS between any two values of the multiple-valued function $S(q_i,t)$ is

$$\Delta S=\oint_{\mathcal{L}}p_i dq_i=2\pi\hbar n,\quad n=0,1,2,\ldots. \tag{8}$$

This equation should be valid for an arbitrary closed curve in q space. The integral in Eq. (8) is the same for any closed curves which can be transformed into one another without crossing a singularity of the integrand (equivalent contours). The authors of Ref. 46 assume that the amplitude $A(q_i,t)$ is also a multiple-valued function of the coordinates, and they write

$$\Psi_0=\sum_k A_k(q,t)\exp\left(\frac{iS_k(q,t)}{\hbar}\right) \tag{9}$$

instead of Eq. (7). Here S_k and A_k are the branches of the multiple-valued functions S and A. Then the requirement of continuity of Ψ_0 leads to

$$\Delta S=\oint_{\mathcal{L}}\nabla S_k\cdot d\mathbf{s}=2\pi\hbar\left(n+\frac{i}{\pi}\oint_{\mathcal{L}}\nabla\ln A_k\cdot d\mathbf{s}\right), \tag{10}$$

where $d\mathbf{s}$ is the length element along the path $\mathcal{L}$.

Since the functions ∇S and $\nabla\ln A$ are multiple-valued (e.g., M-multiple), we can join M sheets of our q space and introduce the notion of a covering space in which the functions S and $\ln A$ become single-valued. The independent (nonequivalent) contours in the covering space give the number of quantization conditions.[46,47]

The increment in the value $\oint_{\mathcal{L}}\nabla\ln A\cdot d\mathbf{s}$ in Eq. (10) should be calculated taking into account the fact that the function $\ln A$ changes at the contour points where A goes to ∞. This occurs on caustic surfaces and surfaces of the points at which the quasiparticle stops (i.e., its velocity becomes zero). Keller and Rubinow[46] obtained the generalized quantization conditions taking into account the contributions from the above specific points in the contour $\mathcal{L}$:

$$\oint_{\mathcal{L}}p_i dq_i=2\pi\hbar\left(n+\frac{d}{4}+\frac{b}{4}\right) \tag{11}$$

(d is the number of intercepts of the contour $\mathcal{L}$ and the caustic surfaces, and b is the number of stopping points). The quantization conditions of Eq. (11) are valid both for the smooth potentials in the Schrödinger equation and for the free motion of a particle in a region confined within hard walls that reflect the particle specularly.

A rigid-wall circle

Keller and Rubinow's method permits construction of asymptotic expressions for the exact wave functions and the eigenvalues of the problem. Here we briefly outline the method for a particular example. Let a particle move freely in a circular region with the radius R restricted by rigid walls. Its behavior can be described by the Schrödinger equation

$$(\Delta+k^2)\Psi=0,\quad k^2=\frac{2m^*E}{\hbar^2}. \tag{12}$$

It is required that Ψ be zero at the boundary. The quasiclassical solution is searched for assuming that for high k values the wave function has the form

$$\Psi=\sum_{j=1}^{N}e^{ikS_j}\left[A_j+\mathcal{O}\left(\frac{1}{k}\right)\right]. \tag{13}$$

Let us assume further that each term in Eq. (13) complies with Eq. (12). Substituting Eq. (13) into Eq. (12) and setting the coefficients of k^2 and k equal to zero, we can obtain the equations for S_j and A_j with any arbitrary j:[46]

$$\begin{cases}(\nabla S)^2=1,\\ 2\nabla S\nabla A+A\Delta S=0.\end{cases} \tag{14}$$

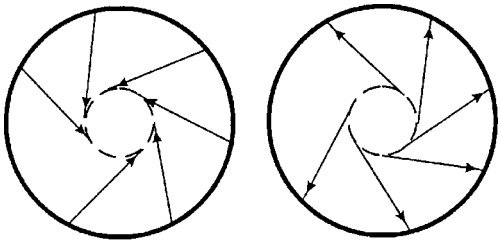

FIG. 1. Two congruences of rays in a circular domain of the cylinder. The concentric circle of radius a_0 is the caustic of these rays.

The first of Eqs. (14) is the eikonal equation of geometrical optics. The other has the meaning of the law of conservation of "probability" for $|A|^2$. $S=\text{const}$ can be interpreted as the wave-front surface. The rays orthogonal to these surfaces are straight lines. To fulfill the boundary condition $\Psi=0$, the terms should enter Eq. (13) in pairs satisfying the conditions:

$$S_j=S_{j'},\quad A_j=-A_{j'},\quad \frac{\partial S_j}{\partial n}=\frac{\partial S_{j'}}{\partial n}. \tag{15}$$

In passing through the caustics the phase with the amplitude A changes by $-\pi/2$, and on reflection at the boundary it changes by $-\pi$ (see Eq. (15)). The quantization condition takes the form[46]

$$\oint_{\mathcal{L}}p_i dq_i=2\pi\hbar\left(n+\frac{d}{4}+\frac{b}{2}\right). \tag{16}$$

To solve the eigenvalue problem, it is necessary to consider all possible rays inside the circular region. These rays are tangent to the circle of radius a_0 which acts as a caustic for them. In this case two families of rays pass through each point of the ring, and each family occupies completely the region inside the circle (Fig. 1). On each event of reflection at the boundary, the rays change over from one family to the other. It is easily seen that in this case the covering space consists of two circular rings which are joined along their peripheries, their radii being R and a_0. Topologically, the covering space is a torus. The torus has only two independent contours which do not contract to a point. Consequently, the number of quantization requirements necessary to describe the motion of the wave inside the circular region reduces to two. Let us choose the circumference with the caustic radius a_0 as one of the integration contours. It does not cross the caustic, and therefore $d=b=0$. On the basis of Eq. (16) this gives the condition of angular momentum quantization:

$$k2\pi a_0=2\pi m,\quad m=0,1,2,\ldots. \tag{17}$$

The other contour on the toroidal surface can be deformed (without affecting the integral) as shown in Fig. 2. Calculating the contour integral, in Eq. (16) and taking into account that $d=b=1$, we can obtain, by means of Eq. (17), a transcendental equation for the eigenvalues of the wave vector:[46]

$$\sqrt{k^2R^2-m^2}-m\arccos\frac{m}{kR}=\pi\left(n+\frac{3}{4}\right),\qquad n,m=0,1,\ldots. \tag{18}$$

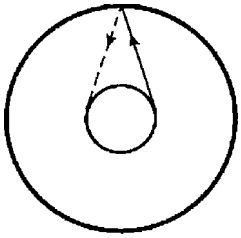

FIG. 2. A closed curve on the toroidal covering space associated with two ray congruences, considered in Fig. 1.

This method also permits us to find an analytical expression for the wave function. Keller and Rubinow compared it with the exact solution of the problem,

$$\Psi \sim J_m(kR)e^{im\theta}, \tag{19}$$

and thus showed that the quasiclassical solutions obtained for eigenfunctions and the eigenvalues are asymptotically exact. In the region between the caustics and the sample boundary, the Debye asymptotics of the Bessel function ($1 \ll m < kR$) is used as an asymptotic approximation to the function $J_m(kR)$. The solution attenuates exponentially inside the caustic ($m > kR$).

SNS contact in zero magnetic field

We can show that similar quasiclassical quantization conditions can be written for structures in which excitations are reflected at the boundary of their localization region by the Andreev mechanism. Let us first consider an SNS contact with flat parallel NS boundaries. We analyze a family of parallel rays (trajectories) directed at a certain angle α to the normal to the film boundary. We choose one of the rays as a path of integration $\mathcal{L}_i$. The covering space can be constructed out of two similar q spaces (of SNS contacts) in which the quasiparticles move in opposite directions. On each Andreev reflection event the amplitude of the wave function of quasiparticle is multiplied by the factor

$$\gamma = \mathrm{e}^{-i \arccos E/\Delta}. \tag{20}$$

For a closed contour $\mathcal{L}_i$ the complete change of the phase on the NS boundaries is:

$$\frac{1}{2\pi}(-i)2 \arccos E/\Delta = \frac{1}{\pi}\arccos E/\Delta. \tag{21}$$

In the case of a current-carrying state, the difference between the superconducting order parameter phases φ of two the given superconductors is added to the phase Eq. (21). Assuming $d=b=0$, we obtain the generalization of Eq. (11) for a SNS contact:

$$\oint_{\mathcal{L}} p_i dq_i = 2\pi\hbar\left(n + \frac{1}{\pi}\arccos\frac{E}{\Delta} \pm \frac{\varphi}{2\pi}\right). \tag{22}$$

Let us denote the quasiparticle momentum inside the N layer as K:

$$K = \begin{cases} p_0 = \sqrt{2m^*(\zeta+E)}, & \text{``particle''} \\ p_1 = \sqrt{2m^*(\zeta-E)}, & \text{``hole''}, \end{cases} \tag{23}$$

where ζ is the chemical potential of the metal minus the energy of the motion along the NS boundary. Proceeding from Eq. (22), we obtain

$$\oint_{\mathcal{L}} K d\mathbf{s} = \int p_0 ds - \int p_1 ds = 2\pi\hbar\left\{n + \frac{1}{\pi}\arccos\frac{E}{\Delta} \pm \frac{\varphi}{2\pi}\right\}. \tag{24}$$

Introduction of the quasiparticle velocity along the path of the motion leads to the expression for the spectrum of the SNS contact which was obtained by Kulik[48]

$$E_n = \frac{\pi\hbar v_{\mathrm{F}}}{\mathcal{L}}\left\{n + \frac{1}{\pi}\arccos\frac{E}{\Delta} \pm \frac{\varphi}{2\pi}\right\}. \tag{25}$$

Andreev reflection of excitations at the cylinder boundaries

Let us deduce an equation for the spectrum of quasiparticles with energies $E<\Delta$ which move inside a normal cylindrical conductor with a superconducting coating. The normal metal is assumed to be pure. Excitations move in it ballistically and experience Andreev scattering at the NS boundary. We shall analyze the features of the quasiparticle trajectories within the system studied. Let us assume that the normal metal initially has no trapped magnetic flux, $\Phi=0$. The tangential components of the wave vector of the quasiparticle are conserved at the NS boundary of the metal during the scattering of a ''particle'' into a ''hole'' (and vice versa). The angular momentum of the ''particle'' and ''hole'' are conserved, too. Since the ''hole'' has a smaller quasimomentum than the ''particle,'' the caustic radius a_1 of the ''hole'' should be larger than the caustic radius a_0 of the ''particle.'' Therefore the angles of incidence of the ''particle'' and the ''hole'' at the NS boundary will be different, that of the ''hole'' being smaller. Thus the quasiparticle trajectory is not strictly recursive. When a certain flux Φ is trapped in the normal cylinder, the angular momentum of the ''hole'' increases to $\hbar(m+\tilde{\eta}/2)$, while that of the ''particle'' decreases to $\hbar(m-\tilde{\eta}/2)$. This implies that at $\Phi\neq 0$ the difference between the angles at which the ''particle'' and the ''hole'' approach the boundary becomes larger. The change in the angular momentum in the case of $\Phi\neq 0$ is caused by the screening superfluid current in the S layer of the structure. The qualitative form of the quasiparticle trajectory inside the cylinder cross section is shown in Fig. 3.

The multidimensional quasiclassical method can be generalized readily to the motion of quasiparticles experiencing Andreev scattering at the boundaries of a circular region. Instead of Eq. (14), we obtain similar separate equations for ''particles'' and for ''holes.'' The wave function $\binom{u}{v}$ of the initial equation (1) in the preassigned field of the vector potential $\mathbf{A}$ ($A_r=A_z=0; A_\theta=\Phi/2\pi r$) is a single-valued function of $\mathbf{r}$ on a complete circuit over the cylinder surface. After the gradient transformation $\mathbf{A}'=\mathbf{A}+\nabla\chi$ using the function $\chi=+\hbar c[\eta]\theta/2e$, the pairing potential Δ becomes real, and the new wave function $\binom{u'}{v'}$ differs from the former $\binom{u}{v}$ in having a factor $(-1)^{[\eta]}$, where $[\eta]$ is the number of quanta of the trapped flux.[43] The phase increment in the wave function of the ''particle'' on the circular contour of radius a_0 is $\oint(k_0+e/\hbar c\mathbf{A}')\cdot d\mathbf{s}=2\pi m$. The phase incre-

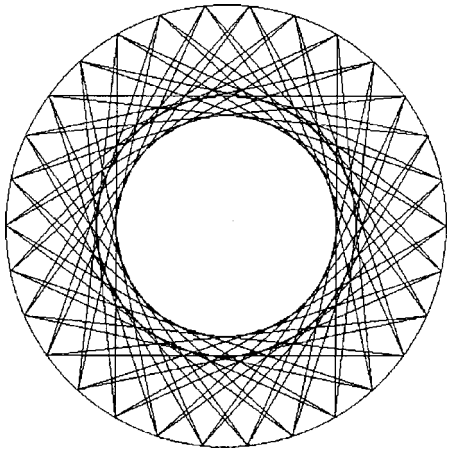

FIG. 3. Quasiclassical picture of the quasiparticle trajectories inside the circular normal domain of a metal coated with a superconducting layer. The ''particle'' and ''hole'' trajectories are tangents to caustics of different radii.

ment of the wave function of a ''hole'' can be found similarly on the contour of radius a_1. As a result, we arrive at the expressions

$$k_0 a_0 = m - \tilde{\eta}/2, \quad k_1 a_1 = m + \tilde{\eta}/2. \tag{26}$$

The derivation of the second equation in (26) takes into account the fact that the effective charge of the ''hole'' is opposite in sign to the charge of the ''particle.''

The problem of the energy eigenvalues can be solved using a geometrical approach. As seen in Fig. 3, the ray tangential to the caustic radius a_0 describes the motion of a ''particle.'' The ray of a ''hole'' is tangent to the caustic radius a_1. Let us first consider the rays describing the motion of the ''particle.'' As in the case of specular reflection from the boundary, the circular ring between the radii R and a_0 contains two families of such rays. Family I includes the rays moving from the NS boundary to the caustic a_0, and family II consists of the rays moving in the opposite direction. At the NS boundary the rays of family I transform into those of family II. After Andreev scattering on the off-diagonal potential, a ''particle'' transforms into a ''hole,'' for

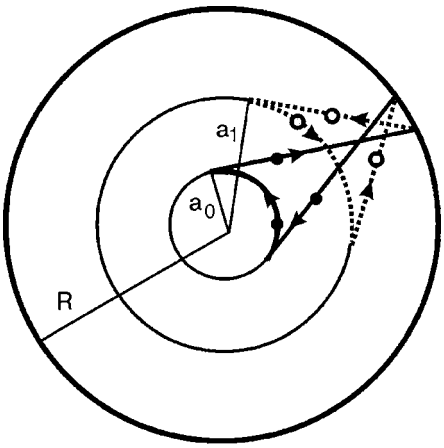

FIG. 4. Shape of the integration path used to derive a quasiclassical equation for the spectrum of Andreev levels. For illustration, two intersection points between the integration path and the NS boundary are mutually shifted so that they could show the processes of ''particle''-to-''hole'' and backward scattering.

which we can also introduce two families of rays moving inside the circular ring and having the radii R and a_1. Thus, in our case the covering space consists of two circular rings for ''particles'' joined along the circumferences of radii R and a_0 and two rings for ''holes'' joined along the circumferences of radii R and a_1. Topologically, this space has the form of two tori, one inside the other, whose surfaces have a common contact line along the radius R. Such surface has only three independent contours which do not contract to a point. Two of them give quantization conditions relating the corresponding angular momentum, quasimomenta, and caustic radii of the ''particle'' and the ''hole'' [see Eq. (26)].

The third contour on the covering surface can be deformed to the shape shown in Fig. 4. The contour integral can be calculated taking into account the condition $\varphi = 0$ and the increment in the wave function phase at each Andreev scattering event. Proceeding from Eq. (26), we thus obtain the equation for the spectrum of quasiparticles inside the cylinder:

$$\sqrt{k_0^2 R^2 - m_0^2} - \sqrt{k_1^2 R^2 - m_1^2} - m_0 \arccos\frac{m_0}{k_0 R} + m_1 \arccos\frac{m_1}{k_1 R} = \pi\left(n + \frac{1}{2} + \frac{1}{\pi}\arccos\frac{E}{\Delta}\right). \tag{27}$$

Here k_0 and k_1 are the wave vectors of a ''particle'' and a ''hole,'' respectively, in the N layer [their expressions are given in Eq. (23)]; $\hbar m_0 = \hbar(m - \tilde{\eta}/2)$ and $\hbar m_1 = \hbar(m + \tilde{\eta}/2)$ are their angular momenta, m is the absolute value of the magnetic quantum number, and $n = 0,1,2...$. The quasiclassical parameter of the problem is $k_0 R \cong k_1 R \cong k_F R \gg 1$.

Note that the coefficient 1/2 within the brackets on the right-hand side of Eq. (27) shows the change in the wave function phase during the quasiparticle scattering at the caustics a_0 and a_1. The number of intersections of the path of integration and the caustic surface is two, as is seen in Fig. 4. We should then put $d = 2$ and $b = 0$ in Eq. (16) and take into account that because of the two Andreev reflections of the quasiparticle at the NS boundary, the phase has the increment $-\arccos E/\Delta$ [see Eq. (21)].

As follows from Eq. (27) the energy ε in units of $\hbar^2/2m^* R^2$ and the quantum numbers m, q are related by the condition: $(k_F^2 - q^2)R^2 \geqslant \varepsilon + m_1^2$. In order to clarify its meaning we introduce the angle ϑ at which the quasiparticle is incident on the NS boundary: $\sqrt{k_F^2 - q^2} = k_F \sin\vartheta$. In this case, for the fixed m the minimal angle of incidence for the quasiparticle with energy ε is equal to $\vartheta_{\min} = \arcsin(\sqrt{\varepsilon + m_1^2}/k_F R)$. Assuming $m_1 \approx 0$, we see that the limiting value of the angle is $\vartheta \sim \sqrt{E/\zeta}$, below which a change of the Andreev reflection to conventional specular reflection on the off-diagonal potential of the superconductor takes place.[49,50]

Equation (27) implicitly determines the dependence of the E levels on the quantum numbers n, m, $\hbar q$: $E_{nm}(q)$.

Let us consider special cases of Eq. (27).

i) Let $m \approx 1$, $\eta \approx 0$. A quasiparticle moves along the cylinder diameter. When the radius R is large, the situation resembles an SNS contact. Indeed, in this case Eq. (27) can give a spectrum resembling that obtained by Kulik, where the phase difference of the order parameters is zero,

$$E_n=\frac{\pi\hbar v_r}{2R}\left(n+\frac{1}{2}+\frac{1}{\pi}\arccos\frac{E}{\Delta}\right), \tag{28}$$

where $v_r=\sqrt{2\zeta/m^*}$.

ii) Let the trapped flux be $[\eta]=1$. The magnetic quantum number $2m$ is then half-integer. Expanding Eq. (27) in a power series in the small parameter $1/k_FR\ll 1$ gives

$$E=\frac{\Delta m}{k_FR}. \tag{29}$$

If $R\approx\xi_0$ (ξ_0 is the coherence length), the spectrum in Eq. (29) coincides with the spectrum of low-lying levels of the vortex lines of a type-II superconductor,[44,45,52] if all magnetic effects are neglected:

$$E=\frac{\pi\Delta^2 m}{2\zeta}.$$

Finally, note the the following particularity of the system, seen from Eq. (27). In the limiting case $k_FR\gg 1$, after expanding the left-hand side of Eq. (27) to first order in $1/k_FR$ and taking the limit $\varepsilon\to 0$ one obtains $\pi\tilde{\eta}/2-\tilde{\eta}m/k_FR=\pi(n+1)$. Thus to zeroth order in $1/k_FR$

$$\tilde{\eta}=2(n+1). \tag{30}$$

We will show below that whenever the trapped flux Φ in the N layer is a multiple of the flux quantum $hc/2e$, the mesoscopic system in question manifests resonance.

DENSITY OF STATES OF NORMAL EXCITATIONS IN A CYLINDER

Let us calculate the density of states $\nu(E)$ for excitations localized in a normal cylinder which experience Andreev scattering at the NS boundary. We proceed from

$$\nu(E)=\sum_{n,m;\sigma}\int dq\,\delta(E-E_{nm}(q)). \tag{31}$$

The summation is over all quantum numbers and the spin σ.

Equation (27) determines the quasiparticle spectrum $E_{nm}(q)$. In the quasiclassical approximation an analytical solution could be obtained. In particular, expanding the left-hand side of Eq. (27) in $1/k_FR\ll 1$ and taking Eq. (23) into account, we obtain

$$E_n(q)=\frac{\pi\hbar v_r(q)}{2R|\sin\alpha/2|}\left(n-\frac{\tilde{\eta}}{2\pi}\alpha+\frac{1}{2}+\frac{1}{\pi}\arccos\frac{E}{\Delta}\right). \tag{32}$$

The spectrum (32) is similar to that obtained by Kulik [48] for an SNS contact. This spectrum corresponds to motion of quasiparticles between two points on the cylinder surface parametrized by the radial angle α, with the distance between these points being $2R|\sin\alpha/2|$. However, contrary to the case of a standard SNS contact, the phase difference $-\tilde{\eta}\alpha/2\pi$ depends on the flux. For given α, the spectrum (32) describes an ''SNS'' contact with an effective density of states $\nu(E;\alpha)$. The total density of states is given by:

$$\nu(E)\sim\int_0^{2\pi}\nu(E;\ \alpha)d\alpha. \tag{33}$$

The spectrum (32) was obtained on the assumption that the quasiparticle energy E was close to the Fermi energy ζ. As was noted in the Introduction, the Andreev levels of the mesoscopic system can shift when the flux changes; at a certain value of the flux they can coincide with ζ. For low energies E, the quasimomenta of a ''particle'' and a ''hole'' (and the radii a_0 and a_1 of their caustics) become practically identical. We may therefore assume that in the description of these two states the quasiclassical trajectories would be simpler in shape than in Fig. 3: when the ''particle'' is reflected from the NS boundary, the ''hole'' comes back to its initial point at the cylinder surface. Within our approximation (32), we should take into account that inside the cylinder cross section there exist a great number of ''SNS contacts'' with the preassigned chord length, i.e., these states possess high degenerate multiplicity about $N\sim 2\pi R/\lambda_B\gg 1$ (λ_B is the de Broglie wavelength). We took this fact into consideration when calculating the density of states of the system in the vicinity of resonance.

As a matter of fact, calculation of the thermodynamic quantities far off resonance should be based on the general equation for the spectrum of quasiparticles, Eq. (27).

The resonance contribution to $\nu(E)$ can be calculated using the spectrum of lower energy levels

$$E_n(q)=\frac{\pi\hbar v_r(q)}{2R|\sin\alpha/2|}\left(n+1-\frac{\tilde{\eta}}{2\pi}\alpha\right). \tag{34}$$

On substituting Eq. (34) into Eq. (31), integrating over q and α, and summing over spin, we obtain

$$\nu(\varepsilon)\sim A\varepsilon\int_0^{\pi}d\alpha \times\sum_{n=-\infty}^{+\infty}\frac{\sin^2\frac{\alpha}{2}\,\alpha\left(n+1-\frac{\tilde{\eta}}{2\pi}\alpha-\varepsilon\sin\frac{\alpha}{2}\right)}{\left(n+1-\frac{\tilde{\eta}}{2\pi}\alpha\right)\left[\left(n+1-\frac{\tilde{\eta}}{2\pi}\alpha\right)^2-\varepsilon^2\sin^2\frac{\alpha}{2}\right]^{1/2}}, \tag{35}$$

where

$$A=\frac{8LRm^*}{\pi^2\hbar^2}\,\frac{2\pi R}{\lambda_B},$$

L is the cylinder height, and $\theta(x)$ is the step function, equal to unity at $x>0$ and to zero at $x<0$. We introduce the dimensionless energy $\varepsilon=E/E_0$, $E_0=\hbar^2/(2m^*R^2)$. As Eq. (35) shows, for a preassigned flux, the denominator of the radicand can become zero at a certain angle $\alpha=\alpha(\Phi)$. When $\varepsilon\to 0$ one has $\alpha_n\simeq(n+1)2\pi/\tilde{\eta}$. In this case the inequalities

$$0\lesssim\alpha_n\lesssim\frac{(n+1)2\pi}{\tilde{\eta}}\lesssim\pi;\quad \eta=\frac{\Phi}{\Phi_0} \tag{36}$$

are fulfilled, which leads to the condition $\eta+[\eta]\gtrsim 2(n+1)$. Thus, with a preassigned flux Φ, the number of terms in the series of Eq. (35) is limited, and it increases with growing Φ.

Prior to calculation of $\nu(\varepsilon)$, let us discuss the question of the contributions of different angles α_n to the resonance amplitude. It is reasonable to assume that because of the factor

$\sin^2\alpha/2$ in the numerator of Eq. (35), the angles $\alpha_n \approx \pi$ are the main contributors to the integral. For such an ''SNS contact,'' the Josephson current flows through the cross section of the cylinder along its diameter. On the other hand, since the resonance condition (35) contains the product of the flux times the angle α, we may expect an extra contribution to the amplitude of the effect from smaller angles α_n when the flux increases. As a matter of fact, this expectation is based on the approximate resonance condition obtained from Eq. (35) in which the first term in the radicand is kept while the second term, $\varepsilon^2 \sin^2\alpha/2$, is dropped.

We thus arrive at the conclusion that the main contribution to the resonance of the density of states appears near the angle $\alpha=\pi$. Introducing the notation $\xi=\pi-\alpha \ll 1$, $a=n+1-\tilde{\eta}/2$, $b=\tilde{\eta}/2\pi$, we obtain the equation for the resonance condition:

$$a^2+b^2\xi^2+2ab\xi-\varepsilon^2\left(1-\frac{\xi^2}{4}\right)=0, \tag{37}$$

whose solution is $\xi \simeq -a/b \pm \varepsilon$. It is seen that for $b\sim 1$, the energy ε and the value of a are both small, but the condition $a \gtrsim \varepsilon$ is always fulfilled. The expression in brackets in front of the radical in Eq. (35) is therefore of the order of the energy ε and cancels with the energy factor of ε in front of the integral sign. The remaining integral is estimated to be a constant of about unity.

The resonance-induced spike of the density of states always appears when the Andreev level coincides with the Fermi energy at a certain flux in the N layer. The sharp increase in the amplitude $\nu(E)$ at $E\to 0$ is caused by the integral contribution of the states of quasiparticles indexed by the quantum number q, which describe the quasiparticle motion along the sample axis.

When the resonance is disturbed, the condition $(n+1-\tilde{\eta}\alpha/2\pi)\neq 0$ is fulfilled, and for low energies $\varepsilon\to 0$ we find

$$\nu^{(0)}(\varepsilon)\sim 2\pi^3\varepsilon\int_0^1 \frac{dx\sin^2\pi x}{\cos^2[2\pi^2 bx]}\sim\varepsilon. \tag{38}$$

Near the resonance, the ratio of the resonance and nonresonance amplitudes of the density of states is

$$\frac{\nu^{\rm res}}{\nu^{(0)}}\sim\frac{1}{\varepsilon}\gg 1. \tag{39}$$

It is thus shown that on variation of the trapped magnetic flux, the density of states of a normal cylindrical conductor coated with a thin superconducting layer ($\sim\xi_0$) is described by a stepped function Φ. The step spacing is equal to a superconducting flux quantum Φ_0 and the step height increases with the flux. Differentiation of the density of states with respect to Φ gives a set of resonance spikes spaced at $hc/2e$.

The physical reason for the features having a period of the superconducting flux quantum Φ_0 is as follows. As is seen in the spectrum of Eq. (27), for preassigned magnetic flux Φ, q, and the energy, there is a highest magnetic quantum number m which can be used to describe the Andreev levels. This quantum number is responsible for the largest caustic realizable for quasiparticles moving ballistically near the cylinder boundary. At a certain value of the changing flux, the caustic ''crawls'' through the NS boundary of the cylinder, an event which is accompanied by a rearrangement of all quantum states. The rearrangement occurs always when the flux trapped in the N layer changes by $\Phi_0=hc/2e$.

To conclude, we note that the mean free path of the quasiparticles was expected to be the largest parameter of the problem. Allowance for the scattering by impurities will decrease the amplitude of the resonance spikes.

CONCLUSIONS

A theory of coherent phenomena in simply connected cylindrical normal conductors with a mesoscopic-scale cross section has been developed in this study. It is assumed that the normal metal is pure and coated with a thin superconducting layer with a thickness of the order of the coherence length ξ_0, and that their electric contact is good. Under these conditions the quasiparticles with energy $E<\Delta$ experience Andreev scattering at the NS boundaries. They move ballistically through the normal metal in the field of the vector potential excited by a narrow solenoid at the center of the conductor. On a single circuit of a quasiparticle along the perimeter of the cylinder cross section, the phase of a ''particle'' (''hole'') wave function changes by $\pm e/hc\oint_{\mathcal{L}}\mathbf{A}\cdot d\mathbf{s}$. This integral is equal to the flux Φ through the surface bounded by the trajectory $\mathcal{L}$. In the field $\mathbf{A}$ excited by the solenoid, the flux Φ is a constant independent of the trajectory shape. The sensitivity to the vector potential field is identical for all the quantum states of the quasiparticles.

If a simply connected cylinder is placed in a weak magnetic field, the situation becomes more complicated. For different quantum states of the quasiparticle the increment in the wave function phase is determined by the flux Φ, which depends on the shape of the trajectory. As follows from studies of quantum coherent phenomena in normal conductors with specular reflection of electrons at a cylinder boundary,[8] the universal period hc/e of the flux oscillations of the thermodynamic quantities is only connected with the states localized near the cylinder boundary.

This study is confined to the effect of the vector potential field on the phase of quasiparticle wave functions, which permits us to investigate the shapes of the quasiclassical trajectories of ''particles'' and ''holes.'' The quasiparticles experience Andreev scattering at the NS boundaries. As a result, a set of Andreev levels appear, which determine the behavior of the thermodynamic quantities of the structure. Within the multidimensional quasiclassical method, a dispersion relation was obtained, which can be used to find the spectrum of Andreev levels. Expanding it in a series in the parameter $1/k_{\rm F}R\ll 1$ (the quasiclassical parameter is $k_{\rm F}R\gg 1$) and keeping only the zero-order terms in the equation, we obtain Eq. (34) for the energy near the Fermi level, which bears resemblance to Kulik's spectrum for an SNS contact.[48] The expression describes the states of the quasiparticles inside the cylinder cross section when they move along the chord connecting two points at the NS boundary of the sample. The chord length depends on the radial angle α at which both the points are visible. The product of this angle and the trapped flux has the meaning of the phase difference

of the contact. The spectrum of Eq. (34) is used to calculate the density of states $\nu(E)$ as a function of the flux Φ, which displays a stepwise behavior. Whenever the flux increases by the value Φ_0, the number of steps increases by one. If the density of states is differentiated with respect to the flux Φ, a set of resonance spikes with a period equal to a superconducting flux quantum appears.

The authors are indebted to A. Kadigrobov for helpful discussions. One of the authors (G. A. G.) thanks the Department of Applied Physics, Chalmers University of Technology and Göteborg University for the invitation to participate in joint research at Göteborg and for warm hospitality. Financial support from the Swedish KVA is gratefully acknowledged. G. A. G. would like to thank A. N. Omelyanchouk for discussions and reading of this manuscript.

*E-mail: gogadze@ilt.kharkov.ua

[1] J. Bardeen, L. N. Cooper, and J. R. Schrieffer, Phys. Rev. **108**, 1175 (1957).
[2] B. S. Deaver, Jr. and W. M. Fairbank, Phys. Rev. Lett. **7**, 43 (1961).
[3] R. Doll and M. Nabauer, Phys. Rev. Lett. **7**, 51 (1961).
[4] F. London, *Superfluids*, Vol. I (Dover, New York, 1950).
[5] Y. Aharonov and D. Bohm, Phys. Rev. **115**, 485 (1959).
[6] C. N. Yang, Rev. Mod. Phys. **34**, 694 (1962).
[7] I. O. Kulik, JETP Lett. **11**, 275 (1970).
[8] E. N. Bogachek and G. A. Gogadze, Zh. Éksp. Teor. Fiz. **63**, 1839 (1972) [Sov. Phys. JETP **36**, 973 (1973)].
[9] T. W. Nee and R. E. Prange, Phys. Lett. A **25**, 582 (1967).
[10] E. N. Bogachek and G. A. Gogadze, JETP Lett. **17**, 115 (1973).
[11] E. N. Bogachek and G. A. Gogadze, Zh. Éksp. Teor. Fiz. **67**, 621 (1974) [Sov. Phys. JETP **40**, 308 (1974)].
[12] E. N. Bogachek, G. A. Gogadze, and I. O. Kulik, Fiz. Nizk. Temp. **2**, 461 (1976) [Sov. J. Low Temp. Phys. **2**, 228 (1976)].
[13] G. A. Gogadze, Solid State Commun. **49**, 277 (1984).
[14] G. A. Gogadze, Fiz. Nizk. Temp. **9**, 1051 (1983) [Sov. J. Low Temp. Phys. **9**, 543 (1983)].
[15] E. N. Bogachek, G. A. Gogadze, and I. O. Kulik, Phys. Status Solidi B **67**, 287 (1975).
[16] W. A. Little and R. D. Parks, Phys. Rev. Lett. **9**, 9 (1962).
[17] R. D. Parks and W. A. Little, Phys. Rev. **133**, 97 (1964).
[18] M. Tinkham, Phys. Rev. **129**, 2413 (1963).
[19] E. N. Bogachek, G. A. Gogadze, and I. O. Kulik, Fiz. Nizk. Temp. **4**, 1156 (1978) [Sov. J. Low Temp. Phys. **4**, 544 (1978)].
[20] N. B. Brandt, D. V. Gitsu, A. A. Nikolaeva, and Ya. G. Ponomarev, JETP Lett. **24**, 272 (1976).
[21] N. B. Brandt, D. V. Gitsu, A. A. Nikolaeva, and Ya. G. Ponomarev, Zh. Éksp. Teor. Fiz. **72**, 2332 (1977) [Sov. Phys. JETP **45**, 1226 (1977)].
[22] N. B. Brandt, E. N. Bogachek, D. V. Gitsu, G. A. Gogadze, I. O. Kulik, A. A. Nikolaeva, and Ya. G. Ponomarev, Fiz. Nizk. Temp. **8**, 718 (1982) [Sov. J. Low Temp. Phys. **8**, 358 (1982)].
[23] I. O. Kulik, Fiz. Nizk. Temp. **13**, 206 (1987) [Sov. J. Low Temp. Phys. **13**, 115 (1987)].
[24] Y. Imry, in *Directions in Condensed Matter Physics*, edited by G. Grinstein and G. Mazenko, World Scientific, Singapore (1986), p. 101.
[25] R. A. Webb, S. Washburn, C. P. Umbach, and R. B. Laibowitz, Phys. Rev. Lett. **54**, 2696 (1985).
[26] V. Chandrasekhar, N. Rooks, S. Wind, and D. Prober, Phys. Rev. Lett. **55**, 1610 (1985).
[27] B. L. Altshuler, A. G. Aronov, and B. Z. Spivak, JETP Lett. **33**, 97 (1981).
[28] D. Yu. Sharvin and Yu. V. Sharvin, JETP Lett. **34**, 272 (1981).
[29] B. L. Altshuler, A. G. Aronov, B. Z. Spivak, D. Yu. Sharvin, and Yu. V. Sharvin, JETP Lett. **35**, 475 (1982).
[30] B. L. Altshuler and A. G. Aronov, in *Electron-Electron Interaction in Disordered Systems*, edited by A. L. Efros and M. Pollak, North-Holland, Amsterdam (1985), p. 1.
[31] S. Washburn and R. A. Webb, Adv. Phys. **35**, 375 (1986).
[32] A. G. Aronov and Yu. V. Sharvin, Rev. Mod. Phys. **59**, 755 (1987).
[33] A. A. Zvyagin and I. V. Krive, Fiz. Nizk. Temp. **21**, 687 (1995) [Low Temp. Phys. **21**, 533 (1995)].
[34] E. N. Bogachek, Fiz. Nizk. Temp. **2**, 473 (1976) [Sov. J. Low Temp. Phys. **2**, 235 (1976)].
[35] C. W. J. Beenakker and H. van Houton, Phys. Rev. B **38**, 3232 (1988).
[36] P. H. M. van Loosdrecht, C. W. J. Beenakker, H. van Houton, J. G. Williamson, B. J. van Wees, J. E. Mooij, C. T. Foxon, and J. J. Harris, Phys. Rev. B **38**, 10162 (1988).
[37] B. Müller-Allinger and A. C. Mota, Phys. Rev. Lett. **84**, 3161 (2000).
[38] P. Visani, A. C. Mota, and A. Pollini, Phys. Rev. Lett. **65**, 1514 (1990).
[39] A. Lodder and Yu. V. Nazarov, Phys. Rev. B **58**, 5783 (1998).
[40] A. F. Andreev, Zh. Éksp. Teor. Fiz. **46**, 1823 (1964) [Sov. Phys. JETP **19**, 1228 (1964)].
[41] A. Kadigrobov, A. Zagoskin, R. I. Shekhter, and M. Jonson, Phys. Rev. B **52**, R8662 (1995).
[42] H. A. Blom, A. Kadigrobov, A. M. Zagoskin, R. I. Shekhter, and M. Jonson, Phys. Rev. B **57**, 9995 (1998).
[43] P. G. de Gennes, *Superconductivity of Metals and Alloys*, Benjamin, New York (1966).
[44] C. Caroli and J. Matricon, Phys. Kond. Materie **3**, 380 (1965).
[45] C. Caroli, P. G. de Gennes, and J. Matricon, Phys. Lett. **9**, 307 (1964).
[46] J. B. Keller and S. I. Rubinow, Ann. Phys. (N.Y.) **9**, 24 (1960).
[47] J. B. Keller, Ann. Phys. (N.Y.) **4**, 180 (1958).
[48] I. O. Kulik, Zh. Éksp. Teor. Fiz. **57**, 1745 (1969) [Sov. Phys. JETP **30**, 944 (1969)].
[49] Yu. K. Dzhikaev, Zh. Éksp. Teor. Fiz. **68**, 295 (1975) [Sov. Phys. JETP **41**, 144 (1975)].
[50] L. Yu. Gorelik and A. M. Kadigrobov, Fiz. Nizk. Temp. **7**, 131 (1981) [Sov. J. Low Temp. Phys. **7**, 65 (1981)].
[51] A. Kadigrobov, R. Shekhter, and M. Jonson, Physica B **218**, 134 (1996).
[52] J. Bardeen, R. Kümmel, A. E. Jacobs, and L. Tewordt, Phys. Rev. **187**, 556 (1969).

This article was published in English in the original Russian journal. Reproduced here with stylistic changes by AIP.

LOW-TEMPERATURE MAGNETISM

Domain structure of the antiferromagnetic insulating state in $Nd_{0.5}Sr_{0.5}MnO_3$

I. O. Shklyarevskiy, M. Yu. Shvedun, and S. L. Gnatchenko

Institute for Low Temperature Physics and Engineering of the National Academy of Sciences of Ukraine, 47 Lenin Ave., 61103 Kharkov, Ukraine

P. J. M. van Bentum, P. C. M. Cristianen, and J. C. Maan

Research Institute for Materials and High Field Magnet Laboratory, University of Nijmegen, Toernooiveld 1, NL-6525 ED Nijmegen, The Netherlands

K. V. Kamenev

Department of Physics and Astronomy, The University of Edinburg, Mayfield Road, Edinburg, EH9 3JZ, United Kingdom

G. Balakrishnan and D. McK Paul

Department of Physics, The University of Warwick, Coventry CV4 7AL, United Kingdom

(Submitted June 21, 2001)
Fiz. Nizk. Temp. **27**, 1250–1257 (November 2001)

Optical reflectivity studies of the ferromagnetic metal (FMM) to antiferromagnetic insulator (AFI) phase transition are performed on $Nd_{0.5}Sr_{0.5}MnO_3$ manganite in a wide temperature and magnetic field range. The formation of a domain structure in the AFI state during the FMM−AFI phase transition is observed. It is shown that the two types of domains observed are energetically equivalent states. On the basis of the experimental results and symmetry analysis we conclude that these domains are crystal twins. The twin domain structure of the AFI state in the $Nd_{0.5}Sr_{0.5}MnO_3$ is visible in reflected unpolarized light due to a different tilting of the surface in the domains. The two-phase domain structure FMM+AFI formed in the vicinity of the phase transition is also studied. It is found that a thermodynamically equilibrium two-phase stripe domain structure does not develop. The absence of the magnetic intermediate state is due to the large energy of the interphase wall, which results in the stripe structure period being much larger than the size of the sample.
[DOI: 10.1063/1.1421457]

INTRODUCTION

In the last decade the perovskite manganese oxides with the basic formula $R_{1-x}A_xMnO_3$ (where R=trivalent rare-earth ion, A=divalent alkaline ion) have been of great interest because of the unusual magnetic and transport properties.[1] The most spectacular effect in the manganites is the colossal magnetoresistance observed in the vicinity of the Curie temperature. Moreover these compounds exhibit interesting phenomena such as charge and orbital ordering, the Jahn–Teller effect, and magnetic- or electric-field-induced phase transitions. In some of them a spontaneous and magnetic-field-induced phase transition from an antiferromagnetic insulating (AFI) to a ferromagnetic metallic (FMM) state takes place.[2–4] The nature of this phase transition is rather complicated and its understanding is yet to emerge.

$Nd_{0.5}Sr_{0.5}MnO_3$ is one of the manganites that demonstrate such a FMM−AFI phase transition.[2–4] The ferromagnetic ordering occurs in this crystal at $T_C=255$ K. At a temperature T_{M-I} near 160 K a spontaneous first-order FMM−AFI phase transition takes place. This transition is accompanied by charge ordering, i.e., spatial ordering of the holes and corresponding spatial ordering of the Mn^{3+} and Mn^{4+} ions. In the temperature range $T<T_{M-I}$ the application of a magnetic field leads to melting of the charge order in $Nd_{0.5}Sr_{0.5}MnO_3$ and induces a transition to the FMM state.[2] The electric conductivity during this transition varies over two orders of magnitude, and the magnetization changes by a value of $2.5\mu_B$ per Mn atom.[2] The FMM−AFI phase transition in $Nd_{0.5}Sr_{0.5}MnO_3$ is also accompanied by considerable changes in the lattice parameters ($\sim 10^{-3}-10^{-2}$) and unit cell volume ($\sim 10^{-3}$).[2,5] It was suggested in early studies[2] that there is no change in the crystal symmetry at this transition (the crystal has orthorhombic symmetry both in the FMM and AFI states). However, recent synchrotron and neutron diffraction investigations have shown that the FMM−AFI transition is accompanied by a lowering of the crystal symmetry from orthorhombic (space group *Imma*) to monoclinic (space group $P2_1/m$).[5,6] In a previous paper[7] we reported that the FMM−AFI phase transition in $Nd_{0.5}Sr_{0.5}MnO_3$ is followed by the formation of a domain structure in the AFI state which is visible in unpolarized white light.

In the present study we have investigated this domain structure in a wide temperature and magnetic field range with the goal of understanding its nature.

EXPERIMENT

The $Nd_{0.5}Sr_{0.5}MnO_3$ crystal was melt-grown by standard floating zone method and had a cylindrical form 3 mm in diameter. X-ray analysis showed it to be a single crystal. The samples were then cut perpendicular to the cylinder axis; their thickness varied from 0.5 to 3 mm. For our experiments the samples were optically polished with diamond paste. To remove the surface strain that occurs as a result of polishing they were annealed for 20 hours at 950 °C in air.

The experiments were performed on two setups. The first one permits simultaneous optical imaging of the domain structure and indirect measurements of the reflected light intensity from the different domains. The samples were mounted in a continuous-flow He cryostat placed in a Bitter magnet with magnetic field range up to 15 T. The image of the sample produced by the reflectance optical microscope was recorded with a CCD camera connected to a video recorder. Nonpolarized white light from a filament lamp was used to image the surface of the sample. The video images were subsequently analyzed to determine the reflected light intensity. In this case an interference filter with $\lambda = 634$ nm was placed after the source of light. Field dependences of the reflected light intensity were obtained by computer processing of the image.

The second setup allows direct measurement of the reflected light intensity. In this case the sample was mounted in an optical He cryostat, where it was placed in a superconducting magnet with a maximum field of 5 T. A He–Ne laser at $\lambda = 633$ nm was used as a source of light with an optical chopper in the beam. The light reflected from the sample was detected with a photomultiplier connected to a lock-in. This setup as well as the previous one allows us to measure the reflected light intensity both from the whole surface of the sample and from separate domains. To measure the intensity of the light reflected from individual domains, the image of the sample was projected on a screen with a diaphragm. By shifting the diaphragm position we could measure the reflected light intensity from different domains. This setup also affords the possibility of visual observation of the domain structure using a reflectance optical microscope and video camera.

The magnetization measurements were carried out with a moving-sample magnetometer in a variable-temperature cryostat and in fields up to 20 T.

EXPERIMENTAL RESULTS

It was found that there are distinct changes in the unpolarized reflected light intensity at the FMM−AFI phase transition in $Nd_{0.5}Sr_{0.5}MnO_3$ (Ref. 7). This effect made possible the optical observation of the two-phase domain state that is formed at this first-order phase transition. Besides, the domain structure in the AFI phase was visually observed and recorded. With temperature decrease a spontaneous FMM−AFI phase transition takes place at $T \approx 154$ K, while temperature increase results in a reverse transition at $T \approx 162$ K. Thus the first-order FMM−AFI phase transition is accompanied by substantial hysteresis. Coexistence of the FMM and AFI phases was observed in a temperature region of about 2 K. The AFI phase was nonuniform with clearly visible domain structure that remained unchanged in the whole temperature range (20–160 K) at zero magnetic field. There were also no variations of the domain structure in a magnetic field up to the field of the phase transition to the FMM state. After a spontaneous or field-induced phase transition to the FMM state and a subsequent reverse transition to the AFI state, the newly formed domain structure was usually different from the previous one. From this fact one can conclude that the domain structure in the AFI state emerges at the FMM−AFI phase transition. This domain structure does not exist in the FMM state.

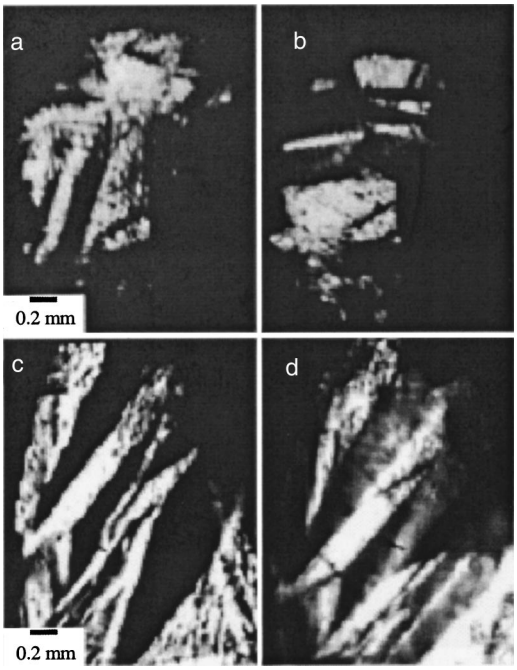

FIG. 1. Domain structure of two $Nd_{0.5}Sr_{0.5}MnO_3$ crystals in the AFI state. Images (a) and (b) show the domain structure after the first and second AFI−FMM−AFI transition cycles, respectively. Images (c) and (d) show a similar sequence for a second crystal.

The photos in Fig. 1 show the domain structure of $Nd_{0.5}Sr_{0.5}MnO_3$ in the AFI state. Two examples are given in Fig. 1, showing the domain structure of the same sample after the first (Fig. 1a) and second (Fig. 1b) AFI−FMM−AFI transition cycle. A comparison of the two images shows that the domain structures formed in successive cycles can be quite different. The images in Fig. 1c and Fig. 1d, respectively, represent a similar sequence on a second sample.

The main features of the domain structure observed in the AFI state are the following. Two types of domains (bright and dark) exist in the AFI state. The domain walls have a favorable orientation (Fig. 1). Two primary directions along which the walls are oriented can be selected in the sample (see Fig. 1a,b).

Figure 2 shows the representative stages in the domain formation during the FMM−AFI phase transition. Figure 2a shows an image of the sample in the homogeneous FMM phase. The transition occurs by the nucleation and subse-

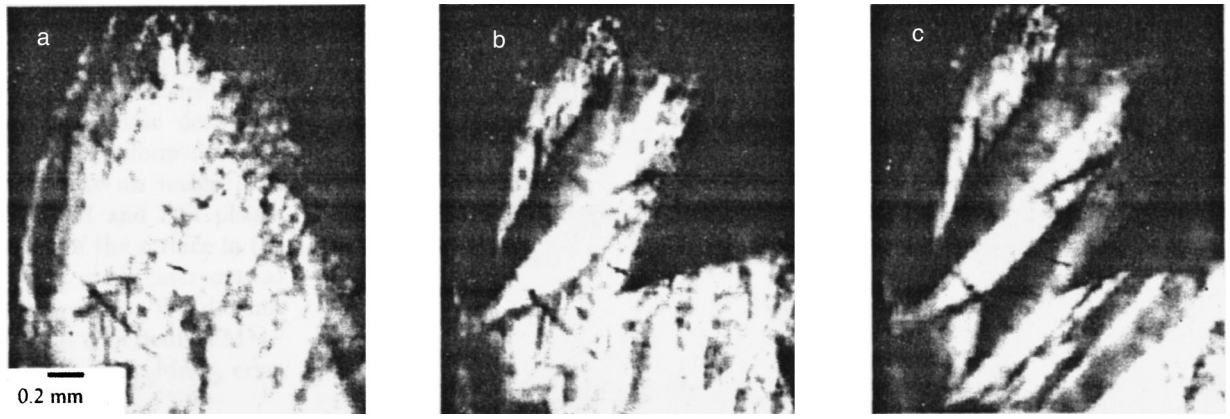

FIG. 2. Images of the field-induced FMM−AFI phase transition in $Nd_{0.5}Sr_{0.5}MnO_3$. The temperature of the sample $T=150$ K. External magnetic field H, T: 1.8 (a), 1.2 (b), 0 (c).

quent propagation of the domains of the energetically favorable phase. As these domains extend, the concentration of the energetically unfavorable phase decreases, until the sample is completely transformed to the AFI phase. Figure 2b represents an image of a two-phase state with both FMM and AFI phases present. Figure 2c is an image of the surface in the fully developed AFI phase but with clear optical contrast in bright and dark domains. We did not find an intermediate state with a periodic FMM−AFI domain structure in the $Nd_{0.5}Sr_{0.5}MnO_3$ crystals.

Field dependences of the reflected light intensity $I(H)$ from the whole surface of the sample were measured to determine the hysteretic AFI−FMM transition fields and the field range where AFI and FMM phases coexist. Typical $I(H)$ curves are shown in Fig. 3a. The reflected light intensity is given in arbitrary units and normalized to the value of the reflected light intensity in the FMM state. The field at which the jump in intensity occurs corresponds to the AFI−FMM phase transition field. The transition field decreases with temperature increase. It is clearly seen that this first-order phase transition is accompanied by a hysteresis in $I(H)$. This hysteresis becomes smaller as the temperature increases. The width of the temperature range of the AFI−FMM phase coexistence also decreases at higher temperatures. The transition width decreases from $\Delta H_{\text{coex}} \approx 1$ T at $T=20$ K to $\Delta H_{\text{coex}} \approx 0.5$ T at $T=140$ K. The change in the reflected light intensity level in the AFI state after a full cycle can be attributed to a different concentration of the bright and dark AFI domains before and after the AFI−FMM−AFI transition. Note that the reflected light intensity in the FMM

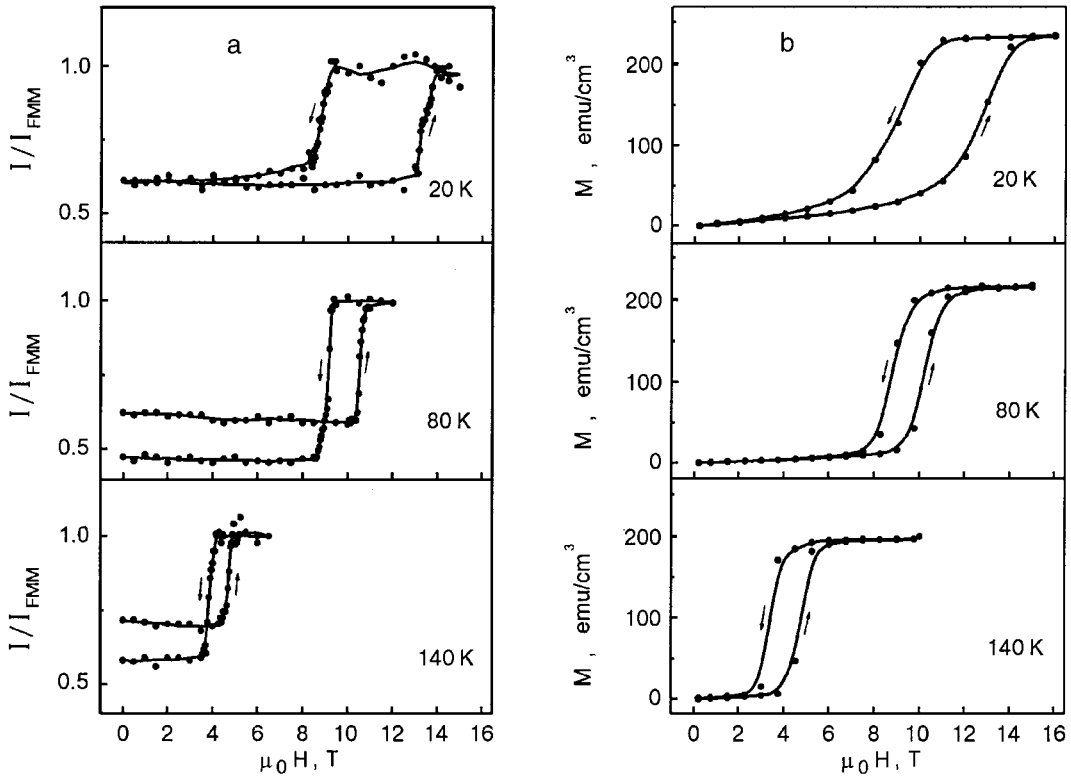

FIG. 3. Field dependences of the integrated reflected light intensity for the whole surface of the sample (a), and field dependences of the magnetization (b). $I(H)$ and $M(H)$ curves are presented for $T=20$, 80, and 140 K. The reflectivity is normalized to the FMM state.

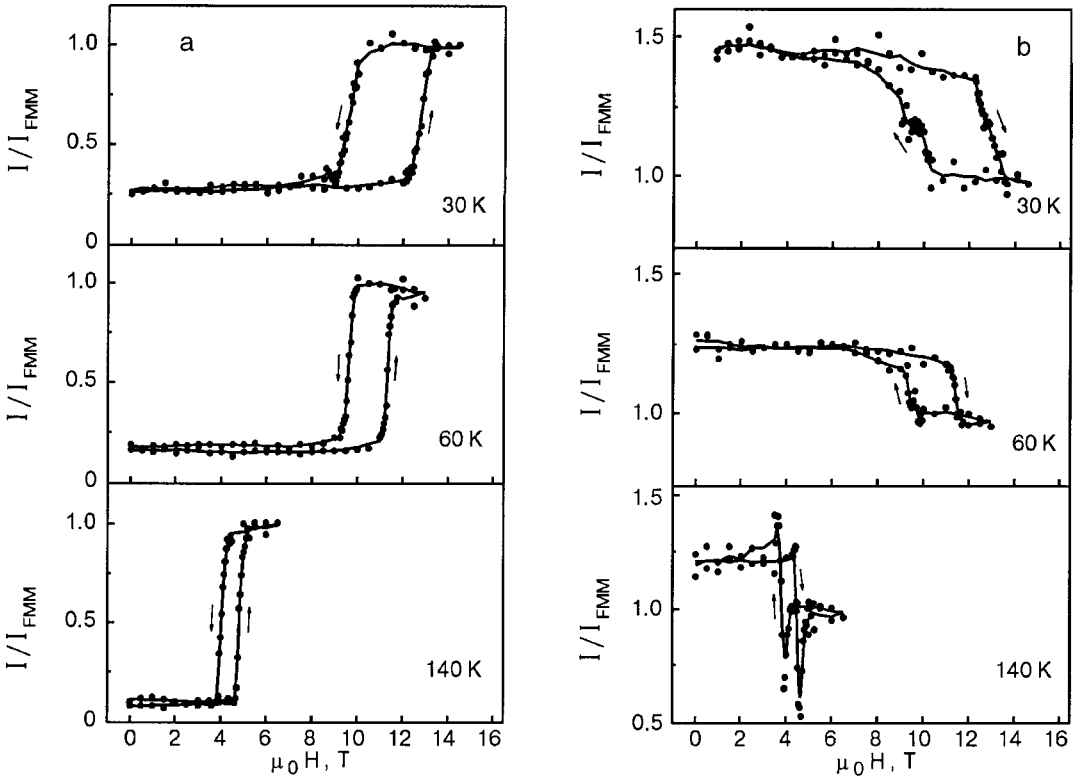

FIG. 4. Field dependences of the reflected light intensity measured for dark (a) and bright (b) domains at the temperatures 30, 60, and 140 K.

state remains practically unchanged (within the experimental error limits $\pm 5\%$) in the present temperature and magnetic field range.

For comparison we measured the field dependences of the magnetization $M(H)$ for the same sample. Typical $M(H)$ curves are shown in Fig. 3b. The width of the phase transition on the $M(H)$ curves is generally larger than that seen on the optical $I(H)$ curves. This indicates some additional inhomogeneity of the bulk of the sample.

To reveal the nature of the domain structure observed in the AFI state the field dependences of the reflected light intensity were also measured for single-domain areas of the sample. Figure 4 shows the $I(H)$ curves for dark (a) and bright (b) domains at different temperatures. The reflected light intensity for dark domains is much lower than for the FMM state, while for bright domains it is higher. It is important to note that the AFI−FMM phase transition occurs at the same magnetic field in the dark and bright domains. Therefore these domains are not thermodynamically different phases but energetically equivalent states. The strongest drop of the reflected light intensity was observed in the $I(H)$ curves for bright domains in the vicinity of the phase transition (see Fig. 4b, bottom curve). Such behavior of the intensity can be associated with changes in the optical properties of the crystal as a result of the elastic strains arising near the interphase wall. These elastic strains undoubtedly must arise because of the large changes in the crystal lattice parameters at the phase transition.[2,5]

As was mentioned above, the domain structure in the AFI state before transition to the FMM state and after reverse transition to the AFI state often differs. Therefore $I(H)$ curves like those presented in Fig. 5 were observed in some cases. Figure 5a shows an $I(H)$ curve that corresponds to the transition from a dark AFI domain to the FMM state and the inverse transition to a bright AFI domain. In Fig. 5b the $I(H)$ dependence that corresponds to the transition from a bright AFI domain to the FMM state and the inverse transition to a dark AFI state is shown.

The $H-T$ phase diagram of $Nd_{0.5}Sr_{0.5}MnO_3$ constructed from the results of the optical studies is shown in Fig. 6. The value of the transition fields in the phase diagram were determined from the $I(H)$ curves for the whole sample and correspond to the center of the field interval of the AFI+FMM phase coexistence. The unfilled symbols corre-

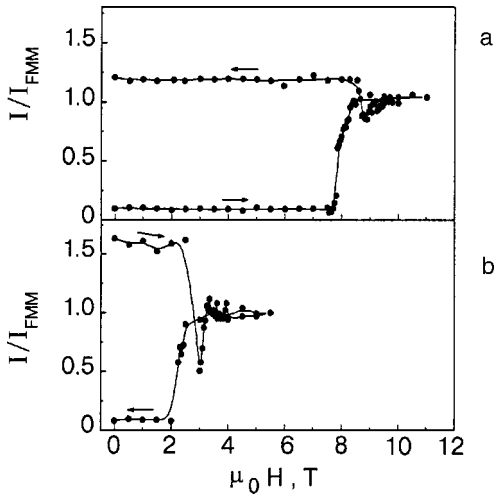

FIG. 5. Field dependences of the reflected light intensity measured in a single domain area of the sample for the cases when after an AFI−FMM−AFI transition cycle at the place of the dark domain a bright one arises, at $T=100$ K (a), and vice versa, at $T=150$ K (b).

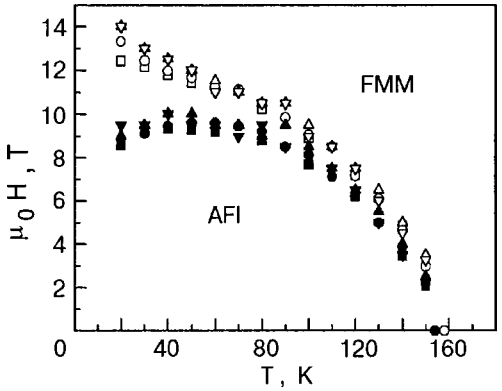

FIG. 6. *H*-T phase diagram of $Nd_{0.5}Sr_{0.5}MnO_3$ constructed from optical studies. The unfilled symbols correspond to the phase transition from the AFI to the FMM state, and the filled symbols correspond to the reverse transition from the FMM to the AFI state. The transition fields were determined from the $I(H)$ dependences for the whole sample (circles) and for the bright (up triangles) and dark (down triangles) domains, and also from the $M(H)$ dependences (squares).

spond to the AFI−FMM phase transition observed with increasing magnetic field and the filled symbols correspond to the reverse transition in decreasing field. The difference between the transition fields obtained for these two cases corresponds to the hysteresis in the $I(H)$ curves. It is clearly seen in Fig. 6 that the hysteresis decreases at higher temperatures.

Another sets of symbols presents the transition field values determined from the $I(H)$ dependences measured separately for dark and bright domains. The phase diagram clearly demonstrates good coincidence of the transition fields for dark and bright domains in the whole temperature range.

The values of the transition fields obtained from the $M(H)$ curves are also indicated in the phase diagram (Fig. 6) for comparison with the optical results. These values were determined in the same way as the transition fields from the $I(H)$ curves. The results obtained from optical and magnetic measurements are in satisfactory agreement. Therefore optical studies probe information about a rather deep surface layer of the sample and represent the bulk properties of the crystal. The influence of the surface on the AFI−FMM transition in $Nd_{0.5}Sr_{0.5}MnO_3$ was not revealed.

The above experiments demonstrate that the two types of domains (dark and bright) observed in the AFI phase are energetically equivalent states formed during the transition from the FMM phase to the AFI phase. It is reasonable to suggest that these domains are crystal twins emerging at the FMM−AFI phase transition, accompanied by a lowering of the crystal symmetry from orthorhombic to monoclinic. However, the problem of the optical contrast in unpolarized reflected light at the crystal twins still remains to be solved.

During visual observation of the domain structure in the AFI state we found that variation of the angle of incidence of light on the sample results in changes of the optical contrast between domains. Dark domains can transform to bright or vice versa, and at a certain angle of incidence the optical contrast between domains may disappear. Moreover, the contrast between domains also vanishes when a microscope objective with a sufficiently large aperture is used. This suggests that during crystal twin formation the surface of the

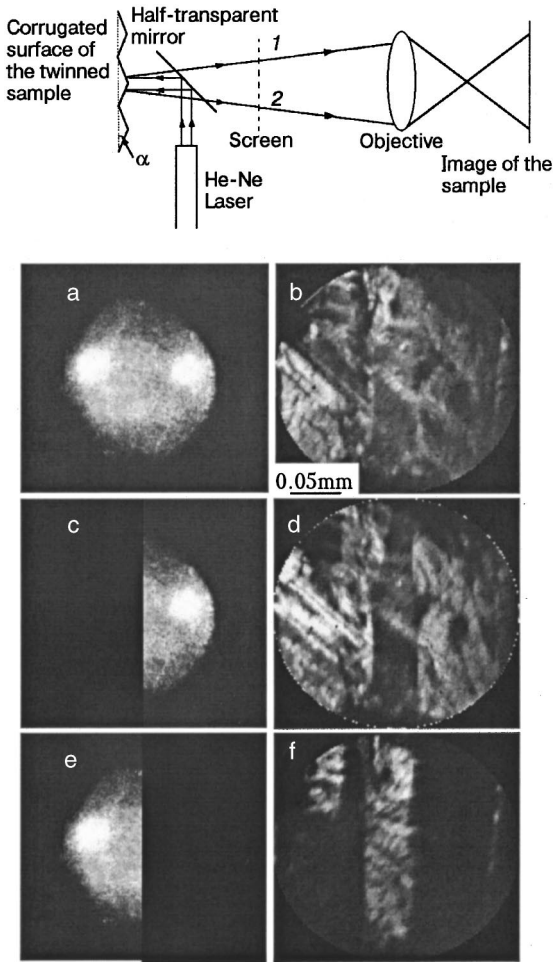

FIG. 7. (Upper panel) The optical setup to demonstrate the origin of the optical contrast between crystal twins. (Lower panel) a — Two white spots on the screen correspond to separate major directions for specular reflection from the corrugated surface of the sample. b — Image of the sample when both reflected beams are captured by the objective. No domain structure is observed. c, d: The first beam is closed off. The domain structure is observed visually. e, f: The second beam is closed off. Inverse changes occur in the contrast of the domain structure.

sample becomes corrugated, and the surfaces of the twins of different types form a certain angle with each other. In this case the light intensities reflected from the surfaces of the different types of twins and captured by the microscope objective can be different, which results in an optical contrast between domains. In other words, part of the light reflected from the surface of the twins of one type is not captured by the objective, and these domains are observed as dark.

To check this suggestion the following experiment was performed. The basic scheme of the optical setup used for this experiment is presented on the upper panel of Fig. 7. A beam from a He−Ne laser illuminates an area of the sample including both types of domains. The reflected light is used to image the surface using a microscope objective. On an intermediate screen we can determine the intensity distribution in the reflected beam. In the FMM phase we observe a single bright spot on the screen, corresponding to the specular reflection of the optically polished surface. However, in the AFI domain phase we find two spots (Fig. 7a). If the optical alignment is such that the light of both spots is used in the image, then no optical contrast is seen between the

different domains (see Fig. 7b). However, if we close off half of the beam with one of the two bright spots (Fig. 7c, e), we can observe the contrast domain structure (Fig. 7d, f). This strongly suggests that the optical contrast between the domains is caused by a different angle of specular reflection for the two types of domains. The estimated tilt angle of the domain surface is $\alpha \approx 1°$.

This experiment allows one not only to explain the existence of the optical contrast, but also to correct the data for $I(H)$. The real change of the reflected light intensity during the AFI−FMM phase transition can be observed only on the $I(H)$ curves for bright domains. A small increase of the reflected light intensity, i.e., a small increase of the reflection coefficient, was observed on these curves at the transition to the AFI phase (Fig. 4b). The decrease in the intensity of the $I(H)$ curves for dark domains and for the whole sample is related to the fact that part of the reflected light was not captured by the objective and registered by the photomultiplier. Thus the curves for dark domains and for the whole sample did not show the real picture of the changes in the reflectance at the transition. However, they were much better than the $I(H)$ curves of the bright domains for the purpose of determining the value of the transition field and the phase coexistence region.

DISCUSSION

As we have said, the cause of the AFI phase inhomogeneity can be the formation of a twin domain structure during the transition to a state with lower crystal symmetry. According to Refs. 5, 6 and 8, the symmetry of $Nd_{0.5}Sr_{0.5}MnO_3$ changes from orthorhombic (space group *Imma*) to monoclinic (space group $P2_1/m$) at the FMM−AFI transition. The formation of the twin domain structure in the AFI state was observed previously in $Pr_{0.5}Sr_{0.5}MnO_3$ by electron diffraction techniques.[9]

Let us perform a symmetry analysis of the twin domain structure that can arise in the asymmetric phase during the phase transition accompanying the lowering of the symmetry from orthorhombic (point group *mmm*) to monoclinic (point group $2/m$). At the structural transition the crystal loses the following symmetry operations: two reflection planes, 2_x and 2_y, and two rotation axes, 2_x and 2_y (the monoclinic axis is the z axis). The lost symmetry operations are indeed twinning operations. Two types of crystal twins can be formed at this phase transition. These twins differ by the sign of the shear deformation in the xy plane and transform one into another by the twinning operations. Monoclinic shear deformations in the two types of twins can be described by the second-rank tensors ε_{ij}^{+} and ε_{ij}^{-} with the following matrices:

$$\varepsilon_{ij}^{+}=\begin{pmatrix} \varepsilon_{11} & \varepsilon_{12} & 0 \\ \varepsilon_{21} & \varepsilon_{22} & 0 \\ 0 & 0 & \varepsilon_{33} \end{pmatrix}, \quad \varepsilon_{ij}^{-}=\begin{pmatrix} \varepsilon_{11} & -\varepsilon_{12} & 0 \\ -\varepsilon_{21} & \varepsilon_{22} & 0 \\ 0 & 0 & \varepsilon_{33} \end{pmatrix}. \tag{1}$$

Consider possible coherent (without any twinning dislocations) walls between these twins. The condition of coexistence of the deformations, i.e., the absence of strains in the wall, is[10]

$$(\varepsilon_{ij}^{+}-\varepsilon_{ij}^{-})x_i x_j = 0. \tag{2}$$

In order for (2) to be an equation of a plane the following additional condition must be satisfied:

$$\det|\varepsilon_{ij}^{+}-\varepsilon_{ij}^{-}| = 0. \tag{3}$$

It is easy to check that in the case considered, the condition (3) is satisfied and the solutions of the equation (2) are two orthogonal planes, $x=0$ and $y=0$. Thus coherent domain walls have to be arranged in these crystal planes.

When the results of the above analysis are compared with the experimental data the following can be seen. The analysis performed shows that two types of crystal twins can arise at the $mmm \rightarrow 2/m$ phase transition. This is consistent with optical observations that also show two types of domains in the AFI state of $Nd_{0.5}Sr_{0.5}MnO_3$. It also follows from the symmetry analysis that coherent walls of two types (planes $x=0$ and $y=0$) occur in the twinned crystal. It is clearly seen from Fig. 1(a, b) that there are two favorable directions of orientation of the domain walls. The slight deviations of the domain walls from these directions can be attributed to the elastic strains always existing in a real crystal. The angle between the two prevalent orientations of the domain walls is 70–80° (Fig. 1a). If the monoclinic z axis is perpendicular to the surface of the sample, then the angle between coherent domain walls oriented in the $x=0$ and $y=0$ planes is equal to 90°. However, if the monoclinic axis is tilted away from the normal to the surface of the sample, as is confirmed by x-ray analysis of our samples, this angle is less, and that explains why the angle between domain walls observed in the experiment differs from 90°.

Thus the results of the symmetry analysis are in good agreement with the experimental data. This allows us to conclude that the domains observed in the AFI state are crystal twins that form at the transition from the orthorhombic FMM phase to the monoclinic AFI phase.

Finally, let us consider some properties of the two-phase state observed near the FMM-AFI phase transition. As was mentioned above, no magnetic intermediate state, i.e., thermodynamically stable periodic two-phase domain structure, forms at this transition. Usually the absence of an intermediate state can be attributed to variability of the transition field in the sample. The intermediate state does not arise if this variability substantially exceeds the value $4\pi N \Delta M$, where ΔM is the magnetization jump at the phase transition and N is the demagnetizing factor. Typically for $Nd_{0.5}Sr_{0.5}MnO_3$ we find $\Delta M = 200-220$ emu/cm^3 (Fig. 3(b)) and a field interval of the intermediate state $\Delta H = 0.3-0.4$ T. This indicates that the absence of the intermediate state is not due to inhomogeneity of the sample.

Apparently a large energy of the interphase wall due to the strong elastic strains is the main reason why the intermediate state does not form. These clastic strains must arise in the vicinity of the interphase wall as a result of the dramatic changes ($\varepsilon \approx 1 \times 10^{-2}$; Ref. 4), in the crystal lattice parameters at the FMM–AFI phase transition. Optical measurements in polarized light give us the possibility of estimating the width of the strained area of the crystal in the wall vicinity $l \approx 60\ \mu$m. If it is assumed that the dominant contribution to the interphase wall energy is the contribution from the elastic strains, the wall energy can be estimated using the following formula

$$\sigma = C\varepsilon^2 l, \tag{4}$$

where C is the elastic constant. For this rough estimation we have neglected the strain inhomogeneity in the vicinity of the wall. Assuming $C \sim 10^{12}$ erg/cm^3, we get $\sigma \approx 6\times 10^5$ erg/cm^2. Using the value obtained for σ, we can estimate the period D of the stripe domain structure of the magnetic intermediate state:[11]

$$D = \left(\frac{\sigma d}{F(\xi)(\Delta M)^2} \right)^{1/2}, \tag{5}$$

where d is the sample thickness, $F(\xi) = 1.71/4$ for $\xi = 0.5$,[11] and ξ is the concentration of the AFI and FMM phases. For $d = 1$ mm and $\Delta M = 210$ emu/cm^3 we get $D \approx 2$ cm. Thus the estimated period of the equilibrium stripe two-phase domain structure substantially exceeds the size of the sample. This explains the absence of the intermediate state at the FMM–AFI phase transition in our experiments.

CONCLUSIONS

The optical studies have shown that a twin domain structure arises in the AFI state as a result of the lowering of the crystal symmetry at the FMM–AFI phase transition. The crystal twins could be imaged in unpolarized light. It was shown that the cause of the optical contrast between the two types of twins is the local tilting of the surface of the twin domains. As far as we know, a twin domain structure has not been observed earlier by this method. Note that the existence of the twin domain structure was confirmed by direct x-ray studies.[8]

It was also shown that no thermodynamically stable striped two-phase domain structure forms at the FMM–AFI phase transition. The absence of the magnetic intermediate state at this transition is due to the large energy of the interphase wall, which results in a stripe domain periodicity much larger than the size of the sample.

[1] A. P. Ramírez, J. Phys.: Condens. Matter **9**, 8171 (1997).
[2] H. Kuwahara, Y. Tomioka, A. Asamitsu, Y. Moritomo, and Y. Tokura, Science **270**, 961 (1995).
[3] Y. Tokura, H. Kuwahara, Y. Moritimo, Y. Tomioka, and A. Asamitsu, Phys. Rev. Lett. **76**, 3184 (1996).
[4] H. Kawano, R. Kajimoto, H. Yoshizawa, Y. Tomioka, H. Kuwahara, and Y. Tokura, Phys. Rev. Lett. **78**, 4253 (1997).
[5] R. Mahendrian, M. R. Ibarra, A. Maignan, F. Millange, A. Arulraj, R. Mahash, B. Raveau, and C. N. R. Rao, Phys. Rev. Lett. **82**, 2191 (1999).
[6] P. M. Woodward, D. E. Cox, T. Vogt, C. N. R. Rao, and A. K. Cheetham, Chem. Mater. **11**, 3528 (1999).
[7] S. L. Gnatchenko, A. B. Chizhik, I. O. Shklyarevskiy, D. N. Merenkov, V. I. Kamenev, Yu. G. Pashkevich, K. V. Kamenev, G. Balakrishnan, and D. McK Paul, Fiz. Nizk. Temp. **25**, 992 (1999) [Low Temp. Phys. **25**, 744 (1999)].
[8] V. Eremenko, S. Gnatchenko, N. Makedonskaya, Yu. Shabakayeva, M. Shvedun, V. Sirenko, J. Fink-Finowicki, K. V. Kamenev, G. Balakrishnan, and D. McK Paul, Fiz. Nizk. Temp. **27**, 1258 (2001) [Low Temp. Phys. **27**, 930 (2001)].
[9] F. Damay, C. Martin, M. Hervieu, A. Maignan, B. Raveau, G. Andre, and F. Bouree, J. Magn. Magn. Mater. **184**, 71 (1998).
[10] J. Sapriel, Phys. Rev. B **12**, 5128 (1975).
[11] V. G. Baryakhtar, A. E. Borovik, and V. A. Popov, Zh. Éksp. Teor. Fiz. **62**, 2233 (1972) [Sov. Phys. JETP **35**, 1169 (1972)].

This article was published in English in the original Russian journal. Reproduced here with stylistic changes by AIP.

X-ray study of $Nd_{0.5}Sr_{0.5}MnO_3$ manganite structure above and below the ferromagnetic metal–antiferromagnetic insulator spontaneous phase transition

V. Eremenko, S. Gnatchenko, N. Makedonska, Yu. Shabakayeva, M. Shvedun,* and V. Sirenko

Institute for Low Temperature Physics and Engineering of the National Academy of Sciences of Ukraine, 47 Lenin Ave., Kharkov 61103, Ukraine

J. Fink-Finowicki

Institute of Physics, Polish Academy of Sciences, 32/46 Al. Lotnikow, 02-668 Warsaw, Poland

K. V. Kamenev

Department of Physics and Astronomy, The University of Edinburg, Mayfield Road, Edinburg, EH9 3JZ, United Kingdom

G. Balakrishnan and D. Mck Paul

Department of Physics, The University of Warwick, Coventry CV4 7AL, United Kingdom

(Submitted June 21, 2001)
Fiz. Nizk. Temp. **27**, 1258–1263 (November 2001)

The crystal structure of the manganite $Nd_{0.5}Sr_{0.5}MnO_3$ is studied at temperature $T=300$ and 77.3 K by means of an x-ray diffractometer. It is shown that the transition from the ferromagnetic metallic state to the antiferromagnetic insulating charge-ordered state is accompanied by a lowering of the symmetry of the structure from orthorhombic to monoclinic. The space-group symmetry of the orthorhombic and monoclinic phases is identified as *Imma* and $P2_1/m$, respectively. Twinning of the crystal and the formation of a twin domain structure with coherent boundaries in the $(00l)$ crystallographic planes are found. © *2001 American Institute of Physics.* [DOI: 10.1063/1.1421458]

INTRODUCTION

Keen interest in the investigation of the manganese-based compounds ($R_{1-x}A_xMnO_3$) with perovskitelike structures is connected with their high potentialities for technical applications due to their colossal negative magnetoresistance.[1] The manganites are also attractive objects for basic physical research primarily for a combination of different phase transformations in the electronic, magnetic, and crystallographic subsystems.

Recent studies of $Nd_{0.5}Sr_{0.5}MnO_3$ have revealed a number of spontaneous phase transitions observed on decreasing temperature. At a temperature $T=250$ K the crystal transforms from a paramagnetic (PM) metallic state to ferromagnetic (FM) metallic one, and at a temperature of about 158 K a first-order phase transition to an antiferromagnetic (AFM) insulating charge-ordered state was observed in this crystal.[2] In a temperature range below $T<158$ K a magnetic field induces the reverse transition to the FM metallic state.[3]

At room temperature the manganite $Nd_{0.5}Sr_{0.5}MnO_3$ is characterized by a perovskitelike orthorhombic structure (Fig. 1), though there is a discrepancy in the published data on identification of the symmetry space group of this crystal. In Refs. 2–5 the $Nd_{0.5}Sr_{0.5}MnO_3$ compound is attributed to the space group *Imma*. In this case its crystal structure is the perovskite one, distorted by rotation of the octahedra with respect to the [101] direction in the perovskite structure. At the same time, in Refs. 1, 6 and 7 the space group of the manganite $Nd_{0.5}Sr_{0.5}MnO_3$ was determined as *Pmma*. This group has lower symmetry as compared with *Imma* and corresponds to a distortion of the ideal cubic perovskite structure by rotation of the octahedra with respect to the [101] and [010] directions.

As the temperature is decreased below 250 K an increase

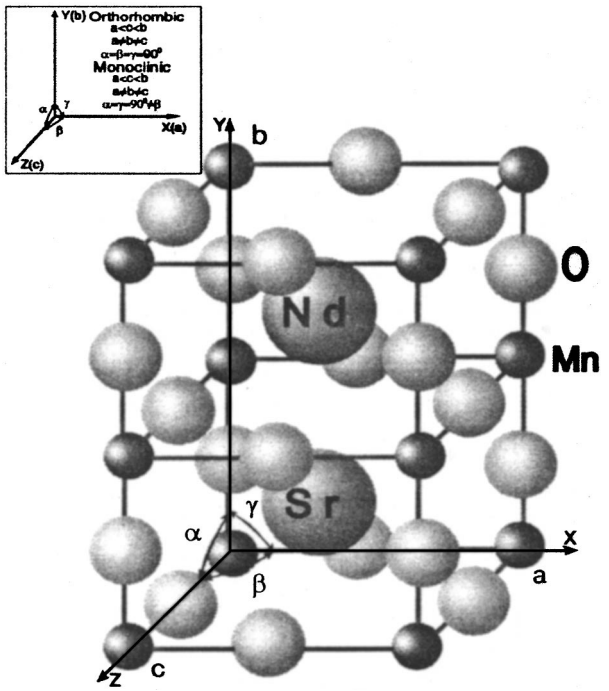

FIG. 1. The unit cell of the manganite $Nd_{0.5}Sr_{0.5}MnO_3$ (the inset shows the chosen spatial axes for the orthorhombic and monoclinic systems).

of the lattice cell parameters a and c and a decrease of the b parameter is observed.[3,6] The lattice symmetry does not change.

The ideas about the crystal structure of $Nd_{0.5}Sr_{0.5}MnO_3$ in the AFM insulating state also diverge. According to the results of Refs. 6–8 the structure of this compound does not change during transition to AFM insulating phase and stays orthorhombic. However, in Refs. 2–5 results were obtained which suggest that the crystal structure in this state becomes monoclinic with the space group $P2_1/m$.

The aim of this work is the investigation and identification of the $Nd_{0.5}Sr_{0.5}MnO_3$ crystal structure in the metallic state at room temperature and in the insulating state below the charge-ordering temperature by means of x-ray scattering measurements.

EXPERIMENTAL TECHNIQUE

Single-crystal and powder samples of the manganite $Nd_{0.5}Sr_{0.5}MnO_3$ were studied. The single crystals were obtained by the floating zone technique at the University of Warwick as well as at the Institute of Physics of the Polish Academy of Sciences. The single crystals were used for analysis of Laue patterns and also for observation and investigation of the twin domain structure by means of ω-scanning. For x-ray diffraction analysis the powders were prepared from single crystals in a commercial dispergator. It should be noted at once that the results obtained for the samples prepared at the University of Warwick and at the Institute of Physics of the Polish Academy of Sciences coincide fairly well.

The single-crystallinity of the samples under study was proved by the Laue patterns. This way of characterizing the samples was chosen as an express and direct one. A thick sample with high x-ray absorption was studied; the reverse Laue patterns were taken, because the reflections in the sample at low angles θ are strongly weakened and are not observed.

The x-ray spectra $I(\theta)$ were registered on a DRON-2.0 diffractometer, using the Bragg–Brentano scheme of focusing (θ–2θ scheme). The complete spectra of the diffracted radiation were obtained, with a subsequent identification of the unit cell system and parameters. The accuracy of the intensity measurements was 0.5%. The lattice parameters were determined to within $\pm 0.01\%$. The other used technique was ω-scanning, when the sample only rotates around the goniometer axis, while the counter is immobile and is mounted at a fixed double angle of diffraction with respect to the primary beam. The latter registering technique was used to obtain the ''reflection curves'' of the single crystal.

The DRON-2.0 diffractometer was also used in the cryogenic experiments: in this case the small-size cryostat for x-ray powder measurements in a temperature range 4.2–300 K was installed.

In the experiment an x-ray tube with a copper anode was used ($\lambda_{CuK_\alpha} = 1.54178$ Å). The spectra were registered in the angle range $2\theta = 20° - 80°$.

In principle the problem of structure analysis is solved for the crystals. However, utilization of the known techniques in structure identification for complex compounds often turns out to be inefficient without computer aids. Accordingly, it is important to modify the common methods of x-ray data processing using modern computer techniques. Here we used an approach[9] based on the differential Lipton technique for indexing the diffraction patterns and estimation of the unit cell parameters a_i ($i = 1,2,3$) for the orthorhombic and monoclinic systems. The classic techniques allow one to estimate only the order of the complex crystal lattice parameter. The differential Lipton technique was used as a basis for the algorithm of the program in order to estimate the parameters a_i and confine them by the least-squares technique. This algorithm included probability distribution for estimations of the lattice parameters and preliminary analysis of the measured and computed scattering amplitudes. Such values of lattice parameters were selected, which corresponded to the local maxima of the probability distribution function. As the latter may have false maxima, which are not associated with real values of the cell parameters, the proposed algorithm provided additional procedures for estimation of the reliability of proposed structure models, which allowed one to exclude false maxima.

EXPERIMENTAL RESULTS AND DISCUSSION

The Laue patterns registered at room and low temperatures are presented in Fig. 2. The point Laue patterns, shown in the picture, unambiguously identify the sample as being a single crystal. In order to avoid the situation in which the sample is a large-grained polycrystal and the incident beam reaches only one of the grains, the sample was shifted by small distances parallel to the film plane. The fact that the patterns obtained in various positions of the sample did not differ proves the single-crystallinity of the sample.

It is important to note that all the reflections on the Laue patterns are double, as is seen from Fig. 2. This circumstance may be explained by mosaicity of the crystal, i.e., it consists of blocks. The misorientation angle calculated from the Laue pattern is about $\sim 0.13°$, which is in good agreement with the low-angle boundary between the blocks.

The low-temperature Laue pattern shows changes in the reflection positions, though it is difficult to estimate the structure change correctly. For that the more accurate and informative x-ray diffraction analysis is required.

Figure 3 presents the diffraction patterns obtained at temperatures of 300 and 77.3 K for the powder sample of $Nd_{0.5}Sr_{0.5}MnO_3$. The low-temperature scanning was similar to that at room temperature, which simplifies considerably a comparative analysis of both diffraction patterns from the same sample at different temperatures. The chosen spatial axes for the unit cells in the orthorhombic and monoclinic systems are presented in Fig. 1.[10]

The quantities 2θ and the reduced intensities were derived for each maximum from the diffraction pattern at room temperature. Every peak was indicated using computer data processing, and the space system was determined. In Fig. 3 the indices of the reflecting plane are indicated near every peak. Together with the extinction laws for the orthorhombic system it clearly shows that at room temperature the $Nd_{0.5}Sr_{0.5}MnO_3$ belongs to the space group *Imma*. For this space group the following laws are valid: $h+k+l=2n$ for lines of the (hkl) type, and $k+l=2n$ for lines of the $(0kl)$ type.[11]

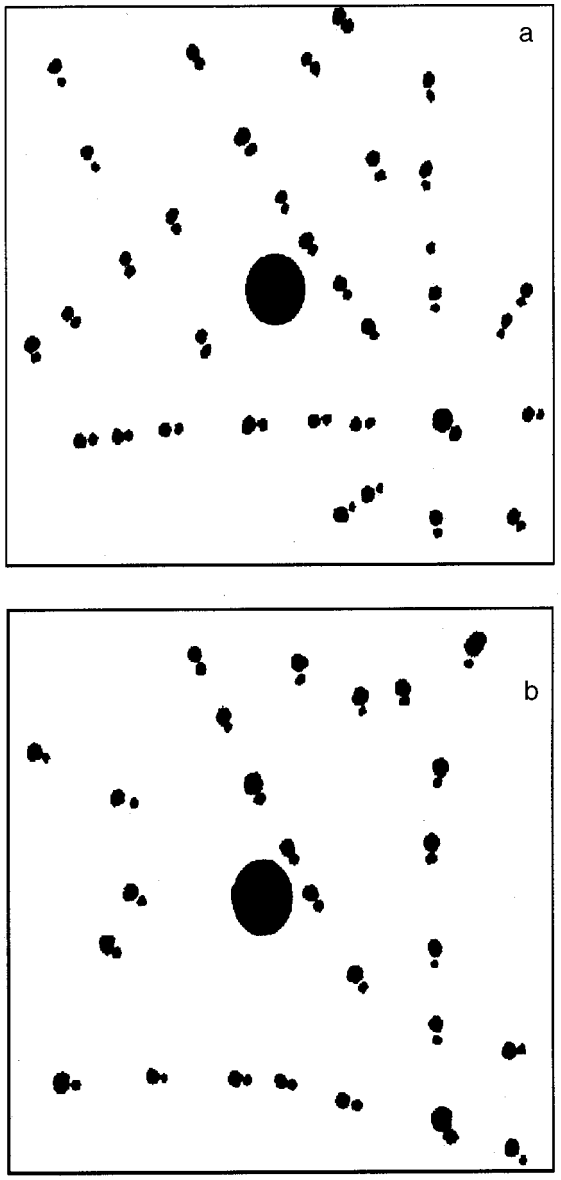

FIG. 2. The Laue patterns for single-crystal $Nd_{0.5}Sr_{0.5}MnO_3$ at $T=300$ (a) and 77.3 (b) K.

The unit cell parameters derived from the diffraction pattern at room temperature were $a=5.4302$ Å, $b=7.6177$ Å, $c=5.4860$ Å.

From a comparison of the diffraction patterns in Fig. 2 the change of the diffraction spectrum in the low-temperature state relative to that at room temperature is clearly seen. However, the large number of superimposed lines does not allow one to perform a qualitative analysis of the crystal lattice modification in the AFM insulating state. Therefore, in the next stage of the investigation the most intense lines were recorded in a discrete mode at both room and low temperatures. The results obtained are presented in Fig. 4. They clearly demonstrate that at low temperature the double maximum (200)/(121) splits into two separate maxima.

The shift and splitting of the diffraction maxima may be induced both by a change of space group and by anisotropy of the thermal expansion. Cooling of our samples is accompanied by a decrease of the cell parameters, which in turn results in a shift of the corresponding diffraction lines. However, the shift of the diffraction lines induced by thermal expansion anisotropy is lower than that induced by a change of a space symmetry group. Besides, the change of lattice parameters due to thermal expansion is smooth, while near 160 K we have a jumplike change of the cell parameters, which is attributed to a change of the space group symmetry. The above consideration are based on the data of Ref. 3.

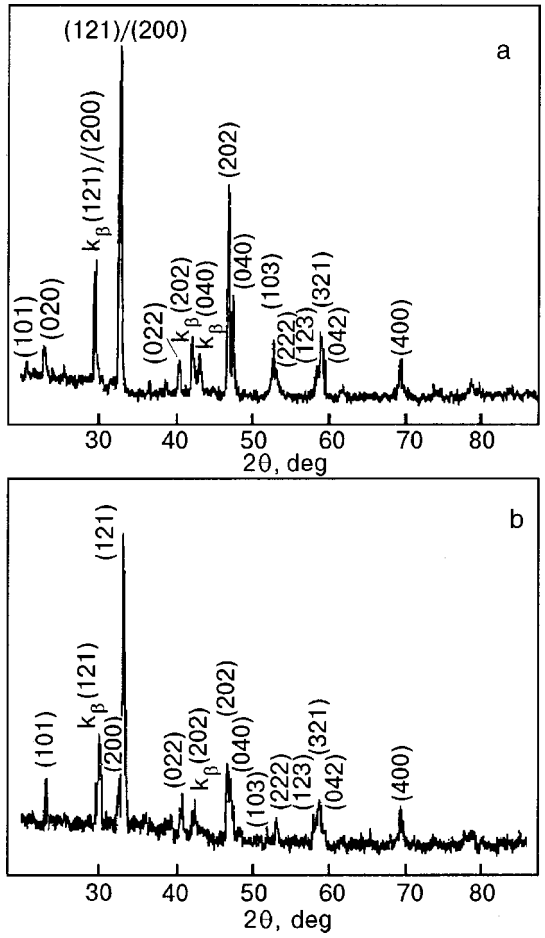

FIG. 3. The diffraction patterns for the $Nd_{0.5}Sr_{0.5}MnO_3$ powder sample at $T=300$ (a) and 77.3 (b) K.

The AFM insulating state, which is observed in the $Nd_{0.5}Sr_{0.5}MnO_3$ manganite below 158 K, is characterized by a monoclinic structure and belongs to the space group $P2_1/m$. The processing of the diffraction spectrum gave the

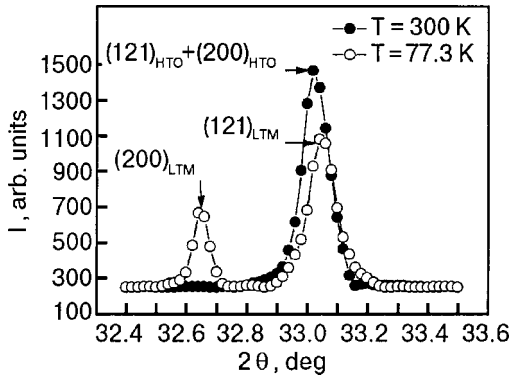

FIG. 4. The results of the discrete recording of the (121) and (200) reflections at $T=300$ and 77.3 K.

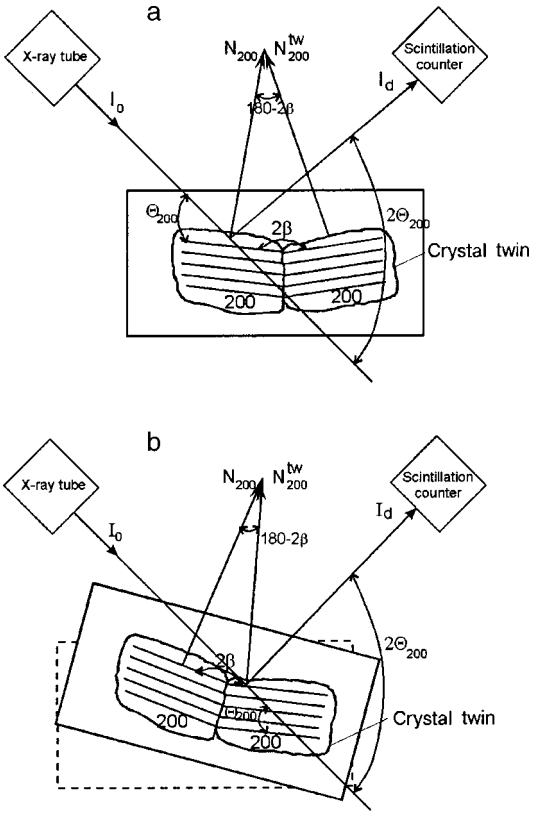

FIG. 5. The principle of twin structure observation in ω-scanning: (a)—the initial position; (b)—rotating the sample into the position corresponding to the crystal twin.

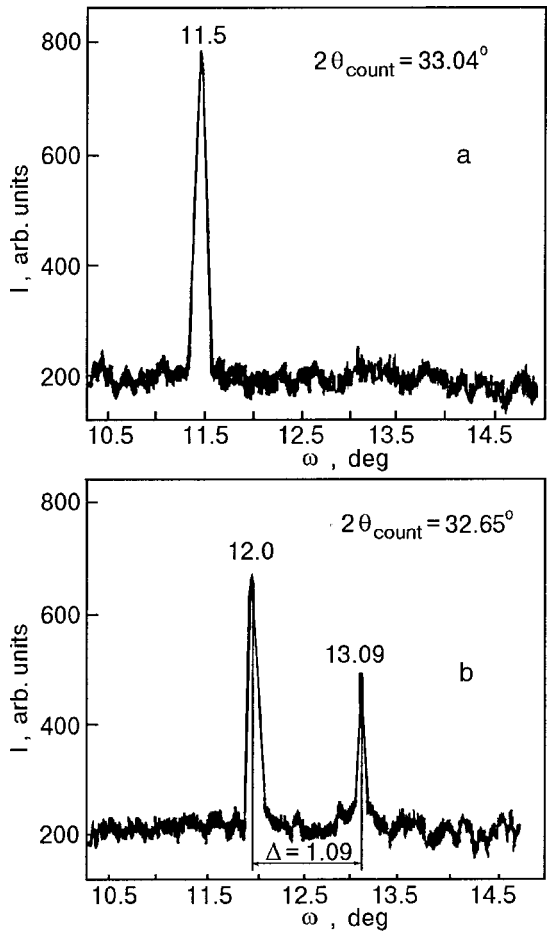

FIG. 6. The results of ω-scanning of the (200) maximum at $T=300$ (a) and 77.3 (b) K.

following unit cell parameters of the monoclinic phase: $a=5.4851$ Å, $b=7.5223$ Å, $c=5.5186$ Å, and the angle $\beta=89.455$ Å.

It is important to note that, as is clearly seen from Fig. 4, in this angle range the diffraction reflections corresponding to the orthorhombic phase are not observed. This suggests that in our case the state of the sample at $T=77.3$ K is homogeneous, i.e., phase separation[5] is not observed.

Consequently, the transition from the FM metallic state to the AFM charge-ordered insulating state is accompanied by a structural transformation. It should be mentioned that at the transition from the orthorhombic phase with space group *Imma* to the monoclinic phase with space group $P2_1/m$ the crystal loses some elements of symmetry, namely 2 reflection planes of the *m* type and, consequently, 2 twofold rotation axes normal to these planes. It is known that at a phase transition with symmetry lowering, a twin domain structure may appear in the low-symmetry phase. In the situation considered, twins may form in the monoclinic phase which are separated by coherent domain boundaries along the planes of the $(00l)$ type. Then in the monoclinic phase of the $Nd_{0.5}Sr_{0.5}MnO_3$ single crystal 2 sets of $(h00)$ planes will exist, with an interplane angle 2β (Fig. 5).

The domain structure in the AFM insulating phase of $Nd_{0.5}Sr_{0.5}MnO_3$ was observed visually in Refs. 12 and 13. It was assumed that the observed nonuniform state is connected with the formation of the twin domain structure at the transition from the orthorhombic to the monoclinic phase. However, the final conclusions as to the nature of the observed domain structure could be derived only from the more-direct measurements, in part from the x-ray study.

In order to reveal the twins, an ω-scanning of the single-crystalline sample relative to the (200) planes was performed. The orthorhombic and monoclinic phases were examined at room ($T=300$ K) and low ($T=77.3$ K) temperatures, respectively.

The principle of the twin structure revelation by ω-scanning is demonstrated schematically in Fig. 5.

The profiles of the interference lines obtained by means of ω-scanning at room ($2\theta=33.04°$) and low ($2\theta=32.65°$) temperatures for the (200) planes are shown in Fig. 6. The curves presented clearly indicate that at low temperature an additional reflection appears, corresponding to the occurrence of the twinned domain structure. Thus the results of an x-ray structural investigation unambiguously prove the formation of the twinned domain structure at the transition from the orthorhombic to the monoclinic phase.

CONCLUSIONS

Our x-ray investigations of the manganitc $Nd_{0.5}Sr_{0.5}MnO_3$ have shown the following:

1. In the orthorhombic phase the crystal structure of $Nd_{0.5}Sr_{0.5}MnO_3$ corresponds to the space group *Imma*. The unit cell of the orthorhombic phase is characterized by the lattice parameters $a=5.4302$ Å, $b=7.6177$ Å, $c=5.4860$ Å.

2. At the transition to the AFM insulating charge-ordered state the crystal symmetry lowers to monoclinic. The sym-

metry of the crystal structure of the manganite in this state is described by the space group $P2_1/m$. The unit cell is characterized by the lattice parameters $a=5.4851$ Å, $b=7.5223$ Å, $c=5.5186$ Å, and the angle $\beta=89.455$ Å.

3. At the transition from the orthorhombic to the monoclinic phase a twinning of the crystal occurs. A twin domain structure with coherent boundaries in the crystal planes $(00l)$ is formed.

*E-mail:shvedun@ilt.kharkov.ua

[1] H. Kuwahara, Y. Tomioka, Y. Moritomo, A. Asamitsu, M. Kasai, R. Kumai, and Y. Tokura, Science **272**, 80 (1996).
[2] R. Mahendiran, M. R. Ibarra, F. Maigan, A. Arulraj, R. Mahesh, O. Revcau, and C. N. R. Rao, Phys. Rev. Lett. **82**, 2191 (1999).
[3] P. M. Woodward, D. E. Cox, T. Vogt, C. N. Rao, and A. K. Cheetham, Chem. Mater. **11**, 3528 (1999).
[4] M. R. Ibarra, J. M. DcTeresa, P. A. Algarabel, C. Marquina, B. García-Landa, L. Morellon, C. Ritter, R. Mahendiran, and A. Del Moral, *Magnetostriction in Mixed Valent Magnetic Oxides, NATO Science Series, ASI-2000, Modern Trends in Magnetostriction Study and Application* **5**, 171 (2000).
[5] C. Ritter, R. Mahendiran, M. R. Ibarra, L. Morellon, A. Maignan, B. Raveau, and C. N. R. Rao, Phys. Rev. B **61**, 9229 (2000).
[6] R. Kajimoto, H. Yoshizawa, H. Kawano, H. Kuwahara, Y. Tokura, K. Ohoyama, and M. Ohashi, Phys. Rev. B **60**, 9506 (1999).
[7] H. Kuwahara, Y. Tomioka, A. Asamitsu, Y. Moritomo, and Y. Tokura, Science **270**, 961 (1995).
[8] H. Kawano, R. Kajimoto, H. Yoshizawa, Y. Tomioka, H. Kuwahara, and Y. Tokura, Phys. Rev. Lett. **78**, 4253 (1997).
[9] V. Bruk, A. Sirenko, and V. Sirenko, ''Visualization of x-ray measurements of complicated structures,'' in *The Materials of the Conf. "Teaching the Science of Condensed Matter and New Materials,"* M. Michelini (Ed.), Udine, 24–30 August (1995), p. 463.
[10] M. P. Shaskolskaya, *Crystallography*, in Russian, Vysshaya Shkola, Moscow (1984).
[11] L. I. Mirkin, Handbook of X-ray Structure Analysis of Polycrystals [in Russian], Gos. Izd.-vo Phys.-Math. Lit., Moscow, (1961).
[12] S. L. Gnatchenko, A. B. Chizhik, I. O. Shklyarevskiy, D. N. Merenkov, V. I. Kamenev, Yu. G. Pashkevich, K. V. Kamenev, G. Balakrishnan, and D. McK Paul, Fiz. Nizk. Temp. **25**, 992 (1999) [Low Temp. Phys. **25**, 744 (1999)].
[13] I. O. Shklyarevskiy, M. Yu. Shvedun, S. L. Gnatchenko, P. J. M. van Bentum, P. C. M. Christianen, J. C. Maan, K. V. Kamenev, G. Balakrishnan, D. McK Paul, and J. Fink-Finowicki, Fiz. Nizk. Temp. **27**, 1250 (2001) [Low Temp. Phys. **27**, 923 (2001)].

This article was published in English in the original Russian journal. Reproduced here with stylistic changes by AIP.

LOW-DIMENSIONAL AND DISORDERED SYSTEMS

Conductance quantization in metal nanowires produced by chemical anodization

V. V. Fisun* and Yu. I. Yanson

B. I. Verkin Physicotechnical Institute for Low Temperatures, Ukrainian National Academy of Sciences, pr. Lenina, 47, Khar'kov, 61103, Ukraine

(Submitted May 5, 2001)
Fiz. Nizk. Temp. **27**, 1264–1267 (November 2001)

Measurements of the conductance of a metal nanowire are performed. A niobium nanowire is produced during etching and subsequent anodization of a macroscopic wire at the location where the wire is preconstricted. At the final stage, before the conductor ruptures, the dependence of the conductivity on the decreasing diameter shows a distinct step structure with horizontal sections approximately corresponding to integral conductance quanta $2e^2/h = 7.75 \cdot 10^{-5}$ S. This phenomenon is explained as a discrete passage of electron wave functions through an atomic-size metal contact between two massive electrodes. © *2001 American Institute of Physics.* [DOI: 10.1063/1.1421459]

The fundamental discoveries made in the field of submicron structures in the last decade have influenced the development of semiconductor technologies. The sizes of the components of computer chips are now approaching 150 nm, which corresponds to only several hundreds of atoms. Consequently, the characteristics of atomic structures are of interest for science and possibly for future technologies.

There are a number of methods for measuring the conductance in nanowires, i.e. wires whose diameter equals the diameter of one or several atoms. The most widely used methods are the STM (scanning tunneling microscope) method[1] and the break-junction method.[2] The STM method employs a fine needle which can be moved very accurately in the vertical and horizontal directions. Initially, this needle is placed against the surface of a flat metal conductor. Then the needle is raised. The metal atoms ''stick'' to the needle as a result of cohesion. As the needle is raised, a thin wire forms between the conductor and the needle. This wire gradually becomes thinner. It is believed that the diameter of this wire reaches the diameter of one atom.[3] Since current flows through the needle contact with the conductor, the conductance of this thinning nanowire can be measured right down to a diameter of the order of one atom can be measured.

A break junction is a method for measuring the conductance of nanowires by stretching of the conductor.[2] A circular notch is made at the center of the conductor and the conductor is glued to a substrate consisting of a special plastic, so that the notch lies between two nearby drops of glue. A slot is cut on the opposite side of the substrate at the location of the notch in order to be able to bend the substrate. The substrate is secured along the edges and buckles before the conductor breaks. Then, using a piezoelectric element, the substrate is slowly unbent, while the contact has not yet been restored. Bending and unbending the substrate produces a nanowire between two parts of the conductor and the electrical conductance of this nanowire is measured.

In the present paper a chemical-reactions-based method is proposed for measuring the thickness and the conductance of metal nanowires. This method is an elaboration of the technique proposed in Ref. 4.

A circular notch is made, using a lathe, at the center of a 0.05 mm in diameter and 3–4 cm long niobium wire. This circular notch decreases the diameter of the wire by a factor of 2–3. This conductor is glued using Stycast 2850 FT glue, so that the notch lies between two nearby drops of glue. Next, the mixture[5] $HF+HNO_3+H_2Om$ (in equal parts) is dripped onto the substrate with the conductor at the location of the notch and the electrical resistance is measured. The etching of the niobium decreases the diameter of the wire and the resistance R starts to increase rapidly. When R reaches 2–2.5 Ω, the acid is washed off the conductor with distilled water. The diameter d of the narrowest part of the wire decreases to 10–15 nm. This estimate follows from Sharvin's relation[6] for a ballistic point contact: $d^2 = (p_F/ne^2)/R$, where p_F is the Fermi momentum, n is the conduction electron density, and e is the electron charge. Next, the conductor is placed into a small reservoir filled with distilled water; a schematic diagram of the reservoir is shown in Fig. 1a. An anodization circuit [Fig. 1a] and a measurement circuit [Fig. 1b] are connected to the wire in the reservoir.

The anodization circuit [Fig. 1a] intended for oxidizing the conductor in the reservoir consists of a platinum electrode P immersed in the water, a potentiometer, an ammeter, and a dc voltage source (100 V). Since the oxygen ions are negatively charged, a positive charge is applied to the niobium conductor in order for the oxidation reaction to occur. The negative electrode is made of platinum to prevent oxidation and etching of the electrode. The potentiometer serves for regulating the anodization current. Since during anodization the niobium wire becomes coated with a layer of a nonconducting oxide, the current in the circuit will decrease and a potentiometer is used to maintain a constant current.

The measurement circuit [Fig. 1b] consists of an ac volt-

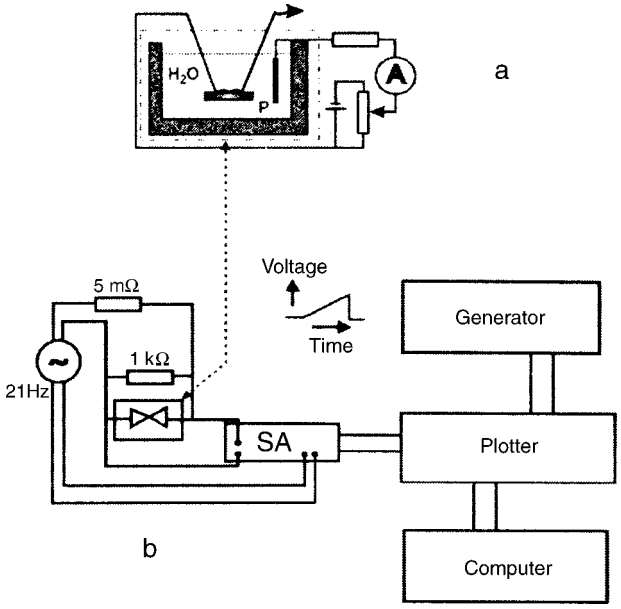

FIG. 1. Anodization circuit (a) and resistance measurement circuit (b). The sample is located in a reservoir with distilled water, P–platinum electrode, A–ammeter. An acoustic generator feeds a frequency of 21 Hz to the sample. The ac voltage on the sample is measured with a synchronous amplifier SA. The sawtooth generator produces a voltage proportional to the time. An analog–to–digital converter and a computer are used to record the measurement data in a file.

age generator with frequency 21 Hz, a 5 MΩ resistor, a accurate 1 kΩ resistor, the experimental sample, a synchronous amplifier, a *XY* Rikadenki potentiometer, a ramp voltage generator, and a computer. The reference voltage from the generator is applied to the synchronous amplifier, and the apparatus measures only the signal that has the same frequency and phase as the generator signal. The 5 MΩ resistor is connected to the generator; this resisance is much larger than that of the experimental sample, so that the generator can be treated as an ac current source. The accurate resistance 1 kΩ is necessary to prevent the measurement apparatus from being overloaded when the contact on the sample is broken. The synchronous amplifier measures the voltage on the sample, which is proportional to the resistance. The Rikadenki plotter is used as an analog–to–digital converter, the output voltage from the synchronous amplifier is fed to the Y coordinate and time is recorded on the X coordinate. The ramp voltage generator gives a signal proportional to the time. The computer writes all data from the plotter to a file.

After the anodization circuit and the measurement circuit are connected to the niobium conductor, the anodization current is set at 10 μA. Oxidation proceeds quite rapidly, and the anodization current decreases rapidly. With the anodization current kept at a constant level using the potentiometer the conductor is anodized while its resistance has not yet reached 1 kΩ (in this case, the diameter of the conductor is 3–4 atoms at the narrowest point). Then, the anodization current is decreased to 0.5–1 μA in order to slow down the anodization process. The entire process takes 1–3 h, depending on the magnitude of the current.

The results are recorded during anodization. The resistance–time curve is observed on the computer monitor. The sample conductance is found using the relation

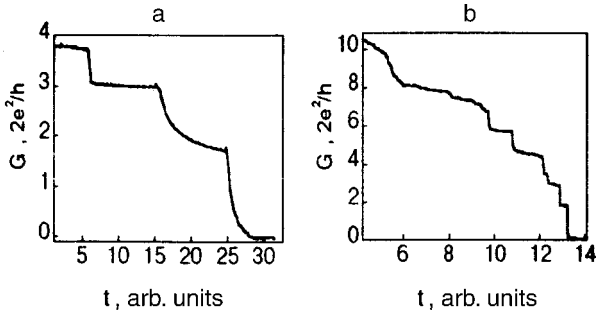

FIG. 2. Conductance G of a nanowire (in units of conductance quanta) versus time for two different contacts: Nb 0307 (a) and Nb 05a (b)

$G_{\text{meas}} - G = G_x$, where G_{meas} is the measured conductance and G is the conductance of the 1 kΩ resistor, equal to 10^{-3} S. The sample conductance obtained is normalized to the conductance quantum $G_0 = 2e^2/h = 7.75 \times 10^{-5}$ S (h is Planck's constant).

Figure 2 shows the time-dependences of the reduced conductance. Before the conductor ruptures, a step change of the conductance occurs as a result of the quantum nature of the propagation of electron waves in a nanoconductor whose transverse size is of the order of the de Broglie wavelength of Fermi electrons. This is indicated by the nearly integral values of the conductance quanta on flat sections of the observed curve. It could be inferred that the transitions between these sections correspond to oxidation of individual niobium atoms. However, this is not so, as one can see from the horizontal section of the conductance prior to complete rupture, which corresponds to a contact diameter of 1 niobium atom. The conductance of 1 niobium atom, as a rule, is higher than 1 quantum.[7] This is because the conductance of a niobium atom is due to several electronic orbits, each of which carries less than 1 quantum.[8] However, the last plateau in the conductance $G(t)$ (see Fig. 2) is most often observed near 2 quanta, which corresponds to a single-atom contact.

In summary, the steps at the last stages of anodization could be due to several factors. In the first place, if the orbital structure of the electronic wave functions of the last niobium atoms is neglected and the decrease in the diameter of the nanowires as a result of oxidation is assumed to be a smooth function, then the steps could be due to the quantum-size effect, where the wavelength of the Fermi electrons is of the order of the transverse size of the constriction. In this simplified model the step height is equal to 1 conductance quantum, while for a cylindrical model of a contact it is equal 2 quanta because of degeneracy.[7] In the second place, as a result of anodization, oxidation itself can occur in a step manner as oxides with various stoichiometry, which disconnect channels from the conductance of a niobium atom which are associated with particular orbits, are formed. In other words, measuring the electrical conductance makes it possible to observe various oxidation steps corresponding to the last niobium atoms.

In the break-junction method the plateau on the steps is ordinarily attributed to elastic stretching of a nanowire, which precedes an abrupt decrease of the diameter as a result of relaxation. We underscore that in our method the horizontal stepped sections are due to other factors.

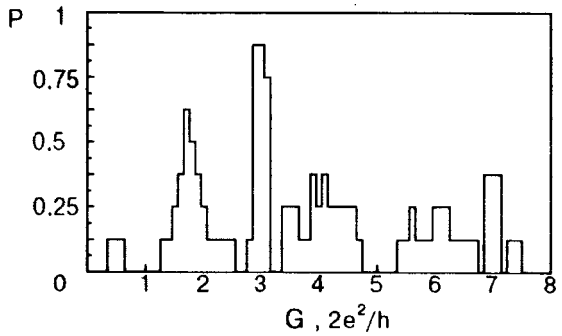

FIG. 3. Probability P of the appearance of a plateau in the time-dependence of the conductance (for eight contacts) (see Fig. 2) as a function of the conductance for Nb nanowires obtained by anodization at room temperature.

Figure 3 displays a histogram reflecting the probability of observing a plateau in the time-dependence of the conductance as a function of the conductance G. The histogram was constructed in a manner so that each plateau corresponds to a rectangle of width 0.2 (in the units $2e^2/h$) and unit height, centered at a value of the conductance where the derivative dG/dt possesses a minimum, i.e. at a point where the functions $G(t)$ are as horizontal as possible. The peaks at $G=1.8$ and 3 are strongest. We compare this histogram with the histogram obtained at Leyden University by the break-junction method at low temperatures (Fig. 4).[8,9] In contrast to our experiments, one wide peak with $G=2.3$ is observed instead of two peaks; this peak is probably due to disordering

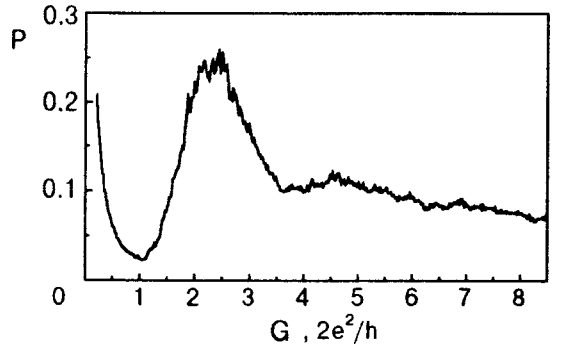

FIG. 4. Probability P of observing a plateau in the curves of the conductance versus the nanowire diameter for 1200 cycles of reduction and rupture of Nb break junctions at $T=16$ K.[8]

of the atoms during the stretching and relaxation of the nanowire at low temperatures. The broadening of the nearby peaks ($G=1.8$ and 3) in our experiments is probably due to the quasistationary arrangement of the atoms of the metal and the oxide and the stepped oxidation of various orbits in the last niobium atoms prior to the break.

Since the intermediate niobium oxides NbO and NbO_2 and various intermediate steps between them possess semimetallic and semiconductor character, the conductor diameter actually decreases continuously. This fundamentally distinguishes the chemical oxidation method from the mechanical STM and break-junction methods.

In summary, we propose a new method for observing conductance quanta in metals. This method is distinguished by simplicity and the absence of deformations in the structure of the metal, as compared with the stretching deformation of nanowires in the STM and break-junctions methods. This method makes it possible to measure the conductance of a metal nanowire whose transverse section decreases quasi-continuously. The method does not require low temperatures; the amount of equipment required is minimal.

We thank I. K. Yanson for posing problem and for constant encouragement.

*E-Mail: fisun@ilt.kharkov.ua

[1] J. K. Gimzewski and R. Moeller, Phys. Rev. B **36**, 1284 (1987); N. Agrait, J. G. Rodrigo, and S. Vieira, *ibid.* **47**, 12345 (1993).
[2] J. Moreland and J. W. Ekin, J. Appl. Phys. **58**, 3888 (1985); C. J. Miller, J. M. van Ruitenbeek, and L. J. de Jongh, Physica C **191**, 485 (1992).
[3] J. M. Krans, C. J. Muller, I. K. Yanson, Th. C. Govaert, R. Hesper, and J. M. van Ruitenbeck, Phys. Rev. B **48**, 14721 (1993).
[4] A. I. Akimenko and I. K. Yanson, Pis'ma Zh. Tekh. Fiz. **4**, 860 (1978) [*sic*].
[5] B. I. Baĭrachnyĭ and F. G. Andryuschenko, *Electrochemistry of Rectifying Elements* (Vishchashkola, Khar'kov State University Presss, Khar'kov, 1985).
[6] Yu. V. Sharvin, Zh. Éksp. Teor. Fiz. **48**, 984 (1965); [Sov. Phys. JETP **21**, 655 (1965).
[7] J. M. Krans, J. M. van Ruitenbeck, V. V. Fisun, I. K. Yanson, and L. J. de Jongh, Nature (London) **375**, 767 (1995).
[8] A. I. Yanson, *Atomic Chains and Electronic Shells: Quantum Mechanisns for the Formation of Nanowires*, Ph.D. thesis, Universiteit Leiden (2001), unpublished.
[9] B. Ludoph, *Quantum Conductance Properties of Atomic-Size Contacts*, Ph.D. thesis, Universiteit Leiden (2001), unpublished.

Translated by M. E. Alferieff

PHYSICAL PROPERTIES OF CRYOCRYSTALS

Xenon excimer compounds with oxygen in inert-gas crystal matrices

A. G. Belov[a] and E. M. Yurtaeva

B. I. Verkin Physicotechnical Institute for Low Temperatures, Ukrainian National Academy of Sciences, pr. Lenina 47, Khar'kov, 61103, Ukraine

(Submitted May 23, 2001)
Fiz. Nizk. Temp. **27**, 1268–1282 (November 2001)

Xenon excimer compounds with oxygen in low-temperature inert-gas (R) crystal matrices are investigated. The transformation of the excimer emission spectrum as a reslt of a change in the Xe concentration is analyzed. It is shown that the luminescence band with a peak near 1.7 eV could be due to the superposition of two bands with $E_{max}=1.8$ and 1.72 eV. The higher-energy band with $E_{max}=1.8$ eV is observed at low xenon concentration, and it can be interpreted as a transition from the $1^1\Pi$ state of the complex XeO* to the lowest state XeO $X^3\Pi$. The band with $E_{max}=1.72$ eV, which predominates in the intrinsic Xe matrix with oxygen impurity and high-concentrated solutions $R+Xe+O_2$ is attributed to emission of the triatomic excimer Xe_2O^*. A comparative analysis of the experimental data and theoretical calculations, obtained for analogous compounds of xenon halides and hydrides as well as the xenon compound with the isoelectronic S atom, is performed. The results suggest that the 3.33 and 3.58 eV bands observed in the xenon matrix belong to emission of charge-transfer complexes $Xe_2^+O^-$ and $Xe_2^+S^-$. © *2001 American Institute of Physics.* [DOI: 10.1063/1.1421460]

1. INTRODUCTION

The energy structure and scintillation characteristics of condensed inert gases and their compounds with other elements are of interest in connection with their use as laser media and for detecting the products of nuclear reactions. The possibility of the existence of strongly bound inert-gas excimer compounds (R) with electronegative elements and radicals Y (H, OH, F, Cl, Br, I) is due to the existence of a bond with charge transfer R^+Y^-.[1] As a result of the high ionization energy of inert gases, the electronic excitation energy corresponding to the formation of excimer complexes of this type is usally 3–5 eV. Compounds with atomic oxygen, which also possesses a negative electron affinity, differ from simpler systems with univalent reagents by the presence of one other form of excimer compounds with a covalent bond RO*. The are formed from unexcited R atoms and excited oxygen atoms O* in the valence states ^1S and ^1D.[1] The electronic excitation energy corresponding to the formation of these molecules does not exceed 4 eV. Thus, a quite complicated system of molecular potentials is characteristic for inert-gas oxides. This system is manifested in the complex structure of the optical spectrum from the near–IR to the VUV range. Of all the inert-gas oxides the xenon excimer compounds with oxygen have been studied most intensively, since they are most stable. Nonetheless, many unresolved questions, concerning the virtually complete difference between the excimer radiation spectra in the gas phase and in the crystal matrix of xenon remain for these compounds.

Our objective in the present work is to investigate the transformation of the luminescence spectra of excimer complexes of xenon and oxygen on transition from the gas phase to a matrix of inert elements. This yields information about the real influence of the matrix on the structure of these complexes and it makes it possible to determine the possibility of the existence of the triatomic complexes $Xe_2^+O^-$. The luminescence of the system $Xe+O_2$ is investigated in the intrinsic Xe matrix and in matrices of lighter inert gases Ne, Ar, and Kr. Analysis of the concentration and dose dependences of the observable luminescence makes it possible to determine the existence of two overlapping bands in the range from 1.5 to 1.9 eV. Various versions of the identification of each of them are considered.

2. XENON EXCIMER COMPOUNDS IN A GAS AND IN A MATRIX

Figure 1 displays the theoretical molecular potentials of xenon excimer compounds with oxygen in the free state[2] and the radiative transitions observed in the experimental spectra. The band system XeO* $2^1\Sigma-1^1\Sigma$ near 2.3 eV is most characteristic for the luminescence of the gas mixture $Xe+O_2$.[3–5] The radiative transition from the same upper state $2^1\Sigma$ to the lowest repulsive term $X^3\Pi$ is manifested as a very narrow emission band with $E_{max}=4.025$ eV. The strongest band in the VUV region of the spectrum is the band with $E_{max}=5.275$ eV; this band is identified as a transition from the lowest state of charge-transfer complex to the ground term $1^3\Pi-X^3\Pi$.[6–8] Several weak maxima at 4.59, 4.25, and 3.76 eV were interpreted as transitions from $1^3\Pi$ to the lowest lying valence state of the complex XeO*: $1^3\Sigma$, $1^1\Sigma$, and $1^1\Pi$, respectively.[7] Finally, we note that a number of early works on the gas systems $Xe+O_2$ reported the observation of continuum radiation in the longest wavelength region near 1.8 eV.[3,5]

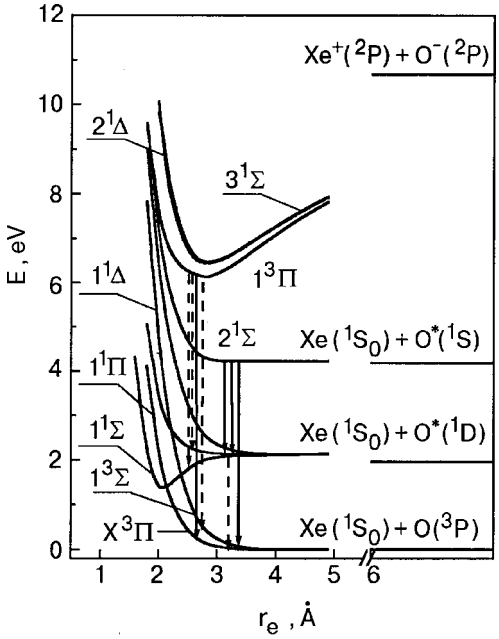

FIG. 1. Potential curves of xenon excimer compounds with oxygen.[2] The arrows show the transitions observed in the experimental emission spectra of the gas phase.

All bands associated with a transition from the state $2^1\Sigma$ XeO* are completely absent in the spectrum of the crystal matrix Xe with oxygen impurity. A comparatively weak band with $E_{\max}=4.9$ eV is observed in the VUV region of the spectrum; this band is present only at low oxygen concentations. The most characteristic excimer radiation associated with the presence of oxygen in Xe crystals are two intense bands with maxima near 3.3 and 1.7 eV.

Despite the fact that there is an entire series of works devoted to the study of these bands,[9–19] the interpretation of their origin is quite contradictory. Specifically, there exist two different interpretations of the emission band with $E_{\max}=1.7$ eV in Xe crystals with oxygen impurity,[9,17] which is the main object of the present investigation.

The wide continuum band with $E_{\max}=1.66$ eV and half–width $\Delta_{1/2}=0.88$ eV was first detected in the mixture Xe $+1\%N_2O$ with excitation by synchrotron radiation with energy $E_{h\nu}=8-10$ eV.[9] A local maximum with $E_{\max}=1.86$ eV was observed on the high-energy edge of this band. We observed a similar structural band near 1.7 eV and radiation with $E_{\max}=3.3$ eV in the spectra of Xe with residual oxygen impurities under excitation by slow electrons with $E_e=200$ eV.[10] It has been investigated in detail.[11,12] The damping kinetics of the luminescence band in the red region of the spectrum at $T=25$ K gives two different radiation decay constants: $\tau_1=110$ ns for $E_{\max}=1.86$ eV and $\tau_2=290$ ns for $E_{\max}=1.66$ eV.[9] According to the energy position of this band, close to the energy of the transition $O^*\ ^1D\rightarrow{}^3P$, it was identified as radiation from XeO* states kinetically coupled with the valence state O* (^1D), specifically, $1^1\Sigma$ and $1^1\Pi$. Since theoretical calculations[20] subsequently showed that the lowest of these terms ($1^1\Sigma$) intersects with repulsive branches of the ground state, the most likely candidate for the radiating state remains the term $^1\Pi$. The excitation spectrum of this band, measured from 8.1 to 10 eV.[9] largely corresponded to the excitation spectrum of Xe_2^* in crystalline xenon.[21]

In Ref. 14 the band width $E_{\max}=1.67$ eV was observed under excitation with laser radiation with lower energies $E_{h\nu}=5$ and 6.4 eV. From this it was concluded that the state XeO* ($1^1\Pi$) could be populated from the state of the charge-transfer complex Xe^+O^-. In Ref. 15 we obtained the photoexcitation spectrum of two bands with $E_{\max}=1.65$ and 3.35 eV at energies from 4.8 to 5.6 eV. Both bands have the same radiative decay time constant $\tau=227$ ns and showed the same temperature behavior and similar variations of intensity as a function of irradiation time. Assuming that the lowest emitting state of Xe^+O^- is $3^1\Sigma$, the authors of Ref. 15 referred the bands with $E_{\max}=1.65$ and 3.35 eV to a transition from this term to the levels $1^1\Pi$ and $1^1\Sigma$ of XeO*, respectively; in addition, the matrix shift of the level $3^1\Sigma$ is estimated to be $\Delta E_S=-0.78$ eV. In this case the rule that terms with identical symmetry cannot intersect with the state $2^1\Sigma$ operates. It was also assumed that the interaction of both levels should result in deepening of the $2^1\Sigma$ potential by approximately 0.7 eV compared with the theoretical values of D_e. At the same time the position of the term $^1\Pi$ remained essentially unchanged. Thus, the question of the character and strength of the interaction of inert-gas excimer compounds with a crystalline environment became especially urgent for resolving the contradictions which have arisen.

Stabilization of excimer molecules in inert-gas matrices is due primarily to the symmetric polarization interaction with the environment, ordinarily characterized by the spectral matrix shift. The emission-band maxima shift to lower energies by $\Delta E_S\sim 0.1$ eV compared with the gas phase, but the other spectral characteristics change very little: shape, half-width, and lifetime.

Another possibility for lowering the energy of the system R+Y in an inert-gas matrix is formation of triatomic molecules $R_2^+Y^-$. The energy gain is much greater in this case and is approximately 1 eV, which corresponds to the binding energy in the molecular ion R_2^+. The radiation of triatomic complexes ordinarily has a larger width and a comparatively longer lifetime than that of diatomic complexes. Compounds of similar type are observed in Ar, Kr, and Xe matrices with halogen and hydrogen impurities. Such molecules can also form in the gas phase under sufficiently high gas-mixture pressure $P>1$ bar.[22] As far as the possibility of triatomic inert-gas compounds with oxygen existing, it has been proved[23,24] that the molecule $Ar_2^+O^-$ is stable in the intrinsic matrix. Evidence of the possibility of the formation of triatomic complexes $Xe_2^+O^-$ has been obtained[13,16] in an analysis of the photoexcitation spectra of the ternary solid solutions $Ne+Xe+O_2$. Nonetheless, it is believed that tiratomic molecules of this type are unstable.[15]

The lack of computational molecular potentials of charge-transfer compounds R^+O^- has for many years made it difficult to identify the complete emission spectrum in crystal systems R+O. In contrast to the potentials of RO*, which were calculated quite a long time ago,[20] the potentials of the compounds Xe^+O^- were obtained *ab initio* only recently.[2] Consequently, all preceding identifications of the spectral bands were based only on estimates of the param-

eters of the potentials obtained from gas-phase experiments and analogs with compounds of this type with halogen and hydrogen atoms. We note that the results of Ref. 2 agree well with the experimental data and earlier calculations for low-lying covalent compounds RO*. At high energies the calculation of Xe^+O^- potentials shows that the lowest state is the triplet term $1^3\Pi$ and the singlet terms $3^1\Sigma$ and $2^1\Delta$ lie approximately 0.3 eV above $1^3\Pi$; this is at variance with the results obtained in Ref. 15.

The effect of the matrix environment of inert gases on excimer molecules with a covalent bond RO* was investigated theoretically in Refs. 18, 25, and 26. According to Ref. 26, the decrease in the energy of the atom $O^*(^1D)$, corresponding to the $1^1\Sigma$ state, is $\Delta E_M \approx 0.04$ eV, and for $O^*(^1S)$ and $O^*(^1P)$ the decrease is $\Delta E_M \approx 0.01$ and 0.11 eV. These results agree reasonably well with the experimentally data. On the other hand, the method used in Ref. 18 to simulate the crystal system Xe+O results in much larger values of the energy gain in the state $1^1\Sigma$, $\Delta E_M \geqslant 1$ eV.

Since the effect of the matrix environment on charge-transfer complexes Xe^+O^- in inert-gas crystals have still not been investigated theoretically, the experimental matrix shifts of the emission bands of halides in Xe can be presented for making comparisons: they are approximately 0.4 ± 0.2 eV.[27] The computed values of the polarization interaction with the medium for $Xe_2^+Cl^-$, for example, are -0.39 eV[28] and agree with the experimental value.

Thus, the question of the nature of excimer compounds in Xe crystals with oxygen impurity and the influence of the matrix environment on their binding energy remains controversial. In some sense the transitional stage from the gas phase to crystalline xenon are matrices of lighter inert gases Ne, Ar, and Kr, whose polarizability increases in the sequence given. Analysis of the transformation of the spectra of XeO* and Xe^+O^- from the lightest to the heaviest matrix can yield substantial information for making a correct identification of the emitting states. Such investigations in this field are still inadequate. The system of transitions from the state $2^1\Sigma$ has been investigated in greatest detail.[29] The measured matrix shift of the radiation $2^1\Sigma - X^3\Pi$ in Ar is only -0.06 eV, and the minimum of the $1^1\Sigma$ potential becomes deeper by 0.1–0.25 eV, depending on the enumeration adopted for the vibrational levels in the gas phase.[29] The transition corresponding to the emission band of XeO* near 1.7 eV in Ne and Ar matrices has been investigated only in Ref. 16. Only one luminescence band was detected in the region 1.5–1.9 eV in a neon matrix with oxygen and xenon impurity; this band has a quite complicated structure consisting of three local maxima. The photoexcitation spectrum of this band was similar to that of Xe_2^* in a Ne matrix. On this basis it was concluded in Ref. 16 that the observed radiation could be due to the formation of the triatomic excimer complex $Xe_2^+O^-$.

3. EXPERIMENTAL PROCEDURE

The radiation of pure crystals of the inert gases Ne, Ar, and Kr as well as their mixtures with oxygen and xenon has been studied by cathodoluminescence analysis using monoenergetic electrons with energy $E_e \approx 0.4-2$ keV. The optical investigations were performed with a continuous-flow helium cryostat with the temperature of the copper substrate regulatable over the range from 2.5 to 78 K. The samples were grown by depositing a gas mixture with the appropriate composition on the cryostat substrate at a temperature close to the sublimation temperature of the most volatile component of the solid solution. The thickness of the polycrystals obtained was $d \approx 1$ μm and the crystals were completely transparent. The measurements were performed at $T = 5$ K.

The initial inert gases contained oxygen impurity $c_{O_2} \approx 10^{-3} - 10^{-4}$ at.%; a mixture with $c_{O_2} = 0.1-1$ at.% was used as a control. The Xe impurity concentration in neon and argon matrices varied from 0.03 to 30 at.%. The radiation was detected using DFS–24 and DFS–8 monochromators in the range 2.5 eV (7500–5000 Å). The spectral resolution was 0.015 and 0.06 nm, respectively. Systematic measurement of the spectral diagrams in definite time intervals made it possible to obtain the dose dependences of the luminescence. At the same time, the intensities of the impurity bands $Xe^*(^3P_2, ^1P_1)$, $Xe_2^*(^3\Sigma_u^+)$, and $O^*(^3S, ^5S)$ were recorded in the VUV range with a VMR–2 monochromator. The shape and position of these bands were quite reliably determined in previous studies. The working vacuum in the cryostat was maintained at the level 10^{-10} bar.

4. EXPERIMENTAL RESULTS

The luminescence spectra of the solid solutions $Xe+O_2$ in a neon or argon (R) matrix contain three types of bands, referring to excitations of the matrix (R^*, R_2^*), noninteracting xenon and oxygen impurities (Xe^*, Xe_2^*, O^*, O_2^*), and heteronuclear excimer compounds of oxygen with the inert atoms of the matrix and xenon impurity (R^+O^-, RO*, XeO*). This radiation covers the range from the far-UV to the near-IR. The present work focused on the system of bands in the spectral range 1.5–2.5 eV (Fig. 2). Additional studies are required to identify several overlapping bands at higher energies from 2.5 to 4 eV, which are due to the Xe impurity. We note only that for concentrations $c_{Xe} > 0.3$ at.% bands with maxima at 3.44 and 3.54 eV, respectively, were observed in the Ne and Ar matrices.

Of the previously identified bands the radiation near 2.2 eV is due to the transition $O^*(^1S \rightarrow ^1D)$ in a Ne matrix and the transition $2^1\Sigma \rightarrow 1^1\Sigma$ ArO* and KrO* in Ar and Kr matrices.[9,30,31] The transition $O^*(^1D \rightarrow ^3P)$ near 1.96 eV was also observed in the neon matrix.[25] In addition, the impurity luminescence spectra in Ne, Ar, and Kr matrices contain the well-known radiation system of ''green'' bands of the complex $XeO^*(2^1\Sigma \rightarrow 1^1\Sigma)$ in the range 2.2–2.5 eV.[3–5,29] The matrix shift of the band maximum (0–8) of this system is $\Delta E_S = E_S^{\max} - E_G^{\max} = 0.076$, -0.027, and -0.016 eV, respectively (according to the enumeration proposed in Ref. 29 for the vibrational states). Our data for Ne and Ar agree well with Ref. 29. In Kr the XeO* bands are too diffuse to make such a comparison; the two narrow bands near 2.15 eV are due to the transition $2^1\Sigma \rightarrow 1^1\Pi$.[29]

We discovered a dependence of the position and width of individual bands of the transition $2^1\Sigma \rightarrow 1^1\Sigma$ on the oxygen concentration in the matrix. Figure 3 displays the corresponding emission spectra in $Ar+1\%Xe+10^{-3}\%O_2$ and $Ar+1\%Xe+1\%O_2$ crystals. At low oxygen content in the

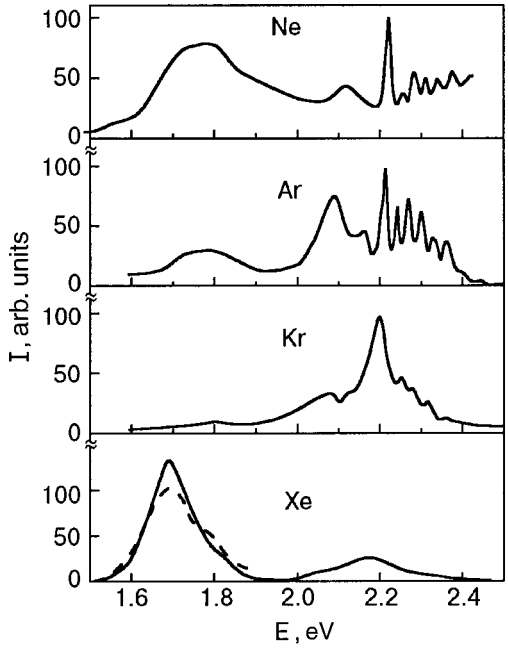

FIG. 2. Luminescence of excimer complexes XeO* in matrices of the inert gases Ne, Ar, Kr, and Xe in the spectral range from 1.5 to 2.5 eV at $T=5$ K with $c_{Xe}=1\%$ and $c_{O_2}=10^{-3}\%$. With the exception of Xe, the spectra are normalized to the maximum intensity for the transition $2^1\Sigma\rightarrow 1^1\Sigma$ RO* near 2.2 eV. In the Xe spectra the broken line corresponds to $T=20$ K.

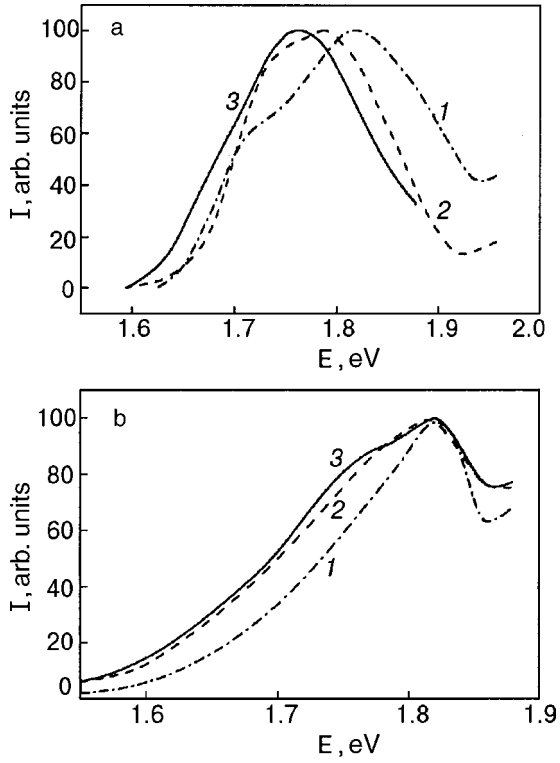

FIG. 4. Bands, normalized to the maximum of the emission spectrum, with E_{max} near 1.7 eV in argon (a) and krypton (b) matrices with different Xe concentrations: 0.1% (*1*), 1% (*2*), and 10% (*3*).

matrix the bands shift to lower energies and broaden, which is especially appreciable for transitions on lower vibrational levels of the state $1^1\Sigma$. We note that the maximum energy shift is 0.012 eV for the (0–5) band. The intensity of the transition $2^1\Sigma\rightarrow 1^1\Sigma$ increases with the Xe concentration up to $c_{Xe}\approx 0.3$ at.%, after which it decreases in the range $c_{Xe}>1$ at.%.

The band with a maximum near 2.1 eV is also characteristic for this region of the spectrum. As far as we know, thus far there exists only a tentative identification of this band as being due to the radiative transition of $(Xe_2O)^*$ in Ne and Ar (Ref. 16) or $(XeO)^*$ in Kr with no identification of the corresponding states.[17] We observed a correlation of the intensity between the 2.1 eV band and the ''green'' bands as a function of the Xe concentration.

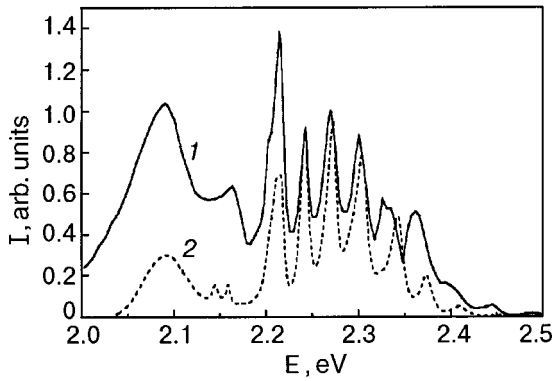

FIG. 3. Luminescence spectra of ''green bands'' of the transition $2^1\Sigma\rightarrow 1^1\Sigma$ XeO* in Ar+1%Xe+10^{-3}%O_2 (*1*) and Ar+1%Xe+1%O_2 (*2*) crystals.

Virtually all spectral bands described above are absent in solid Xe, containing oxygen impurity. The only band appearing in all four matrices is the quite wide continuum in the red region of the spectrum from 1.5 to 1.9 eV. The shape and width of this band depend appreciably on the Xe impurity concentration in neon, argon, and krypton matrices. Figures 4 and 5 show this transformation as a function of c_{Xe} in

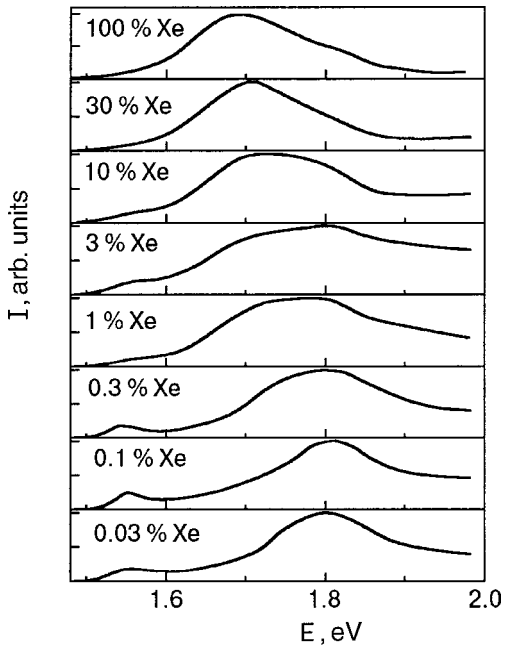

FIG. 5. Evolution of the emission spectrum of the band near 1.7 eV in a neon matrix as a function of the Xe concentration.

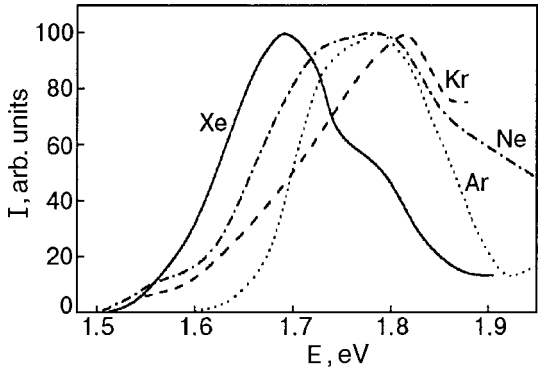

FIG. 6. Normalized, at the maximum, luminescence spectra of Ne, Ar, and Kr crystals with xenon and oxygen impurity concentrations: $c_{Xe}=1\%$ and $c_{O_2}=10^{-3}\%$. The xenon spectrum with the same oxygen impurity is presented for comparison.

argon and neon matrices. In the latter case the characteristic background of the crystal-Ne matrix was subtracted from the total emission contour. Figure 6 compares the luminescence spectra of Ne, Ar, and Kr crystals with only $c_{Xe}=1$ at.%. In all cases presented it is observed that the band splits into two components with maxima near $E_{max}\approx 1.8$ and 1.7 eV. In what follows we shall denote them as X_1 and X_2, respectively. According to Figs. 4 and 5, as the Xe concentration increases, the ratio of the intensities between the maxima changes in favor of the long-wavelength maximum.

Two maxima can also be identified in experiments with various oxygen concentrations. As the oxygen concentration increases, the intensity is redistributed in favor of the short-wavelength band (see Fig. 7).

In the xenon matrix the continuum radiation has only one maximum at 1.7 eV with a quite large half-width $\Delta_{1/2}=0.17$ eV and a weak shoulder in the region 1.8 eV. This gives the band a pronounced asymmetry at high energies. The shoulder becomes more distinct as temperature increases

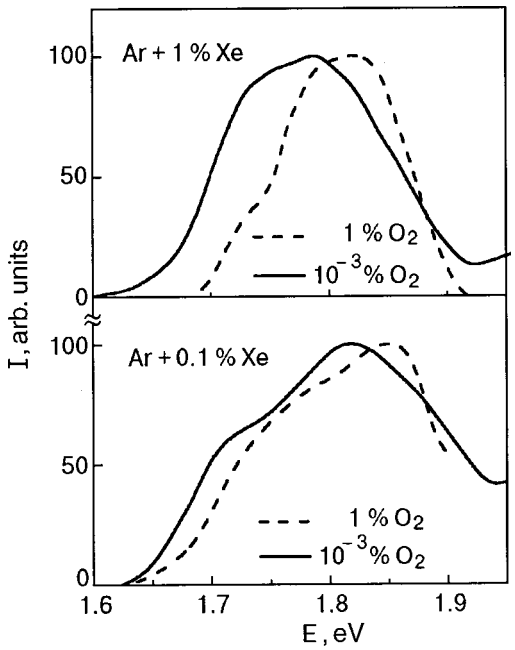

FIG. 7. Influence of different contents of oxygen on the luminescence spectra of $Ar+O_2+Xe$ crystals with $c_{Xe}=0.1$ and 1%.

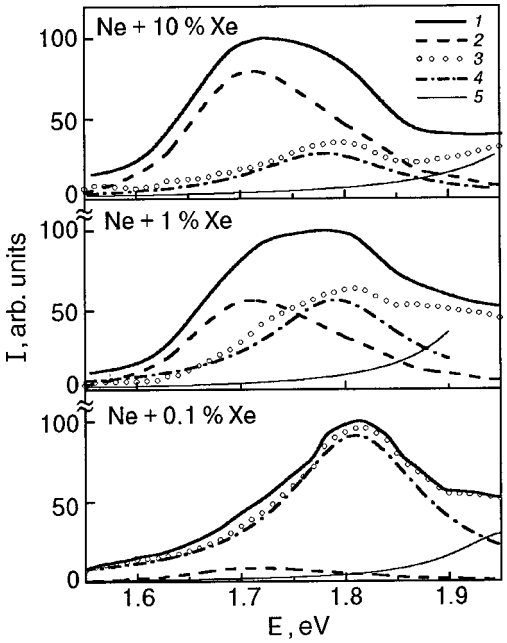

FIG. 8. Decomposition of the luminescence band near 1.7 eV into components: 1) contour of the experimental spectrum, 2) contour of the Xe_2O^* spectrum, 3) result of subtracting the Xe_2O^* contour from the experimental spectrum. The resulting curve is a superposition of the Xe_2O^* bands (4) and the red wing from the high-energy band, presumably associated with impurity Xe_2 (5).

up to 25 K. The continuum in the intrinsic xenon matrix can be associated to the maximum of the luminescence spectrum X_2 in the lightest inert matrices. With respect to the latter, measured in a neon matrix, the continuum under study is shifted in xenon in the direction of lower energies by 0.02 eV. In other matrices the bands X_1 and X_2 overlap too much to make a confident comparison.

The band X_1, obtained from a sample with the lowest Xe and O concentrations, and the band X_2 from samples with high Xe concentration were used to separate the observed band into its components X_1 and X_2. According to Fig. 8 and Table I, the position of the X_1 bands is essentially independent of the xenon concentration, and the half-width of the band is approximately $\Delta_{1/2}\approx 0.16$ eV.

The X_1 band dominates the spectra of all matrices with low xenon concentrations $c_{Xe}\leqslant 0.3\%$. Increasing the concentration at first results in an incresae of both bands, but as c_{Xe} increases, the band X_2 starts to grow before X_1. For $c_{Xe}\geqslant 1\%$ the intensity of the band X_1 starts to decrease, so that the band X_2 becomes dominant. Figure 9a shows the dependence of the intensity ratio of the bands X_2, $XeO^*(2^1\Sigma\rightarrow 1^1\Sigma)$, and $Xe^*(^1P_1)$ on the xenon concentration in Ne matrices. The ratios $I(X_2)/I(XeO^*)$ and $I(X_2)/I(Xe^*)$ clearly increase as c_{Xe} increases. From 0.1 to 10% the band intensity ratio increases approximately by a factor of 50. For

TABLE I. Energies of the maxima and half-widths obtained for the bands X_1 and X_2 by decomposing the experimental spectrum into two components.

Band	E_{max}, eV	$\Delta_{1/2}$, eV
X_1	1.8 ± 0.01	0.16 ± 0.01
X_2	1.715	0.174

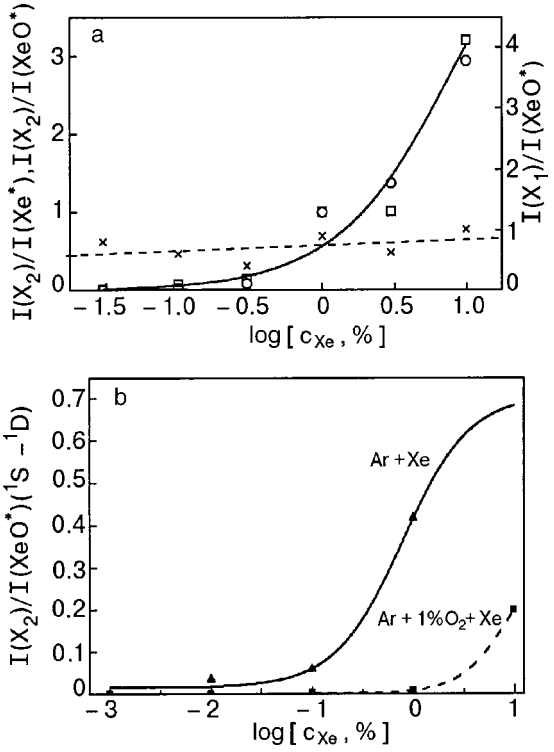

FIG. 9. a) Band intensity ratios $I(X_2)/I(\mathrm{XeO}^*)(2^1\Sigma \rightarrow 1^1\Sigma)$ (□) and $I(X_2)/I(\mathrm{Xe}^*(^1P_1)$ (○) versus the xenon concentration in the Ne matrix; $I(X_2)/I(\mathrm{XeO}^*)$ (×) is presented for comparison; the solid line is the curve of growth of pair centers Xe_2 as a function of concentration; b) $I(X_2)/I(\mathrm{XeO}^*)$ versus the Xe concentration in an Ar matrix with different oxygen content.

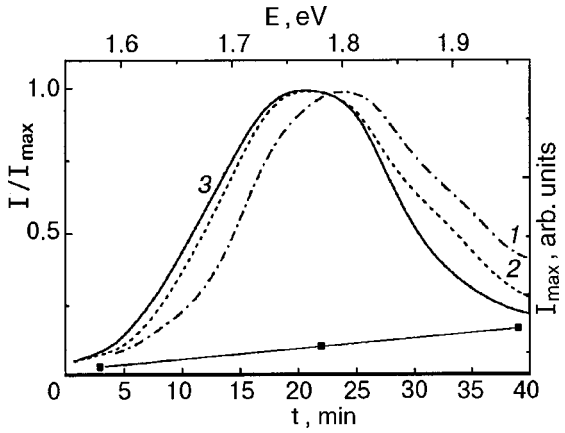

FIG. 10. Effect of the irradiation dose on the luminescence spectrum of the crystal Ne+Xe+O_2 with $c_{Xe}=0.3\%$ and $c_{O_2}=10^{-3}\%$. Irradiation time t, min: 3 (*1*), 22 (*2*), and 389 (*3*). The spectra are normalized at the intensity maximum. The real change in the intensity of the maximum with increasing irradiation time is shown in the bottom part of the figure (■).

comparison, Fig. 9a shows the intensity ratio $I(X_2)/I(\mathrm{XeO}^*)$, which within the limits of stability of the experiment and the accuracy of the separation of the contours X_1 and X_2, is essentially constant.

The analogous dependence of $I(X_2)/I(\mathrm{XeO}^*)$ on the xenon concentration is also observed in Ar crystals (Fig. 9b). We note that in an Ar matrix with low oxygen content $c_{O_2}=10^{-3}\%$ the intensity of the band X_2 increases with substantially lower xenon concentrations compared with the matrix containing 1% O_2. The intensity ratio $I(X_2)/I(\mathrm{XeO}^*)$ is approximately 5 times greater in the argon matrix with low oxygen content. This probably means that the formation efficiency of the complexes responsible for emission of the band X_2 decreases as the impurity oxygen concentration increases.

Figure 10 shows the effect of the irradiation time on the intensity distribution between the bands X_1 and X_2 with impurity content 0.3%Xe and $10^{-3}\%O_2$ in a Ne matrix. According to the figure, as the irradiation dose increases, not only do the intensities of X_1 and X_2 increase, but the relative intensity of these bands changes in favor of X_2 at the initial stage of irradiation. Evidently, this could be due to radiation-stimulated diffusion of xenon impurity in inert matrices.[32]

5. DISCUSSION

A. Diatomic and triatomic excimers in a crystal matrix

Summarizing the results presented above, we shall enumerate the basic features of the continuum emission band in the range 1.5–1.9 eV:

1) for concentrations 0.1 up to 10% Xe this continuum can be represented as a superposition of at least two different bands X_1 and X_2, differing by the position of the maximum, the shape, and the concentration dependence;

2) the band X_1 predominates in the luminescence spectrum at low Xe concentrations and intensifies with increasing oxygen concentration;

3) the band X_2 predominates in the spectrum for high Xe concentrations and decreases as the oxygen concentration increases;

4) as the irradiation dose increases the intensity becomes redistributed between the bands X_1 and X_2 in favor of the latter;

5) the concentration dependence of the intensity of the band X_1 correlates with the concentration dependence of the intensity of the transition XeO* $2^1\Sigma \rightarrow 1^1\Sigma$, while the intensity of the band X_2 increases strongly compared with XeO* with increasing xenon concentration.

These facts make it possible, at the first stage of the discussion, to associate the band X_1 with a diatomic complex $(\mathrm{XeO})^*$ and the band X_2 with triatomic complexes of xenon compounds with oxygen $(\mathrm{Xe_2O})^*$.

The fact that the band X_2 corresponds to the triatomic complex $(\mathrm{Xe_2O})^*$ is confirmed by the fact that the intensity ratios $I(X_2)/I(\mathrm{XeO}^*)$ and $I(X_2)/I(\mathrm{Xe}^*)$ (see Fig. 9a) depend on the xenon concentration essentially identically and reproduce the concentration dependence of the formation probability P_2 of a pair impurity center of xenon with random substitution of a xenon atom for matrix atoms. The probability P_2 can be estimated as[33]

$$P_2 = 1-(1-c)^Z, \quad Z=12, \tag{1}$$

where c is the xenon concentration, Z is the coordination number, and the second term is the probability that a second xenon atom does not appear on random substitution into the first coordination sphere of a given xenon atom. The concentration dependence (1), shown in Fig. 9a (solid line), is identical to $I(X_2)/I(\mathrm{XeO}^*)$ and $I(X_2)/I(\mathrm{Xe}^*)$ within the limits of the experimental variance.

Another, controversial, argument in favor of the conjecture made above is the excitation spectrum of the band X_2 near 1.7 eV in an Ne matrix,[16] which is very similar to the excitation spectrum of Xe_2^* in an Ne matrix,[13] though slightly shifted to lower energies by approximately 0.04 eV. There are also differences in that the relative contribution of impurity exciton-like states of Xe is smaller than in the excitation spectrum of the xenon molecule Xe_2^* in Ne. A similar conclusion can also be drawn by comparing the excitation spectra of the band with $E_{max}=1.66$ eV[9] and Xe_2^*[21] in an intrinsic Xe matrix. Nonetheless, this similarity is still not a final proof that the band X_2 is correctly attributable to a triatomic exciplex $(Xe_2O)^*$, since the molecular state of Xe_2^* in this case can be only an intermediate link for transferring energy from the higher-lying excitonic bands. On this level the direct excitation spectra of this band are more informative. Up to now such investigations have been performed only in the intrinsic xenon matrix, from 4.8 to 5.6 eV.[15] The spectrum obtained agrees well with the excitation energy of this band $E_{exit}=5$ eV and 6.42 eV in Ref. 14. Thus, it can be concluded that the population of the corresponding emission center in the xenon matrix comes from states located somewhat above the dissociation limit $Xe+O^*(^1S)=4.18$ eV.

It is also known that in an Ar matrix the photon excitation energy 5.64 eV makes it possible to fill a certain state of a complex with charge transfer, which is manifested in radiation near 4.3 eV.[29] This state possesses triplet symmetry and fills the state $2^1\Sigma$ nonradiatively.[29] Since the ground state of the excimer XeO is the triplet term $X^3\Pi$ and the lowest state of Xe^+O^- is the triplet term $1^3\Pi$, it is natural to infer that photoexcitation fills, first and foremost, precisely this state $X^3\Pi \rightarrow 1^3\Pi$. The analog of such a transition was recently observed in an argon matrix for Ar^+O^-.[34]

We shall now compare these results with the computed potential $1^3\Pi$ Xe^+O^-.[2] First, the difference of the computed energy[2] 5.77 eV of the radiative transition $1^3\Pi \rightarrow X^3\Pi$ from the experimentally measured energy of this transition in the gas phase 5.3 eV must be taken into account.[6,7] Since the energies of transitions from other states are predicted much more accurately, it can be inferred that the computational error refers to the state $1^3\Pi$ and is approximately $\Delta E_d=0.47$ eV. Taking this correction into account and the fact that the matrix shift of the luminescence of the analogous charge-transfer complexes Xe^+F^- and $Xe_2^+F^-$ in an Ar matrix fluctuates for various states from $\Delta E_S=-0.4$ to -0.5 eV,[27] the energy of the minimum of the term $1^3\Pi$ in an argon matrix can be approximately estimated as

$$E_{min}(1^3\Pi)=E_{teor}(1^3\Pi)-\Delta E_d+\Delta E_S \approx 6.13-0.47-0.45=5.2\ \text{eV}. \quad (2)$$

It is obvious that this state can easily be filled in Ar by an excitation with energy 5.64 eV.[29] It is possible that even in the intrinsic Xe matrix the start of the excitation spectrum near 4.8 eV can correspond to filling of precisely this state.

B. Effect of an additional Xe atom. Can the X_2 band be attributed to the polarization interaction of the excimer $(XeO)^*$ with a neighboring xenon atom?

Before we consider the possible paths of radiative and nonradiative relaxation of excimer states, we must discuss the question of whether or not the bands X_1 and X_2 correspond to different types of excimers $(XeO)^*$ and $(Xe_2O)^*$ or to one and the same compound $(XeO)^*$ but in different lattice sites. Here we have in mind completely isolated impurity sites surrounded by matrix atoms (Ne, Ar, Kr) and sites which possess in their nearest-neighbor environment an additional Xe atom which does not form a chemical bond with an excimer molecule. In the second case the influence of the polarization contribution of the additional Xe atom in the nearest neighbor environment of an excimer molecule on the energy of its radiative transition must be estimated.

Apparently, the most direct answer can be obtained by comparing the luminescence spectra of the transition $2^1\Sigma-1^1\Sigma$ in diatomic molecules XeO* with the same Xe impurity concentration (1%) but different oxygen content (10^{-3} and 1%) (Fig. 3). For low oxygen concentration the presence of an additional Xe atom near a XeO* molecule becomes much more likely, and a red shift of the luminescence band is indeed observed. Nonetheless, the maximum value of this shift is very small (-0.012 eV), much less than the difference in the position of the maxima of the bands X_1 and X_2. The shift of the band with a maximum near 2.1 eV does not exceed -0.002 eV. These values of the shift agree completely with the difference in the binding energy per atom in crystal lattices of argon $D_k(Ar)$ and xenon $D_k(Xe)$.[21] When a single Ar atom from the nearest-neighbor environment of an excimer XeO* is replaced by a Xe atom the approximate estimate of the change in the interaction energy gives

$$\Delta D_k=[D_k(Xe)-D_k(Ar)]/n=0.01\ \text{eV}, \quad (3)$$

where $n=6$ is the number of nearest-neighbor atoms in a substitution site, the most stable position of oxygen in a Ar matrix.[26]

The value presented above is in good agreement with the results for an analogous transition $^1S-^1D$ in the sulfur atom S* in Ar and Xe matrices.[19] We recall that a S atom is isoelectronic with a O atom and has similar interaction energy potentials with the Xe atom, which were also calculated in Ref. 1. The main difference between XeS* and XeO* is that for XeS* $1^1\Sigma$ the lower state $1^1\Sigma$ has a shallower well: $D_e=0.33$ eV.[2] In contrast to XeO*, the radiation $2^1\Sigma \rightarrow 1^1\Sigma$ XeS* is observed not only in Ar and Kr but also in Xe. The corresponding matrix shifts are $\Delta E_S=-0.015$, -0.04, and -0.065 eV.[19] Thus, the difference in the energies of the transition $2^1\Sigma-1^1\Sigma$ in Ar and Xe matrices does not exceed 0.05 eV. This shows that, in the first place, there is no substantial deepening of the $1^1\Sigma$ potential in a Xe matrix and, in the second place, when a single Ar atom is replaced by a Xe atom the energy of the state $1^1\Sigma$ changes by not more than 0.01 eV.

On this basis it can be concluded that the relatively large difference of the energy position of the maxima of the X_1 and X_2 bands $\Delta E=E_{max}(X_1)-E_{max}(X_2)=0.08$ eV is a conse-

quence of the fact that the structures of the corresponding complexes are different.

Nonetheless, it is not due to the character of the internal bond in the complexes. Both bands manifest properties of compounds with a covalent bond. The energy position of the continuum band X_1+X_2 near 1.7 eV changes very little in different matrices, which is characteristic precisely for stretching excitations.[13,19] Conversely, the matrix shift of the radiation of charge–transfer complexes is ordinarily several tenths of an eV. For comparison, we can present the matrix shifts of the radiation of Xe^+F^- in Ar and Ne, which are 0.44 and 0.06 eV, respectively.[27] The strong influence of the matrix on charge–transfer complexes is due to solvation effects arising as a result of the polarization interaction of charge states with the surrounding Ar and Xe lattice.

The X_2 band in a neon matrix is distinguished from the general emission contour even at concentrations $c_{Xe}=0.1\%$ and both bands X_1 and X_2 simultaneously exist in the spectrum practically up to 10 % Xe. In our view this fact does not agree with the suggestion that the matrix shift of a charge–transfer complex is -0.78 eV.[15] It is obvious that for concentrations $c_{Xe}=0.1-1\%$ it is unlikely that quite large regions of accumulation of impurity Xe atoms, where strong polarization interaction could form, resulting in a large lowering of the potential Xe^+O^-, will appear.

There is another fact that seems to contradict the association of radiation near 1.7 eV to a charge–transfer complex Xe^+O^-. The radiative lifetime of the X_2 band in a Xe matrix is, according to different data, $\tau=290$ ns[9] or 227 ns,[15] which is an order of magnitude greater than the lifetime of a charge–transfer complex Xe^+O^- $1^3\Pi$ in the free state $\tau=10$ ns.[6] However, if the observed radiation is due to the transition $3^1\Sigma\rightarrow1^1\Sigma$ (Ref. 15) with a much larger lifetime, the absence of a better resolved transition ($^3\Pi\rightarrow{}^3\Pi$) in the spectrum becomes incomprehensible.

C. Identification of radiating states

According to the energy considerations presented above, there is greater justification for associating the X_1 and X_2 bands to transitions of $(XeO)^*$ and $(Xe_2O)^*$ from states associated with valence excitation of oxygen $O^*(^1D)$. Among the three terms converging to the dissociative limit $Xe(^1S_0)+O^*(^1D)=1.96$ eV, the most likely radiating state, in our view, is the term $1^1\Pi$. It possesses a shallow minimum, in contrast to the purely repulsive state $1^1\Delta$, and does not intersect the repulsive branch of the ground state $X^3\Pi$, in contrast to the term $1^1\Sigma$. The depth of the potential well of the state $1^1\Pi$ in the free molecule is estimated to range from $D_e\approx0.03$ eV[2] to $D_e=0.06$ eV.[4] In a Ar matrix this potential becomes deeper,[29] and in the intrinsic Xe matrix the state $1^1\Pi$ can be even more stable. The state $1^1\Pi$ intersects the repulsive state $1^3\Sigma^-$ at the interatomic distance $r_e=2.25$ Å, i.e. quite far from the position of the potential minima $r_e=3.4$ for 3.6 Å for the $2^1\Sigma$ and $1^1\Pi$ states, respectively.[2] Therefore the nonradiative dissociative annihilation channel of the state $1^1\Pi$, most likely, will be inefficient. On the other hand, if the influence of a charge–transfer complex results at least in a small lowering of the level $1^1\Sigma$, then the probability of nonradiative phonon relaxation between $1^1\Pi$ and $1^1\Sigma$ can decrease substantially. In this case, it is radiative relaxation from the state $1^1\Pi$ that can be most likely in the Xe matrix.

The comparatively short lifetime for the forbidden transition $\tau=227$ ns[15] does not contradict the assumptions made above. We recall that in the gas phase the transition $O^*(^1D\rightarrow{}^3P)$ is forbidden [$\tau=110$ s (Ref. 35)]. In a Ne matrix it decreases to $\tau=32$ s.[25] This decrease of the lifetime is due to the partial removal of the forbiddenness on the transition $^1D\rightarrow{}^3P$ in a crystal matrix and also the formation of molecular bonds. As model calculations show,[26] Xe atoms in the nearest-neighbor environment of an excited atom $O^*(^1D)$ undergo an asymmetric shift in different directions by the amount 0.1–0.2 Å, and the shift of the O* atom itself relative to the central position reaches 1 Å. As a result, a very strong shortening of the lifetime of the radiating state is observed. Thus, for example, for the radiation $O^*(^1S\rightarrow{}^1D)$ in the gas phase $\tau=800$ ns,[35] and for the corresponding transition XeO* $(2^1\Sigma\rightarrow1^1\Sigma)$ in Ar $\tau=112$ ns.[29]

The energy of the transition X_1 corresponds to the theoretically computed potential of $(XeO)^*$.[2] The transition $2^1\Sigma\rightarrow1^1\Sigma$ is predicted there very accurately: $\Delta E_{2-1}=E_{teor}-E_{gas}=-0.05$ eV. On the basis of these data and the radiation energy in the gas phase, we estimated the errors in terming the energies of other valence transitions: $2^1\Sigma\rightarrow X^3\Pi$ ($E_{teor}=4.22$ eV, $\Delta E_{2-X}=0.195$ eV) and $1^1\Pi\rightarrow X^3\Pi$ ($E_{teor}=2.13$ eV, $\Delta E_{1-X}=\Delta E_{2-X}-\Delta E_{1-2}=0.2$ eV). Correspondingly, the energy of the transition $1^1\Pi\rightarrow X^3\Pi$ in a gas should be 1.93 eV. This value agrees to within 0.1 eV with the energy of the X_1 band in Ne. It could be difficult to observe this band in the gas phase because of the symmetry forbiddenness. Nonetheless, the unidentified continuum in the red region of the spectrum, observed in some investigations of a gas mixture of xenon with oxygen,[3,5] could be due precisely to this radiation.

We can also make certain assumptions concerning the relatively narrow band with $E_{max}=2.1$ eV, whose intensity correlates with the transition XeO* $2^1\Sigma\rightarrow1^1\Sigma$. The energy position of this band in various matrices differs approximately by 0.2 eV and is 2.12, 2.09, and 2.07 eV in Ne, Ar, and Kr matrices, respectively. It is not observed in Xe crystals. Judging from the small width, this band corresponds to a transition to a quite flat section of the lower term. Of the energetically suitable states, only potentials of the covalent compounds possess this specific property. On the basis of the working parameters of Ref. 2 the transitions $2^1\Sigma\rightarrow1^1\Delta$ or $3^1\Sigma\rightarrow2^1\Sigma$ could correspond to radiation near 2.1 eV. However, there is not enough experimental information concerning this band to make a final identification of the band. The lifetime $\tau=115$ ns of the band of XeO* with $E_{max}=2.08$ eV in a Kr matrix, measured in Ref. 17, agrees well with the lifetime of the transition XeO* $2^1\Sigma\rightarrow1^1\Delta$ in Kr.[29] This makes it more likely that this band is due to $2^1\Sigma\rightarrow1^1\Delta$. On the other hand, for excitation XeO* with energy $E_{exc}=5.64$ eV in an Ar matrix, the presence of a band near 2.1 eV in the spectrum was not mentioned.[29] This could be due to the fact that the corresponding radiative term lies above E_{exc}, i.e. it is associated to the states $3^1\Sigma$ or $2^1\Delta$.

D. Estimates of transition energies from charge-transfer complexes in a crystal matrix

We shall now consider the influence of the matrix environment on the radiation energy of charge–transfer complexes Xe^+O^-. This makes it possible to estimate the possibility of attributing the continuum band near 1.7 eV to the transition $3^1\Sigma \rightarrow 1^1\Sigma$ and the 3.3 eV band to $3^1\Sigma \rightarrow 1^1\Pi$, proposed in Ref. 15. The Ne matrix, because of its high plasticity and weak polarizability, ordinarily contributes minimal shifts to the emission energy of impurity molecules. For example, the shift of the emission energy of a charge–transfer complex Xe^+F^- is only -0.06 eV.[27] This suggests that the matrix shift for Xe^+O^- radiation in neon is of the same order of magnitude. Thus, the energy splitting between the terms $Xe^+O^-(3^1\Sigma)$ and $XeO^*1^1\Sigma$ in a neon matrix should differ very little from the gas phase, and we can exclude any large deepening of the $1^1\Sigma$ potential by 0.78 eV, as proposed in a xenon matrix.[15] In accordance with the calculations performed in Ref. 2 and taking account of the 0.47 eV correction to achieve agreement between the computational and experimental potentials Xe^+O^-, the proposed energies of the transitions $3^1\Sigma \rightarrow 1^1\Sigma$ and $3^1\Sigma \rightarrow 1^1\Pi$ can be estimated and should be approximately 3.9 and 3.75 eV, respectively. The experiments show that in a neon matrix radiation is not observed in this energy range, and once again the bands X_1 and X_2 are present in the spectrum.

We shall now estimate the energy of the radiative transition in $Xe_2^+O^-$ assuming a simple law that is charcteristic for other charge–transfer complexes of inert gases. We note that diatomic compounds with halides Xe^+G^- and hydrides Xe^+H^- do not occur in the intrinsic Xe matrix, since the triatomic molecules $Xe_2^+G^-$ and $Xe_2^+H^-$ are energetically favored. The radiation of a charge–transfer complex $Ar_2^+O^-$[23,24] is also observed in an Ar matrix with oxygen impurity.[36–38]

According to Table II, the difference in the energies of radiation from the lowest diatomic states in a free state and from triatomic states in an intrinsic xenon matrix is $\Delta E_{G-S} = 1.9-1.8$ eV for a wide range of reagents. In this case, the corresponding radiative transition $Xe_2^+O^- \rightarrow Xe_2O^*$ should be observed in the energy range

$$E_S(Xe_2^+O^-) = E_G(Xe^+O^-) - \Delta E_{G-S}(Xe^+F^-) = 5.275 - 1.92 = 3.35\ \text{eV}, \quad (4)$$

TABLE II. Energies E_{max} of the emission band maxima for certain charge-transfer complexes of Xe with reagents the Y in the gas phase and in a solid Xe Matrix as well as their difference.

Reagent Y	$E_{max}(Xe^+Y^-)$, eV (gas)	$E_{max}(Xe_2^+Y^-)$, eV (solid Xe)	$E_{max}(Xe^+Y^-) - E_{max}(Xe_2^+Y^-)$, eV
D	6.525 [Ref. 46]	4.862 [Ref. 47]	1.663
O	5.275 [Ref. 27]	3.333*	1.942
F	3.520 [Ref. 48]	1.599 [Ref. 27]	1.920
S	5.462 [Ref. 6]	3.583 [Ref. 44]**	1.879
Cl	4.025 [Ref. 48]	2.164 [Ref. 43]	1.862
Br	4.396 [Ref. 48]	2.583 [Ref. 43]	1.813

*Value and identification of this work, see also Refs. 13 and 15.
**This identification is proposed in the present work, see text.

which agrees quite well with the energy 3.33 eV of the band maximum in a Xe matrix. We now estimate the energy position of the radiative term of $Xe_2^+O^-$. The internuclear distance between the ions Xe^+ and O^- in a triatomic molecule is only 5% greater than for a diatomic molecule.[39] The energy of the XeO ground state $X^3\Pi$ with $r(Xe–O) = 2.9$ Å is $E(X^3\Pi) \approx 0.1$ eV.[2] The variance of the theoretical values for the energy of the ground state $X^1\Sigma_g^+$ of the Xe_2 molecule in the region of strong interatomic repulsion is quite large, $E(Xe_2) \approx 0.5 \pm 0.1$ eV (see, for example, Refs. 40 and 41). Consequently, for an equilibrium internuclear distance of the molecular ion Xe_2^+ $r_e = 3.1$ Å[39] we chose the value $E(Xe_2) = 0.5$ eV, which corresponds to the latest experimental data.[42] Thus, the energy position of the minimum of $Xe_2^+O^-$ in a xenon matrix can be approximately estimated as

$$E_{min}(Xe_2^+O^-) = E_S(Xe_2^+O^-) + E_S(X^3\Pi) + E_S(Xe_2) \approx 3.33 + 0.1 + 0.5 = 3.93\ \text{eV}. \quad (5)$$

This energy level was found to be somewhat lower than the state $2^1\Sigma$. This could be why there is no radiation corresponding to the transition $2^1\Sigma \rightarrow 1^1\Sigma$ in a Xe matrix and in lighter matrices with higher Xe concentrations, when impurity pairs Xe_2 are most likely to form.

Continuing the analogy to xenon fluorides, we shall assume that the matrix shifts for $Xe_2^+F^-$ and $Xe_2^+O^-$ are approximately the same, i.e. $\Delta E_S(Xe_2^+O^-) = -0.43$ eV in Xe.[43] Then in the gas phase the radiation from $Xe_2^+O^-$ should be observed for

$$E_G(Xe_2^+O^-) = E_S(Xe_2^+O^-) - \Delta E_S(Xe_2^+O^-) = 3.33 + 0.43 = 3.76\ \text{eV}. \quad (6)$$

Indeed, comparing with the spectrum of the gas mixture $Xe+N_2O$ shows that a quite wide radiation band with a complex structure, which can be a superposition of the emission bands $Xe^+O^-(2^3\Pi \rightarrow X^3\Pi)$[7] and $Xe_2^+O^-$, lies in this region. The difference of the energies of the radiation from diatomic and triatomic molecules is

$$\Delta E(Xe_2^+O^-) = E(Xe^+O^-) - E(Xe_2^+O^-) = 5.275 - 3.76 = 1.51\ \text{eV}, \quad (7)$$

which agrees reasonably well with the analogous energy for xenon fluorides (1.49 eV) in the gas phase.

A similar comparison for the compounds Xe^+S^- and Xe^+Cl^- likewise shows that the radiation energies of diatomic and triatomic excimers are the same. These estimates are presented in Table II. The luminescence band with energy 3.58 eV was observed in a Xe matrix with S as the impurity.[44] Although initially it was attributed to radiation of the compound Xe^+S^-, the authors believe that in this case the matrix shift $\Delta E_S(Xe_2^+O^-) = 1.86$ eV is too large, and they suggested that the transition occurs not into the ground but rather into a valence state correlating with $Xe+S(^1D)$ or $Xe+S(^1S)$. From our viewpoint the presence of such an intercombination transition in the spectrum and the absence of a better resolved transition into the ground state contradicts the association made above. Undoubtedly, the regularities presented are still not absolute proof, but from our standpoint the association of the 3.58 eV band in the Xe matrix to a

transition from $Xe_2^+S^-$ and 3.33 eV to a transition from state $Xe_2^+O^-$ is completely consistent with preceding investigations of excimers in solid matrices. The position of the minimum for $Xe_2^+S^-$ $E_{min}=4.1$ eV, computed analogously, in a Xe matrix was 1.3 eV above the dissociation limit of $Xe+S^*(^1S)$. Thus, the radiative transition XeS^* $2^1\Sigma \rightarrow 1^1\Sigma$ in an intrinsic matrix becomes possible, as is observed experimentally.

Our investigations and the results of Ref. 13 show that the band with $E_{max}=3.3$ eV is observed in the spectrum of solid solutions of Xe in Ar and Xe in Ne only for sufficiently high concentrations $c_{Xe}>0.3\%$. In addition, the lifetime of a state of a charge–transfer complex Xe^+O^- in an Ar matrix is unusually sensitive to the Xe concentration.[29] For $c_{Xe}=4\%$ the lifetime of the emission band of Xe^+O^- near 4.3 eV decreases by almost an order of magnitude from 340 to 49 ns, and the relative intensity of the radiation of Xe^+O^- and XeO^* $(2^1\Sigma)$ decreases and the state $2^1\Sigma$ is no longer filled from higher-lying charge-transfer complexes. Indeed, later calculations[2] showed that the lowest state of Xe^+O^- possesses a triplet symmetry and intersects with the term $2^1\Sigma$ at the top of the potentials. The energy of this state is too low to relax nonradiatively as a result of an interaction with higher-energy states of Xe_2^*. Consequently, we thought that the quenching of Xe^+O^- could be due to the formation of triatomic excimers $Xe_2^+O^-$, which with 4% Xe are statistically entirely likely.

The position of an impurity oxygen atom in the xenon crystal lattice can play an important role in the formation of excimer molecules. An oxygen atom in a Xe matrix can occupy three possible lattice sites: an interstitial site, a substitution site, and a so-called builtin site, which is energetically most favorable.[18] Builtin sites contain most of the impurity oxygen atoms, which start to move to freer substitution sites as the crystal temperature increases to $T\approx 30$ K.[17] In the light of everything said above, it seems possible that triatomic molecules with a covalent bond can form precisely in the builtin interstitial sites, while in less compressed sites substitutions can form predominantly diatomic molecules. Our investigations show that an activation transition corresponds to a change in the shape of the band near 1.7 eV at $T\approx 30$ K (Fig. 2). The largest local maximum 1.8 eV, which forms a shoulder on the luminescence band with $E_{max}=1.7$ eV in crystalline xenon could correspond to diatomic compounds. This assumption completely explains the different lifetime of the components: $\tau_1=110$ ns for $E_{max}=1.86$ eV and $\tau_2=290$ ns for $E_{max}=1.66$ eV.[9]

E. Alternative variants of the identification of the bands X_1 and X_2

To check the possible association of the 1.7 eV band to the radiation of the complex $Xe_2^+O^-$ we shall estimate the energy of a transition from the corresponding lowest state to the term Xe_2O^*, associated with $O^*(^1S)$. Assuming that the energy of the polarization interaction of the matrix with $O^*(^1S)$ has the same value[19] $\Delta E_S(S)\approx 0.1$ eV as for an isoelectronic atom $S^*(^1S)$, and the magnitude of the repulsion potential at $r=2.8$ Å is $\delta E(1^1\Pi)\leqslant 0.03$ eV,[2] the corresponding radiation could be observed with

$$E(Xe_2^+O^-\rightarrow Xe_2O^*)\approx E(Xe_2^+O^-)-E_D+\Delta E_S(S)+\delta E(1^1\Pi)=3.93-1.97-0.1+0.03\approx 1.9\ \text{eV}. \quad (8)$$

This value is appreciably greater than the energy of the observed transition. Nonetheless, considering that such estimates are quite approximate, the assumption made above cannot be completely excluded, and the close similarity of the excitation spectra of the 1.7 and 3.3 eV bands and their lifetime[15] requires additional investigations of this question. We are still inclined toward the previously made association of the radiation near 1.7 eV to a transition from the state of Xe_2O^* on the basis that the energy of this band is essentially independent of the polarization influence of the matrix environment and corresponds numerically to shifts characteristic for a valence transition.[19] It seems to us that the possibility of the existence of such compounds, which is *a priori* excluded in Ref. 26, even though the formally constructed potential presumes such a possibility, need to be reexamined theoretically.

For completeness, several elucidating remarks concerning the ionic centers found in xenon clusters are required. The luminescence bands of Xe clusters near 1.9 and 1.5 eV are classified as transitions from excited ionic states $(Xe_3^+)^*$ or $(Xe_4^+)^*$.[45] The corresponding radiating states are identified as transitions similar to a free ion $Xe_2^+(1/2)_g\rightarrow 1(1/2)_u$ and $2(1/2)_u\rightarrow 1(3/2)_g$.

Even though the indicated bands lie in the energy range of the investigated bands X_1 and X_2, we believe it extremely unlikely that the ionic centers are associated with the observed radiation. In the first place, the excitation spectra of the X_2 band with $E_{max}=1.72$ eV, which were investigated in pure Xe and in a Ne matrix with Xe impurity, lie significantly below the ionization threshold of Xe, which excludes any possibility of associating it to ionic states. As far as the band X_1 with $E_{max}=1.8$ eV is concerned, it is unlikely to be associated to the 1.9 eV band in Xe crystals for purely statistical reasons. In clusters the band with $E_{max}=1.9$ eV is observed only when the number of atoms in them $N\geqslant 10$, which corresponds to the possibility of the formation of excited ionic centers $(Xe_3^+)^*$ or $(Xe_4^+)^*$ with partial charge delocalization.[45] It is obvious that for $c_{Xe}=10^{-2}\%$ it is impossible to achieve such a large accumulation of impurity atoms in a matrix [see Eq. (1)]. Radiation from diatomic molecular ions $(Xe_2^+)^*$ could be observed only at energies below 1.6 eV,[39] and consequently it likewise cannot be associated with the band X_1 which was investigated.

6. CONCLUSIONS

In this work we investigated the luminescence of xenon excimer compounds with oxygen in inert-gas matrices. The dependence of the luminescence spectrum and the intensities of its individual bands on the matrix properties and xenon and oxygen concentrations was analyzed. The change in the form of the continuum luminescence band with maximum near 1.7 eV as a result of a change in the Xe concentration was described by a superposition of two bands of different nature.

The short-wavelength band, whose maximum lies near $E_{\max}=1.8\,\text{eV}$, predominates in weak ternary solutions and can be interpreted as a transition from the state XeO* $(1^1\Pi)$ into the lowest state $X^3\Pi$. The band with $E_{\max}=1.72\,\text{eV}$ is characteristic for strong solutions and an intrinsic Xe matrix with oxygen impurity. It is associated to radiation of the triatomic excimer $Xe_2^+O^*$. This state is probably genetically associated with the excitation $O^*(^1D)$.

The transformation of diatomic complexes into triatomic complexes under the action of exciting radiation, accelerating diffusion of Xe atoms in a Ne lattice, was traced for the example of the ternary solution $Ne+Xe+O_2$.

A comparative analysis of the results with the experimental data and the computed terms, known for similar halide and hydride compounds with xenon as well as for xenon compounds with isoelectronic to oxygen atom S, was performed. As a result the bands 3.33 and 3.58 eV in a xenon matrix with O and S impurity were tentatively associated to radiation of charge–transfer complexes $Xe_2^+O^-$ and $Xe_2^+S^-$.

The currently available experimental and theoretical data are insufficient for making a final identification of the centers associated with excimer radiation of inert gases. This requires further investigations of the concentration dependences of the photoexcitation and photoluminescence spectra.

We thank Doctor of Physicomathematical Sciences A. M. Ratner for his interest in this work and for constructive remarks.

[a)]E-mail: belov@ilt.kharkov.ua

[1] Ch. K. Rhodes [Ed.], *Excimer Lasers* (Springer-Verlag, Berlin, 1979).
[2] M. Yamanishi, K. Hirao, and K. Yamashita, J. Chem. Phys. **108**, 1514 (1998).
[3] C. D. Cooper, G. C. Cobb, and E. L. Tolnas, J. Mol. Spectrosc. **7**, 223 (1961).
[4] J. D. Simmons, A. D. Maki, and J. T. Hougen, J. Mol. Spectrosc. **74**, 70 (1979).
[5] V. Ya. Aleksandrovm, V. Yu. Vinogradov, V. V. Lugovskiĭ, and I. V. Podmoshenskiĭ, Opt. Spektrosk. **41**, 390 (1976).
[6] J. Xu, D. W. Setser, and J. K. Ku, Chem. Phys. Lett. **132**, 427 (1986).
[7] A. Kvaran, A. Ludviksson, W. S. Hartree, and J. P. Simons, Chem. Phys. Lett. **137**, 209 (1987).
[8] S. Neeser, M. Voitik, and H. Langhoff, J. Chem. Phys. **102**, 1639 (1995).
[9] K. M. Monahan and Rehn, J. Chem. Phys. **68**, 3814 (1978).
[10] A. G. Belov, V. N. Svishchev, I. Ya. Fugol', and E. M. Yurtaeva, Fiz. Nizk. Temp. **9**, 1206 (1983) [Sov. J. Low Temp. Phys. **9**, 623 (1983)].
[11] I. Ya. Fugol', A. G. Belov, and E. I. Tarasova, JETP Lett. **43**, 687 (1986).
[12] I. Ya. Yurtaeva, I. Ya. Fugol', and A. G. Belov, Fiz. Nizk. Temp. **16**, 101 (1990) [Sov. J. Low Temp. Phys. **16**, 54 (1990)].
[13] M. Fritsch, *Spektroskopische Untersuchungen in Edelga-soxiden in Edelgasmatrizen* (Experimentelle physikalische Diplomarbeit am Fachbereich Physik der Universität Hamburg, 1991).
[14] H. Krueger and E. Weitz, J. Chem. Phys. **96**, 2846 (1992).
[15] W. G. Lawrence and V. A. Apkarian, J. Chem. Phys. **97**, 2229 (1992).
[16] R. Grünwald, *Fluoreszenspektroskopie an Edelgasoxiden in Edelgas-Matrix* (Experimentelle physikalische Diplomarbeit am Fachbereich Physik der Universität Hamburg, 1992).
[17] A. V. Danilychev and V. A. Apkarian, J. Chem. Phys. **99**, 8617 (1993).
[18] A. V. Danilychev and V. A. Apkarian, J. Chem. Phys. **100**, 5556 (1994).
[19] L. Khriachtchev, M. Pettersson, S. Jolkkonen, and M. Räsänen, Chem. Phys. Lett. **316**, 115 (2000).
[20] T. H. Dunning, Jr. and J. Hay, J. Mod. Opt. **66**, 3767 (1977).
[21] N. Schwentner, E. E. Koch, and J. Jortner, *Electronic Excitations in Condensed Rare Gases* (Springer-Verlag, Berlin, 1985).
[22] R. Sauerbrey, Y. Zhu, F. K. Kittel, and W. L. Wilson, Jr., J. Chem. Phys. **85**, 1299 (1986).
[23] A. G. Belov, I. Ya. Fugol', and E. M. Yurtaeva, Fiz. Nizk. Temp. **24**, 580 (1998) [Low Temp. Phys. **24**, 440 (1998)].
[24] A. G. Belov, I. Ya. Fugol, E. M. Yurtaeva, and O. V. Bazhan, J. Lumin. **91**, 107 (2000).
[25] D. Maillard, J. P. Perchard, J. Fournier, H. H. Mohammed, and C. Girardet, Chem. Phys. Lett. **86**, 420 (1982).
[26] D. Maillard, J. Fournier, H. H. Mohammed, and C. Girardet, J. Chem. Phys. **78**, 5480 (1983).
[27] G. Zerza, G. Sliwinski, N. Schwentner, C. J. Hoffman, D. G. Imre, and V. A. Apkarian, J. Chem. Phys. **99**, 8414 (1993).
[28] I. Last and T. F. George, J. Chem. Phys. **86**, 3787 (1987).
[29] J. Goodman, J. C. Tully, V. E. Bondybey, and L. E. Brus, J. Chem. Phys. **66**, 4802 (1977).
[30] J. M. Brom and H. P. Broida, Chem. Phys. Lett. **33**, 84 (1975).
[31] R. V. Taylor and W. C. Walker, J. Chem. Phys. **70**, 284 (1979).
[32] I. Ya. Fugol', A. G. Belov, V. N. Svishchev, and E. M. Yutaeva, Fiz. Nizk. Temp. **13**, 288 (1987) [Sov. J. Low Temp. Phys. **13**, 163 (1987)].
[33] S. Craydok and A. Hincliff, *Matrix Isolation* (Mir, Moscow, 1978).
[34] M. S. Gudipati, Chem. Phys. Lett. **248**, 452 (1996).
[35] A. A. Radtsig and B. M. Smirnov, *Reference Data on Atomic and Molecular Physics* (Atomizdat, Moscow, 1980).
[36] E. E. Huber Jr., D. A. Emmons, and R. M. Lerner, Opt. Commun. **11**, 155 (1974).
[37] Yu. B. Poltoratskiĭ and I. Ya. Fugol', Sov. J. Low Temp. Phys. **4**, 783 (1978).
[38] T. Reimann, W. L. Brawn, and R. E. Johnson, Phys. Rev. B **37**, 1455 (1988).
[39] W. R. Wadt, J. Chem. Phys. **68**, 402 (1978).
[40] J. S. Cohen and R. T. Pack, J. Chem. Phys. **61**, 2372 (1974).
[41] W. C. Ermler, Y. S. Lee, K. S. Pitzer, and N. W. Winter, J. Chem. Phys. **69**, 976 (1978).
[42] S. Kita, S. Gotoh, T. Hasegawa, and N. Shimakura, J. Chem. Phys. **109**, 9713 (1998).
[43] M. E. Fajardo and V. A. Apkarian, J. Chem. Phys. **89**, 4102 (1988).
[44] S. Tanaka, H. Kajihara, S. Koda, and V. A. Apkarian, Chem. Phys. Lett. **233**, 555 (1995).
[45] A. V. Kanaev, M. C. Castex, L. Museur, R. von Pietrowski, and T. Moller, Phys. Rev. Lett. **75**, 2674 (1995).
[46] A. A. Valsenko, I. S. Lakoba, S. P. Chernov, and P. B. Éssel'bakh, Dokl. Akad. Nauk Arm. SSR **289**, 79 (1986).
[47] P. Gurtler, M. Kraas, and T. Tschentscher, Europhys. Lett. **11**, 115 (1990).
[48] P. J. Hay and T. H. Dunning, J. Chem. Phys. **69**, 2209 (1978).

Translated by M. E. Alferieff

QUANTUM LIQUIDS AND QUANTUM CRYSTALS

Effect of an orientational phase transformation on low-temperature creep in n-H_2

L. A. Alekseeva,* Yu. E. Stetsenko, Yu. V. Butenko, and A. A. Solodovnik

B. I. Verkin Physicotechnical Institute for Low Temperatures, Ukrainian National Academy of Sciences, pr. Lenina, 47 Khar'kov, 61103 Ukraine

(Submitted June 5, 2001; resubmitted June 20, 2001)
Fiz. Nizk. Temp. **27**, 1283–1286 (November 2001)

The low-temperature stationary creep of solid normal hydrogen grown in a polycrystalline form is investigated. The experimental temperature range 1.4–4.2 K includes the temperature T_c of the phase transformation of n-H_2. It is found that as the temperature of n-H_2 decreases to T_c the stationary creep rate of the samples abruptly decreases. This which could be due to stiffening of the n-H_2 lattice as a result of orientational ordering of the orthomolecules. © *2001 American Institute of Physics.* [DOI: 10.1063/1.1421461]

The H_2 molecule is a quantum-mechanical system consisting of four Fermi particles (two protons and two electrons) with half-integer spins. As a result of the requirement that the total wave function be antisymmetric, there exist two nuclear spin modifications of H_2—ortho- and para-, which are described by different sets of rotational states (the quantum numbers J assume the values 0, 2, 4, ... for even total spin of the nuclei $I=0$ and 1, 3, 5, ... for odd total spin $I=1$). At temperatures below 85 K (especially, in a crystal) only the lower states $J=1$ and $J=1$ are occupied (see, for example, Ref. 1). As a result of the loss of the high symmetry characteristic of spherical p-H_2 molecules by orthohydrogen, o-H_2 molecules interact more rigidly in the lattice (primarily via electrostatic quadrupole–quadrupole (EQQ) forces). The hydrogen modifications behave as two fundamentally different and mutually soluble substances. The anisotropic EQQ interaction between orthomolecules for concentrations $x>53\%$ initiates orientational ordering, which occurs at a concentration-dependent temperature T_c and is accompanied by a crystallographic transition from a hexagonal close-packed lattice structure (stable at high temperatures) to a cubic structure. For ortho-H_2 concentration equal to 75% (n-H_2), orientational ordering with a structural change hcp–fcc occurs when the temperature decreases to 1.58 K (see Ref. 2 and the references cited there). The overall crystal symmetry is lowered from $P6_3/mmc$ to $Pa3$.[2,3]

Phase transformations in molecular crystals (for example, in CH_4[3]) lead to a sharp change in a number of plasticity parameters, including the stationary creep rate $\dot{\varepsilon}$, under the action of a constantly applied stress. In hydrogen the phase transformation is accompanied by a change in the positional order of the centers of gravity of the molecules, and in this connection the character of the behavior $\dot{\varepsilon}(T)$ is of special interest.

Up to now there has been no information on the assumed influence of a phase transition on the value of $\dot{\varepsilon}$ for solid normal hydrogen. In the present paper we present the results of an investigation of the temperature dependence of the stationary (steady) creep rate $\dot{\varepsilon}$ in solid n-H_2 for three values of the applied stress σ in the temperature range 1.4–4.2 K, including the phase transition point T_c. A feature indicating that the phase transition influences the plastic deformation rate of n-H_2 is observed is observed in the behavior of $\dot{\varepsilon}(T)$.

Samples 50 mm long and 10 mm in diameter were grown from gaseous H_2 collected above the surface of liquid n-H_2 with purity 99.999 mole %. The gas accumulated under a small excess pressure (in order to create a reserve of H_2 for growing samples and to prevent air from entering) at room temperature in a 12KH18N10T steel injection system. As a result of the extremely low partial pressure of all possible nonhydrogen impurities,[5] at the boiling point of hydrogen the H_2 gas had the highest possible purity and enriched as highly as possible with the main hydrogen components (ortho- and para- in the natural ratio 3:1). n-H_2 was crystallized in a liquid helium cooled gas ampul.[6] As a result of the rapid removal of the vapor above the samples, the samples were freed from the ampul walls. The loading of the samples, annealed at 10–11 K, was performed with a movable rod connected with the core of an electromagnet.[6] The samples grown were polycrystals with 1.5–2 mm grains.

The temperature of the samples was regulated by evacuating vapor above liquid ^{4}He. It was measured according to the helium vapor pressure and monitored with carbon thermometers to within $\pm 10^{-2}$ K. The error of temperature stabilization and the temperature nonuniformity along a sample did not exceed 10^{-1} K. The increase in the sample length was measured with an inductive displacement sensor to within 10^{-5} cm.

Figure 1 displays the temperature dependences of the steady creep rate $\dot{\varepsilon}$ of n-H_2 samples. These curves were obtained for three values of the constant stress σ applied to the samples (0.02, 0.06, and 0.1 MPa). The experimentally obtained values of $\dot{\varepsilon}$ were averaged over several measurements; the deviation from the average did not exceed 3–5%. It is evident in the figure that in the high-temperature phase of n-H_2 all $\dot{\varepsilon}$ temperature dependences presented tend to saturate on cooling, and this tendency tends to be disrupted when the phase transition point, where $\dot{\varepsilon}$ decreases abruptly for all

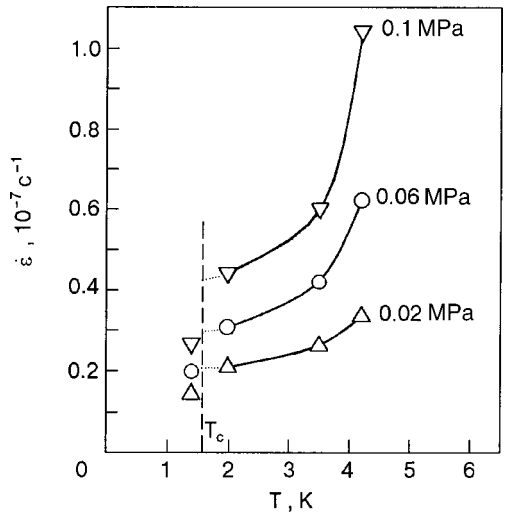

FIG. 1. Temperature dependences of the stationary creep rate $\dot{\varepsilon}$ of n-H_2 polycrystals for various values of the applied stress σ.

three indicated values of σ, is crossed. This shows that the rate of stationary plastic flow n-H_2 is sensitive to the structural phase transformation.

It follows from the measurements of the steady creep rate of n-H_2, which are presented in a wide range of temperatures 2–13 K (see Ref. 2 and the references cited there), that the activation energy of steady creep for temperatures $2\text{ K}<T<4.2\text{ K}$ is close to the characteristic energy of the noncentral EQQ interaction for two neighboring o-H_2 molecules in the lattice (3.2–3.3 K, see Ref. 2). This shows that the quadrupole–quadrupole interaction between orthohydrogen molecules play a determining role in the kinetics of low–temperature creep of n-H_2.

The observed feature in the behavior of $\dot{\varepsilon}$ near the phase transformation point in n-H_2 is due to the difference of the fundamental physical properties of the ortho- and paramodifications of solid H_2—the presence of orientational ordering of o-H_2 molecules and the difference of the structural state of crystalline n-H_2 at temperatures below and above T_c. The results obtained clearly show that the orientational ordering induced among the orthomolecules by the electrostatic quadrupole–quadrupole interaction (as temperature decreases to $T_c=1.58\text{ K}$, the short-range order is accompanied by the appearance of long-range order in the mutual orientations of the orthomolecules in the n-H_2 crystal) and the structural phase transition influence the mechanisms of deformation of n-H_2, which determine the kinetics of the stationary creep of n-H_2 near the phase transition ($1.4<T_2<2\text{ K}$).

It should be noted that the crystallographic fcc–hcp phase transition probably does not play the main role in the change in the plasticity parameters of n-H_2. This result is based on the fact that a temperatures below T_c, where the distribution of the centers of mass of the hydrogen molecules in an n-H_2. polycrystal is characteristic for the fcc structure, the stationary creep rate of the samples is not higher but rather appreciably lower than in the anisotropic hcp structure. To interpret this observation the polycrystalline nature of the experimental samples of n-H_2 and the general specific nature of hcp crystals must be taken into account: comparatively rapid blocking of the deformation of individual grains by neighboring grains because there is no possibility for five slip systems to appear in the grains simultaneously, which is necessary to preserve their continuity. This gives a basis for expecting a higher plasticity in n-H_2 at temperatures below the point of the crystallographic transformation of its structure.

The observed feature of the temperature dependence of $\dot{\varepsilon}$ for n-H_2 agrees qualitatively with the results of the investigation (see, for example, Ref. 4) of the effect of a phase transition on the stationary creep rate of crystalline methane, where the low-temperature phase transition (see Ref. 3 and the references cited there) results at the transition point in an abrupt change of $\dot{\varepsilon}$ by almost two orders of magnitude. Thus, the lower values of the creep rate $\dot{\varepsilon}$, the higher degree of hardening, and the lower plasticity of n-H_2 in the fcc phase at temperatures $T<T_c$ are due primarily to differences in the character of the rotational motion of o-H_2 molecules near the phase transformation temperature and the presence of long-range order in their relative orientations in the crystal.

At temperatures below T_c an o-H_2 molecule undergoes librational oscillations, preserving the arrangement of the centers of gravity at sites of the type $Pa3$ in the close-packed lattice.[2] The equilibrium positions of the axes of the orthohydrogen molecules are directed along the four spatial diagonals of a cube. The disruption arising with the motion of dislocations at temperatures $T<T_c$ not only in the positional but also orientational order in a n-H_2 crystal causes the symmetry axes of the crystal to tilt away from the equilibrium orientations. A transition through the point of the orientational phase transition with increasing temperature is ordinarily accompanied by the appearance of spontaneous deformation (see Ref. 6). It follows from experiment that long-range order in the relative orientations of orthomolecules below the temperature T_c increases the friction in the lattice for dislocations in n-H_2. The facts that as the symmetry of the crystal changes as a result of the hcp–fcc phase transition in n-H_2 and that the structure of the dislocation nuclei changes with the appearance of four sublattices with different orientations of the symmetry axes of the o-H_2 molecules must be taken into account. Instead of isolated dislocations, existing at $T>T_c$, in n-H_2 samples at temperatures $T<T_c$ superdislocations arise[7,8] with antiphase displacement vector $a/2$ [110] (a is the distance between nearest neighbors) and antiphase boundaries. For n-H_2 they separate specific rotational domains[9] characterized by different orientations of the molecular axes of o-H_2. Such domains arise in molecular cryocrystals with a predominant anisotropic EQQ interaction between the molecules. This is probably the reason for the appearance of jump in the creep rate of hydrogen at the transition through the phase transition point T_c. It should be noted that the observed behavior of $\dot{\varepsilon}$ is, to a large degree, similar to the changes observed in the mechanical properties (for example, the microhardness) of heavy molecular crystals of the type C_{60} at their phase transition point[6,10]

We are deeply grateful to V. G. Manzheliĭ, M. A. Strzhemechnyĭ, M. I. Bagatskiĭ, V. D. Natsik, and A. I. Prokhvatilov for helpful remarks and I. V. Legchenkova for assisting in the presentation of the results obtained in this work.

*E-mail: alekseeva@ilt.kharkov.ua

[1] A. Bažzer, *Basic Ideas of Modern Physics* (Atomizdat, Moscow, 1973).
[2] B. I. Verkin and A. F. Prikhot'ko [Eds.], *Cryocrystals* (Naukova dumka, Kiev, 1983); V. G. Manzhelii and Yu. A. Freiman [Eds.], *Physics of Cryocrystals* (AIP Press, Woodbury, New York, 1996).
[3] V. G. Manzhelii, A. I. Prokhvatilov, I. Ya. Minchina, and L. D. Yantsevich, *Handbook of Binary Solutions of Cryocrystals* (Begell House, Inc., New ork, 1996).
[4] V. A. Romanusha, A. V. Leont'eva, and A. Yu. Prokhorov, Fiz. Nizk. Temp. **12**, 545 (1986) [Sov. J. Low Temp. Phys. **12**, 309 (1986)]; A. V. Leont'eva, A. D. Alekseev, V. A. Romanusha, V. A. Strel'tsov, A. Yu. Prokhorov, L. V. Stepanchuk, and L. A. Vashchenko, *ibid.* **15**, 46 (1989).
[5] B. I. Verkin. V. G. Manzhelii, V. N. Grigoriev, V. A. Koval,' V. V. Pashkov, V. G. Ivantsov, O. A. Tolkacheva, N. M. Zvyagina, and L. I. Pastur, *Handbook of the Properties of Condensed Phases of Hydrogen and Oxygen* (Hemisphere Publishing Corp., New York, 1990).
[6] V. D. Natsik, S. V. Lubenets, and L. S. Fomenko, Fiz. Nizk. Temp. **22**, 337 (1996) [Low Temp. Phys. **22**, 264 (1996)].
[7] D. N. Bol'shutkin, Yu. E. Stetsenko, L. A. Indan, and A. A. Khudoteplaya, ''Investigations of creep of solid hydrogen and deuterium'' in *Physical Plastic Deformation Processes at Low Temperatures* (Naukova dumka, Kiev, 1974), p. 345.
[8] Yu. E. Stetsenko, D. N. Bol'shutkin, and L. A. Indan, Fiz. Tverd. Tela (Leningrad) **12**, 3636 (1970) [Sov. Phys. Solid State **12**, 2958 (1970)].
[9] V. V. Belotserkovskiĭ and M. A. Strzhemechnyĭ, Fiz. Nizk. Temp. **15**, 520 (1989) [Sov. J. Low Temp. Phys. **15**, 293 (1989)].
[10] L. S. Fomenko, V. D. Natsik, S. V. Lubenets, V. G. Lirtsman, N. A. Aksenova, A. P. Isakina, A. I. Prokhvatilov, M. A. Strzhemechnyĭ, and R. S. Ruoff, Fiz. Nizk. Temp. **21**, 465 (1995) [Low Temp. Phys. **21**, 364 (1995)].

Translasted by M. E. Aferieff

Oscillations localized near impurity layers in a layered crystal

V. I. Grishaev, M. A. Mamaluĭ, P. A. Minaev, E. S. Syrkin,[a] and S. B. Feodos'ev

B. I. Verkin Physicotechnical Institute for Low Temperatures, Ukrainian National Academy of Sciences, pr. Lenina 47, Khar'kov, 61103, Ukraine

(Submitted May 5, 2001)
Fiz. Nizk. Temp. **27**, 1287–1294 (November 2001)

It is shown that the interaction between vibrational modes polarized parallel and perpendicular to the layers in a strongly anisotropic layered crystal is very weak for frequencies above the van Hove frequency, which corresponds to a transition from closed isofrequency surfaces to surfaces which are open in the weak-coupling direction. Such mode quasisplitting results in quasi-two-dimensional behavior of phonons polarized along layers and quasi-one-dimensional behavior of phonons polarized in a direction perpendicular to the layers and localized near light or strongly coupled impurity atoms or monolayers. © *2001 American Institute of Physics.*
[DOI: 10.1063/1.1421462]

INTRODUCTION

The study of states localized near flat defects of a crystal structure is necessary for understanding the thermodynamic and kinetic properties of real crystals and for solving applied problems of acousto-, opto- and microelectronics (development of waveguide systems, highly sensitive sensors, and so on). A number of works where the resonance states localized in macroscopic-size multilayer crystal structures are studied on the basis of the theory of elasticity have appeared recently (see, for example, Ref. 1). However, because short-wavelength phonons make a large contribution to all vibrational characteristics of such compounds and further miniaturization of technical devices is a practical necessity it is definitely of interest to use the methods of the atomic dynamics of a crystal lattice to study resonance effects.

Here, it is especially important to study localized and quasi-localized vibrations in crystals with strong anisotropy of the interatomic interaction, specifically, in quasi-two-dimensional crystal structures. In the first place, such objects fall between three-dimensional lattices and low-dimensional structures, which differ qualitatively from three-dimensional structures by the formation conditions and characteristics of localized states. In the second place, weak coupling between atoms even in a single crystallographic direction, which is natural for such crystals, makes the localized states (especially near surfaces) very sensitive to external perturbations.

In the present paper oscillations localized near an impurity monolayer in the interior of a layered crystal are studied. It is shown that for sufficiently strong layered anisotropy the behavior of such oscillations is quasi-one-dimensional, which makes it possible to use exactly solvable one-dimensional models, taking into account only the ratios of the elastic moduli of the crystal, to describe states localized near flat defects.

In a strongly anisotropic layered crystal, where atoms of various layers are coupled with one another much more weakly than the atoms in a single layer, the interaction between vibrations polarized parallel and perpendicular to the layers is proportional to the squared small ''anisotropy parameter'' γ—the ratio of the weak interlayer interaction to the strong intralayer interaction ($\gamma \ll 1$).[2] (This phenomenon is usually termed quasisplitting of photon modes.) As a result, the isofrequency surfaces of phonon modes polarized along layers are strongly extended in the direction of weak coupling and are open in this direction in a very wide frequency range, where the spectral properties of the corresponding vibrations are essentially two-dimensional.[1)] The quasi-two-dimensional behavior of phonons polarized along layers signifies that virtually all of them (except extremely long wavelength) are localized in the plane of the layers. On the other hand the isofrequency surfaces corresponding to the phonon branch polarized in the weak-coupling direction (i.e., perpendicular to the layers) do not extend in any crystallographic direction and there are no quasi-low-dimensional singularities in the behavior of the corresponding phonons in an ideal layered crystal.

The flexural stiffness of the layers in virtually all layered crystals (see, for example, Refs. 3–14) is much smaller than the strong intralayer interaction and the maximum phonon frequency for the latter branch is appreciably lower than the maximum frequencies for the two other acoustic branches. It is of the same order of magnitude as the frequencies of the van Hove singularities, corresponding to the transition of isofrequency surfaces of these branches from closed to open, i.e. in this frequency range, where the two-dimensional nature of the phonons polarized in a planar layer is most strikingly manifested, vibrations of an ideal layered lattice which are polarized in the weak-coupling direction are essentially nonexistent. Such vibrations in this frequency range can arise as a result of the presence of definite defects—light or strongly-coupled impurity atoms or impurity monolayers. Indeed, in strongly anisotropic crystals the vibrations of light impurities[15,16] or atoms of light sublattices[17] are very strongly localized in the weak-coupling direction. In addition, the frequency of the corresponding pronounced resonance vibration, as a rule, lies precisely in the range where the isofrequency surfaces of vibrations polarized in the basal plane are open in the weak-coupling direction. Such strong localization of the vibrations in the frequency range where the phonon density of an ideal lattice is by no means small is

due to the absence, in this region of an ideal lattice, of vibrations polarized perpendicular to the layers and to the weak interaction of phonons with this polarization with two-dimensional phonons polarized in parallel to the layers. Quasi-one-dimensional singularities should appear in the behavior of these strongly localized vibrations. To prove this assertion we shall examine vibrations localized near an impurity monolayer in a strongly anisotropic layered crystal.

The most natural classification for describing localized states is one based on a representation of the vibrations as a superposition of diverging waves (in contrast to the conventional decomposition in terms of plane waves[18–21]). The $\mathcal{J}$-matrix method (or the recursion method)[22–25] completely corresponds to such a classification. This method does not employ explicitly the translational periodicity of the lattice and therefore its application to ideal and defective structures is essentially the same. In addition, the nondegeneracy of the spectrum of the operators (of the corresponding $\mathcal{J}$ matrices), which we employ here to describe the vibrations of the system, makes it possible to avoid many computational difficulties.

In the recursion method all spatial displacements of the atoms H are represented, using an appropriate choice of so-called generating vectors $\mathbf{h}_0^{(i)}$, as a direct sum of subspaces $H^{(i)}$ which are invariant under the operator $\hat{\mathcal{L}}$ describing the vibrations of the crystal:

$$\hat{\mathcal{L}}(\mathbf{r},\mathbf{r}')=\frac{\hat{\Phi}(\mathbf{r},\mathbf{r}')}{\sqrt{m(\mathbf{r})}m(\mathbf{r}')},$$

Here $\hat{\Phi}(\mathbf{r},\mathbf{r}')$ is the force-constants matrix, which describes the interaction between atoms occupying points with vectors $\mathbf{r}$ and $\mathbf{r}'$ and $m(\mathbf{r})$ and $m(\mathbf{r}')$ are the masses of these atoms. These subspaces, ordinarily termed cyclic, are linear hulls spanned by a sequence of linearly independent vectors $\{\hat{\mathcal{L}}^n\ \mathbf{h}_0^{(i)}\}_{n=0}^{\infty}$. Orthonormalizing this sequence we obtain an orthogonal basis $\{\mathbf{h}_n^{(i)}\}_{n=0}^{\infty}$ in which the operator $\hat{\mathcal{L}}^{(i)}$, engendered by the operator $\hat{\mathcal{L}}$ in the subspace $H^{(i)}$, is represented by a tridiagonal Jacobian matrix ($\mathcal{J}$ matrix). We shall designate its diagonal matrix elements as $a_n^{(i)}$ $(n=0,1,2,\ldots)$ and the off-diagonal elements as $b_n^{(1)}$. The index i enumerating the subspaces will be used only when various cyclic subspaces must be distinguished.

The distribution of the frequencies of the atomic vibrations in the system is ordinarily expressed in terms of the matrix elements of the Green's operator $\hat{\mathcal{G}}=(\lambda\hat{I}-\hat{\mathcal{L}})^{-1}$ (here λ is the squared frequency and the eigenvalue of the operator $\hat{\mathcal{L}}$). If $\mathbf{h}_0=\mathbf{r}|\mathbf{u}\rangle\in H$ is taken as the generating vector, i.e. the displacement $\mathbf{u}$ of an atom with radius vector $\mathbf{r}$, then the matrix element $\mathcal{G}_{00}(\lambda)\equiv(\mathbf{h}_0,\hat{\mathcal{G}}\mathbf{h}_0)$ will contain complete information about the frequency characteristics of the vibrations of the system, where each atom moves in the direction of the vector $\mathbf{u}$. The conditions for the existence of the imaginary part if $\mathcal{G}_{00}(\lambda)$ determine the limits of the bands of the continuous spectrum of the vibrations, and the magnitude of the imaginary part characterizes the frequency distribution of a given atom within these bands. The spectral density normalized to 1 is

$$\rho_0(\lambda)\frac{1}{\pi}\mathrm{Im}\,\mathcal{G}_{00}(\lambda). \tag{1}$$

The complete distribution function $g(\lambda)$ of the squared frequencies is the arithmetic-mean of the spectral densities generated by the linearly independent vectors $\mathbf{h}_0^{(i)}$.

The function $\mathcal{G}_{00}(\lambda)$ can have poles only outside the continuous spectrum, i.e. in the region where this function is purely real. These poles λ_d determine the squared discrete local frequencies. The residues of the Green's function at the poles

$$\mu_d^{(0)}=\mathrm{r\acute{e}s}_{\lambda=\lambda_d}\mathcal{G}_{00}(\lambda) \tag{2}$$

are the intensities (or weights) of the local vibrations.

The root-mean-square displacement of an atom with radius vector $\mathbf{r}$ as a function of the squared frequency and temperature is proportional to $\rho(\lambda)$ for vibrations with frequencies in a band of the continuous spectrum, and to $\mu_d^{(0)}$ for vibrations with discrete frequencies.

QUASISPLITTING OF PHONON MODES IN A STRONGLY ANISOTROPIC LAYERED CRYSTAL

If the displacements of one atom of a given model in directions parallel and perpendicular, respectively, to the basal plane are taken as the generating vectors $\mathbf{h}_\parallel$ and $\mathbf{h}_\perp$, then, because of the quasisplitting of the phonon modes polarized in these directions,[2] the corresponding spectral densities (1) will be identical, to within the squared small parameter γ, to the phonon densities of the corresponding branches. In what follows we shall treat the spectral functions as functions of the frequency ω and not its square $\lambda\equiv\omega^2$, i.e., the quantities $\nu_i(\omega)\equiv 2\omega\rho_i(\omega^2)$. They satisfy the relations

$$\begin{aligned}\nu_{x,y}(\omega)&\equiv\frac{1}{\pi}\mathrm{Im}(\mathbf{h}_\parallel,\hat{\mathcal{G}}\mathbf{h}_\parallel)=\frac{a^2c}{2(2\pi/\hbar)^3}\\&\times\sum_{q=1}^{2}\oint_{\omega_q(\mathbf{k})=\omega}\frac{dS_q}{|\nabla_k\omega_q(\mathbf{k})|}+O(\gamma^2);\\\nu_z(\omega)&\equiv\frac{1}{\pi}\mathrm{Im}(\mathbf{h}_\perp,\hat{\mathcal{G}}\mathbf{h}_\perp)=\frac{a^2c}{(2\pi\hbar)^3}\\&\times\oint_{\omega_3(\mathbf{k})=\omega}\frac{dS_3}{|\nabla_{\mathbf{k}}\omega_3(\mathbf{k})|}+O(\gamma^2),\end{aligned} \tag{3}$$

were, as usual (see, for example, Ref. 18), the integral extends over the isofrequency surface $\omega_q(\mathbf{k})=\omega$ $(q=1,2,3)$ and dS_q is an element of this surface.

The model of a strongly anisotropic layered lattice should describe the basic distinguishing features of the phonon spectrum of crystals in a given class. First and foremost is the presence of low-frequency short-wavelength acoustic phonons in the spectrum (see, for example,[2] Refs. 3–14): in the weak-coupling direction (in $\mathbf{k}$ space) all three acoustic branches have low frequencies right up to the boundary of the first Brillouin zone, and one of them, polarized in a direction perpendicular to the layers, remains low-frequency for $\mathbf{k}\subset x0y$ also. The dispersion law for this mode for wave vectors in the basal plane, for the case where the flexural

stiffness of the layers is much greater than the weak interlayer interaction, can be quasiflexural.[3,14,18,26] Of course, for the model at hand the conditions for translational and rotational invariance, stability, and transition to the long-wavelength limit of the equations of lattice dynamics in the equations for the theory of elasticity should be satisfied (see, for example, Refs. 18 and 19).

For the model we shall use a body-centered tetragonal lattice and we shall orient the four-fold axis in the direction of weak coupling. Since the atoms in the neighboring layers of such a lattice are shifted relative to one another in the direction of the basal plane, to describe the weak interlayer interaction it is sufficient to consider the central interaction of the nearest neighbors (not lying in the same plane)—the lattice will be stable. To describe the intralayer interaction we shall confine our attention to the interaction of the first and second neighbors in the basal plane, and we shall take account of the central and noncentral interaction between them. The force-constants matrices have the form

$$\mathbf{\Phi}_{ik}(a,0,0) = -\delta_{ik}[\alpha_{\parallel}^{(1)}\delta_{i,x} + \beta^{(1)}(\delta_{i,y} + \delta_{i,z})];$$

$$\mathbf{\Phi}_{ik}(a,a,0) = -\begin{pmatrix} \alpha_{\parallel}^{(2)} & \xi & 0 \\ \xi & \alpha_{\parallel}^{(2)} & 0 \\ 0 & 0 & \beta^{(2)} \end{pmatrix};$$

$$\mathbf{\Phi}_{ik}\left(\frac{a}{2},\frac{a}{2},\frac{a\varepsilon}{2}\right) = -\alpha_{\perp}\begin{pmatrix} 1 & 1 & \varepsilon \\ 1 & 1 & \varepsilon \\ \varepsilon & \varepsilon & \varepsilon^2 \end{pmatrix}.$$

Here a and $c \equiv a\epsilon$ are, respectively, the interatomic distance in the basal plane and in the direction of the four-fold axis. The parameters $\beta^{(1)}$ and $\beta^{(2)}$ describe the noncentral interaction between the first and second neighbors in the basal plane. The condition that the lattice-dynamics equations become the equations of elasticity theory gives the following relation between these parameters: $\beta^{(1)} = -2\beta^{(2)} \equiv \beta$. The same relation follows from the conditions that there be no stresses at the boundary oriented along the basal plane, and we can neglect the relaxation of the force constants on such a free surface.

The parameters $\alpha_{\parallel}^{(1)}$ and $\alpha_{\perp}$ describe, respectively, the central interaction of the nearest neighbors in the basal plane (the strongest in the lattice) and the weak interlayer interaction (also purely central), where $\gamma \simeq \alpha_{\perp}/\alpha_{\parallel}^{(1)}$. The quantity $\alpha_{\parallel}^{(2)}$ characterizes the central interaction of the second neighbors in the same plane, and the parameter $\xi = \alpha_{\parallel}^{(2)} - \beta/2$. This model is stable for positive values of $\alpha_{\parallel}^{(1)}$, $\alpha_{\perp}$, ξ, $\alpha_{\parallel}^{(2)}$, and $0 < \beta < 1$.

The matrix $\Phi_{ik}(0,0,0)$ is obtained from translational invariance. The symmetry operations of the point group D_{4h} can be used to find all other force-constants matrices from those described above.

We shall now analyze the dependence of the quantities $\nu_i(\omega)$ on the parameter γ. All other parameters are fixed: $\alpha_{\parallel}^{(2)} = 0.2\alpha_{\parallel}^{(1)}$, $\beta = 0.05\alpha_{\parallel}^{(1)}$, and $c/a = 2$; the frequency is conveniently measured in terms of $\omega_0 = \sqrt{\alpha_{\parallel}^{(1)}/m}$. Figure 1 shows the evolution of the spectral densities $\nu_{x,y}$. Curve *1* corresponds to $\gamma = 0.03$, which for our choice $c/a = 2$ corresponds to a weakly anisotropic crystal (such as PbI_2). The curve *2* ($\gamma = 0.01$) corresponds to layered crystals where the ratios of the elastic constants $C_{33}/C_{11} \sim C_{44}/C_{11} - 0.1$, which is characteristic for many layered compounds (GaSe, GaS, In_4Se_3, and so on). The curves *3* and *4* correspond to $\gamma = 0.003$ and $\gamma = 0.001$ (even stronger anisotropy—such as in graphite).

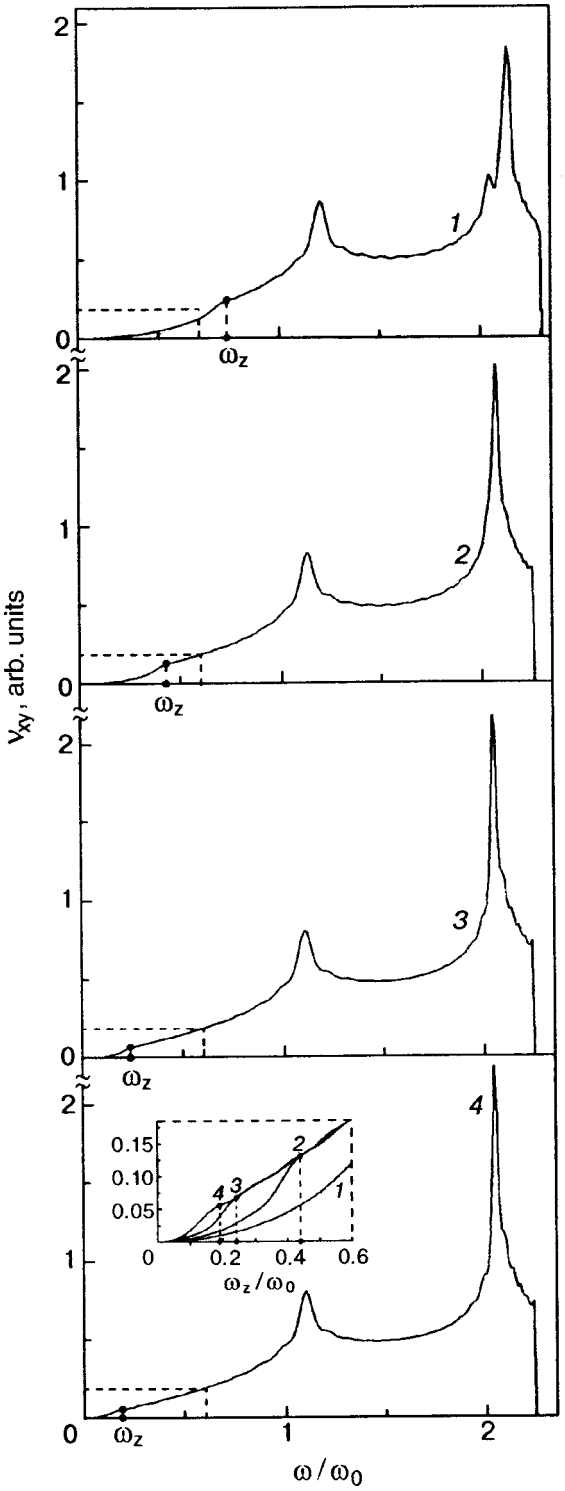

FIG. 1. Evolution of the spectral densities $\nu_{x,y}$ as a function of the anisotropy of the interlayer interaction (parameter γ): $\gamma = 0.03$ (*1*), 0.01 (*2*), 0.003 (*3*), and).001 (*4*).

The spectral densities $\nu_{x,y}(\omega)$ are Debye-shaped up to the frequency ω_z ($\omega_z^2 = 16\alpha_{\perp}/m$) at which the isofrequency surfaces become open in the weak-coupling direction, pos-

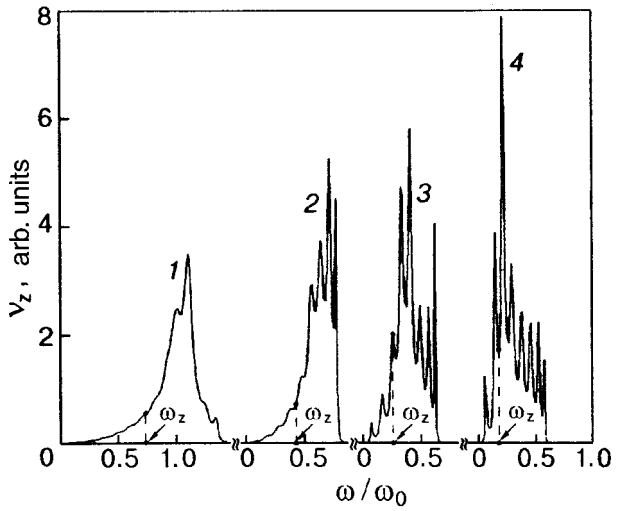

FIG. 2. Evolution of the spectral densities ν_z as a function of the parameter γ (the numbering of the curves is the same as in Fig. 1).

sess a ''kink'' van Hover singularity of this frequency (their curves near this singularity are shown in the inset on an enlarged scale), have a pronounced two-dimensional character, and are essentially independent of $\alpha_\perp$. The maximum vibrational frequency of the lattice is essentially independent of $\alpha_\perp$. The ''two-dimensional'' van Hove singularities, corresponding to a transition from closed to open isofrequency surfaces and vice versa in the direction of propagation of a transverse wave in the basal plane (i.e. the direction k_y for the wave polarized along the abscissa and direction k_x for a wave polarized along the ordinate), are very sharp peaks (when there is no interaction between the layers these van Hove singularities are logarithmic).

A sharp low-frequency peak forms in the spectral densities $\nu_z(\omega)$ with decreasing interlayer interaction (Fig. 2). This peak determines most anomalies of the vibrational thermodynamic properties of such systems (see, for example, Refs. 30 and 31). For $\alpha_\perp < \beta$ the topology of the low-frequency surfaces of a vibrational mode polarized perpendicular to the layers is determined primarily by the quasiflexural term. The strong anisotropy of this term in the basal plane (the isofrequency surfaces extend along the coordinate axes) gives rise to oscillations of the corresponding spectral densities (curves *2–4*).

QUASI-ONE-DIMENSIONAL CHARACTER OF OSCILLATIONS LOCALIZED NEAR AN IMPURITY OR AN IMPURITY MONOLAYER

Quasi-two-dimensionality of the spectral densities $\nu_{x,y}(\omega)$ is observed at frequencies $\omega \gtrsim \omega_z$, i.e., primarily outside the localization region of the spectral density $\nu_z(\omega)$. Consequently, quasi-one-dimensionality is by no means characteristic for vibrations of an ideal layered lattice which are polarized in a direction perpendicular to the layers and interact weakly with quasi-two-dimensional phonons polarized in the basal plane (see Fig. 2).

At the same time the correspondingly polarized vibrations of defect atoms (impurities and impurity monolayers) can easily possess frequencies greater than the van Hove frequency ω_z. In this case their behavior, specifically, the dependence of the frequency on the parameters of a defect, i.e., on the variation of the mass and the force interaction (in this case the interlayer interaction), should be similar to the behavior of *local* vibrations lying outside the bands of the continuous spectrum of a linear chain. It is obvious that in this case the frequency range of localization of the spectral density $\nu_z(\omega)$ will play the role of a band of the continuous spectrum of a linear chain. The impurity distinguished by mass and force interaction in an infinite linear chain can result in the appearance of two local vibrations[32,33]

$$\omega_{l1}^2 = \frac{(\omega^*)^2}{8}\,\frac{1+\eta}{1+\epsilon}\left\{3+\varepsilon-\frac{1-\varepsilon}{\eta}+\frac{3+\varepsilon}{\eta}\times\left\{(1+\eta)\left[\left(\frac{1-\varepsilon}{3+\varepsilon}\right)^2+\eta\right]\right\}^{1/2}\right\};$$
$$\omega_{l2}^2 = (\omega^*)^2\,\frac{(1+\eta)^2}{4\eta}, \tag{4}$$

where ω^* is the upper limit of the band of the continuous spectrum of a linear chain; ε and η are the relative change in mass and the force constant, respectively. Here, the impurity itself vibrates only with one of the local frequencies ω_{l1}, and the second local frequency ω_{l2} corresponds to an antiphase displacement of the nearest neighbors of the impurity (the impurity atom itself is at rest).

Let a light monolayer, coupled with the layers of the main lattice more strongly than the coupling within the layer itself, be embedded in a layered crystal described by the model considered above, i.e., a defect system consisting of three neighboring rows in a layered crystal. In the monatomic lattice approximation, describing the main distinguishing features of the phonon spectrum of strongly anisotropic layered crystals, this simulates, for example, the embedding of a light alkali metal in a layered semiconductor. As a rule, here, $\tilde{c}/\tilde{a} < c/a$ (the *tilda* designates the properties of the impurity atoms). Let $\tilde{m}/m = 0.5$, $\tilde{a}/a$ and $\tilde{c}/a = 1.5$. Since in most cases the light atoms possess the smaller atomic radius, as a rule,[34] $\tilde{\alpha}_\parallel^{(1)} < \alpha_\parallel^{(1)}$. We shall choose the following values of the force constants in the defect system: $\tilde{\alpha}_\parallel^{(1)} = 0.5\alpha_\parallel^{(1)}$; $\tilde{\alpha}_\parallel^{(2)} = 0.1\alpha_\parallel^{(1)}$; $\tilde{\beta} = 0.04\alpha_\parallel^{(1)}$; and, $\tilde{\alpha}_\perp > \alpha_\perp$.

Figures 3a–3d correspond to different values of the interaction between a defective monolayer and the main lattice ($\tilde{\alpha}_\perp$): a—$\tilde{\alpha}_\perp = 0.1\alpha_\parallel^{(1)}$; b—$\tilde{\alpha}_\perp = 0.125\alpha_\parallel^{(1)}$; c—$\tilde{\alpha}_\perp = 0.15\alpha_\parallel^{(1)}$; and, d—$\tilde{\alpha}_\perp = 0.175\alpha_\parallel^{(1)}$. All four figures show the relations (4) $\omega_{l1}(\eta)$ (for $\varepsilon \equiv (\tilde{m}-m)/m = -0.5$) and $\omega_{l2}(\eta)$ (curves *1* and *2*). The figures also show the curves of the spectral densities (as functions of the frequency) generated by displacements in the weak-coupling direction: the atoms in the impurity monolayer (curves *3*) and layers neighboring the impurity layer in antiphase to one another (curves *4*) (ω_m—upper boundary of the band of the continuous spectrum of an ideal layered crystal). Curves *3* contain sharp resonance peaks corresponding to vibrations localized primarily on the impurity monolayer itself. The propagation of these vibrations in the plane of the monolayer (for example, as a result of a noncentral interactomic interaction) gives rise to an additional (''satellite'') peak, whose height decreases sharply when the frequency of the main peak lies outside the

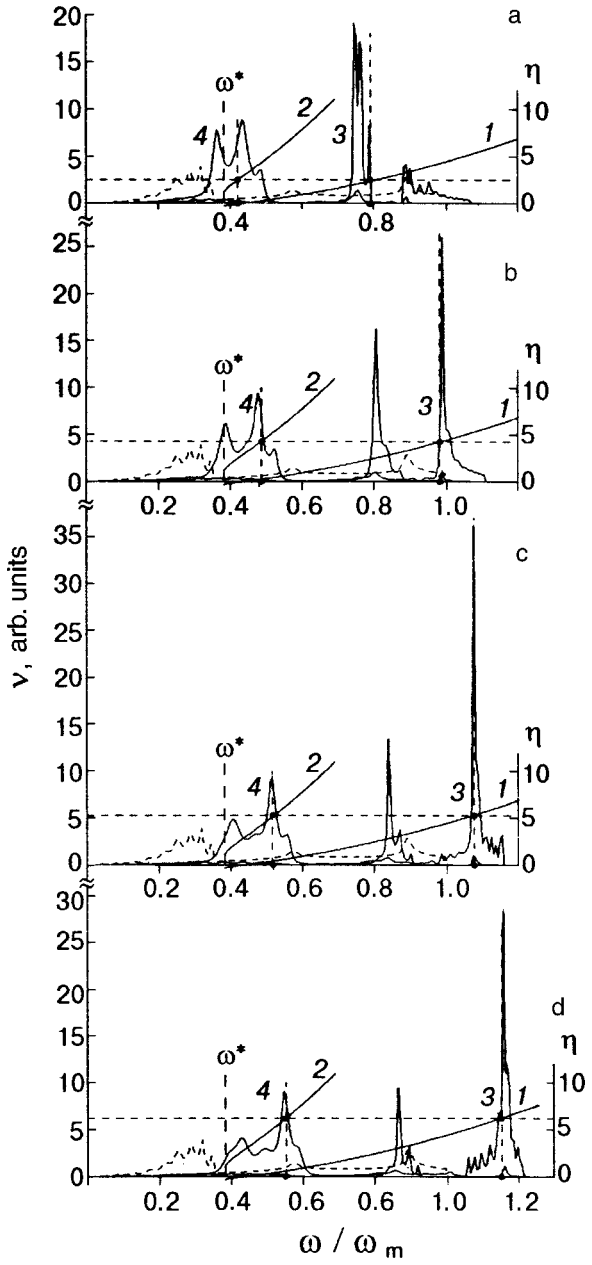

FIG. 3. Illustration of the quasi-one-dimensional behavior of vibrations localized near a light ($\tilde{m}/m=0.5$) strongly coupled ($\tilde{\alpha}_\perp \gg \gamma\alpha_\parallel^{(1)}$)impurity monolayer in the interior of a strongly anisotropic layered crystal ($\gamma=0.01$): $\tilde{\alpha}_\perp=0.1\alpha_\parallel^{(1)}$ (a), $0.125\alpha_\parallel^{(1)}$ (b), $0.15\alpha_\parallel^{(1)}$ (c), and $0.175\alpha_\parallel^{(1)}$ (d). Curves *1* and *2*—the functions (4) $\omega_{l1}(\eta)$ (with $\varepsilon\equiv(\tilde{m}-m)/m=-0.5$) and $\omega_{l2}(\eta)$; curves *3* and *4*—spectral densities $\nu(\omega)$ generated by displacements in the direction of weak coupling of the atoms in the impurity monolayer and layers neighboring the impurity monolayer, in antiphase with one another, respectively. The broken curves show the total phonon density of an ideal lattice.

band of the continuous spectrum of an ideal crystal. Vibrations with frequencies of both of these peaks are essentially absent from the frequency spectra of atoms of other layers (even layers close to the impurity monolayer). The large broadening of the quasilocal peaks on the curves *4* are also due to propagation of vibrations in the plane of the corresponding layers.

The effective maximum frequency, which appears in the expression (4) as a factor, is chosen according to the frequency of the local vibration generated by a light isotopic impurity in the three-dimensional structure of interest to us. Such a vibration is very highly localized. The frequency is noted by the symbol $\omega^*\approx\omega_m\sqrt{C_{33}/C_{11}}$ (the ratio of the elastic moduli $C_{33}/C_{11}\sim 0.1$, just as for many layered semiconductors).

The frequencies of the quasilocal peaks in the curves *3* and *4* agree well with the frequencies ω_{l1} and ω_{l2} for the same value of the parameter η, which for a layered crystal plays the role of the effective change in the interlayer interaction. This identity shows that the vibrations localized near an impurity monolayer are quasi-one-dimensional. The character of the propagation of vibrations in the planes of defective layers (for example, will the ''satellite'' peaks in the curves *3* in Fig. 3d always be sharp?) depends on the interatomic interaction in the plane of the layer (i.e. on the model chosen). However, the frequency of the localized vibrations is essentially model-independent and are determined by the expressions (4), describing the frequencies of local vibrations in a linear chain, even though local frequencies outside the bands of the continuous spectrum are poles of the Green's function of a linear chain and the quasilocal peaks in the corresponding spectral densities of a layered crystal lie in a band of its continuous spectrum and cannot be such poles in our case.

CONCLUSIONS

In summary, quasisplitting of vibrational modes polarized parallel and perpendicular to layers occurs in a strongly anisotropic layered crystal. At frequencies above the van Hove singularity frequency ω_z, corresponding to a transition from closed isofrequency surfaces to ones that are open in the weak-coupling direction, the phonons polarized parallel to the layers are essentially two-dimensional.

In an ideal layered lattice the frequencies of the phonons polarized in the weak-coupling direction are mainly below ω_z and consequently no one-dimensional singularities can be observed in their behavior. At the same time the vibrations of impurity atoms or impurity monolayers having the same polarization can possess frequencies above ω_z, and consequently they can be quasi-one-dimensional.

If the interlayer interaction is stronger for impurity atoms (or atoms of impurity monolayers) than for atoms in the main layered lattice, then quasilocal vibrations with frequencies above ω_z (but below the upper limit of a band of the continuous spectrum of an ideal crystal) will be due to not only the corresponding displacements of the impurity atoms themselves but also the antiphase displacement of atomic layers neighboring the impurity layers, which together with the impurity monolayer form a defect system, in this direction.

Both types of localized vibrations will be quasi-one-dimensional. Their properties (the frequency and the degree of localization) will essentially be independent of the geometry of the layers and the character of the intralayer interaction, i.e. the lattice properties that are due to the specific model under study. Such localized vibrations can be described using the exact analytical expressions (4) obtained for models of linear chains with impurities.

[a)]E-mail: syrkin@ilt.kharkov.ua

[1)]In Ref. 2 this is illustrated for the behavior of van Hove singularities, which are extremely sensitive to the interatomic interaction.

[2)]In addition, low-frequency optical phonons appear in the vibrational spectrum of strongly anisotropic crystals with a complex lattice. See, for example, Refs. 27–29 for a description of their contribution to the vibrational characteristics and the influence of the flexural stiffness of the layers on their behavior.

[1] A. N. Darinski and M. Weihnacht, J. Appl. Phys. **88**, 471 (2000).
[2] A. M. Kosevich, E. S. Syrkin, and S. B. Feodosyev, Phys. Low-Dimens. Semicond. Struct. **3**, 47 (1994).
[3] R. Niclow, N. Wakabayashi, and H. G. Smith, Phys. Rev. B **5**, 4951 (1972).
[4] N. Wakabayashi, H. G. Smith, and R. Shanks, Phys. Lett. A **50**, 367 (1974).
[5] N. Wakabayashi, H. G. Smith, and R. Niclow, Phys. Rev. B **12**, 659 (1975).
[6] W. P. Velon, R. Sherm, and C. Wetlier, Solid State Commun. **15**, 391 (1974).
[7] S. Jandl, G. Z. Brebner, and B. M. Powell, Phys. Rev. B **13**, 686 (1976).
[8] D. E. Monton, J. D. Axe, and F. J. Di Savlo, Phys. Rev. Lett. **34**, 734 (1975).
[9] W. G. Stirling, B. Dorner, and J. D. N. Choeke, Solid State Commun. **18**, 931 (1976).
[10] B. M. Powell, S. Jandl, and F. Levy, J. Phys. C **10**, 3039 (1977).
[11] A. Pelian, K. Kane, and J. Rossat-Mignod, J. Phys. (Paris), Colloq. C **5**, 42 (1981).
[12] B. Dorner, R. E. Ghog, and C. Harbeke, Phys. Status Solidi B **73**, 655 (1976).
[13] G. Z. Brebner, S. Jandl, and B. M. Powell, Nuovo Cimento B **38**, 263 (1977).
[14] H. G. Smith and N. Wakabayashi, in *Dynamics of Solids and Liquids by Neutron Scattering*, edited by S. W. Lovesey and T. Springer (Springer-Verlag, New York, 1980), p. 97.
[15] S. V. Feodos'ev and E. S. Syrkin, Fix. Nizk. Temp. **7**, 1214 (1981) [Sov. J. Low Temp. Phys. **7**, 50 (1981)].
[16] M. A. Ivanov, A. M. Kosevich, E. S. Syrkin, I. A. Gospodarev, Yu. V. Syrkin, and S. V. Feodos'ev, Fiz. Nisk. Temp. **19**, 434 1993) [Low Temp. Phys. **19**, 305 (1993)].
[17] S. B. Feodosyev, I. A. Gorpodarev, A. M. Kosevich, and E. S. Syrkin, Phys. Low-Dimens. Semicond. Struct. **10/11**, 209 (1995).
[18] A. M. Kosevich, *The Crystal Lattice. Phonons, Solitons, Dislocations* (Wiley-Vch, Berlin, 1999).
[19] A. A. Maradudin, E. W. Montroll, G. N. Weiss, and I. P. Ipatova, *Lattice Dynamics and Models of Interatomic Forces, Springer Series in Solid State Sciences* (Springer-Verlag, New York, 1982), Vol. 34.
[20] G. Leibfried and F. Breur, *Point Defects in Metals. Introduction to the Theory* (Springer-Verlag, New York, 1978).
[21] H. Böttger, *Principles of the Theory of Lattice Dynamics* (Academie-Verlag, Berlin, 1983).
[22] V. I. Peresada, in *Physics of Condensed States* (Khar'kov, 1968), No. 2, p. 172.
[23] V. I. Peresada and V. N. Afanas'ev, Zh. Éksp. Teor. Fiz. **58**, 135 (1970) [Sov. Phys. JETP **31**, 98 (1970)].
[24] V. I. Peresada, V. N. Afanas'ev, and V. S. Borovikov, Fiz. Nizk. Temp. **1**, 461 (1975) [Sov. J. Low Temp. Phys. **1**, 227 (1975)].
[25] R. Haydock, in *Solid State Physics*, edited by H. Ehrenreich, F. Seitz, and D. Turnbull (Academic Press, New York, 1980), p. 216.
[26] I. M. Lifzhits, Zh. Éksp. Teor. Fiz. **22**, 475 (1952).
[27] E. S. Syrkin and S. B. Feodos'ev, Fiz. Nizk. Temp. **8**, 760 (1982) [Sov. J. Low Temp. Phys. **8**, 381 (1982)].
[28] E. S. Syrkin, S. B. Feodos'ev, and O. Ya. Shamfarova, Fiz. Nizk. Temp. **17**, 745 (1991) [Sov. J. Low Temp. Phys. **17**, 393 (1991)].
[29] S. B. Feodos'ev and E. S. Syrkin, Fiz. Nizk. Temp. **9**, 528 (1983) [Sov. J. Low Temp. Phys. **9**, 268 (1983)].
[30] A. M. Gurevich, B. Ya. Sukharevskiĭ, and A. V. Alapina, Fiz. Nizk. Temp. **8**, 1111 (1982) [Sov. J. Low Temp. Phys. **8**, 562 (1982)].
[31] E. S. Syrkin and S. B. Feodos'ev, Fiz. Nizk. Temp. **8**, 1115 (1982) [Sov. J. Low Temp. Phys. **8**, 564 (1982)].
[32] E. S. Syrkin and S. B. Feodos'ev, Fiz. Nizk. Temp. **20**, 586 (1994) [Low Temp. Phys. **20**, 463 (1994)].
[33] M. A. Mamaluĭ, E. S. Syrkin, and S. B. Feodos'ev, Fiz. Nizk. Temp. **25**, 72 (1999) [Low Temp. Phys. **25**, 72 (1999)].
[34] S. B. Feodosyev, I. A. Gospodarev, M. A. Mamalui, and E. S. Syrkin, J. Low Temp. Phys. **111**, 441 (1998).

Translated by M. E. Alfrieff.

Crowdions in atomic cryocrystals and metals with fcc and bcc lattices

V. D. Natsik and S. N. Smirnov

B. I. Verkin Physicotechnical Institute for Low Temperatures, Ukrainian National Academy of Sciences, pr. Lenina 47, Khar'kov, 61103, Ukraine

E. I. Nazarenko

V. N. Karazin Khar'kov National University, pl. Svobody, 4, Khar'kov, 61007, Ukraine

(Submitted July 3, 2001)
Fiz. Nizk. Temp. **27**, 1295–1307 (November 2001)

Numerical values are obtained for the parameters of the crystal-field potentials and crowdions (self-energy, effective mass, characteristic length) for Ar and Kr fcc cryocrystals, Cu and Al fcc metals, and α- and δ-Fe bcc metals. The calculations are performed assuming that the interatomic interaction in the crystals can be described by empirical Lenard–Jones and Morse pair potentials. A new algorithm is developed and used for calculating the crystal-field potentials. The algorithm is based on a representation of the crystal lattice as a collection of parallel atomic rows. An analytic expression in the form of a trigonometric series is obtained for the potential describing the interaction between an atom in a close-packed row and the crystal matrix. An explicit analytic expression is also obtained for the energy parameter characterizing the interatomic interaction inside a distinguished row. It is shown that the main condition for weak coupling between close-packed rows and the crystal matrix, admitting the existence of crowdions and the application of the long-wave approximation for describing crowdions, is satisfied in all crystals investigated. © *2001 American Institute of Physics.* [DOI: 10.1063/1.1421463]

INTRODUCTION

Crowdion lattice excitations are one of the interesting objects of investigation in modern crystal physics. Crowdions can play a large role in the dynamics and kinetics of radiation defects, diffusion processes, and certain phenomena of inelastic deformation of crystals.[1–8] In the modern interpretation a crowdion is a nonlinear solitary wave of displacements which arises in close-packed atomic rows and is considered to be an example of a topological soliton.[9–12]

In Ref. 13 the problem of crowdion motion is formulated as a dynamical problem of a three-dimensional crystal lattice. It is shown that the correct separation of nonlinear crowdion excitations and linear elastic deformations in a three-dimensional crystal is possible only in the long-wavelength approximation. This approximation corresponds to crowdions with sufficiently large width $\lambda \gg b$ and sufficiently low velocity $V \ll c$ (b and c are, respectively, the characteristic values of the interatomic distance and the sound velocity in a crystal). When the requirements indicated above are satisfied, it is possible to pass to the continuum limit in the equations describing crowdions, crowdion excitations can be distinguished against the background of small elastic deformations of the crystal, and the description of crowdions can be reduced to the analysis of solitary waves in a one-dimensional Frenkel'–Kontorov crystal. The Frenkel'–Kontorov model of a one-dimensional crystal consists of a chain of strongly interacting atoms which undergo one-dimensional motion on a stationary periodic substrate which creates a relatively weak potential field.[9,10,14,15] When this model is compared with a real crystal, it is assumed that the mobile chain of atoms corresponds to a distinguished atomic row and the periodic potential of the substrate simulates the interaction of this row with the crystal matrix.

In Ref. 13 it is shown that in describing crowdions it can be assumed, to a first approximation, that the crystal matrix is absolutely stiff, i.e. its deformations can be neglected. Then, it is convenient to use the function $u(x,t)$ describing the longitudinal displacement field of the atoms from their equilibrium positions in an ideal crystal, which depends on the coordinate x along the chain and the time t, as the natural dynamic field variable. It is assumed that the directions of the axis $0x$ and the displacement $u(x,t)$ are given by the elementary translations vector **b** of the crystal along the atomic chain under study. The functional energy corresponding to this approximation is

$$H = \frac{1}{b}\int_{-\infty}^{\infty}\left[\frac{m_a}{2}(\dot{u})^2 + \frac{w}{2}(u')^2 + \Phi(u)\right]dx. \tag{1}$$

Here m_a is the mass of the atoms in the distinguished row, w is the interatomic interaction parameter inside the distinguished row, $\Phi(u)=\Phi(u+b)$ is the periodic potential of the crystal field for atoms in the distinguished row (substrate potential), $\dot{u}=\partial u/\partial x$, and $u'=\partial u/\partial x$.

In the present paper we shall consider simple crystals consisting of identical atoms, the interaction between which at a distance **r** is described by a pair potential $U(\mathbf{r})$. In this case the expressions for the parameter w and the potential $\Phi(u)$ are[13]

$$w = \frac{1}{2}\sum_{\rho}\ \rho_i\rho_k\frac{\partial^2 U(\rho)}{\partial\rho_i\partial\rho_k}; \tag{2}$$

$$\Phi(u)=\sum_{\mathbf{R}}\,[U(\mathbf{R}-\boldsymbol{\tau}u)-U(\mathbf{R})],\quad \tau=\frac{\mathbf{b}}{b}. \tag{3}$$

Here the summation extends over the equilibrium positions ρ of the atoms in the distinguished row and the atoms $\mathbf{R}$ of the matrix. The second term in brackets in Eq. (3) defines the reference point for the potential energy, which is chosen so that the potential is nonnegative $\Phi(u)\geqslant 0$.

In our recently published paper[16] the structures and dynamical properties of crowdions were analyzed for an arbitrary periodic potential $\Phi(u)$. The analysis shows that the structure of a crowdion can be described by the solution $u(x,t)$ in the form of a kink characterized by a set of parameters λ_0, λ_m, and λ_m^*:

$$\lambda_0=\sqrt{w/\Phi''(0)},\quad \lambda_m=\sqrt{w/|\Phi''(b/2)|},$$

$$\lambda_m^*=\sqrt{2\Phi_m/|\Phi''(b/2|}. \tag{4}$$

Here $\Phi''(u)=(d^2du^2)\Phi(u)$ and $\Phi_m=\Phi(b/2)$ is the height of the barrier. It was established that for a wide class of single-barrier symmetric potentials $\Phi(u)$ satisfying the condition for applicability of the continuum approximation but differing from the curvature at the minimum $(u=0)$ and maximum $(u=b/2)$ points the relation

$$\lambda_s=2\left[\lambda_0+\lambda_m \arcsin\frac{b}{4\lambda_m^*}\right] \tag{5}$$

can be used to estimate the characteristic width of a static kink λ_s. The second term in Eq. (5) determines the width of the central part of the kink and the first term determines the extent of the ''wings'' of the kink. When the parameter λ_s is used to characterize a crowdion the specific nature of crowdion excitations in real three-dimensional crystals should be taken into account: since the deformation fields of a crowdion at large distances from its center have power-law asymptotic behavior,[13,17] the parameter λ_s is the characteristic size of the crowdion nucleus in a three-dimensional crystal.

A crowdion excitation (just as any stable solitary wave) can be treated as a particle possessing an intrinsic field energy E_s and effective rest mass m_s. For a static crowdion in the Frenkel'–Kontorov model[16] these quantities are given by the expressions

$$E_{s0}=\frac{1}{b}\int_0^b\sqrt{2w\Phi(u)}du,\quad m_s=\frac{m_a}{b}\int_0^b\sqrt{2\Phi(u)/w}du. \tag{6}$$

Taking account of the elastic compliance (deformability) of the crystal matrix could result in a substantial renormalization of the values of these characteristics of a crowdion.[13]

The use of the general assumptions and conclusions of the theory of crowdions to interpret the crowdion-induced physical effects presumes further elaboration of the theory and, first and foremost, that the following problems are solved:

the criteria for the existence of crowdion excitations in specific crystal structures have been established;

the conditions admitting the use of the Frenkel'–Kontorov model and the long-wavelength approximation for describing crowdions in particular specific crystals are known;

the numerical values of the parameter w, the explicit expression for the crystal field potential $\Phi(u)$, and numerical estimates for geometric and energy characteristics of crowdions have been obtained for specific crystals.

Thus far only the first steps toward solving the problems listed above have been made. Specifically, computer calculations of the energies of static crowdion configurations for several fcc and bcc crystals have been performed by molecular-dynamics methods.[2,18–20]

In the present paper we perform a comprehensive analysis of all questions enumerated above for simple atomic fcc and bcc crystals. The analysis is based on the use of classical empirical potentials to describe the interatomic interaction in crystals: the Lennard–Jones potential and the generalized Morse potential. Analytic expressions for the parameter w and the crystal-field potential $\Phi(u)$ are obtained for close-packed atomic rows in such crystals; it is shown that the condition of weak coupling of these rows with the crystal matrix is satisfied; and, an algorithm is proposed for calculating the energy, the effective mass, and the width of crowdions in these rows. The influence of the form of the interatomic interaction potential and the temperature dependence of its parameters on the crowdion parameters is discussed. FCC Ar and Kr cryocrystals, fcc Cu and Al metals, and the bcc α- and δ-Fe metals are chosen as specific examples for which numerical values of the basic parameters of the crystal field and crowdions are obtained.

In the present work a new algorithm, based on a representation of a crystal lattice as a collection of parallel atomic rows is developed and applied used to calculate the crystal-field potentials. This method for calculating the crystal-field potentials admits a natural generalization and can be used for complex multiatomic lattices.

1. ANALYSIS OF THE INTERACTION OF CLOSE-PACKED ATOMIC ROWS WITH A CRYSTAL MATRIX

Let us consider fcc and bcc monatomic crystals where the close-packed atomic rows are oriented along crystallographic directions of the type $\langle 110\rangle$ and $\langle 111\rangle$, respectively. We shall assume that a centrosymmetric pair potential $U(|\mathbf{r}-\mathbf{r}'|)$ ($\mathbf{r}$ and $\mathbf{r}'$ are the coordinates of two arbitrary atoms) describes the interatomic interaction in the crystals. This assumption is considered to be acceptable for a microscopic description of the physical properties of solidified inert gases and simple metals. As a rule, it is widely used in computer simulation of atomic structures of such crystals and defects in them.[21–24]

Let us select an individual close-packed atomic row where the crowdion excitation will be studied: in what follows we shall call this row the reference row. The crystal field $\Phi(u)$ for atoms of a given row, written as a sum (3), is best calculated as follows:

— the crystal matrix is represented as a collection of atomic rows oriented parallel to the reference row;

— summation is performed over the sites in one such row;

— summation is performed over a sequence of rows.

The crystal–geometric substantiation of the proposed procedure is given in the Appendix. Here we note only the main circumstance that determines its effectiveness: the potential $\Phi(u)$ is a periodic function so that it is convenient to represent it as a Fourier series, and the proposed procedure makes it possible to obtain such a representation in an explicit form comparatively easily.

For the calculations we shall use a cylindrical coordinate system with polar axis $0u$ oriented along the reference row. We shall find the potential $\varphi(u-hb, r_\perp)$ which an atomic row oriented parallel to $0u$, possessing a period b, and lying at a distance $r_\perp$ from $0u$ generates at a point u on $0u$ as:

$$\varphi(u-hb, r_\perp)=\sum_{n=-\infty}^{\infty} U(\sqrt{r_\perp^2+(u-hb-nb)^2}),$$

where h is the fractional part of the atomic coordinate on the $0u$ axis. Using the well-known Poisson summation formula[25]

$$\sum_{n=-\infty}^{\infty} f(n)=\sum_{n=-\infty}^{\infty}\int_{-\infty}^{\infty} f(z)\mathrm{e}^{2\pi inz}dz$$

and performing some simple transformations we obtain the following expression for φ in the form of a Fourier series:

$$\varphi(u-hb, r_\perp)=\frac{1}{2}\varphi_0(r_\perp)+\sum_{n=1}^{\infty}\varphi_n(r_\perp)\cos\left(\frac{2\pi n(u-hb)}{b}\right), \quad (7)$$

where

$$\varphi_n(r_\perp)=\frac{4}{b}\int_0^{\infty} U(\sqrt{r_\perp^2+\xi^2})\cos\left(\frac{2\pi n\xi}{b}\right)d\xi,$$
$$n=0,1,2,\ldots\ . \quad (8)$$

The relation (7) also makes it possible to write in the form of a Fourier series the crystal-field potential $\Phi(u)$ for atoms in the reference row, determined by the expression (3). As shown in the Appendix, the reference row can be viewed as an axis of a discrete set of coaxial cylindrical surfaces (coordination cylinders) with numbers N and radii $r_\perp=R_N$, where atomic rows of the same type, corresponding to the matrix, are located parallel to one another. The coordination cylinder with number N contains Z_N atomic rows, which can be shifted with respect to the reference row by a fractional part of the period b, determined by the shift coefficient h_N. The quantities R_N, Z_N, and h_N are crystal–geometric parameters of the lattice; their values for reference rows of the type $\langle 110\rangle$ in a fcc lattice and $\langle 111\rangle$ in a bcc lattice are presented in the Appendix. The arguments given above and the relation (7) make it possible to represent the potential $\Phi(u)$ as a sum of the contributions $\varphi(u-h_Nb, R_N)$ due to a sequence of coordination cylinders.

The advantage of the method of summing over coordination cylinders when calculating the crystal field potential for atoms of a close–packed row in a fcc lattice is fully utilized, since all atomic rows belonging to the same coordination cylinder have the same shifts relative to the reference row and make the same contribution to the desired potential $\Phi(u)$. For a bcc lattice, the atomic rows within an individual coordination cylindrical are divided into two groups with different shifts with respect to the reference row; this makes the calculation somewhat more complicated. Despite this difference, the potential $\Phi(u)$ can be written in the same series form for both types of lattices:

$$\Phi(u)=\sum_{n=1}^{\infty}\Phi_n\sin^2\left(\frac{\pi nu}{b}\right), \quad (9)$$

where the coefficients are given by the relation

$$\Phi_n=-2\sum_{N=1}^{\infty} Z_N\varphi_n(R_N)\cos(2\pi nh_N). \quad (10)$$

The values of the parameters b, R_N, Z_N, and h_N, of course, are different for different types of lattices (see Appendix). Specifically, for a fcc lattice $b=d^{(\mathrm{fcc})}$ is the period of an atomic row of the type $\langle 110\rangle$; for a bcc lattice $b=d^{(\mathrm{bcc})}$ is the period of an atomic row of the type $\langle 111\rangle$; d is the magnitude of the basis vectors of the corresponding primitive cells.

The relations (9) and (10) are valid for an arbitrary centrosymmetric pair potential and make sense if the integrals (8) exist. The specific form of the crystal-field potential $\Phi(u)$ given by Eq. (9) depends on the magnitudes and signs of the coefficients Φ_n. It can be easily shown that the potential $\Phi(u)$ on a single period $[0, b)$ possesses extrema at the points $u=0$ and $u=b/2$. One condition for mechanical stability of the lattice is that $\Phi(u)$ must possess a minimum at the point $u=0$. It will be shown below that all pair potentials $U(r)$ used in the present paper give for fcc and bcc lattices the following result: $u=0$ is a minimum and the point $u=b/2$ is a maximum of the function $\Phi(u)$ i.e.

$$\Phi''(0)=2\left(\frac{\pi}{b}\right)^2\sum_{n=1}^{\infty} n^2\Phi_n>0,$$
$$\Phi''\left(\frac{b}{2}\right)=2\left(\frac{\pi}{b}\right)^2\sum_{n=1}^{\infty}(-1)^n n^2\Phi_n<0. \quad (11)$$

Taking account of the above-listed properties of the potential $\Phi(u)$and using the relation (9) we obtain the following expression for its amplitude:

$$\Phi_m=\Phi(b/2)=\sum_{n=1}^{\infty}\Phi_{2n-1}. \quad (12)$$

The problems listed in the introduction can be solved using twp types of relatively simple empirical potentials which have tested many times in the description of the physical properties of various crystals:

the two-parameter (ε,σ) Lennard–Jones potential

$$U(r)=4\varepsilon\left[\left(\frac{\sigma}{r}\right)^{12}-\left(\frac{\sigma}{r}\right)^{6}\right], \quad (13)$$

which is widely used in the physics of cryocrystals;[26]

the four-parameter $(\varepsilon, r_0, \alpha, m)$ generalized Morse potential

$$U(r)=\frac{\varepsilon}{m-1}\{\exp[-m\alpha(r-r_0)]-m \times\exp[-\alpha(r-r_0)]\}, \quad (14)$$

previously used to describe the mechanical properties of an entire series of cubic metals; the parameter m has been varied from 1.25 to 6[27] (the classical Morse potential is a particular case of the potential (14) with $m=2$).

Substituting the relations (13) and (14) into Eq. (8) and performing the integration we obtain the following:

for the Leard–Jones potential (13)

$$\varphi_n(R_N)=\frac{\pi\varepsilon}{4}\exp\left(-\frac{2\pi nR_N}{b}\right)\left[\frac{1}{2^5 5!}\left(\frac{\sigma}{r}\right)^{12} \times\sum_{k=0}^{5}\frac{(4\pi n)^k(10-k)!}{k!(5-k)!}\left(\frac{b}{R_N}\right)^{11-k}-\left(\frac{\sigma}{r}\right)^6 \times\sum_{k=0}^{2}\frac{(4\pi n)^k(4-k)!}{k!(2-k)!}\left(\frac{b}{R_N}\right)^{5-k}\right]; \quad (15)$$

for the generalized Morse potential (14)

$$\varphi_N(R_N)=\frac{4\varepsilon m\alpha R_N}{m-1}\left[K_1\left(z_{nm}\frac{R_N}{b}\right)\frac{\exp(m\alpha r_0)}{z_{nm}} -K_1\left(z_{n1}\frac{R_N}{b}\right)\frac{\exp(\alpha r_0)}{z_{n1}}\right], \quad (16)$$

where $z_{nm}=\sqrt{4\pi^2n^2+m^2\alpha^2b^2}$ and $K_1(x)$ is a Bessel function with imaginary argument (modified Bessel function of the third kind).

The potential $\Phi(u)$ can be further analyzed and used to obtain the characteristics of crowdions only for specific crystals using computer calculations and the sequences of quantities R_N, Z_N, and h_N presented in the Appendix as well as reference data on the numerical values of the parameters of the empirical potentials (13) and (14). We note only that the quantities $\varphi_n(R_N)$ given by the relations (15) and (16) decay exponentially as the radii R_N and the number n increase, so that the series (9) and (10) converge rapidly; this greatly simplifies the numerical analysis. Specifically, it has been found that for all specific examples considered in the present work the first term in the series (9) determine the potential $\Phi(u)$ with relative accuracy of the order of 0.07–0.01 (see Tables 1–4), i.e., the lattice potential is essentially identical to the model potential proposed in the classical Frenkel'–Kontorov work.[14]

In concluding this section we shall also give expressions which are convenient for calculating the energy parameter w characterizing the interatomic interaction in close-packed atomic rows. Substituting the expressions (13) and (14) into Eq. (2) and performing the summation we obtain:

for the Lennard–Jones potential (13)

$$w=24\varepsilon\left[26\zeta(12)\left(\frac{\sigma}{b}\right)^{12}-7\zeta(6)\left(\frac{\sigma}{r}\right)^6\right], \quad (17)$$

where $\zeta(x)$ is the Riemann zeta function, and

for the generalized Morse potential (14)

$$w=\frac{\varepsilon m(\alpha b)^2}{4(m-1)}\left[m\frac{\cosh(m\alpha b/2)}{\sinh^3(m\alpha b/2)}\exp(m\alpha r_0) -\frac{\cosh(\alpha b/2)}{\sinh^2(\alpha b/2)}\exp(\alpha r_0)\right]. \quad (18)$$

The algorithm described above can be used to calculate the crystal-field potential in a complex crystal lattice whose unit cell contains several types of different atoms. For this the lattice must be represented as a collection of sublattices consisting of identical atoms and a system of atomic rows must be constructed for each sublattice, after which the contributions of these sublattices must be summed taking account of their shifts in accordance with the basis vectors of the crystal lattice.

2. CALCULATIONS OF THE PARAMETERS OF THE CRYSTAL-FIELD POTENTIAL AND CROWDIONS

There are a number of reviews and monographs, for example, Refs. 21–24, devoted to a detailed discussion of the problems of computer simulation of lattice defects. A key question of a computer experiment is the choice of the physical model of a crystal and an adequate description of the interaction of atoms with one another. A strict quantum–mechanical analysis of interatomic interactions in a real crystal is very difficult, so that, as a rule, a number of simplying assumptions concerning the character of the interaction and the form of the potential are used. Specifically, in most calculations the multiparticle forces are neglected, and the crystal energy is written as a sum of interatomic pair interactions.

The contribution of multiparticle interactions is different in crystals with different types of chemical bonds: this contribution is small for solidified inert gases, but it plays a determining role in metal crystals. Although modern electronic theory of metals, in principle, makes it possible to take into account the electronic structure of a metal, specifically, the existence of conduction electrons and the structure of internal electron shells, in the description of interatomic interactions, this path is too difficult a problem in the computer simulation of metal crystals. For this reason, pair empirical potentials are also most often used for metals. In all cases, two criteria are used for choosing the specific empirical potentials: such potentials must correctly reflect the basic features of the chemical bond and it must be possible to express them as simple analytical functions. The simplest empirical pair potentials are used for simulating solidified inert gases—two-parameter power-law functions. The specific nature of metals is most often taken into account by choosing pair potentials in the form of three- or four-parameter exponential functions.

We believe that atomic cryocrystals are a convenient model object for studying the physics of crowdions. The wide spectrum of properties of these crystals is described, for example, in the monograph.[26] All inert gases, except helium, form a fcc crystal. Inert gas atoms possess filled spherically symmetric electronic shells and their interaction can be approximated, to a high degree of accuracy, as a sum of pair potentials. Analysis of multiparticle interactions have shown that their contribution increases with the atomic number of the inert element and is 6% for xenon.

In the present work we performed calculations for argon and krypton. Aside from the small relative contribution of the multiparticle interactions, these crystals are characterized by comparatively small values of the de Boer quantum parameter, i.e. they possess relatively small zero-point vibrational amplitudes, and consequently they can be treated as ordinary crystals with atoms localized at the lattice sites.[9,26]

The Lennard–Jones potential (13) is probably the most popular potential for describing the properties of atomic cryocrystals. The values of the parameters σ and ε are ordinarily determined from gas-phase measurements or according to the size of the lattice constant (extrapolated to 0 K) and the binding energy of the crystal. The values obtained by a number of authors differ somewhat from one another. We employed the values of the parameters σ and ε presented on page 365 of Ref. 26.

We studied the fcc metals Cu and Al as well as bcc α- and δ-Fe. In the calculations of the atomic configurations of defects in cubic metals, the interaction between atoms, as a rule, is described using the Morse potential or its generalization (14). In Refs. 28 and 29 the experimental values of the lattice parameter, the lattice binding energy (per atom), and the bulk modulus were used to determine the parameters of the Morse potential. In addition, it was required that the Born stability criterion hold.[30]

The parameters of the Morse potential for some metals with a cubic lattice were determined in Ref. 28. In Ref. 29 different values of the Morse potential parameters were obtained for Cu and Al, and this potential was used to calculate the energy of stacking faults and the energies and atomic configurations of complete and split locations. The values of the parameters in the generalized Morse potential (14) were calculated in Ref. 27 for a number of cubic metals for six values of m ranging from 1.25 to 6. In the calculation the values of the parameter m, the lattice parameter, and the elastic constants C_{11} and C_{12} were given. In the present work we employed the values of the parameters of pair potentials from Refs. 27–29; the values of the lattice parameters and the binding energies of the crystals were taken from Refs. 31–33.

In computer simulation of crystals, taking account of the thermal expansion is a separate problem. In the investigation of the desired temperature dependences of the geometric and energy parameters of crowdions and of the lattice potential we took account of only the temperature dependence of the lattice parameter, making the assumption that the parameters of the pair potentials are temperature-independent quantities. The temperature dependences of the lattice parameters for Ar and Kr were taken from Ref. 26. To estimate the values of the crowdion parameters in Cu and Al at premelting temperatures, for definiteness we took as the reference points the melting temperature of these metals and calculated for them the values of the lattice parameters, using experimental data on thermal expansion.[34]

It is well-known that iron has three crystalline modifications. Two of them possess a bcc lattice. The low-temperature α phase is stable below 1184 K and the high-temperature δ phase is stable above 1673 K. We performed calculations for these crystal modifications using a single Morse potential whose parameters can be found in Ref. 28. The values of the lattice parameters are presented in Ref. 31 for several temperatures.

TABLE I. Crowdion and crystal-field parameters in cryocrystals.

Crystal	Ar		Kr	
T, K	5	80	5	80
Φ_1, eV	0.12	0.08	0.17	0.13
$\Phi_2/\Phi_1\times10^2$	−6.6	−7.0	−6.6	−6.8
$\Phi_3/\Phi_1\times10^3$	1.5	1.6	1.5	1.5
Φ_m, eV	0.12	0.08	0.17	0.13
ω, eV	0.01	0.61	1.41	1.02
ω/Φ_m	8.36	7.54	8.39	7.89
λ_s/b	2.76	2.64	2.76	2.69
m_s/m_a	0.30	0.31	0.30	0.31
E_{s0}, eV	0.30	0.19	0.42	0.31

2.1 Atomic cryocrystals

The computational results for Ar and Kr for two values of the temperature 5 K and 80 K are presented in Table I.[1)]

It is evident from Table I that the weak-coupling condition for the distinguished atomic row and the matrix surrounding this row, as well as the main condition for the applicability of the long-wavelength approximation w/Φ_m can be regarded as satisfied at all temperatures. Our numerical estimates of the crowdion width $\lambda_m/b\approx2.7$ and the crowdion effective mass $m_s\approx0.3m_a$ also support this conclusion.

We shall now discuss in greater detail the properties of the potential $\Phi(u)$, which is determined completely by its coefficients Φ_n. It is obvious that the absolute values of these coefficients decreases rapidly with increasing n (for this reason we present only the values of the first three coefficients), and their signs alternate. According to the existing classification[15,16] the crystal-field potentials $\Phi(u)$ which we obtained for Ar and Kr are single-barrier potentials. Since the coefficient $\Phi_1>0$, according to Eq. (11) these potentials possess a minimum at the point $u=0$ and a maximum at the point $u=b/2$. The amplitude of its first harmonic determines the amplitude of the potential $\Phi(u)$ to within 0.2%, since the second harmonic in Eq. (12) does not change the amplitude of the potential but rather only changes the form of the potential: Φ_1 and Φ_2 possess different signs, and when Φ_2 is taken into account the slopes of the maxima of the potential increase somewhat and the slopes of the minima decrease somewhat. The modulus of the ratio of the second derivatives at the extrema points of the potential is approximately 1.7 and increases very little with increasing temperature. At 80 K the absolute values of the coefficients Φ_n decreased by approximately a factor of 1.5 for Ar and 1.3 for Kr, but the relative magnitudes $|\Phi_n/\Phi_1|$ increase only about 68%. Thus, the very small contribution of the highest harmonics to the potential $\Phi(u)$ tends to increase somewhat with increasing temperature.

The parameter w decreases with increasing temperature by a factor of 1.7 for Ar and 1.4 for Kr. It is the temperature-dependence of the parameters w and Φ_1 that determines primarily the temperature-dependence of the crowdion energy. The crowdion energy decreases with increasing temperature approximately by a factor of 1.6 for Ar and 1.3 Kr. However, the parameters λ_s and m_s change very little with increasing temperature.

TABLE II. Crowdion and crystal-field parameters in Cu.

Potential	27		28		29	
m	1.25	2	6		2	
Φ_1, eV	1.66	1.66	1.67	1.60	1.47	1.33
$\Phi_2/\Phi_1\times10^3$	−9.2	−9.7	−10.6	−10.6	−9.0	−9.5
$\Phi_3/\Phi_1\times10^5$	3.3	3.7	4.4	3.9	3.3	3.6
Φ_m, eV	1.66	1.66	1.67	1.60	1.47	1.33
ω, eV	24.5	25.5	28.9	24.3	23.3	20.3
ω/Φ_m	1.48	15.4	17.3	15.1	15.9	15.3
λ_s/b	3.34	3.41	3.62	3.38	3.46	3.39
m_s/m_a	0.23	0.23	0.22	0.23	0.23	0.23
E_{s0}, eV	5.70	5.83	6.22	5.58	5.24	4.64
T, K			293			1356

TABLE III. Crowdion and crystal-field parameters in Al.

Potential	29		28	
T, K	293	932	293	932
Φ_1, eV	1.20	1.11	1.21	1.11
$\Phi_2/\Phi_1\times10^3$	−8.5	−8.9	−9.2	−9.7
$\Phi_3/\Phi_1\times10^5$	3.0	3.2	3.4	3.6
Φ_m, eV	1.20	1.11	1.21	1.11
ω, eV	19.5	17.4	19.0	16.9
ω/Φ_m	16.2	15.7	15.7	15.2
λ_s/b	3.50	3.44	3.44	3.38
m_s/m_a	0.22	0.23	0.23	0.23
E_{s0}, eV	4.33	3.93	4.30	3.87

The crowdion energy in atomic cryocrystals was found to be quite large: even for premelting temperatures in Ar it is more than two times greater than the binding energy of an atom in the lattice, which is 0.08 eV. It is interesting that the binding energy for the Ar and Kr lattices, calculated at 80 K on the basis of the model being studied, decreased by only 4% and 2%, respectively, compared with its value at 0 K. In conclusion, we note the following result which is helpful for making practical estimates: calculating the crowdion energy on the basis of only the first harmonic of the potential $\Phi(u)$ (i.e. in the classical Frenkel'–Kotorov model) overestimates the value with an error of the order of 5%.

2.2. FCC metals

The computational results for Cu and Al are presented in Tables II and III, respectively.

The conditions for the existence of crowdions and the applicability of the long-wavelength approximation $w/\Phi_m \gg 1$ for these crystals holds much better than for cryocrystals.

The general laws characteristic for all of our potentials are as follows. The signs of the first several coefficients Φ_n alternate and the absolute values of the coefficients decrease with increasing n much more rapidly than for cryocrystals: the ratio $|\Phi_2/\Phi_1|$ is of the order of 10^{-2}, and the value of Φ_3/Φ_1 does not exceed 5×10^{-5}. As a result, the amplitude of its first harmonic essentially determines the amplitude of the potential $\Phi(u)$. Taking account of the second harmonic increases very little the slopes of the maximum and decreases the slopes of the minimum, but this refinement is of no practical value.

The generalized Morse potential (14) used currently for simulating metal crystals possesses an additional parameter m, which gives wider possibilities for varying the potential compared with the classical potential, for which $m=2$. In this connection, it is desirable to discuss the influence of m on the crystal-field and crowdion parameters which we are studying. Analyzing crowdions in Cu, we performed calculations for six values of the parameter m and established that the m-dependences of all quantities which we studied are monotonic. Consequently, to illustrate the effect of m on the values of the working parameters we presented the results for the standard value $m=2$ and for two limiting values: $m=1.25$ and 6. Table II shows that for values of the parameter m within the indicated limits all crystal-field and crowdion parameters change very little. The following regularity is noted: the larger the number of the harmonic, the more strongly its amplitude increases with increasing m However, since the coefficients Φ_n, themselves, starting with $n=3$, are very small, this property essentially is of only theoretical interest. The parameter w increases most strongly with increasing m; this increases the ratio w/Φ_m by approximately a factor of 1.17 and the crowdion self-energy E_{s0} by approximately a factor of 1.09. The width and effective mass of the crowdion vary much less, and as m increases, the ratio m_s/m_a decreases and the ratio λ_s/b increases. It can be concluded, on the whole, that varying the form of the potential by varying the parameter m in Eq. (4) does not substantially change the numerical values of the parameters and does not lead to the appearance of qualitatively new features. We also note that the magnitudes of the working parameters are essentially the same for the forms of the Morse potentials proposed in Refs. 28 and 29.

A calculation of the binding energy for the Cu lattice using the family of potentials (14) and the parameters proposed in Ref. 27 gives for different values of m a variance of the values of the order of 35%. The smallest difference from the experimental value 3.5–3.6 eV is obtained with $m=2$.

For the reasons presented above, to investigate the influence of temperature on the crowdion parameters we confine ourselves to calculations using only the classical Morse potential. It is evident from Tables II and III that the parameter w and the crowdion energy E_{s0} change most strongly with increasing temperature: approximately by 10–15%. Thus, the temperature dependence of the crystal-field and crowdion parameters in fcc metals is weaker than in cryocrystals.

In both metals the crowdion energy is greater than the binding energy of an atom in the lattice. For Cu this excess corresponds to approximately a factor of 1.5 at 293 K and 1.32 at premelting temperatures. For Al the difference is somewhat smaller: a factor of 1.3 at 293 K and 1.2 at premelting temperatures.

In concluding this section we shall discuss one other important question. Previously, the energy of a crowdion configuration of atoms in Cu crystals was calculated on the basis of a discrete–continuum computer model, which did not assume absolute stiffness of the crystal matrix. In the initial variant of the model of Ref. 2, the value 3.20 eV was obtained for the crowdion energy, and the value 4.59 eV was obtained in the improved variant in Ref. 19. The latter value is approximately 20–30% smaller than our estimates ob-

TABLE IV. Crowdion and crystal-field parameters in α- and δ-Fe.

Crystal	α-Fe		δ-Fe
T, K	293	1073	1698
Φ_1, eV	0.98	0.90	0.84
$\Phi_2/\Phi_1\times10^3$	5.5	5.7	5.9
$\Phi_3/\Phi_1\times10^5$	−3.0	−3.2	−3.4
Φ_m, eV	0.98	0.90	0.84
ω, eV	35.9	32.4	30.2
ω/Φ_m	36.7	36.2	35.9
λ_s/b	5.15	5.11	5.09
m_s/m_a	0.15	0.15	0.15
E_{s0}, eV	5.35	4.87	4.57

tained on the basis of the undeformed (absolutely stiff) crystal matrix. It follows from the general theory of crowdions[13] that this difference is always present, and the comparison made above gives its sign and an estimate of its scale.

2.3. BCC metals

The results of numerical calculations for α- and δ-Fe at several temperatures are presented in Table IV. The most important result for bcc metals is that the condition for the existence of crowdions and the applicability of the long-wavelength approximation $w/\Phi_m \gg 1$ holds with a large margin at all temperatures. The ratio w/Φ_m is two times greater than for fcc metals. This results in an appreciably larger numerical value of the crowdion width $\lambda_s/b \approx 5.1$ and smaller effective mass $m_s/m_a = 0.15$.

For bcc metals the absolute values of the coefficients Φ_n likewise decrease rapidly with increasing n, just as for fcc metals. However, their signs alternate in a different order: the first two coefficients Φ_1 and Φ_2 are positive. Consequently, taking account of the second harmonic in Eq. (9) increases the slopes of the minimum and decreases the slopes of the maximum of the potential $\Phi(u)$. This change is small, since the modulus of the ratio of the second potentials at the extrema of the potential is approximately 0.96, but nonetheless for this form of the potential $\Phi(u)$ the extent of the crowdion periphery decreases and its central part is more sharply distinguished. At the same time, the relative contribution of the second harmonic is almost half that in fcc metals, so that the potential $\Phi(u)$ in α- and δ-Fe is closest to a purely harmonic potential.

The influence of temperature on the crystal-field and crowdion parameters for α- and δ-Fe are of the same order of magnitude as for fcc metals: the crowdion energy E_{s0} decreases approximately by a factor of 1.17 as the homological temperature varies from 0.16 to 0.94. The energy E_{s0} is greater than the binding energy of an atom in the fcc lattice by approximately 26% at 293 K and 8% at premelting temperatures.

Computer simulation of intrinsic local defects in bcc metals was performed in Ref. 35 and the crowdion energy in α-Fe was found to be ≈ 4 eV. Our estimate of E_{s0}in the stiff crystal matrix approximation is approximately 30% greater than this value. This discrepancy makes it possible to estimate the decrease in the crowdion energy as a result of elastic relaxation of the bcc lattice.

CONCLUSIONS

In this work we presented a comprehensive analytical and numerical analysis of a number of questions concerning the problem of crowdion excitations in simple atomic crystals with fcc and bcc structures. The following basic results were obtained.

A new algorithm, based on a representation of the crystal lattice as a collection of parallel atomic rows, was developed and applied for calculations of the crystal-field potentials. An analytical expression in the form of a trigonometric series was obtained for the potential $\Phi(u)$ describing the interaction between an atom in a close-packed row and the crystal matrix. An explicit analytic expression was also obtained for the energy parameter w characterizing the interatomic interaction within a distinguished row. The calculations were performed assuming that the interatomic interaction in crystals can be described by the empirical Lennard–Jones and Morse pair potentials.

Numerical values were obtained for the crystal-field parameters for Ar and Kr fcc cryocrystals, Cu and Al fcc metals, and α- and δ-Fe bcc metals. It was shown that the form of the potential $\Phi(u)$ in the crystals studied is nearly monoharmonic: the contribution of higher-order harmonics does not exceed 7% in cryocrystals and is less than 1% in metals.

It was shown that the main condition whereby the close-packed rows are weakly coupled with the crystal matrix, making possible the existence of crowdions, and the application of the long-wavelength approximation for describing crowdions, holds in all of the crystals studied. The ratio of w to the amplitude of the crystal-field potential $\Phi_m = \max\Phi(u)$ is approximately 8 for fcc cryocrystals, 15 for fcc metals, and can reach 36 for bcc metals. In all such lattices the characteristic crowdion width is several times greater than the parameter of a close-packed row.

Numerical values were obtained for the basic parameters of crowdions: the self-energy, the effective mass, and the characteristic length. All values obtained agree with existing published data.

It was established that the approximation of an absolutely rigid crystal matrix and the one-dimensional Frenkel'–Kontorov model make it possible to obtain estimates of the crowdion energy which are approximately 20–30% higher than the values obtained by molecular-dynamics methods.

We are grateful to A. S. Kovalev for his interest in this work and for helpful discussions.

APPENDIX

It is well known that the lattice of an ideal crystal can be obtained by infinitely repeating in space a single unit cell using a triplet of basic translations—noncoplanar vectors $\mathbf{d}_1$, $\mathbf{d}_2$, and $\mathbf{d}_3$.[36] Together with the representation of a crystal lattice as a collection of sites, in certain cases it is helpful to represent this lattice as a collection of straight parallel atomic rows. Such a representation is obtained naturally if all transfers of the unit cell are first performed using one of the basic translations: for example, repeating the translation $\mathbf{d}_1$ of any site of the unit cell gives an infinite row of identical points with period d_1. The remaining two translations will result in parallel transport of the atomic row obtained and form a

system of rows of the same type, consisting of identical atoms. The crystal basis determines the relative arrangement of the indicated systems of atomic rows and types of atoms in each system, and the number of systems of atomic rows is equal to the number of sites of the unit cell. We recall that for a lattice consisting of p types of different atoms the unit cell contains at least p sites.

Since the choice of a unit cell (triplet of basic translations $\{\mathbf{d}_i\}$) is not unique, the representation of the crystal as a collection of atomic rows is likewise not unique. When the crystal lattice is partitioned into a collection of atomic rows, the direction of the rows can be given using any vector from a set of vectors formed by all possible triplets $\{\mathbf{d}_i\}$.

If a simple (monotonic) crystal lattice possesses a primitive cell, then it can be constructed using translations only of a single site. The primitive cell of an fcc lattice corresponds to a triplet of vectors whose components in a Cartesian coordinate system tied to four-fold symmetry axes are: $\mathbf{d}_1=(a/2)(1,1,0)$, $\mathbf{d}_2=(a/2)(1,0,1)$, and $\mathbf{d}_3=(a/2)(0,1,1)$. All vectors have the same length $d=a/\sqrt{2}$ (a is the lattice parameter), which corresponds to the minimum distance between two atoms. Therefore, a monatomic fcc lattice can be obtained using two-dimensional translations of a single close-packed atomic row with crystallographic direction of the type $\langle 110\rangle$.

A primitive cell of a bcc lattice corresponds to the triplet of vectors $\mathbf{d}_1=(a/2)(1,1,1)$, $\mathbf{d}_2=(a/2)(1,1,-1)$, and $\mathbf{d}_3=(a/2)(1,-1,-1)$, which have the same length $d=a\sqrt{3}/2$, equal to the minimum distance between two atoms in this lattice. Therefore, a monatomic fcc lattice can be obtained using a two-dimensional translation of a single close-packed atomic row with crystallographic direction of the type $\langle 111\rangle$.

The basis vectors of primitive rhombohedral cells of fcc and bcc lattices uniquely determine the collection of close-packed atomic rows comprising a simple crystal. Of course, in a system of close-packed rows there are no distinguished rows—all atomic rows are equivalent (isotypic). However, the description of the lattice in a skewed basis is not always optimal; it is often more convenient to switch to a rectangular coordinate system by combining one of the axes of the system, for example, for definiteness the $0x$ axis, with the axis of one of the close-packed atomic rows (we called this row the reference row), placing the origin of coordinates at one of the sites of the row. Then the $y0z$ plane is also the crystallographic plane of the type (110) in an fcc lattice and a plane of the type (111) in a bcc lattice. The points of intersection of the axes of close-packed rows with this plane form planar networks, which are shown in Fig. 1.

In an fcc lattice the structure of these intersection points is formed by superposing two equidimensional rectangular grids (with edge ratio $1:\sqrt{2}$), which are displaced relative to one another by half the diagonal of a rectangle. The sites of only one grid coincide with the sites of the crystal lattice and the atoms occupy these sites, while the sites of the other grid are unoccupied. The first grid corresponds to atomic rows of the type (110), which are not displaced along the $0x$ axis relative to the chosen reference row, and the second grid corresponds to rows which are displaced along its axis by half a period, equal to $a/(2\sqrt{2})$.

In a bcc lattice the structure of the points where the axes

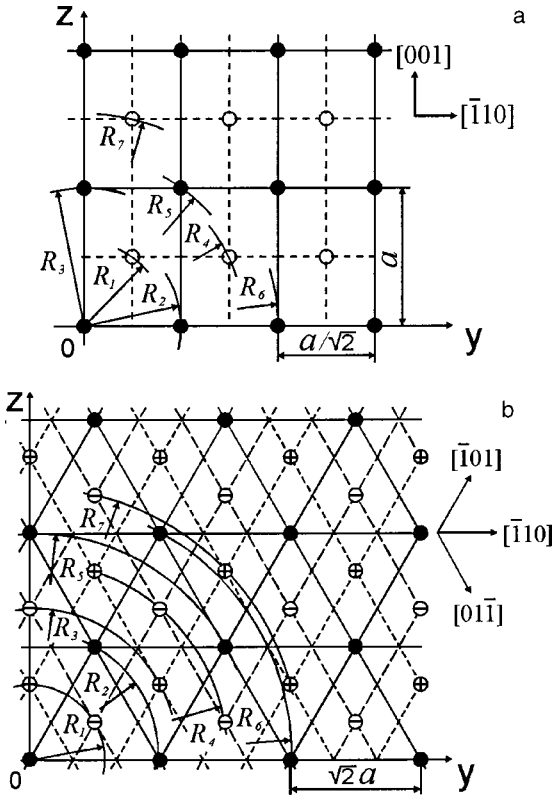

FIG. 1. Two-dimensional grids formed by points of intersection of the axes of close-packed atomic rows with crystallographic direction $\langle 110\rangle$ in an fcc lattice and $\langle 111\rangle$ in a bcc lattice with the (110) and (111) planes respectively: ●—grid sites coinciding with the lattice sites and occupied by atoms; ○,⊕, ⊖—grid sites which do not correspond to lattice sites; R_1, R_2, . . .—radii of the first several coordination cylinders. A two-dimensional grid in an fcc lattice; the atomic rows corresponding to the sites ○ are shifted along the $0x$ axis by half the period $a/\sqrt{2}$ (a); two-dimensional grid in a bcc lattice; the atomic rows corresponding to the sites ⊕ are shifted along the $0x$ axis by 1/3 of the period ($\sqrt{3}a/2$) in the positive direction and those corresponding to the sites ⊖ are shifted by 1/3 of the period ($\sqrt{3}a/2$) in the negative direction (b).

of the crystallographic rows with directions [111] intersect a (111) plane is formed by superposing three regular triangular grids, consisting of equilateral triangles with edge length $\sqrt{2}a$ (such grids are ordinarily called close-packed 3^6 grids[37]). These grids are shifted relative to one another in the direction of the height of the triangle by a distance equal to 2/3 of the height, which corresponds to $\sqrt{3/2}a$. The sites of only one grid coincide with the sites of the crystal lattice, and it corresponds to the atomic rows which are not shifted along the $0x$ axis relative to the chosen reference row. The second grid corresponds to atomic rows, which are displaced along the $0x$ axis by 1/3 of its period, equal to $\sqrt{3}a/6$. The third grid corresponds to atomic rows which are shifted along the $0x$ axis by 2/3 of its period, which is $a/\sqrt{3}$. It can also be assumed that these rows are shifted along the $0x$ axis by an amount equal to $-1/3$ of its period.

The quantitative structural characteristics of the local environment of the reference row are the number of neighbors (first, second, and so on) and the corresponding distances to them. In our case it is natural to use terminology matched with the generally accepted crystal–structural concepts, so that in what follows we shall employ the following terms:

Nth coordination cylinder with radius R_N and coordination number Z_N ($N=1,2,\ldots$).

A. Sequence of coordination cylinders for an fcc lattice

For an fcc lattice the radii of the coordination cylinders and the coordination numbers are determined by the following sequences:

$$\frac{R_N}{d}\equiv\frac{\sqrt{2}R_N}{a}=\left\{\frac{\sqrt{3}}{2},1,\sqrt{2},\frac{\sqrt{11}}{2},\sqrt{3},2,\frac{\sqrt{19}}{2},\sqrt{6},3\frac{\sqrt{3}}{2},2\sqrt{2},\ldots\right\}, \tag{A1}$$

$$Z_N=\{4,2,2,4,4,2,4,4,8,2,\ldots\}. \tag{A2}$$

Analysis shows that all atomic rows in the same coordination cylinder possess the same displacement (along the $0x$ axis) relative to the reference row. To characterize this shift, to each coordination cylinder we associate one dimensionless coefficient h_N, equal in absolute magnitude to the shift in units of d and assuming the value 0 if the shift is zero and the value 1/2 if the shift is $d/2$. The values of h_N are given by the sequence

$$h_N=\{1/2,0,0,1/2,0,0,1/2,0,1/2,0,\ldots\}. \tag{A3}$$

B. Sequence of coordination cylinders for a bcc lattice

For a bcc lattice the sequences of the radii of the coordination cylinders and the coordination numbers are as follows:

$$\frac{R_N}{d}\equiv\frac{2R_N}{a\sqrt{3}}\left\{\frac{2\sqrt{2}}{3},2\sqrt{2/3},\frac{4\sqrt{2}}{3},\frac{2\sqrt{14}}{3},2\sqrt{2},4\sqrt{2/3},\frac{2\sqrt{26}}{3},\frac{8\sqrt{2}}{3},\frac{2\sqrt{38}}{3},2\sqrt{14/3},\ldots\right\}, \tag{A4}$$

$$Z_N=\{6,6,6,12,6,6,12,6,12,12,\ldots\}. \tag{A5}$$

The distribution of shifts h_N of the atomic rows in this case exhibits the following features. All atomic rows belonging to the same coordination cylinder are either undisplaced or are displaced relative to the reference row. If there is a displacement, then half the atomic rows belonging to the coordination cylinder have a shift $+d/3$ and the other half have a shift $-d/3$. Having noted this feature, to each coordination cylinder we associate a single indicator of the absolute magnitude of the shift—the coefficient h_N, which is zero if the shift is 0 and 1/3 if the shift is $\pm d/3$ The values of the parameter h_N are determined by the following sequence:

$$h_N=\{1/3,0,1/3,1/3,0,0,1/3,1/3,1/3,0,\ldots\}. \tag{A6}$$

[1)] It is well known that the law of corresponding states holds very well for solidified inert gases, i.e., on the homological temperature scale the temperature dependences of the lattice characteristics of such crystals are identical.[26] This circumstance makes it possible to extend the results of Table I to Xe.

[1] H. R. Paneth, Phys. Rev. **80**, 708 (1950).
[2] L. Tewordt, Phys. Rev. **109**, 61 (1958).
[3] J. Friedel, *Dislocations* (Mir, Moscow, 1967).
[4] J. Manning, *Diffusion Kinetics of Atoms in Crystals* (Mir, Moscow, 1971).
[5] A. Seeger, Phys. Status Solidi **38**, 235 (1970).
[6] L. M. Brown, Scr. Metall. **8**, 1045 (1974).
[7] C. h. Wao and W. Frank, J. Nucl. Mater. **137**, 7 (1985).
[8] Yu. E. Golovin and F. I. Tyurin, Fiz. Tverd. Tela (St. Petersburg) **42**, 1818 (2000) [Phys. Solid State **42**, 1865 (2000)].
[9] A. M. Kosevich, *Physical Mechanics of Real Crystals* (Naukova dumka, Kiev, 1981).
[10] A. M. Kosevich and A. S. Kovalev, *Introduction to Nonlinear Physical Mechanics* (Naukova dumka, Kiev, 1989).
[11] J. L. Lem, *Introduction to the Theory of Solitons* (Mir, Moscow, 1983).
[12] A. S. Davydov, *Solitons on Molecular Systems* (Naukova dumka, Kiev, 1988).
[13] V. D. Natsik and E. I. Nazarenko, Fiz. Nizk. Temp. **26**, 283 (2000) [Low Temp. Phys. **26**, 210 (2000)].
[14] Ya. I. Frenkel', *Introduction to the Theory of Metals* (Nauka, Leningrad, 1972).
[15] O. M. Braun and Yu. S. Kivshar, Phys. Rep. **306**, 1–2 (1998).
[16] V. D. Natsik, S. N. Smirnov, and E. I. Nazarenko, Fiz. Nizk. Temp. **27**, 316 (2001) [Low Temp. Phys. **24**, 233 (2001)].
[17] A. M. Kosevich and A. S. Kovalev, "The theory of dynamical crowdions in strongly anisotropic media" in *Dislocation Dynamics* (Naukova dumka, Kiev, 1975).
[18] A. Seeger and E. Mann, J. Phys. Chem. Solids **12**, 326 (1960).
[19] R. A. Johnson and E. Brown, Phys. Rev. **127**, 446 (1962).
[20] R. A. Johnson and E. Brown, Phys. Rev. **134**, A1329 (1964).
[21] V. M. Agranovich and V. V. Kirsanov, Usp. Fiz. Nauk **118**, 3 (1976).
[22] V. V. Kirsanov and A. N. Orlov, Usp. Fiz. Nauk **142**, 219 (1984).
[23] Yu. A. Osip'yan (Ed.), *Crystal Defects and Their Computer Simulation* (Nauka, Leningrad, 1980).
[24] Yu. A. Osip'yan (Ed.), *Computer Simulation of Defects in Metals* (Nauka, Leningrad, 1990).
[25] E. Madelung, *Mathematical Methods of Physics* (Fizmatgiz, Moscow, 1960).
[26] B. I. Vrkin and A. F. Prikhot'ko [Eds.], *Cryocrystals* (Naukova dumka, Kiev, 1983).
[27] F. Milstein, J. Appl. Phys. **44**, 3825 (1973).
[28] L. A. Girifalco and V. G. Weizer, Phys. Rev. **114**, 687 (1959).
[29] R. M. J. Cotterill and M. Doyama, Phys. Rev. **145**, A465 (1966).
[30] M. Born and H. Kuhn, *Dynamical Theory of Crystal Lattices* (Izd. Inostr. Lit., Moscow. 1958).
[31] A. Guinier, *X-Ray Diffraction Analysis of Crystals* (Gos. Izd. Fiz.-mat. lit., Moscow, 1961).
[32] G. V. Samsonov (Ed.), *Physicochemical Properties of the Elements* (Naukova dumka, Kiev, 1965).
[33] C. Kittel, *Introduction to Solid State Physics* (Gl. red. fiz.-mat. lit., Nauka, Moscow, 1975).
[34] S. I. Novikiva, *Thermal Expansion of Solids* (Nauka, Moscow, 1974).
[35] J. N. Harder and D. J. Bacon, Philos. Mag. A **58**, 165 (1988).
[36] Yu. I. Sirotin and M. P. Shaskol'skaya, *The Principles of Crystal Physics* (Gl. red. fiz.-mat. lit., Nauka, Moscow, 1975).
[37] W. Pierson, *The Crystal Chemistry and Physics of Metals and Alloys* (Mir, Moscow, 1977), Part 1.

Translated by M. E. Alferieff

Impedance and specific heat of RM_4Al_8 and RAg_6In_6 compounds

A. M. Gurevich

B. I. Verkin Physicotechnical Institute for Low Temperatures, Ukrainian National Academy of Sciences, pr. Lenina 47, Khar'kov, 61103, Ukraine

V. M. Dmitriev

B. I. Verkin Physicotechnical Institute for Low Temperatures, Ukrainian National Academy of Sciences, pr. Lenina 47, Khar'kov, 61103, Ukraine; International Laboratory of High Magnetic Fields and Low Temperatures, 95 Gajowicka Str., 53-421, Wroclaw, Poland

V. N. Eropkin

B. I. Verkin Physicotechnical Institute for Low Temperatures, Ukrainian National Academy of Sciences, pr. Lenina 47, Khar'kov, 61103, Ukraine

B. Yu. Kotur

I. Fanko L'vov State University, ul. Kirilla i Mefodiya, 6, L'vov, 79005, Ukraine

N. N. Prentslau

B. I. Verkin Physicotechnical Institute for Low Temperatures, Ukrainian National Academy of Sciences, pr. Lenina 47, Khar'kov, 61103, Ukraine

V. Suski

International Laboratory of High Magnetic Fields and Low Temperatures, 95 Gajowicka Str., 53-421, Wroclaw, Poland; W. Trzebiatowski Institute of Low Temperatures and Structure Research, Polish Academy of Sciences, P. O. 1410, 50-950, Wroclaw, Poland

A. V. Terekhov and L. V. Shlyk

B. I. Verkin Physicotechnical Institute for Low Temperatures, Ukrainian National Academy of Sciences, pr. Lenina 47, Khar'kov, 61103, Ukraine

(Submitted June 6, 2001)
Fiz. Nizk. Temp. **27**, 1308–1316 (November 2001)

The results of experimental investigations of the temperature dependences of the surface resistance and specific heat of ternary rare-earth compounds are presented: $LuFe_4Al_8$, $ScFe_4Al_8$, $CeFe_4Al_8$, $CeCr_4Al_8$, YFe_4Al_8, YCr_4Al_8, YMn_4Al_8, UCu_4Al_8, $LaAg_6In_6$, and $PrAg_6In_6$, which have $ThMn_{12}$ structure. It is shown that at a certain temperature, characteristic for each compound with Fe, Cr, and Mn, below the Néel temperature a jump is observed in the total impedance and specific heat. At lower temperatures a negative magnetoresistance is observed in these compounds in weak magnetic fields. Superconducting phases are found in the compounds $ScFe_4Al_8$ ($T_c=6$ K), YCr_4Al_8 ($T_c=4.5$ K), YFe_4Al_8 ($T_c=6$ K), and $PrAg_6In_6$ ($T_c=8.3$ K). © *2001 American Institute of Physics.* [DOI: 10.1063/1.1421464]

INTRODUCTION

The crystal structure and magnetic properties of ternary compounds RM_4Al_8 (R=La, Ce, Pr, Nd, Sm, Gd, Tb, Dy, Ho, Er, Tm, Yb, Lu, Y, Th; M=V, Cr, Mn, Fe, Co, Ni, Cu) in various combinations are described in Refs. 1–5. They all possess $ThMn_{12}$ type structure. The results of experimental investigations of the low-frequency impedance and specific heat of the polycrystalline compound $LuFe_4Al_8$, where only the iron atoms possess a magnetic moment, are presented in Refs. 6,7. The following features of the compounds were noted in Ref. 6.

Anomalies of the temperature dependences of the specific heat $C(T)$ and ohmic losses $R_s(T)$, due to antiferromagnetic ordering, with maximum at $T=100.5$ K are observed in the temperature range 98–108 K. It was found that another phase transition occurs in a narrow (~ 2 K) temperature range between T_0 (minimum of R_s) and T_1 (maximum of R_s). This transition is accompanied by an anomalous increase of the specific heat near T_1 and by an abrupt increase of ohmic losses between T_0 and T_1 (the jump width <10 K). A weak constant magnetic field partially or completely removes the increase in the resistance. Negative magnetoresistance is observed in the temperature range $T_2<T<T_1$. A superconducting phase (not more than 5%) is observed in the compound for $T_c \leqslant 24$ K. This is confirmed by the presence of the Meissner effect, a singularity in the behavior of the specific heat, levitation, and resistive and magnetic measurements. The results can be explained by the fact that below T_1 the magnetic structure is a layered antiferromagnetic superlattice "magnetic Fe–nonmagnetic Lu–magnetic Fe."[5] In

such a system the spin-dependent scattering of charge carriers, resulting in a negative magnetoresistance, is important. The superconducting state probably arises only in layers where there is no magnetic moment, which is the reason for the small amount of the superconducting phase.

The results presented in the present paper are essentially a continuation of the experimental investigations presented in Refs. 6–10. The goal was to obtain answers to the following questions.

Are the phase transition near T_1 and the superconducting phase observed only in $LuFe_4Al_8$ or do they also occur in other compounds in this family?

If these phase transitions also exist in other compounds, then how do the magnetic properties of the R and M elements affect them?

To this end investigations of the magnetoresistant properties of $LuFe_4Al_8$ were continued and the temperature dependences of the specific heat and active part of the impedance of polycrystalline samples $ScFe_4Al_8$, $CeFe_4Al_8$, $CeCr_4Al_8$, YFe_4Al_8, YCr_4Al_8, YMn_4Al_8, UCu_4Al_8, $LaAg_6In_6$, and $PrAg_6In_6$, which also possess $ThMn_{12}$ structure,[9,10] were continued. These compounds were chosen for the following reasons.

The magnetic properties of Ce, Sc, and Y atoms differ substantially (for example, the magnetic susceptibility of Ce is $\chi = 2.5\times10^{-3}$ and that of Sc is $\chi = 1.810^{-5}$). This makes it possible to determine the influence of the magnetic properties of R elements on the total impedance and specific heat of the compounds investigated.

At the same time replacing the strong magnetic Fe by a weak antiferromagnet Cr and weak paramagnet Mn determines the influence of the magnetic properties of M elements.

The compounds $CeFe_4Al_8$ and YMn_4Al_8 are also interesting in that two magnetic elements Ce and Fe are present in the first one and two virtually nonmagnetic elements Y and Mn are present in the second one.

The precious metal Ag and Cu, which can possess transition-metal properties, are present in the compounds UCu_4Al_8, $LaAg_6In_6$, and $PrAg_6In_6$.

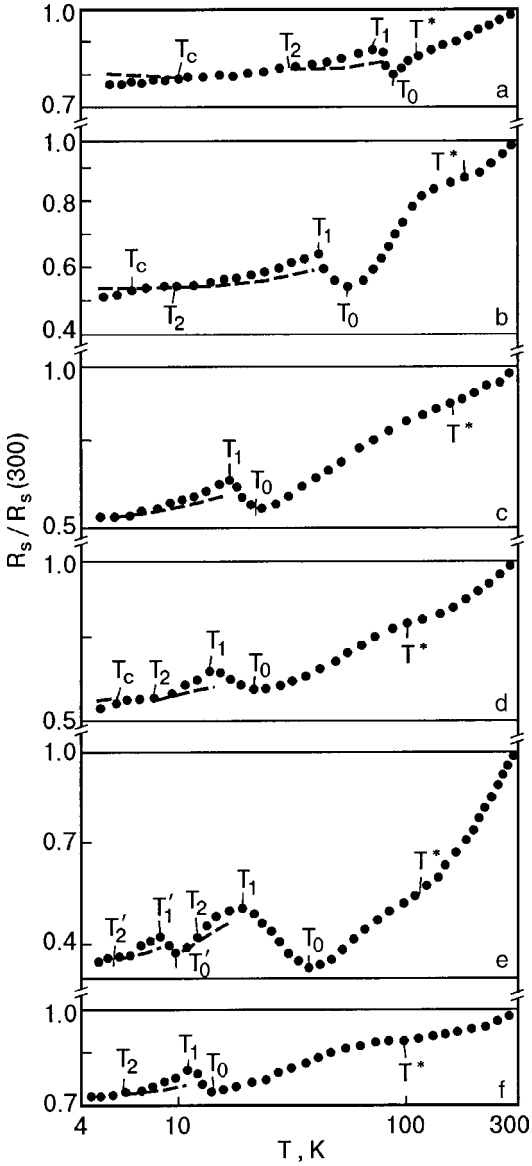

FIG. 1. Temperature dependences of the surface resistance R_s, scaled to $R_s(300)$, of the compounds $LuFe_4Al_8$ (a), $ScFe_4Al_8$ (b), $CeFe_4Al_8$ (c), YCr_4Al_8 (d), $CeCr_4Al_8$ (e), and YMn_4Al_8 (f).

SAMPLES AND MEASUREMENT PROCEDURE

Arc and induction melting were used to obtain the polycrystalline.

The complicated cross section of the samples made it impossible to calculate their resistivity. Consequently, the surface resistance R_s was measured by a contact-free resonator method. The measurement setup and procedure are described in Refs. 6 and 11. The surface resistance was measured at 10 MHz for compounds with M=Fe, Cr, and Mn and 5 MHz for compounds with M=Cu and Ag.

Just as in Ref. 6, indium was used as the reference sample.

The specific heat of the samples $CeCr_4Al_8$, YCr_4Al_8, and YMn_4Al_8 in the temperature range 1.5–20 K and UCu_4Al_8 in the temperature range 1.5–95 K was measured by the absolute calorimetry method. The presence of many peaks and the extremely wide temperature range where the anomalies are observed can be explained by the multiphase nature of the compounds, which made it necessary to take measures to homogenize the samples by annealing. The specific heat of the samples YCr_4Al_8, $CeFe_4Al_8$, and YMn_4Al_8 was measured before and after annealing for 7 days at 800 °C.

EXPERIMENTAL RESULTS

Figure 1 shows the temperature dependences of R_s, scaled to the surface resistance at room temperature $R_s(300)$, for the compounds $LuFe_4Al_8$ (a), $ScFe_4Al_8$ (b), $CeFe_4Al_8$ (c), YCr_4Al_8 (d), $CeCr_4Al_8$ (e), and YMn_4Al_8 (f).

It was established experimentally (see Fig. 1) that in all compounds named above the temperature dependence of the reduced surface resistance is observed above some temperature T^* characteristic for each compound.

(The values of T^*, T_0, T_1, T_2, T_c, $R_{s0}/R_s(300)$, and $A/R_s(300)$, whose meaning is discussed below, are presented in Table I.)

TABLE I. Characteristic temperatures and resistive parameters of the experimental compounds RM_4Al_8.

Compound	T^*	T_0	T_1	T_2	T_c	$R_{s0}/R_S(300)$	$A/R_s(300)$, K^{-2}
	K						
$LuFe_4Al_8$	100	77–97	74–95	30	24	0.78	1.52×10^{-5}
$ScFe_4Al_8$	180	50	42	10	6	0.518	7.46×10^{-3}
$CeFe_4Al_8$	180	20	17	<4.2		0.496	2.56×10^{-4}
YCr_4Al_8	100	18	15	8	4.5–4.9	0.552	3.0×10^{-4}
$CeCr_4Al_8$	160	25; 10	20; 8	10; 6			
YMn_4Al_8	100	13.5	12	8		0.755	3.35×10^{-4}
YFe_4Al_8		55	50	30	6	0.8	
UCu_4Al_8						0.65	
$LaAg_6In_6$						0.58	
$PrAg_6In_6$					8.3	0.69	

In all experimental compounds, just as in $LuFe_4Al_8$ (see Figs. 4a and 5 in Ref. 6), a transition accompanied by an abrupt increase in R_s and negative magnetoresistance is observed at certain temperature T_1 and exists up to a certain temperature $T_2<T_1$. In Fig. 1 the broken lines show the values of $R_s(T)/R_s(300)$ for all compounds in a $H=50$ Oe magnetic field.

The temperature dependence of the surface resistance R_s of the compounds $ScFe_4Al_8$, $CeFe_4Al_8$, YCr_4Al_8, and YMn_4Al_8, in the temperature range T_1-T_8 can be described by the equation

$$R_s(T)=R_{s0}+AT^2. \tag{1}$$

Figure 2 shows (solid lines) the dependences $R_s(T)/R_s(300)$ for the compounds YMn_4Al_8 *(1)* and $CeFe_4Al_8$, *(2)*, calculated using Eq. (1) taking account of the parameters presented in the table; the dots in the figure represent the experimental values.

In certain samples of $LuFe_4Al_8$ the dependence $R_s(T)$ can also be described by the Eq. (1) in the temperature interval T_1-T_2. Figure 1a shows the temperature dependence of R_s for precisely such a sample. However, as follows in Ref. 6, the temperature dependence of R_s of some $LuFe_4Al_8$ samples in the interval T_1-T_2 does not follow a quadratic law, but rather can be described by the expression $R_s\propto T^n$, $n<1$.

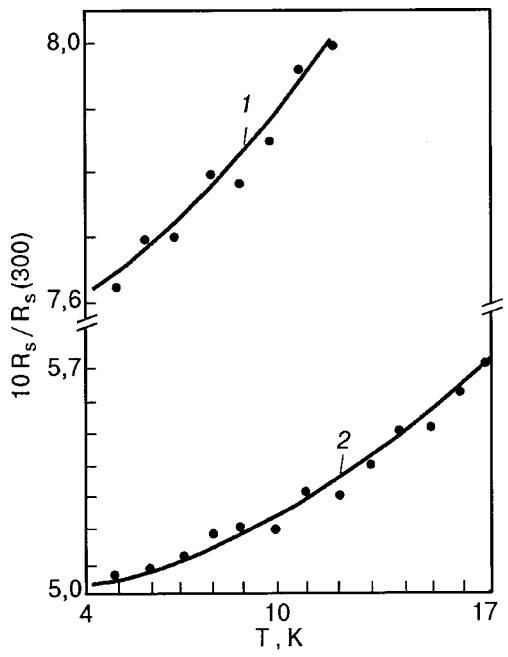

FIG. 2. Computed (solid lines) and experimentally determined (dots) temperature dependences $R_s/R_s(300)$ for YMn_4Al_8 *(1)* and $CeFe_4Al_8$ *(2)*.

For the $CeCr_4Al_8$ sample a series of anomalies is observed in the form of a wavy variation of the resistance and negative magnetoresistance in a certain temperature range below each maximum value of the resistance (see Fig. 1e). Thus, there are several values of T_1 and T_2 for this compound.

In $ScFe_4Al_8$ and YCr_4Al_8 a negligible amount of a superconducting phase appears at a certain temperature T_c which is several degrees below T_2, just as in $LuFe_4Al_8$.[6,7] This is evident from the results obtained in measurements of $R_s(T)$ in a 50 Oe magnetic field (see Fig. 1, broken lines). Below T_c the magnetoresistance is positive.

The influence of annealing on the parameters of the compounds should be noted.

Figure 3 shows the temperature dependences of the specific heat of the compound YCr_4Al_8; these curves were obtained before (Fig. 3a, curve *1*) and after (Fig. 3a, curve *2*) annealing. The figure also shows the temperature dependences of the specific heat of YMn_4Al_8 samples (Fig. 3a, curve *3*) and $CeCR_4Al_8$ samples (Fig. 3b, curve *3*) after annealing. The specific heat measurements were conducted serially; the initial temperature, the heating rate up to the initial temperature of a series, and the temperature "step" were varied. Such an experiment made it possible to establish the sensitivity of the specific heat to the indicated parameters in the temperature ranges where specific heat anomalies are observed.

For YCr_4Al_8 sample these are the intervals 7.5–10 K and 11.5–18 K, and for YMn_4Al_8 the interval is 10–15 K (Fig. 3). The dependence of the specific heat on the kinetic parameters and thermal past history of the sample indicates the presence of hysteresis, which identifies the phase transformations as first-order transitions.

Figure 4 displays data on the temperature dependences of the specific heat and resistance of the compound YCr_4Al_8. Just as for $LuFe_4Al_8$, a correlation is observed between the specific heat anomalies of the specific heat and resistance. At temperature T_1 a weak magnetic field starts to affect the resistance (Fig. 4a, dotted line), and at temperature T_2 the field no longer has an effect, while at T_c a superconducting

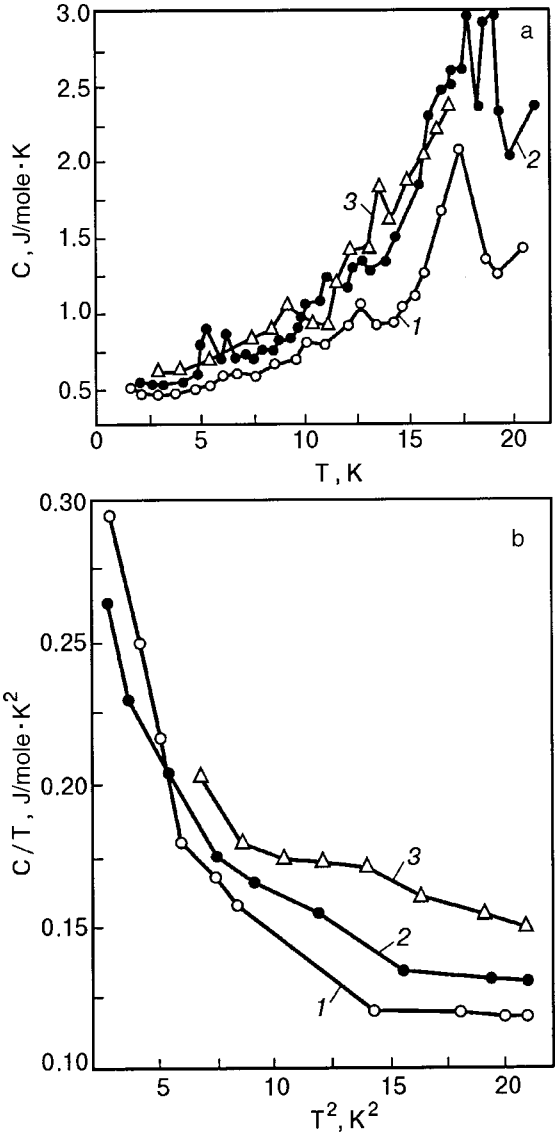

FIG. 3. Temperature dependences of the specific heat of the compound YCr_4Al_8 before *(1)* and after *(2)* annealing and YMn_4Al_8 after annealing (3) (a). The temperature dependences of the specific heat of the annealed compounds YCr_4Al_8 *(1)*, YMn_4Al_8 *(2)*, and $CeCr_4Al_8$ *(3)* in the coordinates $C/T(T^2)$ (b).

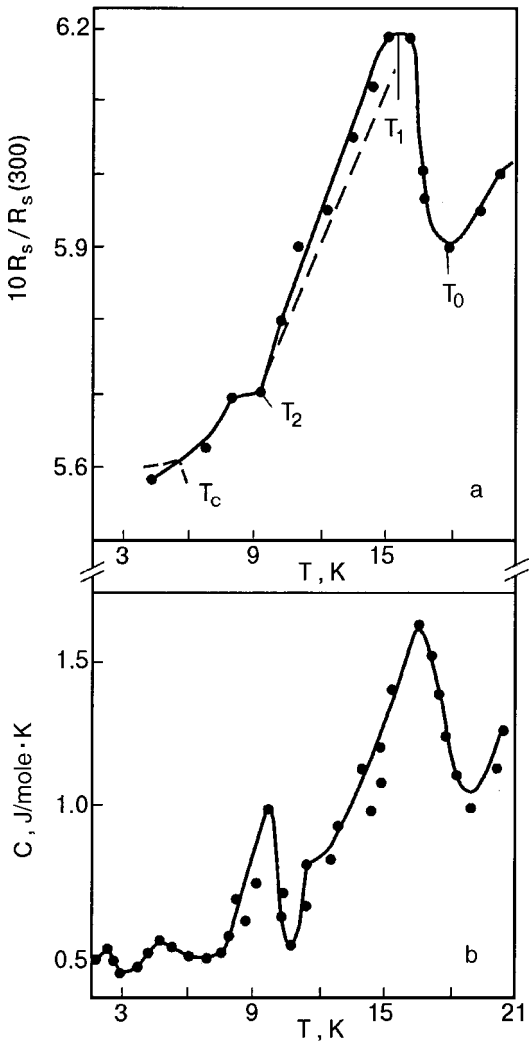

FIG. 4. Temperature dependences $R_s/R_s(300)$ (a) and C (b) for the compound YCr_4Al_8.

phase is formed. The singularities in the behavior of the specific heat are observed precisely at these temperatures.

Figure 5 shows the temperature dependences of the specific heat of the compound YCr_4Al_8 in the temperature range where the superconducting phase is formed prior to annealing (curve *1*) and after annealing (curve *2*) of the sample. It follows from the figure that annealing increases T_c and increases the amplitude of the anomaly in C. At the same time, according to measurements of R_s, an increase in the percentage of the superconducting phase as a result of annealing is not observed, though a constant magnetic field starts to have an effect at higher temperatures (4.5 K before annealing and 4.9 K after heat treatment).

Figure 6 shows the temperature dependences $R_s(t)$ and the reactive component of the total impedance X_s (*2*) of the compound $LuFe_4AL_8$ at $H=0$ and $H=50$ Oe: R_s (*3*) and X_s (*4*), scaled to $R_s(85)$ and $X_s(85)$, respectively. A correlation between the temperature dependences $R_s(T)$ and $X_s(T)$ is clearly seen in the figure.

In Ref. 6 it is indicated that the application of a constant magnetic field ($H\sim 50$ Oe) at $T<T_1$ virtually completely eliminates the abrupt increase of the surface resistance in the

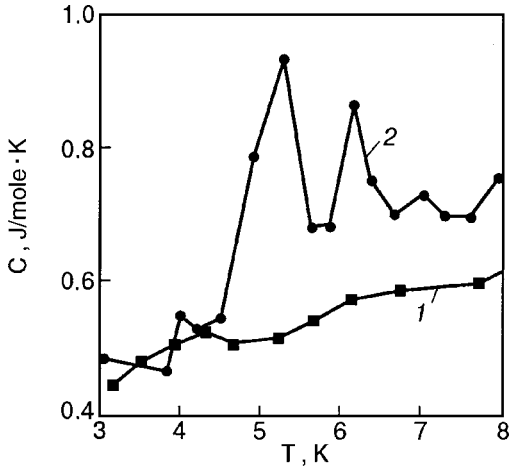

FIG. 5. Temperature dependences of the specific heat of the compound YCr_4Al_8 before *(1)* and after *(2)* annealing.

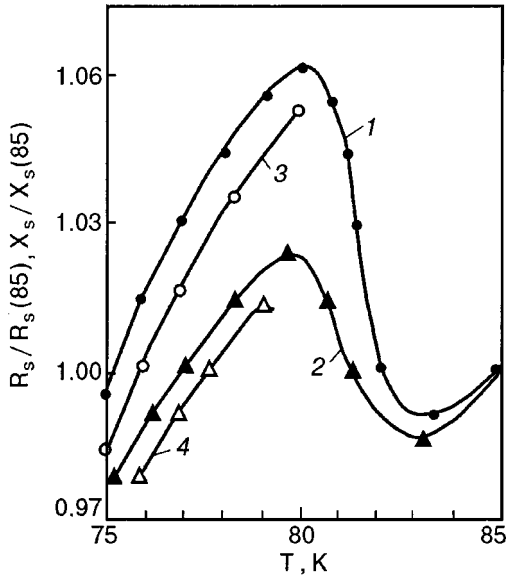

FIG. 6. Temperature dependence of the active R_s *(1)* and reactive X_s *(2)* components of the impedance of the compound $LuFe_4Al_8$ with $H=0$ and same for $H=50$ Oe R_s *(3)* and X_s *(4)*.

compound $LuFe_4Al_8$. However, $LuFe_4MAl_8$ samples where the amplitude of the anomaly in R_s at $T=T_1$ is large were also investigated. In these samples an abrupt decrease of R_s with increasing constant magnetic field is observed. Figure 7 shows the dependence $R_s(H)$ of one such sample at $T=30$ K.

It should be noted that in certain samples (for example, in YMn_4Al_8) the post-annealing amplitude of the abrupt increase in R_s and the influence of a constant magnetic field on the ohmic losses decrease.

Measurements of $R_s(T)$ for UCu_4AL_8 and also the compounds $LaAg_6In_6$ and $PrAg_6In_6$ in the temperature range

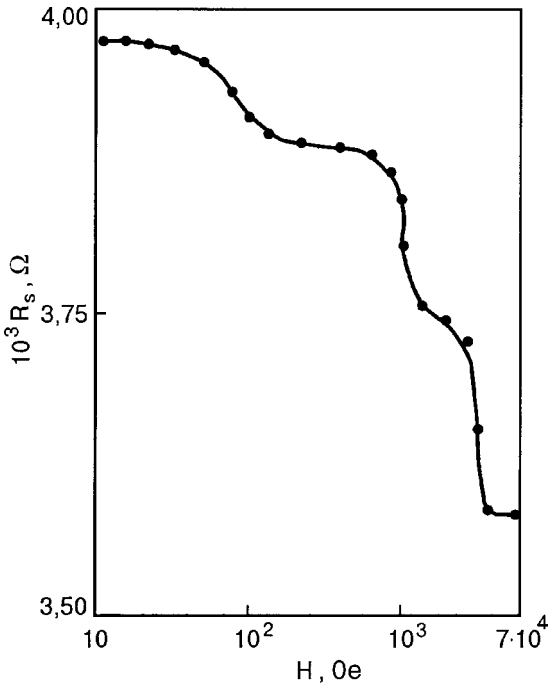

FIG. 7. Surface resistance R_s of the compound $LuFe_4Al_8$ versus the magnetic field intensity at $T=30$ K.

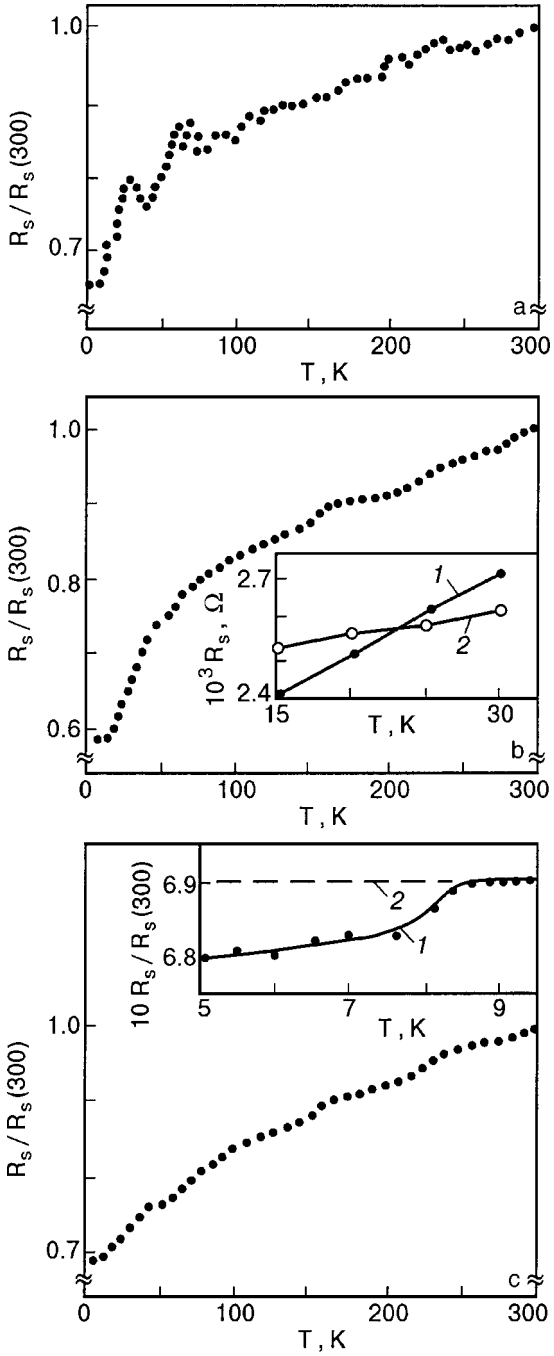

FIG. 8. Temperature dependences of $R_s/R_s(300)$ of the compounds UCu_4Al_8 (a), $LaAg_6In_6$ (b), and $PrAg_6In_6$ (c). Inset in Fig. 8b: $R_s(T)$ of the compounds $LaAg_6In_6$ *(1)* and $PrAg_6In_6$ *(2)* in the temperature range 15–30 K. Inset in Fig. 8c: $R_s(T)/R_s(300)$ for the compound $PrAg_6In_6$, $H=0$*(1)* and $H=500$ Oe *(2)*.

4.5–300 K were performed in order to compare the characteristics of the dependences $C(T)$ and $R_s(T)$ of transition and precious metal based compounds. The specific heat of the compound UCu_4AL_8 was measured in the temperature range 2–95 K. The dependences $R_s(T)/R_s(300)$ for these compounds are presented in Fig. 8: UCu_4Al_8 (a), $LaAg_6In_6$ (b), and $PrAg_6In_6$ (c) and the curve $C(T)$ for UCu_4Al_8 is presented in Fig. 9. The inset in Fig. 8b shows the dependences $R_s(T)$ for the compounds $LaAg_6In_6$ *(1)* and $PrAg_6In_6$ (2) in the temperature range where they intersect. The inset in Fig. 8c shows the temperature dependence of $R_s/R_s(300)$

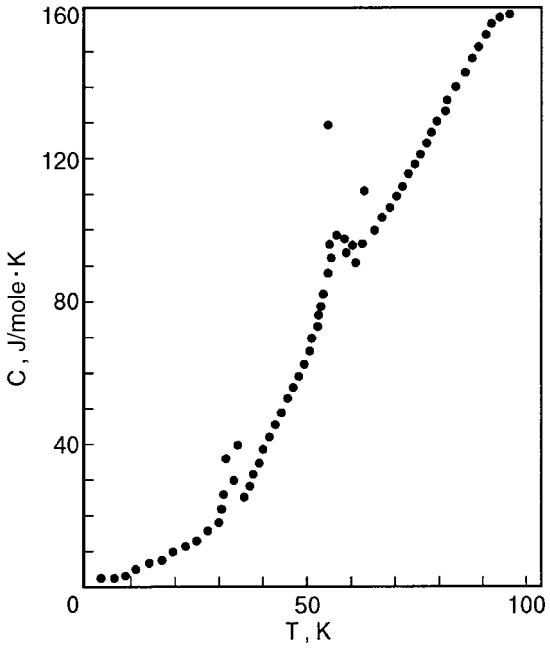

FIG. 9. Temperature dependence of the specific heat of the compound UCu_4Al_8.

$PrAg_6In_6$ in the temperature range 5–9 K, measured at $H=0$ (curve *1*) and in a constant magnetic field 500 Oe (curve *2*).

DISCUSSION

Analyzing the results obtained, we note first the general features of the physical characteristics of the experimental compounds of the system RM_4Al_8.

In all experimental compounds with transition metals the temperature dependence of R_s possesses a linear section, which is a characteristic indicator for compounds with rare-earth elements. A linear dependence is observed in the paramagnetism region. A phase transition accompanied by an essentially abrupt increase of resistance occurs at temperatures $T<T^*$. At temperatures below the phase transition the resistance decreases with temperature, and the slope of the change is different for different samples. Nonetheless, a common typical sign of the indicated phase transition is a negative magnetoresistance, which is observed for all experimental samples in temperature range T_1-T_2 in a weak ($\sim$50 Oe) constant magnetic field. In addition, not only R_s but also X_s and therefore the total impedance are sensitive to the transition and a magnetic field, as is evident in Fig. 6.

The above-described features in the behavior of R_s at $T<T_1$ are probably common to all families of compounds RM_4Al_8 with transition metals.

According to Refs. 1–3, this is because all compounds of this type possess the same magnetic structure with three magnetic sublattices: R and two M sublattices. At the Néel temperature T_N they all undergo an antiferromagnetic ordering, and for $T_1<T_N$ there occurs a magnetostructural phase transition where antiferromagnetically coupled layers, separated by layers of a rare-earth metal, which can be nonmagnetic, weakly magnetic, or magnetic, are formed. In other words, a ''magnet–rare-earth–magnet'' superlattice, whose electric parameters are sensitive to a weak constant magnetic field, forms.

If the boundary region between the antiferromagnetic layers is nonmagnetic, then superconductivity occurs precisely here, and therefore a ''magnet–superconductor–magnet'' superlattice is formed. This explains the small amount of superconducting phase. In different compounds the M and R atoms can possess a magnetic moment; this changes the conditions for the appearance of a superconducting phase. The more pronounced the magnetic properties of R, the less superconducting phase is formed. Indeed, in compounds with scandium with a strongly magnetic transition metal Fe the superconducting phase is formed though in smaller quantities than in a compound with Lu. At the same time, in compounds with cerium—a strong paramagnet—superconductivity is not observed, at least at temperatures $T\leqslant 2$ K. In addition, as asserted in Ref. 12, magnetic ordering is not observed in $CeCr_4Al_8$. In Ref. 12 a large value of the Sommerfeld constant γ, obtained at low temperatures and indicating the presence of heavy fermions in this compound, is noted. Figure 3b (curve *3*) shows our curve of C/T versus T^2 for $CeCr_4Al_8$. Our results agree to within 10–15% with the data presented in Ref. 12.

The compound YCr_4Al_8, consisting of nonmagnetic yttrium and a weak antiferromagnet chromium, is interesting. For this compound $T_c=4.5$ K. But our preliminary investigations of a YFe_4Al_8 crystal indicate that replacing Cr with Fe increases T_c up to 6 K.

The large (0.22 J/mole$\times$K^2) value of γ in the compound YCr_4Al_8 is interesting (Fig. 3b, curves 1, 2). We recall that in $LuFe_4Al_8$ $\gamma=0.075$ J/mole$\times$K^2.

We note that a superconducting phase likewise is not formed in the compound YMn_4Al_8. This compound contains virtually nonmagnetic yttrium and weakly magnetic manganese. Manganese can be magnetic or nonmagnetic depending on the Mn–Mn distance. The critical distance $d_c=2.6$ Å; for $d<d_c$ the magnetic moment vanishes. This should be noted in connection with the following circumstances. Our results for the dependence of the specific heat $C(T)$ and resistance $R(T)$ of the compound YMn_4Al_8 differ from the dependences presented in Ref. 13, where no anomalies were observed in the behavior of the specific heat in the range 1.5–200 K. Our sample at low temperatures exhibits anomalies which are accompanied by hysteresis. Such a discrepancy could be due to the existence of a phase with Mn in our samples; such a phase possesses a magnetic moment and undergoes magnetic ordering at low temperatures.

We note nonetheless that the compounds $CeFe_4Al_8$, $CeCr_4Al_8$, and YMn_4Al_8 exhibit the same characteristic behavior as systems exhibiting superconductivity: an abrupt increase of the electric resistance at a certain temperature, accompanied by a negative magnetoresistance with decreasing temperature. (It has not been ruled out that in these compounds a superconducting phase can form at lower temperatures.)

It is evident in Figs. 8a and 9 that two noticeable anomalies are observed in the regular dependences $R_s(T)$ and $C(T)$ of the compound UCu_4AL_8: in the region 30–40 K and near 60 K. Small anomalies in $R_s(T)$ were also observed in the

temperature range 225–200 K. It is known that for $UCu_{4+x}Al_{8-x}$ T_N is sensitive to the concentration ratio of the components. For $x=0$ $T_N=40$ K and decreases to 5 K for $x=1.5$.[9] For our samples the degree of deviation from stoichiometry is unknown. Consequently, we attribute the anomalies at $T=30-40$ K to antiferromagnetic ordering. Since these temperatures are somewhat below 40 K, the remaining anomalies could be due to imperfection of the samples.

It should be noted that in contrast to systems of the type RFe_4Al_8, a negative magnetoresistance is not observed in the UCu_4Al_8 system.

Just as in $\rho(T)$ in Ref. 10, anomalies are not observed in the temperature dependences of R_s for compounds $LaAg_6In_6$ and $PrAg_6In_6$ in the temperature range 5–300 K. This confirms that there is no antiferromagnetic ordering in this temperature range. Comparing the dependences $R_s(T)$ and $\rho(T)$ from Ref. 10 shows that all experimental temperatures the standard relation of electrodynamics is satisfied: $R_s \sim \rho^{0.5}$.

The behavior of the superconducting phase in the compound $PrAg_6In_6$ with $T_c=8.3$ K was quite unexpected. It was known previously that a superconducting phase exists in the pseudoternary compound $Pr(Rh_{0.85}Ru_{0.15})B_4$ $T_c=2.3$ K[14] and in $PrRu_4As_{12}$with $T_c=2.4$ K.[15] The data on the high-temperature superconductor $PrBa_2Cu_3O_x$ presented in Refs. 16–18 are especially interesting. Unusual properties of this compound were observed in these works. Its structural and physical properties were nonuniform and they depended strongly on the technological conditions under which the samples were obtained. Thus, the samples can be insulators, metals, or superconductors with T_c ranging from 0 to 80 K. The amount of the superconducting phase also fluctuates over wide limits. This indicates once again the great importance of further comprehensive investigations of ternary rare-earth compounds fabricated by different technological techniques. A superconducting phase is not observed in UCu_4Al_8 and $LaAg_6In_6$ samples, at least above 4.5 K.

CONCLUSIONS

In summary, the observation of superconductivity in the compounds $LuFe_4Al_8$, $ScFe_4Al_8$, YFe_4Al_8, YCr_4Al_8, and $PrAg_6In_6$ makes it possible to talk about a new class of superconductors, whose superconductivity is associated with the magnetic state of the compounds.[1]

It should be noted that the properties of the samples could depend in many ways on the preparation technology; such properties are very sensitive to stoichiometry. For example, in the compound RFe_xAl_{12-x} antiferromagnetism, which appears at $x=4$, transforms as x increases into a spin glass and then into ferromagnetism. This could explain the contradictions existing in the literature concerning the properties and parameters of compounds belonging to this family.

It should be noted that the abrupt increase of the resistivity near the Néel temperature was observed previously in binary compounds RMn_{12}, likewise possessing $ThMn_{12}$ structure.[19] Consequently, it is of interest to determine the general and distinguishing features of magnetic ordering in ternary and binary compounds with the same structure.

Further investigations of high quality samples, preferably single crystals, are required in order to discuss the questions of Fermi or non-Fermi liquid behavior of the compounds, the type of magnetic, structural, and superconducting transitions, the values of their characteristic parameters, the presence of heavy fermions, and other properties.

We thank V. N. Svetlov, E. L. Kravchenko, and V. B. Stepanov for their contributions to the annealing work performed on some of the experimental samples.

This work was supported by the Ukrainian Ministry of Education and Science, contract No. 2M/75–2000.

[1)]When this article was already in publication, two works (K. Shimizu, T. Kiura, S. Furomoto, K. Takeda, K. Kontani, U. Onuki, and K. Amaya, Nature **412**, 316 (2001); S. Saxena and P. Littlewood, Nature **412**, 290 (2001)), where superconductivity of pure iron at $T<2$ K under strong compression was reported, appeared. In this connection we would like to note that, for example, in a $ScFe_4Al_8$ single crystal the Fe–Fe distance is 2.52 Å instead of 2.86 Å in pure metallic iron (J. Stepien-Damm, private communication). Therefore, iron in a $ThMn_{12}$ type crystal lattice is subjected to strong chemical compression (about 12%). Consequently, it could be that the superconductivity that we observed is due to the superconductivity of chemically compressed iron and chromium sublattices.

[1] K. H. Buschow, J. H. N. Van Vucht, and W. Van der Hoogenhoff, J. Less-Common Met. **50**, 145 (1976).
[2] A. M. Van der Kraan and K. H. J. Buschow, Physica **86**, 93 (1997).
[3] K. H. J. Buschow and A. M. Van der Kraan, J. Phys. F: Met. Phys. **8**, 921 (1978).
[4] J. A. Paixao, S. Langridge, S. A. Sorensen, B. Lebech, A. P. Gonsalves, G. H. Lander, P. J. Provn, P. Burlet, and E. Talik, Physica B **234–236**, 614 (1997).
[5] P. Schobinger-Papamantelles, K. H. J. Buschow, and C. Ritter, J. Magn. Magn. Mater. **186**, 21 (1998).
[6] A. M. Gurevich, V. M. Dmitriev, V. N. Eropkin, L. A. Ishchenko, N. N. Prentslau, and L. V. Shlyk. Fiz. Nizk. Temp. **25**, 19 (1999) [Low Temp. Phys. **25**, 10 (1999)].
[7] A. M. Gurevich, V. M. Dmitriev, V. N. Eropkin, L. A. Ishchenko, N. N. Prentslau, and L. V. Shlyk, in *Abstracts of Reports at the 31st Conference on Low-Temperature Physics* (Moscow, 1998), p. 142.
[8] S. Suski, B. Kotur, and K. Wochowski, Physica B **281-282**, 81 (2000).
[9] W. Suski, in *Handbook of the Physics and Chemistry of Rare Earths*, edited by Karl A. Gschneidner, Jr. and LeRoy Eyring (Elsevier, New York, 1996).
[10] V. I. Zaremba, Ya. M. Kalychak, Ya. V. Galadzhun, W. Suski, and K. Wochowski, J. Solid State Chem. **145**, 216 (1999).
[11] V. M. Dmitriev, M. N. Ofitserov, and N. N. Prentslau, Radiotekhnika **97**, 91 (1993).
[12] H. Ido, T. Nishioka, and M. Kontani, J. Magn. Magn. Mater. **177–181**, 385 (1998).
[13] I. H. Hagmusa, J. C. P. Klaasse, E. Bruk, F. R. de Boer, and K. H. J. Buschow, J. Alloys Compd. **299**, 21 (2000).
[14] D. C. Johnson, Solid State Commun. **24**, 699 (1977).
[15] J. Shirotani, T. Uchimumi, K. Ohno, C. Sekine, Y. Nakazawa, K. Kanoda, S. Todo, and T. Yagi, Phys. Rev. B **56**, 7866 (1997).
[16] H. A. Blackstead, J. D. Dow, B. B. Shrisey, J. S. Horwits, M. A. Black, P. J. McGinn, A. E. Klunzinger, and D. G. Pulling, Phys. Rev. B **54**, 6122 (1996).
[17] Z. Zou, J. Ye, K. Oka, and Y. Nishihara, Phys. Rev. Lett. **80**, 1074 (1998).
[18] J. Ye, Z. Zou, A. Matsushita, K. Oka, Y. Nishihara, and T. Matsumoto, Phys. Rev. B **58**, 619 (1998).
[19] Y. Amako, H. Nagai, and K. Adachi, J. Phys. Soc. Jpn. **62**, 3355 (1993).

Translated by M. E. Alferieff

LOW-TEMPERATURE PHYSICS OF PLASTICITY AND STRENGTH

Effect of low temperatures on deformation localization in supersaturated Al–Li alloys

T. V. Grigorova, N. V. Isaev,* V. D. Natsik, and S. É. Shumilin

B. I. Verkin Physicotechnical Institute for Low Temperatures, Ukrainian National Academy of Sciences, pr. Lenina 47, Khar'kov, 61103, Ukraine

(Submitted June 5, 2001)
Fiz. Nizk. Temp. **27**, 1317–1322 (November 2001)

Active loading at temperatures 295, 77, and 0.5 K is used to study the parameters of the stretching curve and the plastic deformation distribution in quenched and aged Al–Li alloys with 7.0 and 10.4 at.% lithium. It is shown that for aged alloys, in contrast to quenched alloys, the strength is characteristically high, the plasticity reserves are low, and the deformation distribution (macroscopic sections of deformation localization) is nonuniform, if loading is conducted at room and low temperatures (295 and 77 K). The deformation of quenched and aged alloys under deep cooling (at temperature 0.5 K) is distributed more homogeneously through the samples. The results are attributed to the influence of low temperatures on the rate of thermally activated processes, controlling the motion of dislocations through impurity barriers and the deformation-diffusion dissolution of δ' precipitates. © *2001 American Institute of Physics.* [DOI: 10.1063/1.1421465]

INTRODUCTION

The plasticity of supersaturated alloys exhibits a number of interesting features due to two effects: aging and the associated dispersion hardening.[1] Particles of a new phase (precipitates), arising in the solvent matrix as a result of aging, are a major factor influencing the dislocation multiplication and mobility in alloys. The size and volume fraction of precipitates and the plasticity parameters of an alloy depend very strongly on the conditions of aging, first and foremost, its duration Δt_a and temperature T_a. Another factor influencing the kinetics of plastic deformation of an alloy is the deformation temperature T_d of the sample. The temperature T_d determines the rate of elementary thermally activated processes, which make it possible for dislocations to overcome impurity atoms and precipitates.

At close to room temperatures aging of Al–Li alloys containing more than 5 at.% lithium is accompanied by the formation of coherent precipitates of a δ' phase (Al_3Li) with a $L1_2$ superlattice in an fcc aluminum matrix.[2] The appearance of δ' precipitates makes the plastic deformation process in a supersaturated alloy specific primarily due to the mechanism by which slipping dislocations shear the precipitates.[2,3] It is well known that plastic deformation of the fcc matrix of aluminum is produced by conservative motion of whole dislocations of the slip system $\{111\}\langle 110\rangle$. However, in an $L1_2$ superstructure such dislocations are not whole. Shearing a δ' precipitate, they form an anitphase boundary in it, increasing the deforming stress. In addition, transverse slip of these dislocations from the $\{111\}$ into the $\{010\}$ plane can occur inside a precipitate, as a result of which steps appear on the dislocation lines and additional stress is required to overcome these steps. Since transverse slip in precipitates is a thermally activated process, the additional stress required for plastic deformation of the alloy at a fixed rate is strongly temperature-dependent.

Another feature, arising as a result of phase decomposition, of plastic deformation in a supersaturated Al–Li alloy is spatial nonuniformity of plastic flow, detected at room temperature.[4] The new defects—antiphase boundary inside a δ' precipitate shearing a dislocation and steps on the surface of the precipitate—increase the internal energy of the precipitate. As a result of the thermally activated diffusion of lithium, some precipitates dissolve during plastic flow and precipitate-free channels, where dislocation motion is facilitated, form in the crystal. Localization of plastic flow in such channels results in deformation hardening (formation of dissolution clusters in them), opening of cracks, and premature fracture of the sample.

Transverse slip of dislocations inside precipitates and deformation–diffusion dissolution of precipitates are thermally activated processes that can be suppressed at low temperatures. Consequently, the laws of plastic flow of supersaturated Al–Li alloys under sufficiently deep cooling should differ from the laws described in the reviews Refs. 2 and 3. It has already been shown in Ref. 5 that the δ'-precipitate-associated decrease of the yield stress at temperatures below 50 K is compensated by an increase in the yield stress in the solid solution (in the regions between precipitates) as a result of the thermally activated motion of dislocations through local barriers. As a result of the superposition of two processes with opposite temperature sensitivity, the total yield stress of the alloy is athermal. The present work is devoted to studying the influence of low and superlow temperatures on the localization of plastic deformation in supersaturated Al–Li alloys with various phase compositions: homogeneous quenched alloys and aged heterogeneous alloys, containing precipitates of a second phase, are studied.

1. EXPERIMENTAL PROCEDURE

Supersaturated Al–Li alloys with 7.0 and 10.4 at.% lithium were investigated. The flat polycrystalline samples (grain diameter 0.31 and 0.44 mm, respectively) were paddle-shaped with a $15\times3\times1\,\mathrm{mm}^3$ working part. The samples were subjected to homogenizing annealing at 800–810 K for 5 h, quenching in ''ice water,'' and aging up to 7.5 h at $T_a=473\,\mathrm{K}$. The aging regime chosen, on the basis of structural investigations,[6–8] produces a large increase of the radius and volume fraction of δ' precipitates: for average lithium concentrations 7 and 10 at.% the particle radii are 10–15 and 15–20 nm and the volume fractions of the particles are 0.03–0.06 and 0.15–0.20, respectively.

The quenched and aged samples were deformed by stretching at the constant rate $\dot{\varepsilon}=10^{-4}\,\mathrm{s}^{-1}$ in a cryostat at temperatures $T_d=295$, 77, and 0.5 K. Liquid nitrogen and liquid He^4 and He^3 were used for cryostating.

The influence of the aging time Δt_a and the deformation temperature T_d on the parameters of the stretching curve load P—absolute elongation Δl and on the macroscopic plastic deformation distribution along the sample was studied. To this end, prior to deformation, a thin needle was used to deposit 15 markers spaced every 1 mm on the entire working part of a sample and the deformation of various sections of the sample was estimated according to the displacement of the markers in an optical microscope. The displacement measurement error was 0.01 mm.

2. EXPERIMENTAL RESULTS AND DISCUSSION

2.1. Stretching curves

The load–elongation curves $P(\Delta l)$ for samples of Al–Li alloys deformed after homogenization and quenching and after aging are displayed in Figs. 1 and 2. The load P, the elongation up to rupture $\Delta l_{\max}$, and the hardening factor of the quenched samples increase with decreasing deformation temperature T_d. This is characteristic for most aluminum–based solid solutions.

The stretching diagrams in Figs. 1 and 2 have distinct critical values of the load P_0 which correspond to the onset of plastic flow. In addition, for all experimental samples used in this work the maximum elongation and change in the transverse sections remain very small compared with the initial lengths l_0 and transverse sections S_0. Consequently, the yield point $\sigma_0=P_0/S_0$ and the maximum relative deformation $\varepsilon_{\max}=\Delta l_{\max}/l_0$ can be regarded as the plasticity parameters of the alloys.

The plasticity parameters of the alloys change substantially as a result of aging at $T=473\,\mathrm{K}$: an increase in the yield point σ_0 is accompanied by a sharp decrease in the plasticity reserves $\varepsilon_{\max}$ compared with the quenched state. Figure 3 shows the yield stress σ_0 and the maximum elongation $\varepsilon_{\max}$ versus the aging time Δt_a of the alloy Al–10.4 at.% Li, deformed at $T_d=295$, 77, and 0.5 K. The quantity σ_0 increases appreciably, and the plasticity reserve $\varepsilon_{\max}$ decreases for $\Delta t_a<4$ h; further aging does not increase σ_0 or decrease $\varepsilon_{\max}$. We call attention to the characteristic features of the deformation of the alloys Al–Li at sub-Kelvin temperatures: at $T_d=0.5\,\mathrm{K}$ the plasticity reserve $\varepsilon_{\max}$ even increases; in addition, abrupt deformation (abrupt change in the load, see inset in Fig. 1), whose study falls outside the scope of the present work, is observed in quenched and aged alloys deformed at $T_d=0.5\,\mathrm{K}$.

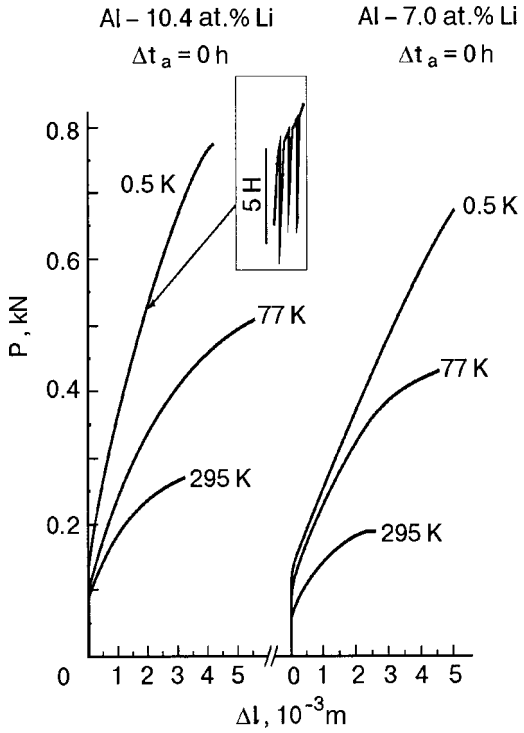

FIG. 1. Load–elongation curves $P(\Delta l)$ of quenched Al–Li alloys ($\Delta t_a=0$ h) deformed at temperatures $T_d=295$, 77, and 0.5 K.

The parameters σ_0 and $\varepsilon_{\max}$ show similar behavior as a function of Δt_a and T_d for the alloys Al–7.0 at.% Li.

2.2. Deformation distribution along the sample

Observations of individual sections ($i=1,2,\ldots,15$) of the working part of the deformed samples showed that the character of the deformation distribution along a sample depends strongly on the aging time Δt_a and the temperature T_d. Typical histograms illustrating the relative deformation $\varepsilon_i=\Delta l_i/l_i$ of individual sections of a sample are displayed in Figs. 4 and 5. The data correspond to average deformations $\bar{\varepsilon}\leqslant 0.08$.

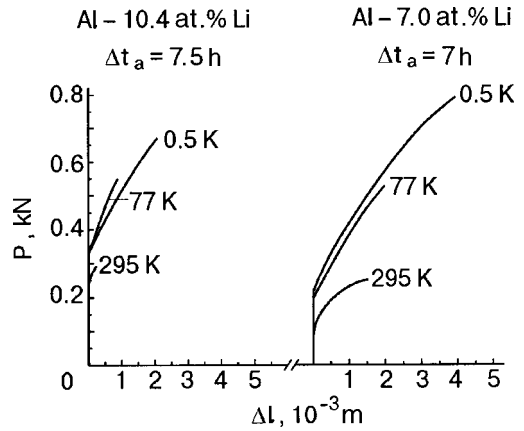

FIG. 2. Load–elongation curves $P(\Delta l)$ of aged Al–Li alloys deformed at temperatures $T_d=295$, 77, and 0.5 K.

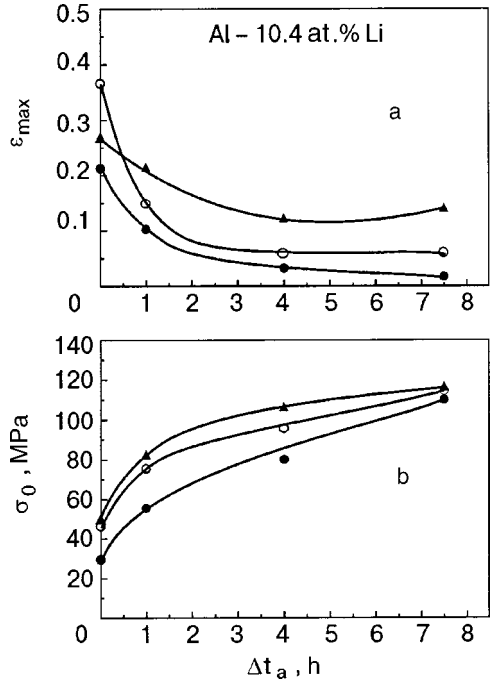

FIG. 3. Maximum deformation ε_{max} (a) and yield stress σ_0 (b) versus aging time for the alloy Al–10.4 at.% Li deformed at temperatures $T_d=295$ (●), 77 K (○), and 0.5 K (▲).

Comparing the relative deformation of various sections of quenched and aged samples, deformed at $T_d=295$, 77, and 0.5 K, we note the following features:

1) a nonuniform distribution of deformation (sections of deformation localization) is observed only in aged samples containing precipitates of a second phase (Fig. 5);

2) at temperature T_d the quenched (Fig. 4) and aged (Fig. 5) samples deform with the same degree of uniformity.

The influence of the decomposition of a supersaturated solid solution and of the formation of precipitates during aging on deformation localization in individual sections of the samples is illustrated in Fig. 6. Histograms of a Al–10.4 at.% Li sample are presented here. This sample was first deformed after homogenization and quenching (A), then

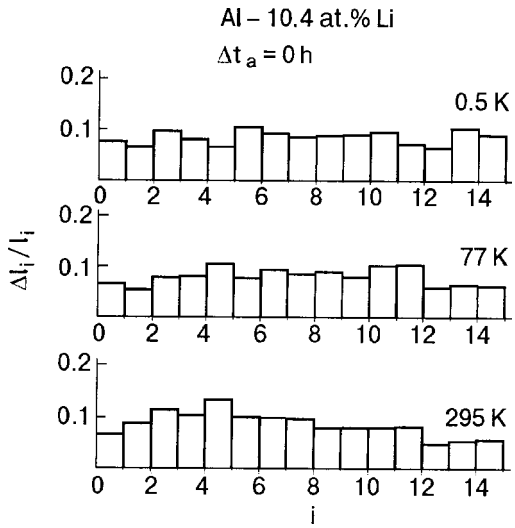

FIG. 4. Distribution of the relative deformation in a quenched Al–10.4 at.% Li sample deformed at the indicated temperatures.

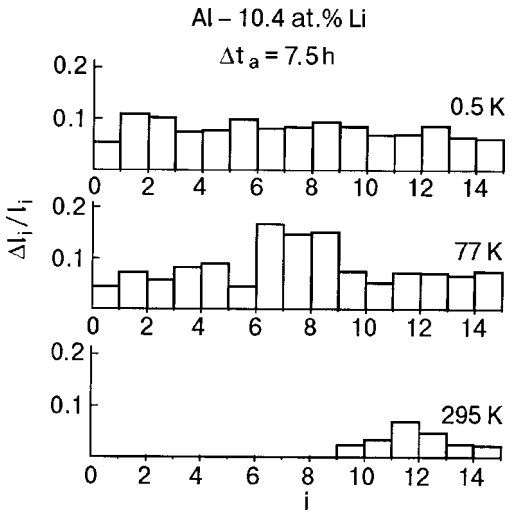

FIG. 5. Distribution of the relative deformation in an aged Al–10.4 at.% Li sample deformed at the indicated temperatures.

aged for 1.5 h, and once again deformed (B). The histogram A illustrates the comparatively uniform deformation distribution characteristic for single-phase alloy, while sections of deformation localization can be seen in histogram B. The tests were also performed in the opposite sequence: first an aged sample was deformed and then the sample was homogenized and deformed once again. The deformation localization sections arising at the first stage vanished after homogenizing annealing. However, this result could be due not only to the phase composition of the sample but also the relaxational processes occurring at high annealing temperature.

The variance D^2 of the quantity $\varepsilon_i=\Delta l_i/l_i$ can serve, to a first approximation, as a parameter characterizing the degree of nonuniformity (localization) of deformation:

$$D^2=\frac{1}{15}\sum_{i=1}^{15}\left(\frac{\varepsilon_i}{\overline{\varepsilon_i}}-1\right)^2,$$

where

$$\overline{\varepsilon_i}=\frac{1}{15}\sum_{i=1}^{15}\varepsilon_i.$$

The estimates of the variance for different aging times and deformation temperatures of the alloy Al–10.4 at.% Li are presented in Fig. 7. The variance of the local deformations along the samples is similar for the alloy Al–7.0 at.% Li.

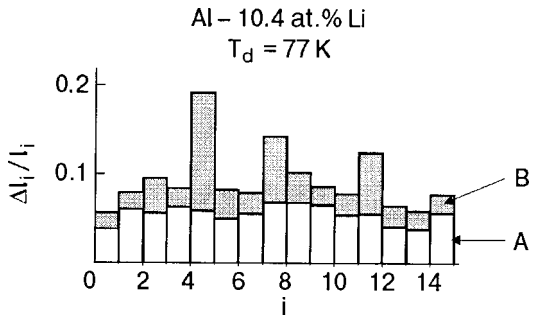

FIG. 6. Distribution of the relative deformation in a Al–10.4 at.% Li sample deformed at 77 K after quenching (A) and after aging (B) for 1.5 h.

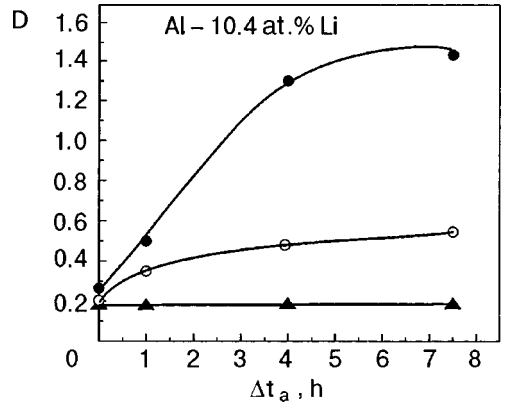

FIG. 7. Variance of the relative deformation as a result of aging of the alloy Al–10.4 at.% Li for Δt_a and deformation at temperatures $T_d = 295$ K (●), 77 K (○), and 0.5 K (▲).

It is evident from Figs. 4 and 7 that the plastic deformation of quenched samples for moderately low and sub-Kelvin temperatures is distinguished by a high degree of uniformity: this case corresponds to quite low values $D \approx 0.2-0.3$. Aging of the samples for $\Delta t_a \leqslant 4$ h creates the prerequisites for deformation localization, but such localization appears only for deformation at room and moderately low temperatures; here, the quantity D, increases by a factor of 2–6 (Fig. 7). Localization is not observed for deformation of aged samples at sub-Kelvin temperatures. It is also seen in Fig. 7 that long-time aging with $\Delta t_a > 4$ h does not increase D, i.e. it does not intensify the localization effect.

The dependence $D(\Delta t_a, T_d)$ shown in Fig. 7 qualitatively agrees with the experimental dependence $\varepsilon_{\max}(\Delta t_a, T_d)$ in Fig. 3: deformation localization is the prerequisite for decreasing the plasticity reserves of the sample.

It was previously believed that localization degrades the macroscopic characteristics of an alloy for large deformations $\varepsilon \approx 0.2$ at room and high temperatures.[4,6] The fundamental possibility of localization for small deformations was simulated in Ref. 9. In our experiments an increase in the parameter D characterizing the degree of localization is observed even for deformations $\varepsilon \approx 0.08$ and depends strongly on the temperature T_d. The weak localization of deformation at sub-Kelvin temperatures confirms the hypothesis mentioned in the introduction that thermally activated processes are the basis of this phenomenon: low temperatures prevent deformation-stimulated dissolution of precipitates and formation of channels free of precipitates of a second phase. Here, the plasticity reserve of the alloy does not decrease, but rather the yield stress remains high as a result of the increase in the friction stress in the matrix.

It should be noted that macroscopic-scale localization of plastic deformation of the alloys Al–Li was detected and analyzed previously in real[4] and computer[9] experiments: precipitate-free channels were of the order of $10^{-5}-10^{-4}$ mm wide. In our experiments macroscopic 1 mm wide deformation-localization zones were studied. It is natural infer that such large-scale deformation localization is due to spatial fluctuations, arising as a result of deformation-diffusion dissolution of precipitates, of the distribution of free channels.

3. CONCLUSIONS

Two qualitative conclusions can be drawn from the experimental data obtained in this investigation:

— the deformation kinetics and the plasticity parameters of supersaturated Al–Li alloys at moderately low and room temperatures depend strongly on the aging time and therefore on the size and volume fraction of δ' precipitates; this is due to the specific manner in which dislocations shear the precipitates and to the deformation–diffusion dissolution effect;

— under deep cooling, when thermally activated processes are suppressed, quenched and aged Al–Li alloys characteristically show a combination of high strength and a plasticity reserve.

We thank S. N. Smirnov and V. S. Fomenko for helpful recommendations.

*E-mail: isaev@ilt.kharkov.ua

[1] V. Gerold, ''Precipitation hardening'' in *Dislocations in Solids*, edited by F. R. N. Nabarro (1979), Vol. 4, p. 219.
[2] I. N. Fridlyander, K. V. Chuistov, A. L. Berezina, and N. I. Kolobnev *Aluminum–Lithium Alloys: Structure and Properties* (Naukova dumka, Kiev, 1992).
[3] E. Nembach, Prog. Mater. Sci. **45**, 276 (2000).
[4] Y. Brechet, F. Louchet, C. Marchionni, and J. L. Verger-Gaugry, Philos. Mag. A **56**, 353 (1987).
[5] N. V. Isaev, V. V. Pustovalov, V. S. Fomenko, and S. É. Shumilin, Fiz. Nizk. Temp. **22**, 99 (1996); [Low Temp. Phys. **22**, 74 (1996)].
[6] T. H. Sanders, Jr. and E. A. Starke, Jr., Acta Mater. **30**, 927 (1982).
[7] V. Gerold, H.-J. Gudladt, and J. Lendvai, Phys. Status Solidi A **131**, 509 (1992).
[8] K. Triuncauf, J. Pesicka, C. Schlesier, and E. Nembach, Phys. Status Solidi A **131**, 345 (1992).
[9] A. Kalogeridis, J. Pesicka, and E. Nembach, Acta Mater. **47**, 1953 (1999).

Translated by M. E. Alferieff

SHORT NOTES

Oscillatory acoustoelectronic effect in quasi-two-dimensional conductors in a quantizing magnetic field

O. V. Kirichenko* and V. G. Peschanskiĭ

B. I. Verkin Physicotechnical Institute for Low Temperatures, Ukrainian National Academy of Sciences, pr. Lenina 47, Khar'kov, 61103, Ukraine

(Submitted May 24, 2001)
Fiz. Nizk. Temp. **27**, 1323–1326 (November 2001)

It is shown that the quasi-two-dimensional character of the electron energy spectrum of a layered conductor results in a large decrease of the absorption of longitudinal sound propagating in a direction normal to the layers in a quantizing magnetic field. © *2001 American Institute of Physics.* [DOI: 10.1063/1.1421466]

Acoustoelectronic phenomena in degenerate conductors in a sufficiently strong magnetic field are very sensitive to the form of the electronic energy spectrum.[1,2] They were successfully used to reconstruct from the experimental data the Fermi surface—the main characteristic of the conduction electron spectrum in metals. At low temperatures, where the temperature broadening of the Fermi distribution function of charge carriers is much smaller than the splitting between the magnetic field quantized energy levels, the dependence of the damping decrement of the sound on the magnetic field H has the form of giant oscillations.[3]

At such low temperatures the damping of sound waves in degenerate conductors is due primarily to the interaction of charge carriers with the wave. With adequate accuracy the absorption of acoustic energy per unit time per unit volume of a conductor is equal to the dissipative electron function

$$Q = T\dot{S}, \tag{1}$$

where T is the temperature and S is the entropy density of the electrons. The quantity S is determined by the relation[4,5]:

$$S = -\mathrm{Tr}\{\hat{f}\ln\hat{f} + (1-\hat{f})\ln(1-\hat{f})\}, \tag{2}$$

where the nonequilibrium statistical operator $\hat{f}$ satisfies the kinetic equation

$$\frac{\partial\hat{f}}{\partial t} + \hat{\mathbf{v}}\cdot\frac{\partial\hat{f}}{\partial\mathbf{r}} + [\hat{H}_0 + \hat{H}_1, \hat{f}] = \hat{W}_{\mathrm{coll}}\{\hat{f}\}. \tag{3}$$

The sound wave excites the accompanying electromagnetic wave and renormalizes the electron energy ε by the amount $\delta\varepsilon = \Lambda_{ij}u_{ij}$. This perturbation of the electronic system by lattice vibrations takes account of the correction $\hat{H}_1$ to the unperturbed electron Hamiltonian $\hat{H}_0$. Here $\hat{\mathbf{v}}$ is the electron velocity operator, u_{ik} is the crystal deformation tensor, and Λ_{ik} is the deformation potential tensor taking account of the conservation of the number of electrons. The summation in Eq. (2) extends over all variables defining the state of the electrons, including the spin variables.

The collision operator $\hat{W}_{\mathrm{coll}}$ takes account of the interaction of electrons with various scatterers—impurity atoms, lattice defects, phonons, and others. According to the principle of detailed balance, the collision operator acting on the equilibrium statistical operator $\hat{f}_0$ gives zero, i.e., $\hat{W}_{\mathrm{coll}}\{\hat{f}_0\} = 0$.

We shall assume that the perturbation of the electron system by a sound wave with frequency ω is weak, and in the expression

$$\dot{S} = \mathrm{Tr}\left\{\hat{W}_{\mathrm{coll}}\{\hat{f}\}\ln\frac{1-\hat{f}}{\hat{f}}\right\} \tag{4}$$

we shall confine our attention to the asymptote with respect to the small deviation of the statistical operator from the equilibrium operator $\hat{f}_1 = \hat{f} - \hat{f}_0$.

In the linear approximation in the weak perturbation of the electrons by a sound wave the collision operator $\hat{W}_{\mathrm{coll}}\{\hat{f}\}$ is a linear integral operator acting on $\hat{f}_1$. For greater clarity in calculating the dissipative function Q we shall employ the τ approximation for the collision operator, which makes it possible to represent this operator as the operator multiplying $\hat{f}_1$ by the collision frequency $1/\tau$:

$$\hat{W}_{\mathrm{coll}}\{\hat{f}_1\} = -\frac{\hat{f}_1}{\tau}. \tag{5}$$

In the collisionless limit, i.e. for $\omega\tau \gg 1$, the explicit form of the collision integral is immaterial, and for $\omega\tau \ll 1$ the representation of $\hat{W}_{\mathrm{coll}}\{\hat{f}_1\}$ in the form (5) is adequate in many cases, for example, for the propagation of longitudinal sound in the direction of a magnetic field $\mathbf{H} = (0, 0, H)$. We shall examine this case below and we shall calculate the sound damping constant Γ, equal to the ratio of the dissipative function to the acoustic energy flux density $\rho u^2\omega^2 s/2$, where ρ is the crystal density, s is the sound speed, and u is the displacement of the ions.

For longitudinally polarized sound there is no need to take account of the electromagnetic fields generated by the acoustic wave. When such fields are neglected only the di-

agonal components of the statistical operator differ from zero. Using the kinetic equation it is easy to obtain for the matrix element f_1^{nn} the expression

$$f_1^{nn}(P_y,p_z)\left(ikv_z-i\omega+\frac{1}{\tau}\right)=-\frac{\partial f_0(\varepsilon_n)}{\partial\varepsilon_n}\Lambda_{ij}^{nn}(P_y,p_z)\dot{u}_{ij}, \tag{6}$$

where k is the wave number. We employed the Landau gauge for the vector potential $\mathbf{A}=(0,Hx,0)$ of the magnetic field. Aside from the projection of the momentum p_z, another good quantum number is the projection of the generalized momentum P_y, which is related with the kinematic momentum p_y as $P_y=p_y+eHx/c$. The continuously varying p_z and P_y and the discrete quantum number n, which enumerates the energy levels of an electron in a magnetic field, were chosen as the independent variables defining the state of an electron.

The sound absorption coefficient can be easily found for an arbitrary electronic energy spectrum. For definiteness we shall consider a layered conductor with a quasi-two-dimensional electronic energy spectrum with the very simple form

$$\varepsilon(\mathbf{p})=\frac{p_x^2+p_y^2}{2m}-\eta v_0\frac{\hbar}{a}\cos\frac{ap_z}{\hbar} \tag{7}$$

under conditions where

$$T\ll\hbar\Omega\ll\eta\mu. \tag{8}$$

Here a is the disetance between the layers, v_0 is the Fermi velocity, $\Omega=eH/mc$, m and e are the electron mass and charge, c is the speed of light, and $\eta\ll1$ is the quasi-two-dimensionality parameter.

A component of the deformation potential can be described as

$$\Lambda_{zz}=\eta mv_0^2\cos\frac{ap_z}{\hbar}. \tag{9}$$

The electron energy levels neglecting the spin splitting

$$\varepsilon_n=\hbar\Omega\left(n+\frac{1}{2}\right)-\eta v_0\frac{\hbar}{a}\cos\frac{ap_z}{\hbar} \tag{10}$$

depend only on the two variables n and p_z, and the dissipative function of the electron system assumes the quite simple form

$$Q=-\frac{2eH}{c(2\pi\hbar)^2}\sum_n\int_0^{2\pi\hbar/a}dp_z\frac{\partial f_0(\varepsilon_n)}{\partial\varepsilon_n}\frac{k^2\omega^2|\Lambda_{zz}\dot{u}|^2\tau}{1+\tau^2(kv_z-\omega)^2}. \tag{11}$$

Substituting

$$\frac{\partial f_0}{\partial\varepsilon_n}=-\frac{1}{4Tc\hbar^2[(\varepsilon_n-\mu)/2T]}$$

into Eq. (10) and using the dimensionless variable $x=ap_z/\hbar$ we obtain the following expression for the damping constant:

$$\Gamma=\Gamma_0\eta^2\frac{\hbar\Omega}{T}kv_0\tau\sum_n\int_0^{2\pi}dxF(x)G_n(x), \tag{12}$$

where $\Gamma_0=mNv_0\omega/4\pi\rho s^2$, N is the charge carrier density, μ is the chemical potential, and

$$F(x)=\frac{\cos^2x}{1+\tau^2(\eta kv_0\sin x-\omega)^2},$$

$$G_n(x)=\cosh^{-2}\left[\frac{-\mu+\Omega\hbar\left(n+\frac{1}{2}\right)-(\eta\hbar v_0/a)\cos x}{2T}\right].$$

For $\omega\tau\ll s/\eta v_0$ the function $F(x)$ possesses sharp peaks of the order of $1/k\eta v_0\tau$ wide, but in a wide range of acoustic frequencies such that $\omega\tau<1$, the functions are $G_n(x)$ are sharper. The width of the peaks of these functions is of the order of $(T/\eta\mu)^{1/2}$ and they are associated with the sharpest peaks in the acoustic energy absorption. They occur for magnetic fields satisfying the condition

$$\mu-\hbar\Omega\left(n+\frac{1}{2}\right)\pm\eta\frac{\hbar v_0}{a}=0. \tag{13}$$

The electron density of states has a singularity, which gives rise to a sharp increase of the acoustic energy absorption by electrons. The height of the peaks for $kv_0\tau\ll\mu/T$ is

$$\Gamma^{\max}\simeq\Gamma_0\frac{\hbar\Omega}{(T\mu)^{1/2}}\eta^{3/2}kv_0\tau, \tag{14}$$

and outside the peak the background part of the function $\Gamma(H)$ is $(T/\eta\mu)^{1/2}$ times smaller than $\Gamma^{\max}$. Compared with an istropic metal, longitudinal sound propagating in a direction normal to the layers of a quasi-two-dimensional conductor decays very weakly, and a plot of its dependence on the magnetic field $\Gamma(H)$ lies much below the analogous curve $\Gamma_M(H)$ for an isotropic metal. For example, for $kv_0\tau<(\mu/T)^{1/2}$ the ratio of the maximum values of the absorption coefficient is

$$\frac{\Gamma^{\max}}{\Gamma_M^{\max}}\simeq\eta^{3/2}. \tag{15}$$

Figure 1 shows Γ/Γ_0 versus the magnitude of a strong magnetic field.

It is easy to show that the magnetic field dependence of the absorption coefficient is qualitatively the same for arbitrary quasi-two-dimensional electronic energy spectrum. For

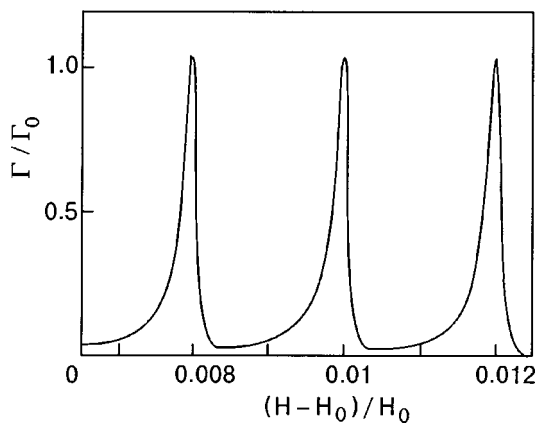

FIG. 1. Γ/Γ_0 versus $(H-H_0)/H_0$, where H_0 satisfies the relation $\Omega(H_0)/\mu=0.02$; $\eta=0.01$, $\omega\tau=0.1$, $kv_0\tau=5\times10^2$, $\mu/2T=10^4$.

an arbitrary dispersion law for charge carriers the electron density of states has a singularity, where the area of the section of the Fermi surface by the plane $p_z = \text{const}$ has an extremum as a function of p_z. Thus, the extremal area of the section of the Fermi surface determines the period of the oscillations of $\Gamma(H)$.

The relations presented above, as noted above, are valid in the semiclassical approximation, where $\eta\mu \gg \hbar\Omega$ and the chemical potential is essentially independent of the magnetic field strength. In the opposite limiting case $\hbar\Omega > \eta\mu$ the complex dependence of μ on H can no longer be ignored in Eq. (13). This case merits a separate investigation, especially for $\hbar\Omega \gg \eta\mu$, where the maximum of the absorption of acoustic energy splits into a doublet with the splitting proportional to the quasi-two-dimensionality parameter of the conductor.

The case examined above is the only case where anomalous acoustic transmission of a quasi-two-dimensional conductor occurs. For transversely polarized acoustic wave propagating in the direction of a magnetic field oriented in a direction normal to the layers an electromagnetic with electric field lying in the plane of the layers is excited. The result is that the Joule losses become very substantial, and as a result the sound absorption coefficient in the layered quasi-two-dimensional conductor is equal in order of magnitude to the absorption coefficient in a normal metal with the same charge carrier density.

*E-mail: kirichenko@ilt.kharkov.ua

[1] A. B. Pippard, Philos. Mag. **2**, 1147 (1958).
[2] É. A. Kaner, V. G. Peschanskiĭ, and I. A. Privorotskiĭ, Zh. Éksp. Teor. Fiz. **40**, 214 (1961) [Sov. Phys. JETP **13**, 147 (1961)].
[3] V. L. Gurevich, V. G. Skobov, and Yu. D. Firsov, Zh. Éksp. Teor. Fiz. **40**, 786 (1961) [Sov. Phys. JETP **13**, 552 (1961)].
[4] E. M. Lifshitz and L. P. Pitaevskiĭ, *Statistical Physics* (Nauka, Moscow, 1965), Part 2.
[5] D. N. Zubarev, *Nonequilibrium Statistical Thermodynamics* (Nauka, Moscow, 1971).

Translated by M. E. Alferieff

Identification of the stripe state of a $YBa_2Cu_3O_{6+x}$ superconductor according to optical absorption data

V. V. Eremenko, V. N. Samovarov,* V. L. Vakula, M. Yu. Libin, and S. A. Uyutnov

B. I. Verkin Physicotechnical Institute for Low Temperatures, Ukrainian National Academy of Sciences, pr. Lenina 47, Khar'kov, 61103, Ukraine

V. M. Rashkovan

Instituto Politécnico Nacional de México, Esime, Culhuacán, México

(Submitted June 21, 2001)
Fiz. Nizk. Temp. **27**, 1327–1331 (November 2001)

The doublet structure of the electron–bimagnon absorption band with maxima at 2.145 and 2.28 eV is observed for the first time for the metallic phase of $YBa_2Cu_3O_{6+x}$ with $x=0.85$ ($T_c=88$ K). As the YBCO film cools down, the doublet band arises quite sharply near the pseudogap state at $T<130$ K and remains in the superconducting phase at $T<T_c$. In the superconducting transition region the amplitude of each doublet component increases. Comparing with data on the splitting of the neutron scattering peak in YBCO [P. Dai *et al.*, Phys. Rev. Lett. **80**, 1738 (1998)] showed that the splitting of the absorption band reflects the formation of a stripe superstructure consisting alternating dielectric and metallic quasi-one-dimensional stripes.
 [DOI: 10.1063/1.1421467]

1. The question of the coexistence of antiferromagnetic (AF) and superconducting (SC) phases in copper-oxide HTSCs is now one of the most controversial questions in the problem of superconductivity. For these materials the question of the nature of the pseudogap (PG) state, preceding superconductivity in the temperature range $T_c<T<T^*$, is just as acute. These questions can be answered, for example, using the spin-echo, nuclear relaxation, angle-resolved photoemission spectroscopy methods (see the reviews in Refs. 1–4. Neutron scattering methods are especially informative.[5,6] However, at the present time there is no generally accepted point of view concerning the nature of the SC and PG states in copper-oxide HTSCs. Nonetheless, the conclusion that superconductivity in these compounds is associated with the phase separation of samples into dielectric (with short-range AF ordering) and metallic quasi-one-dimensional stripe phases[3–8] sounds increasingly more convincing. The metallic stripes with quasi-one-dimensional motion of holes are separated by dielectric stripes, which together form a superstructure that fluctuates in time and space.[3–7] Each stripe is several lattice constants wide. A static stripe structure can exist in manganates and nickelates.[8] Apparently, the stripe structure was first predicted theoretically in Ref. 9.

In the present paper we present the results of optical investigations, which we believe will lead to progress in the solution of questions concerning the PG and SC states on the basis of the stripe superstructure model. The results were obtained by absorption optical spectroscopy of YBCO films. In many respects this method has no analogs for classical low-temperature superconductors and can be regarded as a new independent method for investigating the superconductivity of HTSCs. The sensitivity of absorption spectra in the energy range 1 eV, much greater than the energy of the SC gap, to superconductivity was proved in Refs. 10–12. Diagnostics of the PG state on the basis of the absorption spectra in the visible-frequency range is presented in Ref. 13. The central results of these investigations can be formulated as follows.

1. In the metallic phase of $YBa_2Cu_3O_{6+x}$ an absorption band $A+J$ at ≈ 2.2 eV, identified as an electron–bimagnon band, arises in the region of formation of the PG state at temperatures $T<T^*$. When the samples are cooled below T^* this band appears even if it is absent in the metallic phase at room temperature. In the AF phase the intensity of the band increases sharply on cooling below the Néel temperature T_N.

2. In the SC phase the entire spectral composition of the intraband and interband optical absorption becomes ''frozen,'' and the electron–bimagnon band $A+J$ becomes temperature-independent.

These experimental data can serve as proof of the magnetic nature of the PG state and evidence for the spin-fluctuation mechanism of superconductivity in cuprate HTSCs.

In the present work we investigated the fine structure of the electron–bimagnon absorption band $A+J$ with temperature passage through the PG and SC states. The currently widely discussed data on inelastic neutron scattering in cuprate HTSCs served as the motivation for such experiments. The neutron experiments showed that near T_c the peak of the inelastic neutron scattering by incommensurate AF fluctuations (see Ref. 5 and references cited there), which is attributed to phase separation of the sample into dielectric and metallic stripes of a dynamic character,[3–7] splits near T_c.

2. Temperature investigations of the absorption spectra $\alpha(\omega)$ of $YBa_2Cu_3O_{6+x}$ films with $x\approx 0.3$ (dielectric AF phase) and $x\approx 0.85$ (metallic phase) were performed in the

temperature range 170–200 K. The critical temperature T_c for the metallic film was 88 K with SC transition width ≈ 1 K. The single-crystal films possessed *c* orientation relative to the $SrTiO_3$ substrate and their thickness was $l = 2300$ Å . The measurements of the absorption coefficient $\alpha(\omega)$ (optical density αl) were performed in unpolarized light ($\mathbf{E} \perp \mathbf{c}$). The absorption of the films was measured in the frequency range 1.8–2.6 eV, which contains the electron–bimagnon absorption band $A+J$. The YBCO absorption bands are identified in greater detail and the methodological features of the measurements are presented in preceding works.[13,14]

3. We start with the data for a dielectric film. First we note that at 300 K the absorption spectrum of such a film is typical for the dielectric phase of $YBa_2Cu_3O_{6+x}$ with $x < 0.4$.[13,14] The visible-frequency part of the absorption spectrum is described by a sum of three components: $\alpha l(300\ \mathrm{K}) = (\alpha l)_A + (\alpha l)_{A+J} + (\alpha l)_{CT}$, where $(\alpha l)_A$ is the narrow-band *A* component; $(\alpha l)_{A+J}$ is the narrow-band $A+J$ component; and, $(\alpha l)_{CT}$ is the continuum component of interband transitions through the optical gap $E_g = 1.7-1.8$ eV. The Gaussian contours

$$\alpha l(E) = \frac{\mu}{\sigma\sqrt{\pi}} \exp\left[-\frac{(E-E_0)^2}{2\sigma^2} \right], \qquad (1)$$

where σ is the variance of the contour, μ is the amplitude coefficient, and E_0 is the position of the maximum, describe the narrow-band components well. According to Refs. 13 and 14, the *A* component is due to transitions through the optical gap from the correlation maximum of the density of states at the top of the valence band (in the metallic phase the Fermi level shifts into the region of this maximum). At 300 K the parameters of the *A* contour in a dielectric are usually $E_0 \approx E_g$, $\sigma_A = 0.14-0.17$ eV, $\mu_A = 0.4-0.6$ eV. For our YBCO samples the parameters fell into this range of values. The $A+J$ band is split from the *A* band by the bimagnon excitation energy $\hbar\omega_{2m} \approx 3J \approx 0.3$ eV, where $J \approx 0.1$ eV is the exchange interaction energy of the spins in a CuO_2 plane. $A+J$ transitions arise as a result of *A* transitions but with the additional creation of two magnons with energy corresponding to the boundary of the Brillouin zone. At 300 K the parameters of the $A+J$ contour in $YBa_2Cu_3O_{6+x}$ for $x \approx 0.3$ were $E_0 = 2.055$ eV, $\sigma_{A+J} = 0.16$ eV, and $\mu_{A+J} = 0.32$ eV. As temperature decreases, the dielectric YBCO transforms into the AF phase, and for $x \approx 0.3-0.35$ the Néel temperature $T_N = 250-200$ K. In the AF phase, as a result of a decrease in magnon damping, the dispersion of the *A* and $A+J$ bands is smaller than at 300 K, and the amplitude of these bands, i.e. the oscillator strength of the transitions, increases.[14]

Figure 1 shows for the AF phase of $YBa_2Cu_3O_{6.3}$ the difference spectra of the optical density $\Delta(\alpha l)_{A+J} = \alpha l(T) - \alpha l(140\ \mathrm{K})$ in the frequency band of the $A+J$ contour for temperatures 20, 44, and 102 K. It is evident that the $A+J$ band in the AF phase does not possess a fine structure and is described well by a single Gaussian contour (1), shown in Fig. 1 (solid curve). The narrow-band $A+J$ absorption band lies against the background of temperature variations for the continuum interband absorption band, for which $\Delta(\alpha l)_{CT} = \alpha l_{CT}(T) - \alpha l_{CT}(140\ \mathrm{K}) \approx -0.05$. Generally speaking, the difference spectrum $\Delta(\alpha l)_{A+J}$ should be determined by the difference of two Gaussian contours (1) with different temperatures. However, if the variance of the Gaussian is a weak function of temperature in the AF phase, then the difference $\Delta(\alpha l)_{A+J}$ itself is essentially a pure Gaussian with $\sigma_{A+J} = \mathrm{const}$ and amplitude coefficient $\Delta\mu_{A+J} = \mu(T) - \mu(140\ \mathrm{K})$. The results presented in Fig. 1 show that for $T < T_N \approx 200$ K the variance of a contour is $\sigma_{A+J} = 0.05$ eV, i.e. in the AF state it decreased several fold, but even in the AF phase itself the variance changes very little on cooling from 140 to 200 K. At the same time, as one can see from Fig. 1, the oscillator strength of the $A+J$ transition increases appreciably as the temperature in the AF phase decreases. Thus, on cooling from 140 to 102 K the addition to the amplitude coefficient is $\Delta\mu_{A+J} = \mu(102\ \mathrm{K}) - \mu(140\ \mathrm{K}) = 0.0036$ eV, and with further cooling to 44 K $\Delta\mu_{A+J} = 0.01$ eV. Thus, in the dielectric phase, for a transition from the short-range AF ordering with $T > T_N$ to long-range AF ordering with $T < T_N$ the variance of the $A+J$ band decreases, the amplitude of the band (optical transition probability) increases and continues to increase right up to 44 K. At temperatures $T \leqslant 44$ K all temperature variations vanish (see Fig. 1). The temperature-independence of the absorption spectra is typical for exciton (electron)–magnon absorption in classical AF crystals at temperatures close to and below the spin-wave gap energy.[15] For dielectric $YBa_2Cu_3O_{6+x}$ this gap is $\Delta_N/k_B \approx 40-60$ K,[16] which explains the absence of variations in the spectra as temperature decreases below 44 K. It should be noted that in the AF phase the Gaussian $A+J$ contour is structureless in the entire experimental temperature range.

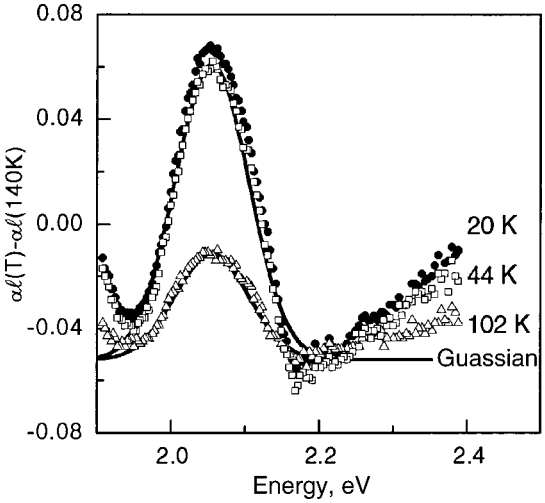

FIG. 1. Temperature variations for the difference absorption spectra $\Delta\alpha l = \alpha l(T) - \alpha l(140\ \mathrm{K})$ of a $YBa_2Cu_3O_{6.3}$ film in the antiferromagnetic phase at different temperatures. The solid lines show the model curves in the form of single Gaussian curves. Key: 1) Energy, eV; 2) Gaussian.

4. We now consider the optical data obtained for the superconducting metallic film $YBa_2Cu_3O_{6+x}$ ($x \approx 0.85$) at temperatures from 170 to 200 K. Both the formation temperature of the PG state $T^* = 120-130$ K and the SC transition temperature $T_c = 88$ K fall into this range. The value $T^* = 120-130$ K was obtained in a number of other independent measurements.[1] We note immediately that at room temperature the electron–bimagnon band $A+J$ was absent in the absolute absorption spectra of this film because the mag-

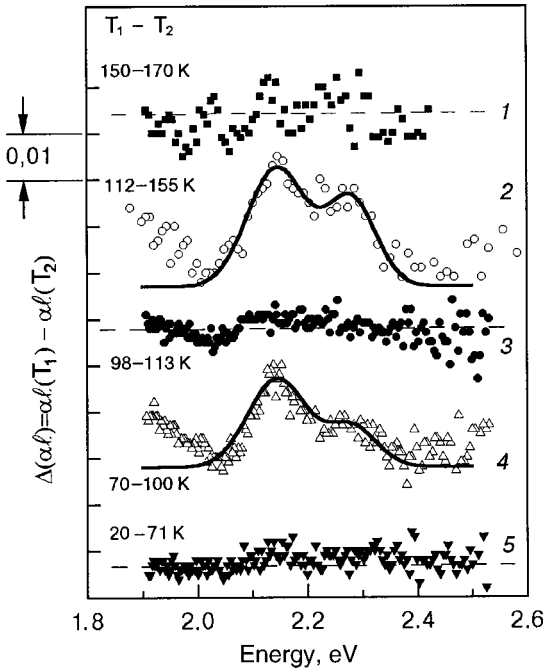

FIG. 2. Temperature variations of the absorption spectra $\Delta\alpha l-\alpha l(T_1)-\alpha l(T_2)$ for a YBCO superconducting film. The temperatures T_1-T_2 for each measurement range are presented to the left of the experimental data. The data *2* correspond to the formation region of the pseudogap and the data *4* to the superconducting states. The solid lines show model curves in the form of a sum of two Gaussians.

nons decay and an electron–hole pair forms in the metallic phase (as shown in our work,[14] at 300 K the $A+J$ maximum shifts and rapidly decays with increasing doping; traces of this maximum can be observed only in undoped films with $x<0.7$).

Figure 2 shows the difference absorption spectra $\Delta(\alpha l)_{A+J}=\alpha l(T_1)-\alpha l(T_2)$, measured in definite temperature ranges on cooling of the film. The data labeled with the number *1* refer to the temperature range from $T_2=170$ K to $T_1=150$ K, i.e. for the region $T>T^*$. It is evident that as temperature decreases, the narrow-band component $A+J$ does not appear (more detailed measurements show that it is absent from the entire range 300–150 K). The data *2* refer to the temperature range 155–112 K, including T^*. It is clearly seen that as the formation temperature of the PG state is crossed, the electron–bimagnon peak does not simply arise, but rather it appears in the form of a doublet band with maxima at $E_{01}=2.145$ eV and $E_{02}=2.28$ eV. (At energies below 2 eV the increase in absorption is due to the appearance of an A contour with maximum near 1.7 eV.[13]) The solid curve shows the sum of two Gaussians of this $A+J$ doublet with $\sigma_1^{A+J}=0.053$ eV, $\sigma_2^{A+J}=0.045$ eV, and $\mu_1^{A+J}=0.0024$ eV, $\mu_2^{A+J}=0.0015$ eV. We underscore that for the PG state the variance of each doublet is essentially the same as that for the AF phase of the dielectric. With further cooling the temperature variations for the doublet which arises vanish (data *3*) in the temperature range from $T_2=113$ K to $T_1=98$ K ($T_c<T<T^*$), $\Delta(\alpha l)_{A+J}=0$. However, according to the data *4*, when the SC transition ($T_c=88\,K$) is crossed in the temperature range 100–70 K, the amplitudes of each peak increase additionally, i.e. the probability of electron–bimagnon excitation increases. The amplitude correction $\Delta\mu_1^{A+J}=0.0018$ eV and $\Delta\mu_2^{A+J}=0.0007$ eV, which corresponds to $\approx 50\%$ of the initial amplitudes of the components with passage of the PG state in the temperature range 112–155 K. The variance of the contour (magnon damping) does not change on passage through T_c. With further cooling from 70 to 20 K, even in the SC phase there are no temperature variations of absorption ($\Delta(\alpha l)_{A+J}=0$, data 5), i.e. the doublet structure itself of the $A+J$ band and the parameters of the band remain unchanged in the entire region of the SC state.

5. Briefly summarizing the results obtained, we note first that in the metallic phase of YBCO the electron–bimagnon band possesses a doublet structure similar to that observed in the inelastic neutron scattering peak. This is the first observation of such an effect in HTSC optics. Optical investigations clearly show that the doublet structure arises on passing through the PG state. Neutron scattering data have made it possible to observe the doublet structure at temperatures only several degrees above T_c.[5] Our optical investigations show quite unequivocally that the doublet structure reflecting the stripe state in $YBa_2Cu_3O_{6+x}$ appears quite sharply precisely near $T^*=120-130$ K. The energy splitting between the doublet components $\Delta E=0.14$ eV can be compared with the neutron scattering data. Thus, according to the neutron data, for YBCO near optimal doping the difference of the wave vectors for incommensurate spin fluctuations responsible for the splitting of the inelastic neutron scattering peak is $\Delta k=0.2$ Å^{-1}. This splitting corresponds, to a first approximation, to the energy difference $\Delta E=\Delta k\hbar v=0.12$ eV, where $\hbar v=0.6$ eV·Å is the velocity of spin waves in YBCO.[17] The quantity ΔE corresponds to the splitting of the dispersion curve for magnons, because of the appearance of the stripe superstructure. The neutron value Δk and the optical value ΔE of the splittings agree well with one another. The results presented probably serve as the first optical proof of the stripe structure of the PG state. It can also be asserted that the formation of the PG state is a necessary condition for the appearance of superconductivity in YBCO. The doublet structure of the ''magnon'' absorption band remains in the temperature range of the SC phase. This undoubtedly attests to the compatibility of the short-range AF order and superconductivity, and superconductivity is probably established as a result of the global phase coherence between the metallic stripe phases formed in the PG state.

We also call attention to a nontrivial effect which appears with the formation of the SC state. It turns out that for formation of the SC phase the probability of electron–bimagnon excitation increases substantially, but the variance of the Gaussian contours, i.e. the damping of the magnons, remains practically unchanged. This result definitely requires a special theoretical analysis.

On the methodological level our results also show that optical absorption spectroscopy can be used actively to determine the nature of superconductivity in cuprate HTSCs, especially in polarization measurements. The high information content of this method cannot to be compared with its limited use at low frequencies for classical superconductors with the standard electron–phonon pairing mechanism.

In closing, we wish to thank the scientific group of Professor G. Zaĭmann-Ishchenko (Erlangen University, Germany) for providing the YBCO films for the experiments.

*E-mail: samovarov@ilt.kharkov.ua

[1] T. Timusk and B. Statt, Rep. Prog. Phys. **62**, 61 (1999).
[2] Yu. A. Izyumov, Usp. Fiz. Nauk **169**, 225 (1999).
[3] G. G. Sergeeva, Yu. P. Stepanovskiĭ, and A. V. Chehckin, Fiz. Nizk. Temp. **24**, 1029 (1998) [Low Temp. Phys. **24**, 771 (1998)].
[4] S. G. Ovchinnikov, Usp. Fiz. Nauk **167**, 1043 (1997).
[5] S. G. Dai, H. A. Mook, and F. Dogan, Phys. Rev. Lett. **80**, 1738 (1998).
[6] V. J. Emergy, S. A. Kivelson, and O. Zachar, Phys. Rev. B **56**, 6120 (1997).
[7] V. M. Loktev and S. G. Sharapov, Condens. Matter Phys. **11**, 131 (1997).
[8] Yu. G. Pashkevich, V. A. Blinkin, V. P. Gnezdilov, V. V. Tsapenko, V. V. Eremenko, P. Lemmens, M. Fishcher, M. Grove, G. Güntherodt, L. Degiorgi, P. Wachter, J. M. Tranquada, and D. J. Buttrey, Phys. Rev. Lett. **84**, 3919 (2000).
[9] J. Zaanen and O. Gunnarsson, Phys. Rev. B **40**, 7391 (1989).
[10] I. Fugol, B. Saemann-Ischenko, V. Samovarov, Yu. Rybalko, V. Zhuravlev, Y. Ströbel, B. Holzäpfel, and P. Berberich, Solid State Commun. **80**, 201 (1991).
[11] C. H. Rüscher, M. Götte, C. Quimann, and G. Güntherodt, Physica C **204**, 30 (1992).
[12] I. Ya. Fugol, V. N. Samovarov, and M. Yu. Libin, Fiz. Nizk. Temp. **25**, 459 (1999) [Low Temp. Phys. **25**, 459 (1999)].
[13] V. V. Eremenko, V. N. Samovarov, V. L. Vakula, M. Yu. Libin, and S. A. Uyutnov, Fiz. Nizk. Temp. **26**, 1091 (2000) [Low Temp. Phys. **26**, 809 (2000)].
[14] V. V. Eremenko, V. N. Samovarov, V. N. Svishchev, V. L. Vakula, M. Yu. Libin, and S. A. Uyutnov, Fiz. Nizk. Temp. **26**, 739 (2000) [Low Temp. Phys. **26**, 541 (2000)].
[15] V. V. Eremenko, I. S. Kachur, V. G. Piryatninskaya, and V. V. Slavin, Fiz. Nizk. Temp. **18**, 380 (1992) [Low Temp. Phys. **18**, 258 (1992).
[16] V. L. Alsenov and V. V. Kabanov, Phys. Rev. B **49**, 3524 (1994).
[17] Yu. A. Izyumov, N. M. Plakida, and Yu. N. Skryabin, Usp. Fiz. Nauk **159**, 621 (1989).

Translated by M. E. Alferieff

LETTER TO THE EDITOR

Nonmagnetic spinguides and spin transport in semiconductors

R. N. Gurzhi,* A. N. Kalinenko, A. I. Kopeliovich, and A. V. Yanovskiĭ

B. I. Verkin Physicotechnical Institute for Low Temperatures, Ukrainian National Academy of Sciences, pr. Lenina 47, Khar'kov, 61103, Ukraine
(Submitted July 23, 2001)
Fiz. Nizk. Temp. **27**, 1332–1334 (November 2001)

The construction of a spinguide—a semiconductor channel with walls consisting of a dilute magnetic semiconductor with very large Zeeman splitting and transmitting electrons only with one type of polarization—is proposed. Such channels can be sources of spin-polarized current in nonmagnetic conductors. They can be used for creating fast switches of the spin-polarization direction of the electric current and for transmitting spin polarization over large distances (even larger than the spin-flip length). The selective transparency of the walls gives rise to new size transport effects. © *2001 American Institute of Physics.* [DOI: 10.1063/1.1421468]

1. Interest in spin transport phenomena has been increasing constantly in the last few years. One of the most important problems in this field is obtaining a spin-polarized current in nonmagnetic semiconductors (NS), because combining magnetic conservation information with electronic counting in a single semiconductor device gives a variety of obvious technological advantages. In ordinary ferromagnetic conductors the electric current is polarized to the extent that the density of states differs for up and down spins; there are a number of difficulties in obtaining a stationary spin polarization in NS. The simplest idea—passage of current through a ferromagnetic metal–semiconductor interface[1]—permits polarizing the current only to a fraction of a percent.[2] This inefficiency is due, on the one hand, to the substantial difference of the conductivities of the ferromagnetic metal and semiconductor and, on the other, to the fact that in metal ferromagnets with good polarizability the electron mean-free path lengths are short compared with the spin-flip length.

A new, extremely effective method of spin polarization of the electric current in NS was recently realized experimentally.[3] In this experiment, a sample of a diluted magnetic semiconductor (DMS) based on $Be_xMn_yZn_{1-x-y}Se$ with giant splitting of the spin subbands in a magnetic field (the effective g factor of the Zeeman splitting is of the order of 100; the properties of DMS are reviewed in Refs. 4 and 5) was used as a spin filter. The idea of a spin filter is based on the fact that a situation where the Fermi level in the DMS lies below the bottom of one of the spin subbands is entirely realistic and, consequently, at sufficiently low temperatures energy conservation forbids the spin-flip process. In addition, the DMS in this experiment has a remarkable similarity to the NS used (gallium-arsenide based semiconductor) right up to the crystal lattice parameters being the same. Since spin flip in NS, being a relativistic effect, corresponds to large travel distances (in some substances up to 100 μm),[3,6] a system of serially connected DMS and NS samples is ideally suited for spin polarization of the current. Correspondingly, almost 100% polarization of the current flowing from DMS into NS is obtained in the experiment of Ref. 3.

An important problem in using spin filters is that it is impossible to switch rapidly the direction of the polarization because strong magnetic fields are used. The switching time even for a not very strong magnetic field is long compared with any mesoscopic, including diffusion, times. The generation of strongly nonuniform fields with an alternating sign on microscopic scales is also technologically a difficult problem. One possibility of creating miniature and fast spin-polarization switches that eliminates the indicated problems is to use the ''nonmagnetic spinguides'' proposed in the present paper.

2. *Nonmagnetic spinguides*. A nonmagnetic spinguide is a channel (tube or strip) made of an NS with walls made of DMS. In contrast to Ref. 3, in this case the electric current flows along, and not perpendicular to, the interface (Fig. 1). It is assumed that the spinguide walls transmit electrons with one polarization and reflect electrons with the other polarization. The NS is unpolarized in the absence of current (in an equilibrium situation). However, the current passed along the spinguide will be polarized, since the nonequilibrium electrons with spins possessing one polarization will leave the channel. But, for this, the DMS must be grounded. Otherwise, if spin-flip processes are absent, the same unpolarized current as at the entrance will occur at the exit from the channel.

Let us consider a diffusion transport regime where the diffusion length δl is much less than the channel width w: $\delta l = \min\{r_c, l_i\} \ll w$, where r_c is the cyclotron radius and l_i is the electron–impurity mean-free path. In this paper electron–electron collisions are neglected; this is clearly valid at temperatures of the order of several degrees Kelvin. Let $\mu_{\uparrow,\downarrow}$ be the electrochemical potentials of carriers with up and down spins, respectively. The electric current densities $J_{\uparrow,\downarrow} = -e^{-1}\sigma\cdot\nabla\mu_{\uparrow,\downarrow}$ (for simplicity, it is assumed that the conductivity σ is the same in the NS and DMS). For defi-

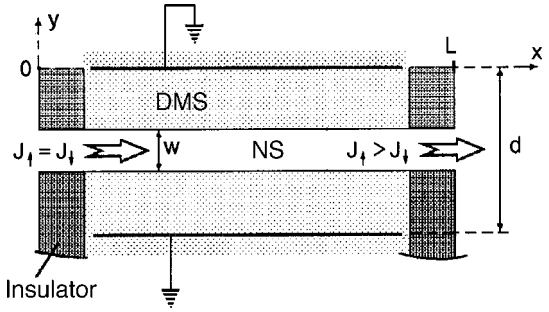

FIG. 1. Spinguide scheme: L channel length, w channel width, d distance between grounding contacts.

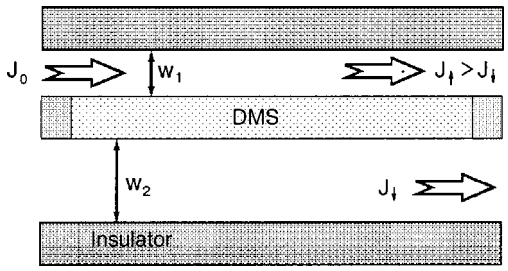

FIG. 2. Entrainment through the DMS interlayer: w_1, w_2 channel widths.

niteness, we assume that the spinguide walls pass only electrons with downward spin, i.e. at the channel boundaries $\partial\mu_\uparrow/\partial y=0$ (it is assumed that there is no dependence on the coordinate z). The grounding condition must be added to this: $\mu=0$ at the grounding contacts. Let unpolarized current $J_0=2J_\uparrow(x=0)=2J\mu_\downarrow(x=0)$ be fed into the input. The diffusion equation $\Delta\mu_{\uparrow,\downarrow}=0$, taking account of these boundary conditions, can be solved exactly. For $L\gg d$, where d is the distance between the grounding contacts, the current $J_\downarrow$ at the channel exit will decrease exponentially with increasing channel length: $J_\downarrow\propto\exp\{-\pi L/d\}$. Taking account of the trivial result $J_\downarrow=J_0/2$ it is easy to see that the spin polarization of the current at the channel exit approaches 1 exponentially with increasing L:

$$\alpha=\frac{J_\uparrow-J_\downarrow}{J_\uparrow+J_\downarrow}=1-c\exp\left\{-\frac{\pi L}{d}\right\},\quad c\sim 1. \tag{1}$$

It is obvious that the spin polarization of the current α depends very strongly on the geometry of the grounding contacts.

Evidently, the direction of the spin polarization in the spinguide is opposite to the polarization in the spin-filter scheme of Ref. 3 with the same polarization of the DMS. Therefore, combining the spin filter and spinguide with electrostatic valves it is easy to switch the spin polarization of the current.

We note that the spin-flip processes in NS have a much weaker effect on the current polarization in a spinguide than in a spin filter. In the latter the spin polarization of the current decays over a distance $\lambda_s=\sqrt{l_i l_s}$, where l_s is the mean-free path length relative to spin-flip processes in the NS. The spin-flip processes in a spinguide appear much differently. They have virtually no effect on the polarization ($\lambda_s\gg d$) and lead only to a decrease of the total current over a distance λ_s (in the geometry shown in Fig. 1—exponentially).

We shall indicate one other possible formulation of the experiment—"spin entrainment" (Fig. 2). An unpolarized current is introduced into channel 1, and in the process a completely polarized current—$\alpha=1$—arises in channel 2, separated from channel 1 by a DMS interlayer. The polarization at the exit of channel 1 will depend on the relative width of the channels. If the thickness of the DMS interlayer is less than w_1 and w_2 and $L\gg w_1$, w_2, we have

$$\alpha=\frac{1-\gamma}{1+\gamma},\quad \gamma=\frac{w_1}{w_1+w_2}. \tag{2}$$

The current in channels 1 and 2 are oppositely polarized, and the total current along the two channels is, naturally, unpolarized. Curiously, in the limit of a wide channel 2, $w_1\ll w_2\ll L$, the polarized currents will be divided equally between the channels, i.e. a completely spin-polarized current $J_\uparrow=J_0/2$, equal in magnitude and opposite in polarization to the current in channel 2, will flow in channel 1. The derivation of Eq. (2) assumed that a potential equal to the potential at the exit from channel 1 is applied to the exit from channel 2. (The potential at the exit from channel 1 in our model is determined by the magnitude of the current J_0.) The polarization current in the channels can be controlled by varying the potential at the exit from channel 2.

3. On this basis, spinguides make it possible to achieve a high degree of current polarization in a nonmagnetic conductor. Although the spin filters employed also give a high degree of polarization, spinguides could be helpful in controlling the spin-polarization current and polarization transport over large distances even in the presence of spin-flip processes. In addition, under conditions of selective transparency of the interfaces curious features of the galvanomagnetic phenomena in such systems could appear. Specifically, we note that delocalized states in a magnetic field at the DMS–NS interface (corresponding to classical hopping orbits) will be completely spin-polarized.

*E-mail: gurzhi@ilt.kharkov.ua

[1] H. X. Tang, F. G. Monzon, R. Lifshitz, M. C. Cross, and M. L. Roukes, Phys. Rev. B **61**, 4437 (1999).
[2] G. Shmidt, D. Ferrand, L. A. T. Filip, L. W. Molenkamp, and B. J. van Wees, Phys. Rev. B **62**, R4790 (2000).
[3] R. Fiederling, M. Keim, G. Reuscher, W. Ossau, G. Schmidt, A. Waag, and L. W. Molenkamp, Nature (London) **402**, 787 (1999).
[4] N. B. Brandt and V. V. Moschchalkov, Adv. Phys. **33**, 193 (1984).
[5] I. I. Lyapilin and I. M. Tsidil'kovskiĭ, Usp. Fiz. Nauk **146**, 35 (1985).
[6] V. F. Gantmakher and I. B. Levinson, *Scattering Current in Metals and Semiconductors* (Nauka, Moscow, 1984).

Translated by M. E. Alferieff

CHRONICLE

Cryogenic scientific instrument building at the LT-32 conference

É. Ya. Rudavskiĭ

B. I. Verkin Physicotechnical Institute for Low Temperatures, Ukrainian National Academy of Sciences, pr. Lenina 47, Khar'kov, 61103, Ukraine

Fiz. Nizk. Temp. **27**, 1335–1336 (November 2001)

[DOI: 10.1063/1.1421469]

A number of leading companies and scientific centers exhibited new cryogenic and vacuum technology in the recent low-temperature physics LT-32 conference in Kazan' (October 2000).[1] A special exhibit of scientific cryogenic instrument building was organized. Participant's included Oxford Instruments Superconductivity (Great Britain), Leiden Cryogenics (Holland), Nanoway Oy and University of Jyvaskyla (Finland), the Scientific–Industrial Associations ''Vakuummash'' and ''Élekon'' (Kazan'), and the Institute for Semiconductors of the Ukrainian National Academy of Sciences (Kiev).

In a plenary report Professor V. A. Mikheev noted that Oxford Instruments Superconductivity, which he represents, is now the main developer and manufacturer of various equipment for fundamental and applied research in low-temperature physics. The company leads in developing scientific apparatus for modern cryogenics and for generating strong magnetic fields and low and superlow temperatures and for producing superconductor systems, vacuum technology, and electronics. Here, a high-resolution NMR system, the first such system in the world, with a 21.1 T superconducting magnet operating at 900 MGz was developed and implemented experimentally. This system, which sets a record with respect to its parameters, gives physicists a new high-sensitivity tool for studying three-dimensional structures of various objects. The company has also developed the Teslatron superconducting magnetic system, which makes it possible simultaneously to produce magnetic fields up to 20 T and to cool the experimental sample below 10 mK. Extensive use of superconducting magnets for magnetic separation of different minerals was noted.

Oxford Instruments Superconductivity has also developed diverse systems for physical research at superlow temperatures in solid-state physics, for cooling a new generation of gravitational-wave attennas, for experiments on detecting ''dark'' matter, for superfluid gyroscopes, and for experiments with scanning tunneling microscopes. The Kelvinox dilution refrigerators make it possible to cool down to 7 mK and the Heliox evaporation refrigerators with ^{3}He make it possible to perform measurements down to 250 mK. Recently, dilution refrigerators with a cryogenic circulation cycle, which do not require a complicated piping system and strongly decrease the level of vibrations, were developed using the cryogenic adsorption technique. Many of these developments were presented at the Oxford Instruments exhibit. A helium transfer apparatus with very low losses was also demonstrated.

Leiden Cryogenics introduced to the participants at the conference the company's models of modern dilution refrigerators, which are oil-free and use in the circulation system convenient turbomolecular pumps. The simplest refrigerators developed—the MSK type—are 27 or 50 mm in diameter and 900 mm long. They make it possible to obtain temperatures down to 50 mK with cooling power 30–40 μW at 120 mK. Some models are made completely of plastic, including heat exchangers, which is especially convenient when working with rapidly varying magnetic fields. Another series of dilution refrigerators—the MNK type—corresponds to machines with average cooling power 100–700 μW at 120 mK and give temperatures 40–70 mK. The diameter of the vacuum jacket in these refrigerators ordinarily is 80 mm. The most powerful dilution refrigerators developed—the DRS series—have a cooling power of 3000 μW at 120 mK and 20 μW at 12 mK. The minimum attainable temperature in these refrigerators is 5 mK.

J. P. Pekola, representing Jyvakyla University and and Nanoway Oy (Finland), described in his section report new developments in cryogenic technology. A microcooling method based on electron tunneling through a normal metal–insulator–superconductor contact was described. This idea, proposed about 20 years ago in an investigation of nonequilibrium superconductivity, was recently realized by the author. With an appropriate bias voltage on the contact the ''hot'' electrons can be removed from the normal metal and a thermally insulated phonon system can ultimately be cooled. Using copper as the normal metal and aluminum as the superconductor, cooling from 0.3 to 0.1 K with cooling power exceeding 10 pW was achieved. Such refrigerators can be used in astronomy to cool highly sensitive alpha-particle or x-ray detectors. A microcalorimeter employing superconducting film sensors and operating near the transition temperature was also proposed for this purpose.

Another Jyvakyla development was also presented at the exhibit—a so-called Coulomb blockade nanothermometer. This device can be used to determine the absolute temperature via measurements of the differential resistance of small tunneling junctions as a function of the bias voltage. The thermometer is essentially insensitive to magnetic fields, it operates at temperatures in the range 20 mK–30 K, and its absolute error is 0.5%.

The Kazan' Scientific–Industrial Association ''Vakuummash'' presented new developments in vacuum technology. The products include two-rotor vacuum pumps (Roots type), plate–rotor vacuum pumps, rotational vacuum units, membrane vacuum pumps, and vacuum compressor–pumps. The Association has also developed a new generation of high-vacuum diffusion vapor–oil pumps with an extended range of working pressures at low vacuum, including booster vapor–oil pumps and high-vacuum diffusion units. An electric discharge getter–ion vacuum pump, operating in the pressure range $1.3\times10^{-3}-6.6\times10^{-8}$ Pa, is suggested for physical experiments where a high or ultrahigh oil-free vacuum is required. The Association also presented several models of vacuum metallization setups for depositing metal coatings, nitrides, oxides, or multilayer coatings in vacuum. Diverse models of vacuum valves with manual, electromechanical, or electromagnetic drive are also offered.

Another Kazan' Scientific–Industrial Association ''Élekom'' presented at the conference various air-tight seals, and the Institute for Semiconductors of the Ukrainian National Academy of Sciences from Kiev introduced a DVT-1 diode thermometer operating in the temperature range 4.2–500 K and possessing high sensitivity and good reproducibility.

[1] V. G. Peschanskiĭ, É. Ya. Rudavskiĭ, and D. A. Tayurskiĭ, Fiz. Nizk. Temp. **27**, 565 (2001) [Low Temp. Phys. **27**, 417 (2001)].

Translated by M. E. Alferieff

PERSONALIA

Aleksandr Il'ich Akhiezer—In commemoration of his 90th Birthday

Fiz. Nizk. Temp. **27**, 1337–1338 (November 2001)
[DOI: 10.1063/1.1421470]

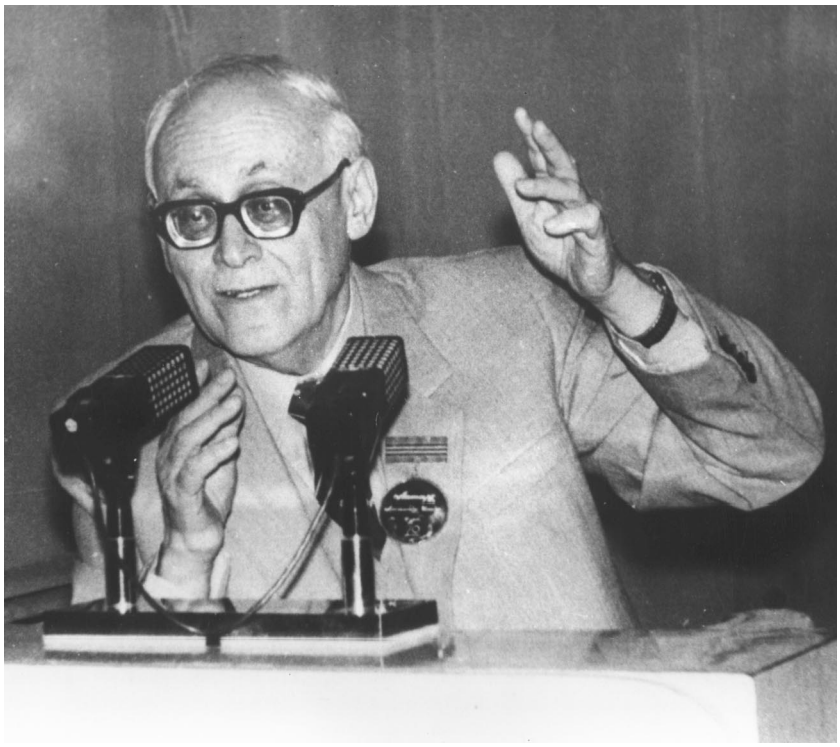

On October 31, 2001 ninety years will have passed since the day that Aleksandr Il'ich Akhiezer, Academician of the Ukrainian National Academy of Sciences, remarkable scientist, leading theoretical physicist, and unusual person, was born.

A. I. Akhiezer was born in Cherikov in Belorus into the family of a district doctor. He began his scientific career in 1935 in Khar'kov in the L. D. Landau Theoretical Division at the Ukrainian Physicotechnical Institute (UPTI). Throughout his life Aleksandr Il'ich loved and admired his teacher Landau.

In 1938 A. I. Akhiezer became the director of the theoretical division at UPTI (after Landau) and remained in this position until 1988. A. I. Akhiezer's interests include quantum electrodynamics, elementary particle physics, nuclear physics, the theory of linear accelerators, solid-state physics and magnetism, plasma physics, magnetohydrodynamics, the theory of the interaction of charged particles with crystals. A. I. Akhiezer has made a leading contribution to these fields of physics. He was a scientist with encyclopedic knowledge and intuition of great genius.

A. I. Akhiezer was an original scientific leader, teacher of a number of generations of theoretical physicists, and one of the creators of the Khar'kov School of Theoretical Physics. Some of his students are founders of scientific schools. A. I. Akhiezer's students include 33 doctors and 72 candidates of physicomathematical sciences, seven members of the Ukrainian National Academy of Sciences (Academicians V. G. Bar'yakhtar, D. V. Volkov, S. V. Peletminskiĭ, A. G. Sitenko, Ya. B. Faĭnberg, and Corresponding Members of the Ukrainian National Academy of Sciences K. N. Stepanov and P. I. Fomin). The Institute of Theoretial Physics at the National Science Center ''Khar'kov Physicotechnical Institute'' was created under the initiative and efforts of A. I. Akhiezer and is now named after him.

Aleksandr Il'ich's pedagogical work found appropriate fruition in the publication of a large number of textbooks and scientific monographs. They include world-renowned monographs on quantum electrodynamics, nuclear theory, spin waves, plasma electrodynamics, statistical physics, the electrodynamics of high energies in matter, and the theory of fundamental interactions as well as textbooks on virtually all

branches of general physics. These books have played a leading role in the training of highly skilled physicists.

A. I. Akhiezer was awarded orders and medals for his pedagogical and organizational work. He was awarded the L. I. Mandel'shtam, N. N. Bogolyubov, and S. A. Davydov Academic Prizes, the I. Ya. Pomeranchuk International Prize, and the Ukrainian State Prize in Science and Technology.

Everyone who had the good fortune to associate with him remembers him as a talented man with enormous erudition, inexhaustible energy, optimism and enormous working capacity, amazing charm and kindness, sociability, and witiness.

V. G. Bar'yakhtar, S. Ya. Braude, M. S. Brodin, Yu. I. Gorobets, B. V. Grinev, V. V. Eremenko, A. G. Zagorodniĭ, I. I. Zalyubovskiĭ, V. F. Zelenskiĭ, V. F. Klepikov, V. I. Lapshin, D. N. Litvinenko, V. M. Loktev, V. G. Manzheliĭ, A. G. Naumovets, I. M. Neklyudov, O. F. Nemets, S. V. Peletminskiĭ, S. M. Ryabchenko, V. P. Seminozhenko, A. G. Sitenko, V. V. Slezov, K. N. Stepanov, V. T. Tolok, Ya. B. Faĭnberg, P. I. Fomin, N. F. Shul'ga, V. M. Yakovenko, and Ya. S. Yatskiv.

Translated by M. E. Alferieff

ERRATA

Erratum: Structural investigations of superconducting multilayers consisting of semiconducting materials [Low Temp. Phys. 27, 93 (February 2001)]

A. I. Erenburg and Yu. V. Bomze

B. Verkin Institute for Low Temperature Physics and Engineering, 47 Lenin Ave., 61164 Kharkov, Ukraine

N. Ya. Fogel

B. Verkin Institute for Low Temperature Physics and Engineering, 47 Lenin Ave., 61164 Kharkov, Ukraine; Department of Applied Physics, Department of Environmental Inorganic Chemistry, and Department of Engineering Metals, Chalmers University of Technology, S-41296, Göteborg, Sweden

A. Yu. Sipatov and A. I. Fedorenko

Kharkov State Polytechnic University, 27 Frunze Street, 61002 Kharkov, Ukraine

V. Langer and M. Norell

Department of Applied Physics, Department of Environmental Inorganic Engineering Chemistry, and Department of Engineering Metals, Chalmers University of Technology, S-41296, Göteborg, Sweden

Fiz. Nizk. Temp. **27**, 1339 (November 2001)

[DOI: 10.1063/1.1421471]

The corrected Figure 1 should be as follows:

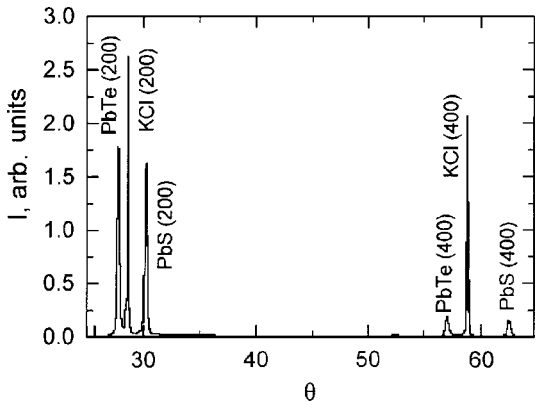

FIG. 1. Diffractogram of PbTe/PbS SL.

Translated by M. E. Alferieff

